



**HAL**  
open science

# Borane adsorption on MgO nanoparticles for increased catalytic activity in the cycloaddition of CO<sub>2</sub> on epoxides

Cyprien Poucin

► **To cite this version:**

Cyprien Poucin. Borane adsorption on MgO nanoparticles for increased catalytic activity in the cycloaddition of CO<sub>2</sub> on epoxides. Material chemistry. Sorbonne Université, 2023. English. NNT : 2023SORUS142 . tel-04885093

**HAL Id: tel-04885093**

**<https://theses.hal.science/tel-04885093v1>**

Submitted on 14 Jan 2025

**HAL** is a multi-disciplinary open access archive for the deposit and dissemination of scientific research documents, whether they are published or not. The documents may come from teaching and research institutions in France or abroad, or from public or private research centers.

L'archive ouverte pluridisciplinaire **HAL**, est destinée au dépôt et à la diffusion de documents scientifiques de niveau recherche, publiés ou non, émanant des établissements d'enseignement et de recherche français ou étrangers, des laboratoires publics ou privés.



Sorbonne Université

Ecole doctorale 397, Physique et Chimie des Matériaux

*Laboratoire de Chimie de la Matière Condensée de Paris (LCMCP)*

# **Borane adsorption on MgO nanoparticles for increased catalytic activity in the cycloaddition of CO<sub>2</sub> on epoxides**

Par **Cyprien POUCIN**

Thèse de doctorat de Chimie de Sorbonne Université

Dirigée par Dr. Sophie CARENCO

Devant un jury composé de :

MAMMERI Fayna	Maitresse de conférence – Université Paris Cité	Rapporteuse
HUC Vincent	Directeur de recherches – Université Paris-Saclay	Rapporteur
LAUNAY Franck	Professeur – Sorbonne Université	Examineur
CARENCO Sophie	Directrice de recherches – Sorbonne Université	Directrice de thèse



# Abstract

Carbon dioxide capture and valorisation have become major challenges for the future decades. Capture technologies are already mature enough to start being implemented at industrial scale but valorisation technologies are still lacking. This thesis work focuses on the development of new catalysts for CO<sub>2</sub> chemical valorisation. The bibliographic introduction emphasizes the potential alkaline earth oxides for CO<sub>2</sub> capture and valorisation due to their ability to easily form carbonates, as well as the recent development of Frustrated Lewis Pair (FLP) chemistry for the activation of small molecules like CO<sub>2</sub>. We propose a strategy to synthesize magnesium oxide nanoparticles functionalised with borane ligands to create FLP-like interaction at the surface and increase the catalytic activity of the nanoparticles in the cycloaddition of CO<sub>2</sub> on epoxides.

In the first part of this work, the synthesis of magnesium oxide nanoparticles by precipitation-calcination is studied. Reaction parameters like calcination temperature and post-synthesis washings are shown to impact the nanoparticles morphology and surface state. The second part of this work focuses on borane adsorption on MgO nanoparticles with and without presence of CO<sub>2</sub>. Proof of a MgO-CO<sub>2</sub>-BPh<sub>3</sub> interaction is found using infrared spectroscopy analyses. A unique interaction between MgO and the chloroborane BCl<sub>2</sub>Ph is evidenced by a visual colour change of the nanoparticles and by infrared spectroscopy. The last part of this work focuses on the catalytic study of the cycloaddition reaction. Comparison between the different MgO catalysts confirms the importance of the nanoparticles synthesis parameters on their activity. Adsorption of borane modifies the MgO activity and/or selectivity depending on the reaction solvent. The addition of BCl<sub>2</sub>Ph increases the activity of the MgO catalyst by a factor 10 but also reduces the selectivity toward cyclic carbonate. Impact of temperature, concentration and reaction duration on the catalytic performances of this nanoparticle-ligand pair is studied to unveil the origin of this unreported synergy between MgO and BCl<sub>2</sub>Ph.

## Abstract

La capture et la valorisation du dioxyde de carbone sont devenus des défis majeurs pour les décennies à venir. Les technologies de capture sont déjà suffisamment matures pour être mises en œuvre à l'échelle industrielle, mais les technologies de valorisation font encore défaut. Ce travail de thèse se concentre sur le développement de nouveaux catalyseurs pour la valorisation chimique du CO<sub>2</sub>. L'introduction bibliographique souligne le potentiel des oxydes alcalino-terreux pour la capture et la valorisation du CO<sub>2</sub> en raison de leur capacité à former facilement des carbonates, ainsi que le développement récent de la chimie des Paires de Lewis Frustrées (FLP) pour l'activation de petites molécules comme le CO<sub>2</sub>. Nous y proposons une stratégie de synthèse de nanoparticules d'oxyde de magnésium fonctionnalisées avec des ligands boranes pour créer une interaction de type FLP à la surface et augmenter l'activité catalytique des nanoparticules dans la cycloaddition du CO<sub>2</sub> sur des époxydes.

Dans la première partie de ce travail, la synthèse de nanoparticules d'oxyde de magnésium par précipitation-calcination est étudiée. Les paramètres de réaction tels que la température de calcination et les lavages post-synthèse ont un impact sur la morphologie et l'état de surface des nanoparticules. La deuxième partie de ce travail se concentre sur l'adsorption de boranes sur les nanoparticules de MgO avec et sans présence de CO<sub>2</sub>. La preuve d'une interaction MgO-CO<sub>2</sub>-BPh<sub>3</sub> est apportée par des analyses de spectroscopie infrarouge. Une interaction unique entre MgO et le chloroborane BCl<sub>2</sub>Ph est mise en évidence par un changement de couleur visuel des nanoparticules ainsi que par spectroscopie infrarouge. La dernière partie de ce travail se concentre sur l'étude catalytique de la réaction de cycloaddition. La comparaison entre les différents catalyseurs MgO confirme l'importance des paramètres de synthèse des nanoparticules sur leur activité. L'adsorption de boranes modifie l'activité et/ou la sélectivité de MgO en fonction du solvant de réaction. L'ajout de BCl<sub>2</sub>Ph augmente l'activité du catalyseur MgO d'un facteur 10 mais réduit également sa sélectivité vers la formation du carbonate cyclique. L'impact de la température, de la concentration et de la durée de la réaction sur les performances catalytiques de ce couple nanoparticule-ligand est étudié afin de dévoiler l'origine de cette synergie inédite entre MgO et BCl<sub>2</sub>Ph.

# Table of contents

<b>Chapter I: Global warming calling for CO<sub>2</sub> mitigation.....</b>	<b>11</b>
<b>I. Variability of CO<sub>2</sub> atmospheric concentration .....</b>	<b>15</b>
1. Pre-industrial CO <sub>2</sub> atmospheric concentration .....	15
2. Impact of the industrial revolution.....	16
<b>II. Earth surface temperature.....</b>	<b>18</b>
1. Earth radiative budget without greenhouse effect.....	18
2. Greenhouse effect and radiative forcing.....	19
<b>III. Strategies to reduce CO<sub>2</sub> atmospheric concentrations by the end of the century .....</b>	<b>19</b>
1. History of the comprehension of the earth climate system .....	19
2. Current strategies for CO <sub>2</sub> mitigations.....	20
<b>IV. Necessity for CO<sub>2</sub> capture and valorisation .....</b>	<b>21</b>
<b>V. Conclusion.....</b>	<b>22</b>
<b>Chapter II: Toward the design of a new active catalytic systems for CO<sub>2</sub> valorisation.....</b>	<b>25</b>
<b>I. CO<sub>2</sub> valorisation in industrial processes .....</b>	<b>29</b>
1. Reactivity of CO <sub>2</sub> molecules.....	29
a. Thermodynamic considerations .....	29
b. Orbital considerations .....	31
2. Direct CO <sub>2</sub> usage .....	31
3. Industrial processes using CO <sub>2</sub> .....	33
a. Urea synthesis.....	33
b. Salicylic acid synthesis .....	33
c. Dry reforming of methane.....	34
d. CO <sub>2</sub> electro-reduction .....	34
<b>II. The recent development of Frustrated Lewis Pair catalysis for the conversion of CO<sub>2</sub>.....</b>	<b>36</b>
1. The concept of Frustrated Lewis Pair catalysis .....	36
2. FLPs for CO <sub>2</sub> activation.....	36

3.	Non-molecular FLPs.....	38
III.	Forming a FLP interaction between a nanoparticle surface and its ligands to activate CO <sub>2</sub> : the NanoFLP project.....	39
IV.	Materials known for CO <sub>2</sub> adsorption and/or activation in catalysis.....	40
1.	Materials with Lewis base properties: alkaline-earth oxides .....	40
a.	Generalities on heterogeneous solid bases .....	40
b.	Basicity scale for heterogeneous solid bases.....	41
c.	Intrinsic bifunctionality of heterogeneous basic oxides .....	43
d.	Alkaline-earth oxides and their affinity toward CO <sub>2</sub> .....	43
2.	MgO: synthesis and applications .....	45
a.	Generalities on magnesium-based materials .....	45
b.	Synthesis of MgO precursor .....	46
c.	Calcination of the precursor to form MgO.....	47
d.	Applications of MgO .....	49
e.	MgO in catalysis .....	49
3.	CaO: synthesis and applications .....	51
a.	Calcium oxide synthesis.....	51
b.	Application of CaO for CO <sub>2</sub> capture.....	51
c.	CaO in catalysis .....	52
V.	Classical molecular acids used in the FLP adducts: boranes.....	53
1.	Boranes in catalysis .....	53
2.	Boranes for CO <sub>2</sub> activation .....	54
VI.	Approach for the design of a NanoFLP pair for CO <sub>2</sub> activation.....	55
<b>Chapter III: Synthesis of basic alkaline-earth oxides nanoparticles and activity in the Claisen-Schmidt condensation.....</b>		<b>63</b>
I.	Experimental section .....	68
II.	Synthesis of simple and mixed oxide nanoparticles by precipitation-calcination .....	70
1.	Synthesis of MgO .....	70
a.	Precipitation-calcination synthesis .....	70
b.	Modification of the calcination temperature .....	72
c.	Modification of the washing step .....	73
2.	Synthesis of CaO .....	75
3.	Attempts to synthesise MgO-CaO mixed oxides.....	77

Table of contents

4. Attempts to synthesize MgO-M (M = Co, Ni, Cu) .....	81
<b>III. Surface state of MgO nanoparticles.....</b>	<b>87</b>
1. Ageing of MgO nanoparticles under ambient air .....	87
2. IR spectrum of MgO nanoparticles .....	87
3. Repeatability of the MgO synthesis .....	89
<b>IV. MgO nanoparticles as catalyst in the Claisen-Schmidt condensation .....</b>	<b>90</b>
1. The Claisen-Schmidt condensation .....	90
2. Activity of the synthesized MgO nanoparticles .....	91
a. First catalytic test.....	92
b. Comparison to Bain study.....	94
3. Activity of the pair MgO+BPh <sub>3</sub> .....	95
4. Conclusion .....	96
<b>V. Conclusion.....</b>	<b>97</b>
<b>VI. Annexes.....</b>	<b>98</b>

**Chapter IV: Adsorption of CO<sub>2</sub> and boranes on MgO surfaces.....101**

<b>I. Carbonate formation on MgO surface .....</b>	<b>105</b>
1. IR spectroscopy theory and experimental works .....	105
2. Modelling the adsorption of CO <sub>2</sub> on surfaces.....	106
<b>II. Experimental section .....</b>	<b>108</b>
<b>III. Surface carbonates on MgO nanoparticles.....</b>	<b>110</b>
1. MgO nanoparticles after the synthesis and impact of air exposition.....	110
2. Variability in MgO IR spectrum .....	111
3. IR spectra of MgO <sub>washed</sub> and MgO <sub>1000</sub> .....	113
4. Carbonation of MgO nanoparticles under pure CO <sub>2</sub> .....	114
<b>IV. Adsorption of boranes.....</b>	<b>117</b>
1. Adsorption of BPh <sub>3</sub> on MgO in toluene.....	117
a. Impact of BPh <sub>3</sub> addition on colloidal stability of MgO suspension.....	117
b. Infrared study of the adsorption of BPh <sub>3</sub> on MgO.....	118
c. Infrared study of the adsorption of BPh <sub>3</sub> and CO <sub>2</sub> on MgO .....	120
2. Borane screening.....	122



3.	Adsorption of BCl <sub>2</sub> Ph on MgO .....	125
V.	Conclusion .....	129
VI.	Annexes .....	130

## Chapter V: MgO-based catalysts in the cycloaddition of CO<sub>2</sub> on epoxides.....137

I.	Cycloaddition of CO <sub>2</sub> on epoxides as a valorisation pathway.....	142
1.	The cycloaddition reaction.....	142
2.	Reaction mechanism .....	143
3.	Reported catalysts.....	144
a.	Homogeneous catalysts.....	144
b.	Heterogeneous catalysts.....	144
c.	Use of a heterogeneous Lewis acid catalyst with a homogeneous Lewis base co catalyst.....	145
4.	Reported reaction between boranes and epoxides.....	146
5.	Objectives of the chapter .....	148
II.	Experimental section.....	149
III.	Cycloaddition in neat conditions.....	150
1.	Performances of MgO nanoparticles.....	151
a.	First catalytic test.....	151
b.	Kinetic study.....	153
c.	Temperature study.....	154
d.	Tests with other catalysts .....	155
2.	Polymerization of epoxide .....	157
a.	Tests with tris(pentafluorophenyl)borane .....	157
b.	Tests with triphenylborane.....	158
3.	Combining the Lewis base nanoparticles and the Lewis acid ligands .....	162
a.	First attempt with MgO+BPh <sub>3</sub> .....	162
b.	Repeatability of the experiment .....	163
c.	Impact of the temperature .....	164
d.	Impact of borane concentration.....	165
e.	Attempts with other catalysts +BPh <sub>3</sub> .....	166
4.	Inverting the NanoFLP .....	169
a.	Phosphines as molecular Lewis bases.....	169
b.	Impact of the temperature.....	171
5.	Conclusion .....	172
IV.	Cycloaddition in DMF.....	173
1.	Reported impact of DMF in the cycloaddition of CO <sub>2</sub> on epoxides.....	173
2.	Cycloaddition of CO <sub>2</sub> on EpBz in DMF catalysed by MgO+BPh <sub>3</sub> .....	174

## Table of contents

a.	Impact of the reaction temperature.....	176
b.	Impact of BPh <sub>3</sub> concentration .....	178
3.	Conclusion .....	179
<b>V.</b>	<b>Cycloaddition in toluene.....</b>	<b>180</b>
1.	Performance of MgO+BPh <sub>3</sub> .....	182
2.	Dimerization of cyclic carbonate .....	186
a.	Identification of the secondary product .....	186
b.	Impact of the borane concentration .....	189
c.	Impact of the NMR tube concentration on chemical displacements.....	190
d.	Impact of the temperature .....	191
e.	Conclusion .....	192
3.	Performances of modified MgO nanoparticles.....	193
a.	Calcium containing MgO nanoparticles .....	193
b.	Transition metal containing MgO nanoparticles .....	195
4.	Borane screening.....	196
<b>VI.</b>	<b>Understanding the interaction between MgO and BCl<sub>2</sub>Ph.....</b>	<b>199</b>
1.	Parameter variation .....	200
a.	Blanc reaction .....	200
b.	Kinetic study.....	201
c.	Impact of the borane loading .....	202
d.	Impact of temperature .....	204
2.	Supernatant activity test.....	206
3.	Post mortem analysis .....	209
4.	Mechanism proposition.....	210
a.	One component experiments .....	211
b.	Two components experiments .....	212
c.	Three components experiments .....	218
d.	Four components experiment .....	224
e.	Mechanism proposition .....	226
<b>VII.</b>	<b>Conclusion .....</b>	<b>231</b>
<b>VIII.</b>	<b>Annexes .....</b>	<b>232</b>
	<b>Chapter VI: Conclusion.....</b>	<b>249</b>
	<b>Appendix .....</b>	<b>255</b>

## Table of contents

# **Chapter I**

## **Global warming calling for CO<sub>2</sub> mitigation**



# Table of contents

<b>I.</b>	<b>Variability of CO<sub>2</sub> atmospheric concentration .....</b>	<b>15</b>
	1. Pre-industrial CO <sub>2</sub> atmospheric concentration .....	15
	2. Impact of the industrial revolution .....	16
<b>II.</b>	<b>Earth surface temperature.....</b>	<b>18</b>
	1. Earth radiative budget without greenhouse effect.....	18
	2. Greenhouse effect and radiative forcing.....	19
<b>III.</b>	<b>Strategies to reduce CO<sub>2</sub> atmospheric concentrations by the end of the century</b>	<b>19</b>
	1. History of the comprehension of the earth climate system .....	19
	2. Current strategies for CO <sub>2</sub> mitigations.....	20
<b>IV.</b>	<b>Necessity for CO<sub>2</sub> capture and valorisation.....</b>	<b>21</b>
<b>V.</b>	<b>Conclusion.....</b>	<b>22</b>

In the past decades, environmental preoccupations became a major driver of human activity: innovation now aims to reduce the impact of mankind on the earth system. There are many environmental issues at stakes, ranging from biodiversity extinction to ocean acidification through atmospheric pollution, many interconnected complex problems. Among them, global warming is probably the most emblematic one due to its mediatisation.

This PhD project started few months after the publishing of the special IPCC (Intergovernmental Panel for Climate Change) report concerning the 1.5 °C global temperature increase<sup>1</sup>. In our opinion, this period marked a turning point in the way climate change and ecology were perceived by the general public. We wanted to participate to the collective effort and decided to orientate our project toward environmental considerations, more specifically toward CO<sub>2</sub> mitigation.

Even if the core of the PhD project will not directly focus on earth atmosphere and greenhouse effect, we wanted to remind the scientific basics in this first chapter. Most of the data came from Cyril Crevoisier course entitled “Greenhouse gases – Challenges and observations” at Ecole Polytechnique.

## I. Variability of CO<sub>2</sub> atmospheric concentration

### 1. Pre-industrial CO<sub>2</sub> atmospheric concentration

CO<sub>2</sub> has been a molecule naturally present in the atmosphere as being part of the global carbon cycle. Measurements made by measuring the CO<sub>2</sub> content in bubbles trapped inside ice cores in Vostock (Antartica) allowed to retrieve the CO<sub>2</sub> atmospheric concentration of past hundreds of years up to 800,000 years ago (Figure 1:).

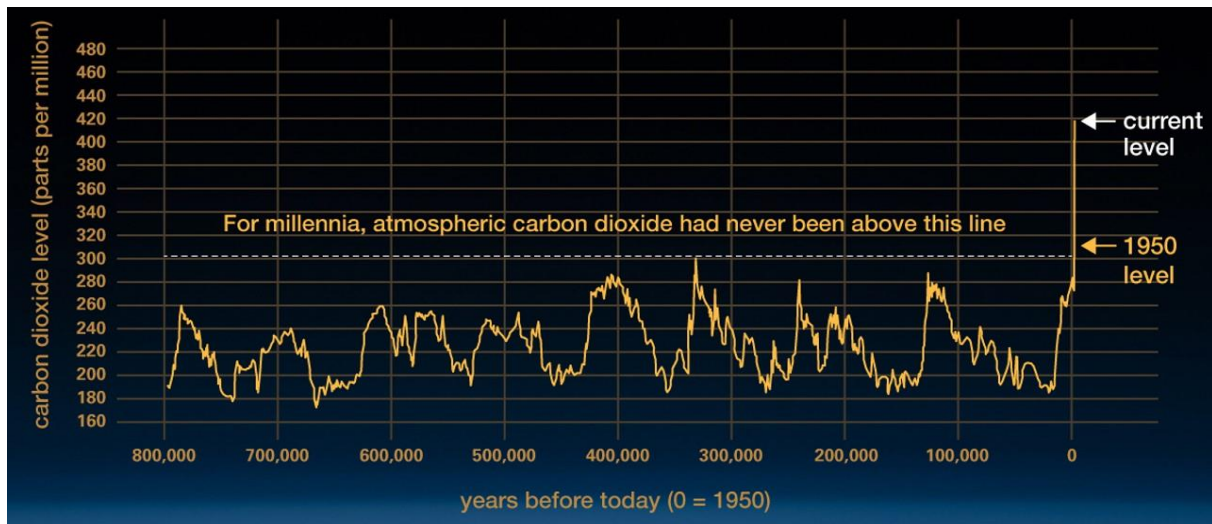


Figure 1: CO<sub>2</sub> concentration for the last 800,000 years, from Nasa<sup>2</sup>.

This time series showed the presence of a natural variability in the carbon dioxide atmospheric concentration. This variability was linked to what is called the Milankovitch cycles: variation of the earth rotation around the sun that modifies the received solar radiation by the earth. The three main variables are eccentricity, precession and tilt (Figure 2:). The Milankovitch cycles periodicity is roughly 150,000 years and it is what explained the presence of different glacial era in the last thousands of years. Due to these cycles, the CO<sub>2</sub> atmospheric concentration naturally oscillates between 180 and 300 ppm in glacial and interglacial era respectively. We are currently in a natural peak of the cycle, an interglacial era with a high concentration of atmospheric carbon dioxide. Pre industrial CO<sub>2</sub> atmospheric concentration was estimated to be 280 ppm.



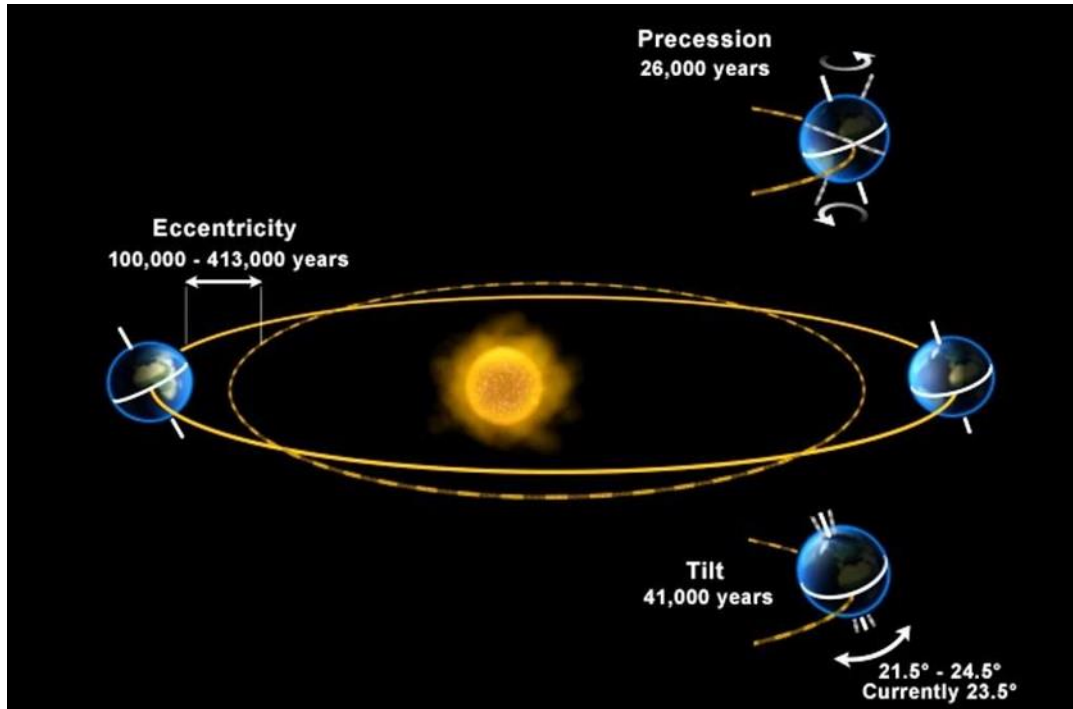


Figure 2: Milankovitch cycles, from University Corporation for Atmospheric Research<sup>3</sup>.

## 2. Impact of the industrial revolution

XIX<sup>th</sup> century was a prolific period for humanity with development of science and technology. One of the major turning point was the invention of steam engine that started the industrial revolution. The principle was the following: heating water by burning coal to create movement. This might seem trivial, but it has been what provided mankind energy for the past 200 years. However, the chemical reaction involved in the process, coal combustion, does not only produce energy, but also emits a product: carbon dioxide (Scheme 1:). Energy production and energy consumption have been closely linked to CO<sub>2</sub> emissions in the atmosphere.



Scheme 1: Coal combustion equation.

The increase of fossil fuel usage as a source of energy after the industrial revolution lead to a rise of CO<sub>2</sub> emissions in the atmosphere. This caused the CO<sub>2</sub> atmospheric concentration to significantly increase starting from the 1850s, going from 250 ppm (pre-industrial level) to 415 ppm (current level). Direct CO<sub>2</sub> atmospheric measurements were made at the Mauna Loa observatory starting from 1950. This time series clearly showed the constant increase of CO<sub>2</sub> atmospheric concentration in the recent years (Figure 3:).

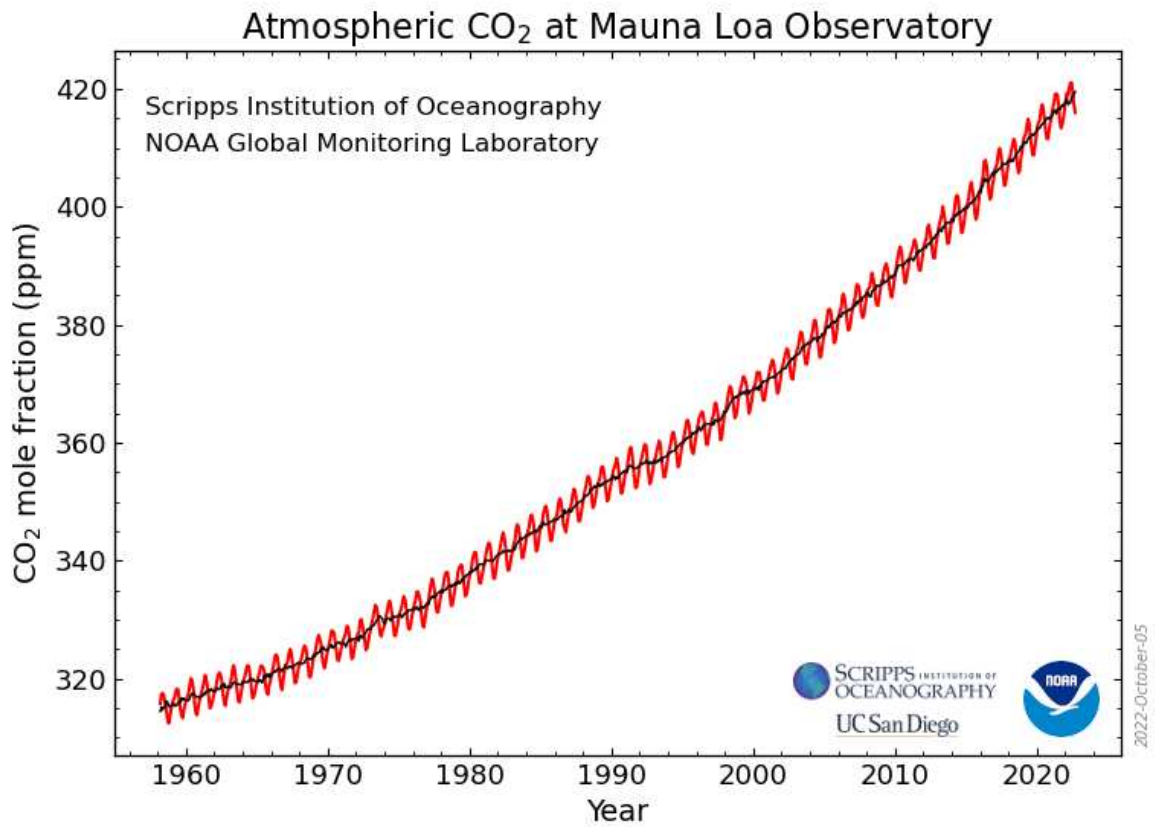


Figure 3: Recent evolution of the CO<sub>2</sub> atmospheric concentration. Red curve represents the direct measurement with seasonal variation, and black curve represents the data smoothed over 12 months. From Mauna Loa Observatory<sup>4</sup>.

## II. Earth surface temperature

### 1. Earth radiative budget without greenhouse effect

The simplest model to approximate the earth temperature is called a radiative budget. The idea is to consider the earth as a perfect black body which temperature would be determined by the energy it received (Figure 4:). The sun light radiation is partially directed toward the earth (342 W/m<sup>2</sup>). A part of the incoming radiation is reflected (107 W/m<sup>2</sup>) and the rest is absorbed (235 W/m<sup>2</sup>). This absorbed radiation heats the earth, leading to the reemission of the same amount of energy (235 W/m<sup>2</sup>).

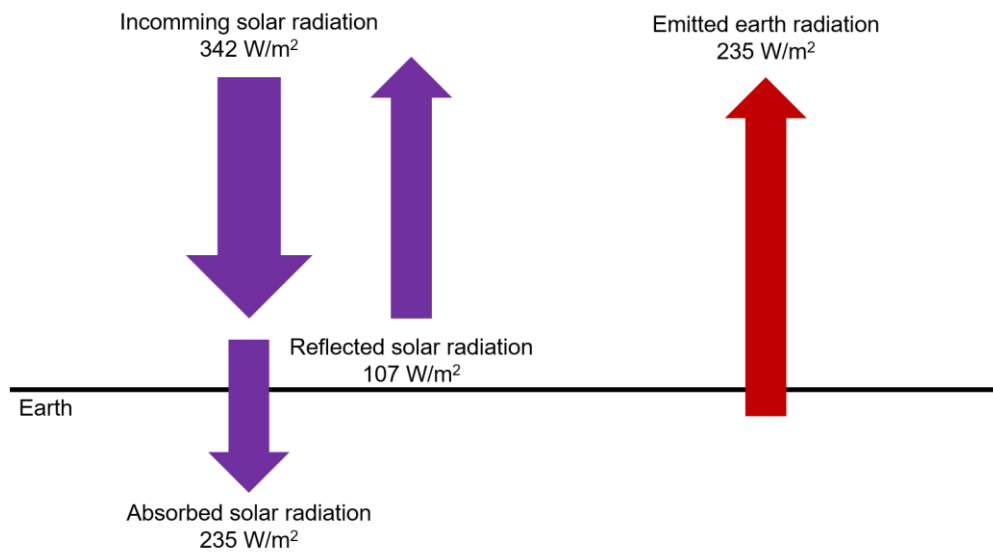


Figure 4: Simplified earth radiative budget without greenhouse effect.

The amount of energy emitted by a black body and its temperature are related by the Stefan-Boltzmann equation (Scheme 2:). Using this formula with the radiation emitted by the earth (235 W/m<sup>2</sup>), we find a temperature equal to 254 K, or -19 °C. This result is lower than expected since the observed earth surface temperature is 288 K, or 15 °C. This difference is due to the greenhouse effect.

$$M = \sigma T^4 \longleftrightarrow T = (M/\sigma)^{0.25}$$

M = Energetic flux per surface unit

T = Surface temperature

$\sigma$  = Stefan-Boltzmann constant =  $5.670374 \cdot 10^{-8} \text{ W/m}^2/\text{K}^4$

Scheme 2: Stefan-Boltzmann law.

## 2. Greenhouse effect and radiative forcing

Greenhouse gases are gases present in the atmosphere that absorb IR radiations in the domain where earth emits. The main greenhouse gases are  $\text{H}_2\text{O}$ ,  $\text{CO}_2$ ,  $\text{CH}_4$  and  $\text{N}_2\text{O}$ . Their presence modifies the earth radiative budget by creating a radiative forcing (Figure 5:). Part of the energy emitted by the earth will be absorbed by the atmosphere (around 33 %, depending on the greenhouse gases concentration) and reemitted toward the earth. The effective energy the earth receives will be higher than what it receives only coming from the sun. It means that the temperature of the surface will be higher too. When using the Stefan-Boltzmann law, we obtained a surface temperature of 280 K, or 7 °C. This is still not exact but already closer to reality.

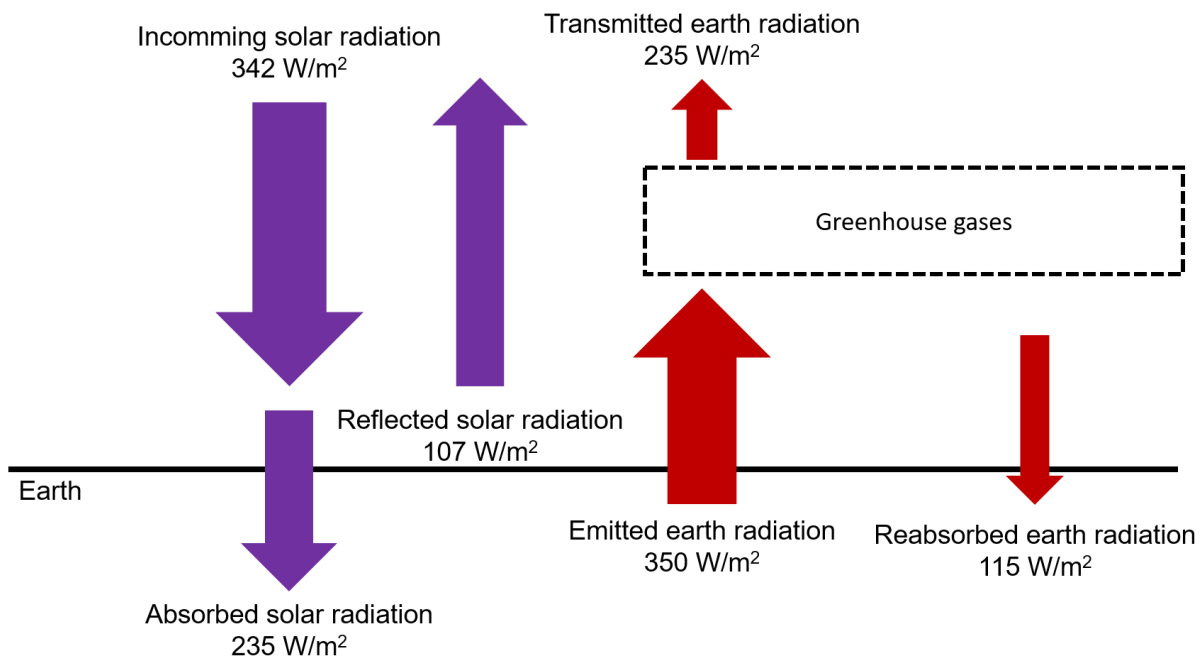


Figure 5: Simplified earth radiative budget taking into account greenhouse effect.

## III. Strategies to reduce CO<sub>2</sub> atmospheric concentrations by the end of the century

### 1. History of the comprehension of the earth climate system

The realisation that fossil fuel usage could cause a modification of the climate came earlier than many would think. Svante Arrhenius, the famous Swedish chemist, already realised the impact that an increase of  $\text{CO}_2$  concentration in the atmosphere would have on the climate<sup>5</sup>. Many scientists in the XX<sup>th</sup> century made similar observations, like Ernest Fisher postulating that mankind should be considered as a geological force<sup>6</sup>, or Roger Revelle and Hans Suess realising the dynamic equilibrium between the atmosphere and the oceans for  $\text{CO}_2$  exchanges would be impacted by anthropogenic emissions<sup>7</sup>.

More and more credit was given to the warnings of the scientists in the second half of the XX<sup>th</sup> century. In 1988, the Intergovernmental Panel on Climate Change (IPCC) was created. It was an organism charged to collect data from research groups working on the climate subject all around the world. Until now, the IPCC published six assessment reports; with the latest recently published in 2022. Recent reports not only focused on observing the evolution of the climate, but also in proposing solutions to mitigate global warming.

## 2. Current strategies for CO<sub>2</sub> mitigations

Even if it was not the only issue, CO<sub>2</sub> management seemed to have become the main focus of the general policies concerning global warming mitigations. The annual Conference of the Parties (CoP) has been gathering representatives of each country every year to evaluate the current climate trajectory and fix objectives aiming climate change mitigation. The CoP 21 of 2015 was famous for setting the following objective: “limit global warming to well below 2, preferably 1.5, degrees Celsius above pre-industrial levels”. It was then the duty of each country to set concrete measures to attain the objectives set by the CoP.

Several leverages could be used to limit CO<sub>2</sub> atmospheric concentrations. Reduction of the energy consumption (energy efficiency, sobriety), reduction of the carbon footprint of the energy (decreasing the part of fossil fuel in the energetic mix for the benefit of less carbonated energy sources like renewables or nuclear) and direct reduction of the CO<sub>2</sub> atmospheric concentrations (Carbon Capture Usage and Storage, CCUS)(Figure 6:).

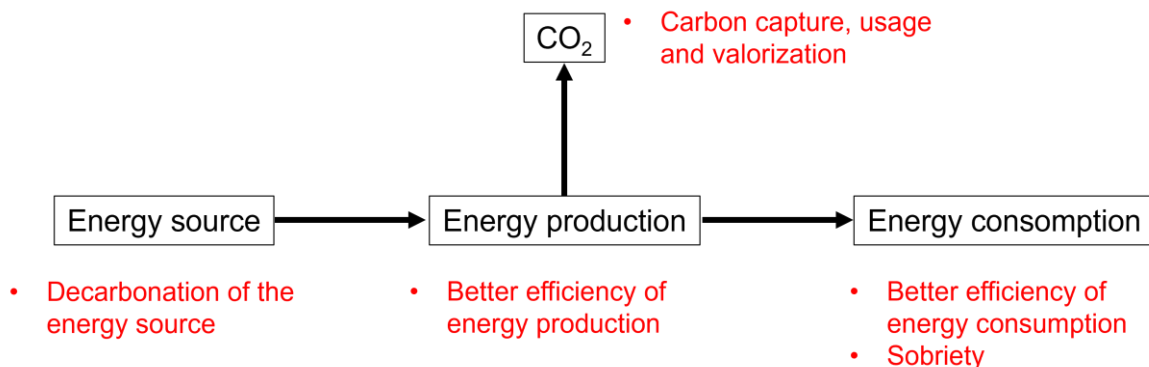


Figure 6: Summary of CO<sub>2</sub> mitigation strategies.

## IV. Necessity for CO<sub>2</sub> capture and valorisation

To give an order of magnitude, the IEA published in 2021 a report on pathway to respect the CoP 21 objectives<sup>8</sup>. This means reaching a net zero CO<sub>2</sub> emissions by the end of 2050. To do so, they proposed solutions in the energetic mix evolution, the development of less carbonated mobility, etc. They also estimated the necessity for CO<sub>2</sub> capture and valorisation evolution (Table 1:). The current level of CO<sub>2</sub> emission is 50 Gt/year, and the current level of captured CO<sub>2</sub> is 40 Mt/year. The IEA estimates an evolution from 40 to 7600 Mt/year of captured CO<sub>2</sub>, a multiplication by a factor of 200.

	2020	2030	2050
<b>Total CO<sub>2</sub> captured (Mt CO<sub>2</sub>)</b>	<b>40</b>	<b>1 670</b>	<b>7 600</b>
<b>CO<sub>2</sub> captured from fossil fuels and processes</b>	<b>39</b>	<b>1 325</b>	<b>5 245</b>
Power	3	340	860
Industry	3	360	2 620
Merchant hydrogen production	3	455	1 355
Non-biofuels production	30	170	410
<b>CO<sub>2</sub> captured from bioenergy</b>	<b>1</b>	<b>255</b>	<b>1 380</b>
Power	0	90	570
Industry	0	15	180
Biofuels production	1	150	625
<b>Direct air capture</b>	<b>0</b>	<b>90</b>	<b>985</b>
Removal	0	70	630

Table 1: Estimation for CCUS evolution in the future years, from IEA Net Zero report<sup>8</sup>.

The current level of captured carbon is very low compared to the emission level. This is mostly due to the current economic non viability of the CO<sub>2</sub> capture process. Several options exist to incite carbon capture: taxing CO<sub>2</sub> emissions, reducing the cost of CO<sub>2</sub> capture, and finding value in CO<sub>2</sub> through valorisation. Progress still has to be made in these last fields to reach the objectives set by the IEA.

## V. Conclusion

This chapter gave the basic understanding of climate change and the solutions being put in place to mitigate the elevation of the global temperature. Progresses and efforts have to be made in every part of the chain, from development of less carbonated energy sources to reduction of the energy consumption whether by optimisation or sobriety. CO<sub>2</sub> capture and valorisation on its own will never be able to tackle the CO<sub>2</sub> issue, but it is still a valuable tool that might be necessary to compensate some CO<sub>2</sub> emissions that will not be avoidable.

However, for CO<sub>2</sub> capture and valorisation to be widely used, economic viability has to be reached. In our opinion, the most promising way to reach economic viability is to develop CO<sub>2</sub> valorisation. If carbon dioxide can be used for example in the pharmaceutical industry as a carbon source, it would incite its capture.

What is the current state of CO<sub>2</sub> valorisation? What are the technological locks? How could we develop new way to valorise CO<sub>2</sub>?

This work will focus on CO<sub>2</sub> valorisation through catalysis, but Chapter 2 will present a state of the art on CO<sub>2</sub> valorisation and propose an approach for the design of new catalytic systems. Chapter 3 will focus on the synthesis of heterogeneous catalysts, Chapter 4 will focus on the functionalisation of these catalysts by adsorption of ligands, and Chapter 5 will focus on the catalytic studies for CO<sub>2</sub> valorisation. Chapter 6 will be the general conclusion of our work.

## Bibliography

- (1) IPCC. *Global Warming of 1.5°C*; Cambridge University Press, 2022. <https://doi.org/10.1017/9781009157940>.
- (2) Nasa. The relentless rise of carbon dioxide – Climate Change: Vital Signs of the Planet [https://climate.nasa.gov/climate\\_resources/24/graphic-the-relentless-rise-of-carbon-dioxide/](https://climate.nasa.gov/climate_resources/24/graphic-the-relentless-rise-of-carbon-dioxide/) (accessed Oct 20, 2022).
- (3) University Corporation for Atmospheric Research. COMET® at the University Corporation for Atmospheric Research (UCAR) pursuant to a Cooperative Agreements with the National Oceanic and Atmospheric Administration, U.S. Department of Commerce. ©1997-2009 University Corporation for Atmospheric Research. AI [https://chem.libretexts.org/Courses/Portland\\_Community\\_College/CH100%3A\\_Everyday\\_Chemistry/07%3A\\_Climate\\_and\\_the\\_Environment/7.07%3A\\_Additional\\_Reading\\_-\\_Milankovitch\\_Cycles](https://chem.libretexts.org/Courses/Portland_Community_College/CH100%3A_Everyday_Chemistry/07%3A_Climate_and_the_Environment/7.07%3A_Additional_Reading_-_Milankovitch_Cycles) (accessed Oct 20, 2022).
- (4) US Department of Commerce, N. G. M. L. Global Monitoring Laboratory - Carbon Cycle Greenhouse Gases.
- (5) Arrhenius, S. Les Oscillaions Séculaires de La Température à La Surface Du Globe Terrestre. *Rev. générale des Sci. pures appliquées* **1899**, No. 10, 337–342.
- (6) Fischer, E. Der Mensch Als Geologischer Faktor. *Zeitschrift der Dtsch. Geol. Gesellschaft* **1915**, 67 (2), 112–147.
- (7) REVELLE, R.; SUESS, H. E. Carbon Dioxide Exchange Between Atmosphere and Ocean and the Question of an Increase of Atmospheric CO<sub>2</sub> during the Past Decades. *Tellus* **1957**, 9 (1), 18–27. <https://doi.org/10.1111/J.2153-3490.1957.TB01849.X>.
- (8) IEA. Net Zero by 2050 – Analysis <https://www.iea.org/reports/net-zero-by-2050> (accessed Oct 21, 2022).



Global warming calling for CO<sub>2</sub> mitigation

# **Chapter II**

## **Toward the design of a new active catalytic systems for CO<sub>2</sub> valorisation**



# Table of contents

<b>I.</b>	<b>CO<sub>2</sub> valorisation in industrial processes .....</b>	<b>29</b>
1.	Reactivity of CO <sub>2</sub> molecules.....	29
a.	Thermodynamic considerations .....	29
b.	Orbital considerations .....	31
2.	Direct CO <sub>2</sub> usage .....	32
3.	Industrial processes using CO <sub>2</sub> .....	33
a.	Urea synthesis.....	33
b.	Salicylic acid synthesis.....	33
c.	Dry reforming of methane.....	34
d.	CO <sub>2</sub> electro-reduction .....	35
<b>II.</b>	<b>The recent development of Frustrated Lewis Pair catalysis for the conversion of CO<sub>2</sub>.....</b>	<b>36</b>
1.	The concept of Frustrated Lewis Pair catalysis .....	36
2.	FLPs for CO <sub>2</sub> activation.....	36
3.	Non-molecular FLPs.....	38
<b>III.</b>	<b>Forming a FLP interaction between a nanoparticle surface and its ligands to activate CO<sub>2</sub>: the NanoFLP project .....</b>	<b>39</b>
<b>IV.</b>	<b>Materials known for CO<sub>2</sub> adsorption and/or activation in catalysis.....</b>	<b>40</b>
1.	Materials with Lewis base properties: alkaline-earth oxides .....	40
a.	Generalities on heterogeneous solid bases .....	40
b.	Basicity scale for heterogeneous solid bases.....	41
c.	Intrinsic bifunctionality of heterogeneous basic oxides .....	43
d.	Alkaline-earth oxides and their affinity toward CO <sub>2</sub> .....	43
2.	MgO: synthesis and applications .....	45
a.	Generalities on magnesium-based materials .....	45
b.	Synthesis of MgO precursor.....	46
c.	Calcination of the precursor to form MgO.....	47
d.	Applications of MgO .....	49
e.	MgO in catalysis .....	49
3.	CaO: synthesis and applications .....	51
a.	Calcium oxide synthesis.....	51
b.	Application of CaO for CO <sub>2</sub> capture.....	51
c.	CaO in catalysis .....	52
<b>V.</b>	<b>Classical molecular acids used in the FLP adducts: boranes.....</b>	<b>53</b>

<b>1. Boranes in catalysis .....</b>	<b>53</b>
<b>2. Boranes for CO<sub>2</sub> activation .....</b>	<b>54</b>
<b>VI. Approach for the design of a NanoFLP pair for CO<sub>2</sub> activation.....</b>	<b>55</b>

# I. CO<sub>2</sub> valorisation in industrial processes

## 1. Reactivity of CO<sub>2</sub> molecules

### a. Thermodynamic considerations

The climate crisis raised interest in CO<sub>2</sub> valorisation in the last decades<sup>1</sup>. The main problem encountered when trying to transform CO<sub>2</sub> came from the stability of the molecule. Transforming CO<sub>2</sub> into another carbon containing molecule such as alcohols or hydrocarbons often cost energy. This is intrinsic to the reaction and no technological progress can change that. The main notable exception is mineral carbonates that are more stable than CO<sub>2</sub> molecules and tend to form without energy input. Figure 1: compares the Gibbs free energy of different carbon containing molecules.

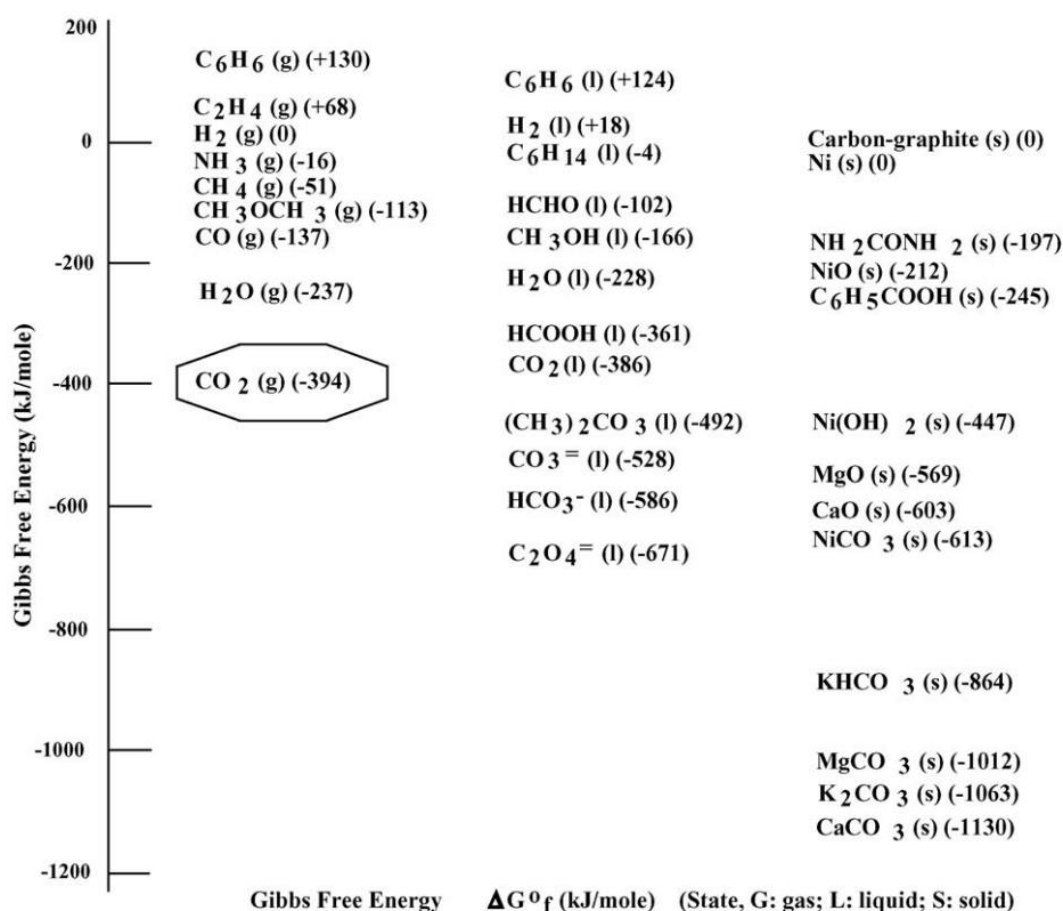


Figure 1: Gibbs free energy considerations for CO<sub>2</sub> valorisation, from Song's review<sup>1</sup>.

We could see that CO<sub>2</sub> in its gaseous form had a Gibbs free energy of -394 kJ/mol, compared to -137 kJ/mol for CO<sub>(g)</sub>, -51 kJ/mol for CH<sub>4(g)</sub>, 0 kJ/mol for graphite<sub>(s)</sub>, or +68 kJ/mol for C<sub>2</sub>H<sub>4(g)</sub>. The stability of carbon dioxide makes reactions involving its transformation energy demanding. For example, the reforming of methane using H<sub>2</sub>O (steam reforming) has a lower  $\Delta H^{\circ}$  than the reforming of methane using CO<sub>2</sub> (dry reforming) with a 41 kJ/mol of CO difference (Figure 2:). Replacing water by CO<sub>2</sub> in such a large scale industrial process would correspond to an increase in the cost of synthetic gas (CO and H<sub>2</sub>) production that companies cannot afford.



Figure 2: Standard enthalpy of reaction associated to steam reforming and dry reforming of methane.

Strategies for CO<sub>2</sub> valorisation can be divided in four categories (Figure 3):

- direct use of CO<sub>2</sub> without transformation,
- energy input (heating, photo-activation, microwave, etc...),
- use of high energy starting molecules (like NaH),
- targeting synthesis of high stability carbon containing molecules/materials (like mineral carbonates).

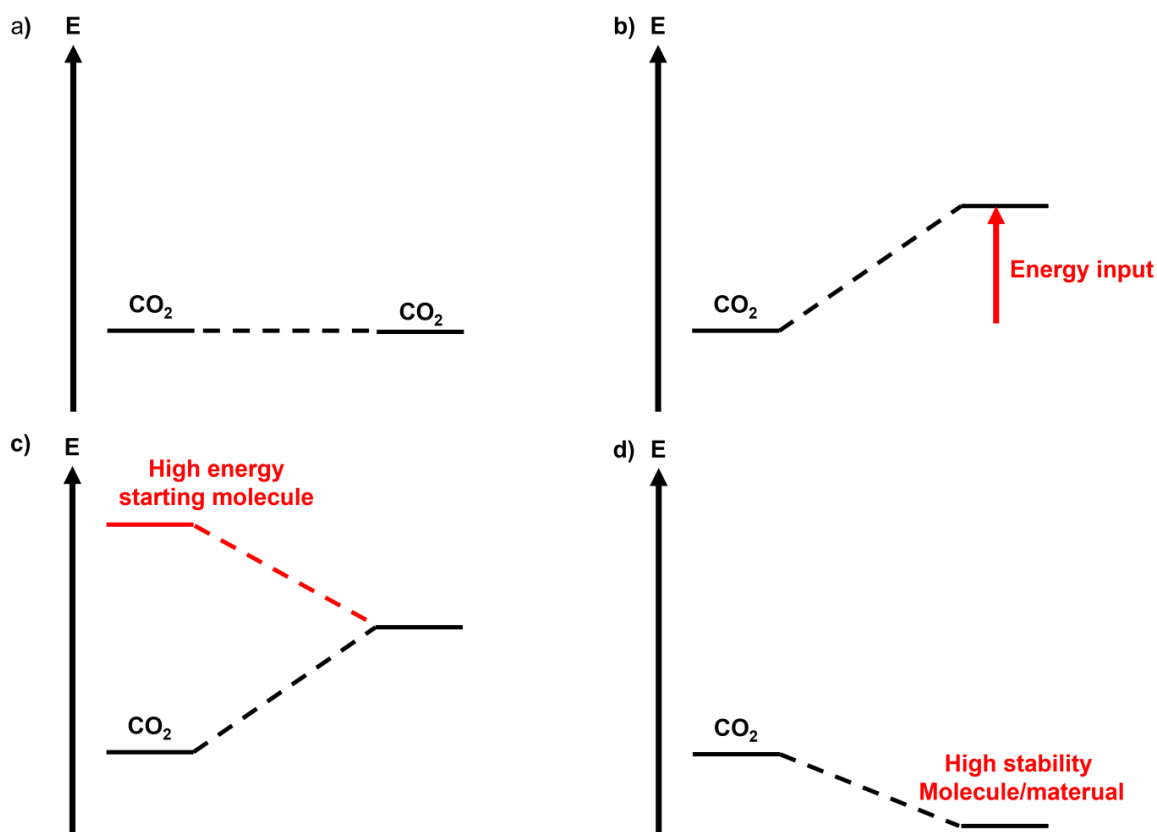


Figure 3: CO<sub>2</sub> valorisation strategies. a) direct utilisation, b) use of an energy input, c) use of high energy starting molecules, d) targeting the synthesis of high stability carbon containing molecules/materials.

## b. Orbital considerations

The orbital diagram of  $\text{CO}_2$  molecule has been studied extensively in the past<sup>2</sup> (Figure 4:). The highest occupied molecular orbital (HOMO) is only located on the oxygen atoms. This translates in a nucleophilic character of these atoms. The lowest unoccupied molecular orbital (LUMO) is mainly located on the carbon atom. This translates in an electrophilic character of this atom.

When the  $\text{CO}_2$  molecule is bent, the energy level of the  $2\pi_u$  orbitals (former LUMO) decreases with a split up of the energy level due to the symmetry loss. The energy of out of plane orbital decreases less than the one of the in plane orbital. This means that the electrophilic behaviour of the carbon atom is enhanced and that the molecule will react preferentially through in plane interaction. On the other hand, energy level of the  $1\pi_g$  orbital (former HOMO) is less affected by this change. We can also observe a split up of the energy level, but it is accompanied by an increase of the energies of both the out of plane and the in plane orbitals. The fact that the energy level almost does not change means that the nucleophilic behaviour of the  $\text{CO}_2$  molecule is not strongly impacted by its bending.

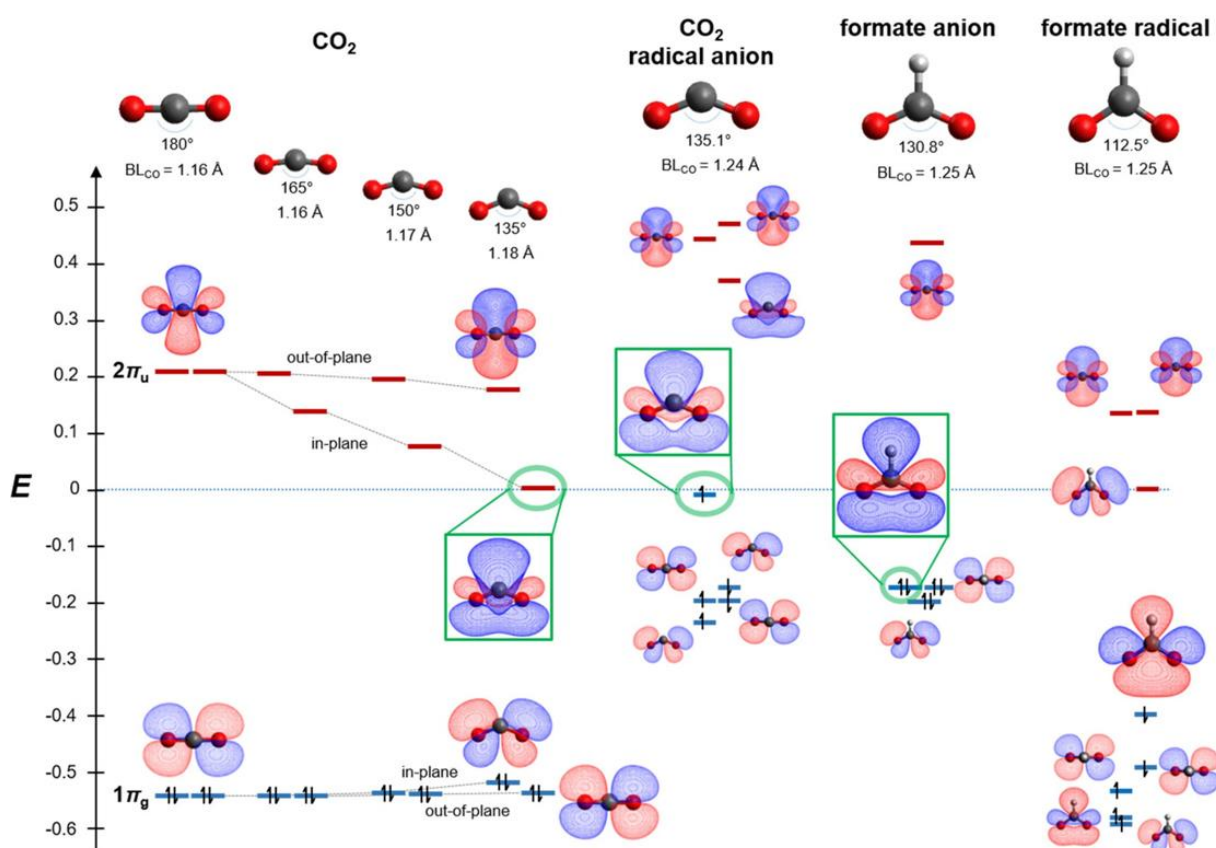


Figure 4: Orbital energy diagrams with characteristic  $\text{OCO}$  angle and  $\text{CO}$  bond length of  $\text{CO}_2$  in the linear and bent forms, radical  $\text{CO}_2^-$ , formate ion, and formate radical, from Alvarez et al.<sup>2</sup>.



## 2. Direct CO<sub>2</sub> usage

The easiest way to valorise CO<sub>2</sub> is its direct usage without further transformations. It was found to be useful in chemistry as a solvent (supercritical CO<sub>2</sub>) or cooling agent (dry ice), in pharmaceutical as an inert gas, in the beverage industry for carbonation, in the electronic industry to increase water conductivity, etc. The most common CO<sub>2</sub> usage are listed by Song et al. in their review<sup>1</sup> (Table 1:).

Sectors	Industrial applications
Chemicals	<ul style="list-style-type: none"> <li>CO<sub>2</sub> is used in chemical synthesis and for controlling reactor temperatures.</li> <li>CO<sub>2</sub> is employed to neutralize alkaline effluents.</li> <li>CO<sub>2</sub> is used as a blowing agent for polyurethane and polystyrene foam production and for blow molding manufacturing of plastic bottles, and containers.</li> <li>CO<sub>2</sub> is used under supercritical conditions for purifying or dyeing polymer, animal or vegetable fibers</li> </ul>
Pharmaceuticals	<ul style="list-style-type: none"> <li>CO<sub>2</sub> is used for making chemicals such as salicylic acid and Aspirin; for use as an inert gas, and for supercritical fluid extraction.</li> <li>CO<sub>2</sub> is used for product transportation at low temperature (-78 °C) and also acidification (pH) of wastewater.</li> </ul>
Foodstuffs	<ul style="list-style-type: none"> <li>Liquid CO<sub>2</sub> can be used as cryogenic fluid in chilling or freezing operations or as dry ice for temperature control during the storage and distribution of foodstuffs.</li> <li>Packaging of foodstuffs to increase the shelf life of many food products due to its inerting properties and its growth inhibiting effect of CO<sub>2</sub> on micro-organisms.</li> <li>Stunning of pigs and poultry in slaughterhouses instead of using electrical stunning.</li> </ul>
Beverage	<ul style="list-style-type: none"> <li>Carbonation of beverages such as soft drinks, mineral water or beer.</li> <li>Supercritical CO<sub>2</sub> is used to remove caffeine from coffee beans by extraction.</li> <li>CO<sub>2</sub> is used as shielding gas for preserving drink quality, and propellant gas for emptying tanks of drinks.</li> <li>CO<sub>2</sub> is also used in drinking water treatment in modern water works together with lime or chalk.</li> </ul>
Healthcare	<ul style="list-style-type: none"> <li>CO<sub>2</sub> produces close-to-physiologic atmospheres for the operation of artificial organs.</li> <li>CO<sub>2</sub> is used as a component in a mixture of oxygen or air as respiratory stimulant to promote deep breathing. It is also used for the surgical dilation by intra-abdominal insufflation</li> </ul>
Environment	<ul style="list-style-type: none"> <li>Small amount of liquid CO<sub>2</sub> can be used in recycling of waters from Acid Mine Drainage.</li> <li>Waste water treatment and waste liquid treatment by injection of CO<sub>2</sub> for the pH of liquid effluents. CO<sub>2</sub> is an excellent alternative to sulfuric acid for pH balance control.</li> </ul>
Pulp and paper	<ul style="list-style-type: none"> <li>CO<sub>2</sub> enables sharp tuning of the pH of recycled mechanical or chemical pulps after an alkaline bleaching.</li> <li>CO<sub>2</sub> can be used in the Tall Oil neutralization and for increasing the performance of paper machines.</li> <li>Precipitated calcium carbonate obtained from CO<sub>2</sub> and CaO is used as a whitener for the paper industry.</li> </ul>
Electronics	<ul style="list-style-type: none"> <li>CO<sub>2</sub> is usually used as a cooling medium in environmental testing of electronic devices.</li> <li>CO<sub>2</sub> can be used to add conductivity to ultrapure water.</li> <li>CO<sub>2</sub> can also be used as an environmentally friendly supercritical fluid for removing photoresist from wafers.</li> </ul>
Metals industry	<ul style="list-style-type: none"> <li>CO<sub>2</sub> is typically used as an inert gas or for environment protection.</li> <li>CO<sub>2</sub> is used for red fume suppression during scrap and carbon charging, for nitrogen pick-up reduction during tapping and for bottom stirring.</li> <li>CO<sub>2</sub> is used for fume suppression during ladle transfer of matte (Cu/Ni production) or bullion (Zn/Pb production) in the non ferrous metallurgy.</li> <li>Special grades of CO<sub>2</sub> are used in CO<sub>2</sub> lasers.</li> </ul>
Laboratories & analysis	<ul style="list-style-type: none"> <li>Supercritical CO<sub>2</sub> is the mobile phase in both supercritical chromatography and supercritical fluid extraction applications.</li> </ul>
Safety and others	<ul style="list-style-type: none"> <li>CO<sub>2</sub> is used as carbon dioxide snow for fire extinguishers;</li> <li>pH control and regulation of waste waters, swimming pools, etc.</li> </ul>

Table 1: Direct CO<sub>2</sub> utilisations, adapted from Song et al.<sup>1</sup>.

### 3. Industrial processes using CO<sub>2</sub>

Despite its inert character, CO<sub>2</sub> have been used in industrial processes. The energy cost was often high, so large scale installations were necessary to limit the energy consumption. We listed the most prominent large scale reactions involving CO<sub>2</sub> as well as some reactions showing potential for the future of carbon dioxide valorisation.

#### a. Urea synthesis

Urea synthesis has been a breakthrough in the 19<sup>th</sup> century It was first discovered by Friedrich Wöhler in 1828<sup>3</sup>. The urea molecule is a highly efficient nitrogen vector: light and easily transportable with a high nitrogen content/mass ratio. 90 % of the world production of urea has been used for the agriculture as fertilizer.

The first synthesis discovered in 1828 involved silver cyanate and aluminium chloride. The reaction later evolved to the Bosch-Meiser urea process in 1922, involving liquid ammonia and gaseous CO<sub>2</sub> under high pressure (140-175 bar) and high temperature of 190 °C (Figure 5:).

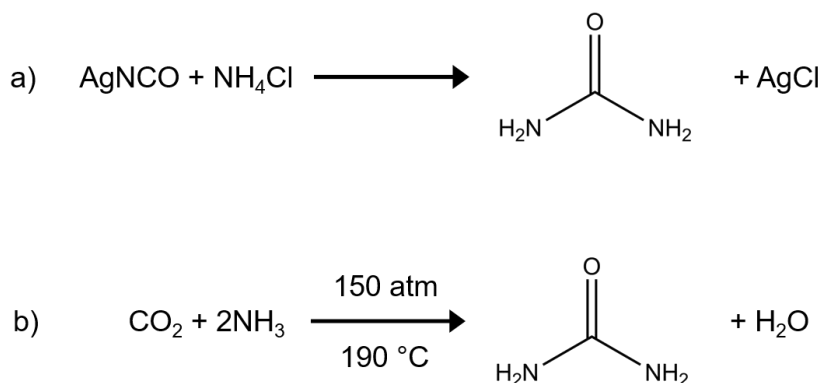


Figure 5: Urea synthesis as discovered by Wöhler in 1828, and in the Bosch-Meiser process.

#### b. Salicylic acid synthesis

Salicylic acid has been used for medical purposes long before it was synthesized in laboratory<sup>4</sup>. Reports mentioned the extraction of salicylic acid from white willow (*Salix Alba*) in Greek antiquity. The synthesis of the molecule was developed in 1860 with the Kolbe-Schmit synthesis. Salicylic acid has been used as the precursor for the synthesis of aspirin, one of the most widely used medication nowadays, since the end of the 19<sup>th</sup> century.

The Kolbe-Schmit synthesis involved the treatment of sodium phenolate with carbon dioxide at high temperature and pressure (100 atm, 125 °C), and the treatment of the product with a strong acid acid like sulphuric acid (Figure 6:).

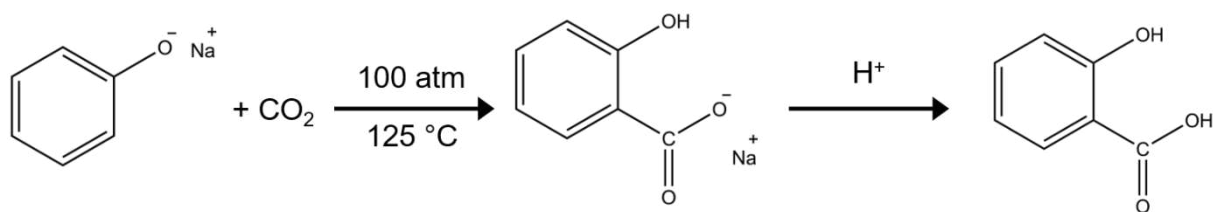


Figure 6: Kolbe-Schmitt reaction for salicylic acid synthesis.

### c. Dry reforming of methane

We mentioned earlier the reforming of methane as a potential CO<sub>2</sub> consuming reaction. Steam reforming has been a method for the production of syngas (dihydrogen and carbon monoxide) from methane and water (Figure 7:). The reaction requires the use of a catalyst such as nickel-alumina, that have been extensively studied in the 1950s. On top of the reaction between methane and water, the produced CO molecules also react with water to form CO<sub>2</sub> and H<sub>2</sub> via the water-gas shift reaction. These reactions are endothermic and requires high temperatures around 800-900 °C at 30 bar pressure.

Since the increase of interest around CO<sub>2</sub> valorisation, the dry reforming reaction, involving the use of CO<sub>2</sub> and methane to produce H<sub>2</sub> and CO, has been considered. The industrial development of this reaction has been challenging: as mentioned earlier, this reaction is more endothermic and requires more energy, the produced H<sub>2</sub> can react with CO<sub>2</sub> via the water-gas shift reaction to produce CO and water, and the formation of coke on the catalyst can quickly lead to its deactivation. Presence of O<sub>2</sub> has shown to prevent coke formation and increase the overall performance of the reaction. This lead to the development of tri reforming where CH<sub>4</sub>, H<sub>2</sub>O, CO<sub>2</sub> and O<sub>2</sub> are mixed together to combine steam reforming, dry reforming and methane oxidation at the same time<sup>5</sup>.

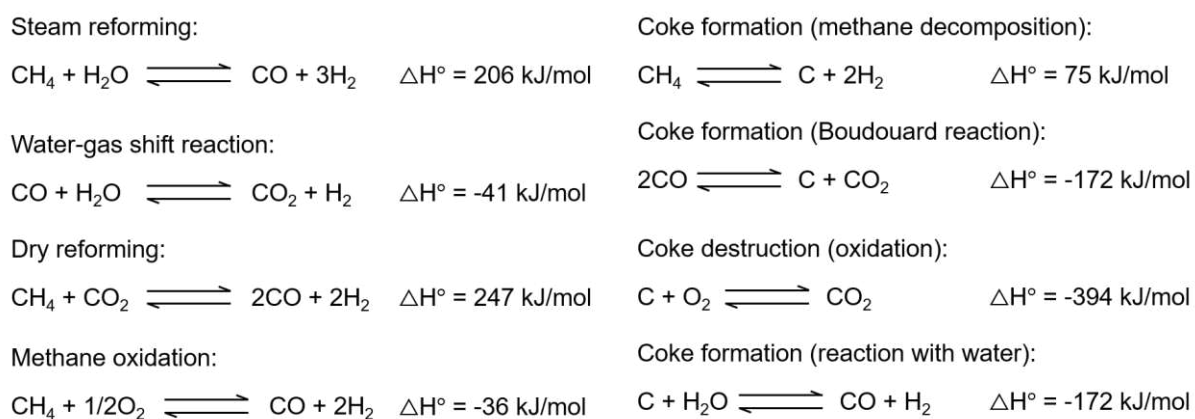


Figure 7: Reactions of steam reforming, water-gas shift, dry reforming and coke formation.

### d. CO<sub>2</sub> electro-reduction

Progress in electro-catalysis in the recent years also proved to be of interest when considering CO<sub>2</sub> valorisation at low temperature<sup>6</sup> (i.e. lower than 100 °C). The most technologically ready reaction would be the electrochemical conversion of CO<sub>2</sub> into CO (Figure 8:) where pilot units are already being tested. Direct conversion of CO<sub>2</sub> into formic acid is the second most promising reaction. Conversion of CO<sub>2</sub> into C<sub>2</sub> products using electrochemistry is still in its early stages.

Formation of CO:



Formation of formic acid:

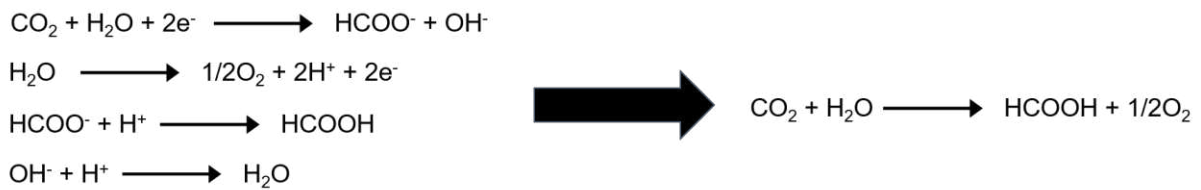


Figure 8: CO<sub>2</sub> conversion using electrochemistry to form CO or formic acid.

## II. The recent development of Frustrated Lewis Pair catalysis for the conversion of CO<sub>2</sub>

### 1. The concept of Frustrated Lewis Pair catalysis

Reactions achieving CO<sub>2</sub> transformations are often expensive due to the stability of the molecule. Adding to that, most of the time a catalyst has to be present for the reaction to take place. Due to their high performances, most of the catalytic studies (for CO<sub>2</sub> conversion but also for all reactions in general) are interested in metal-containing catalysts, especially noble metals like platinum, ruthenium and rhodium. Reduction of the cost of the catalyst often leads to potential replacements for these expensive metals with cheaper ones (such as nickel, copper and cobalt), with enzymes, or with carbon-based materials such as graphite or carbon nanotubes.

It was in this trend that emerged in the 2006 the concept of Frustrated Lewis Pair catalysis. It was a concept first formulated by Stephan et al.<sup>7</sup> where a Lewis acid and a Lewis base, both sterically hindered, could form a catalyst for reversible H<sub>2</sub> cleavage (Figure 9:). In another study, they used the bulky borane B(C<sub>6</sub>F<sub>5</sub>)<sub>3</sub> (usually called BCF) with P<sup>t</sup>Bu<sub>3</sub> and showed that even if the formation of the Lewis acid-base adduct should stabilize the two molecules, the bulky groups surrounding the active centers would prevent it. However, this frustrated interaction created a reactive center that could reversibly cleave an H<sub>2</sub> molecule.

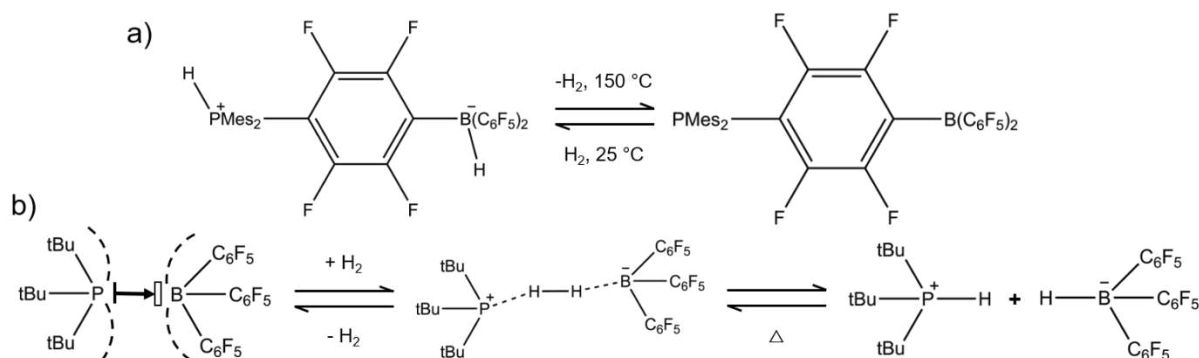


Figure 9: a) First evidenced FLP reaction as described by Stephan et al. in 2006<sup>7</sup>, b) reversible cleavage of H<sub>2</sub> by a FLP composed of P<sup>t</sup>Bu<sub>3</sub> and BCF.

### 2. FLPs for CO<sub>2</sub> activation

The development of FLP chemistry has continued in the last decades, showing new Lewis acids, new Lewis bases that could act as FLP catalysts, and new reactions that could be catalysed by such FLPs<sup>8</sup>. Several small molecules showed to be activated by FLPs such as H<sub>2</sub>, NO<sub>2</sub>, SO<sub>2</sub>, and CO<sub>2</sub><sup>9</sup>. In our case, it was the activity toward carbon dioxide that retained our attention, a subject that F.-G. Fontaine reviewed in 2016<sup>10</sup>.

Among the main CO<sub>2</sub> activation pathways involving FLP, the first one is the simple capture where the Lewis acid bonds to an oxygen atom of the CO<sub>2</sub> molecule, and the Lewis base bonds to

the carbon atom, forming zwitterionic products. For example, Erker et al.<sup>11</sup> showed that the use of  $\text{P}^t\text{Bu}_3$  and  $\text{BCF}$  would lead to such product (Figure 10:a). Other pathways revolve around the reduction of the  $\text{CO}_2$  molecule, using reductive agents such as silanes (hydrosilylation), boranes (hydroboration), or hydrogen (hydrogenation). For example, Anker et al.<sup>12</sup> showed that it was possible to catalyse the hydroboration of  $\text{CO}_2$  to a methanol equivalent using a magnesium hydride/borane FLP (Figure 10:b). Berkefeld and coworkers<sup>13</sup> showed that it was possible to transform  $\text{CO}_2$  into methane using a silane/borane adduct (the silane playing both the role of hydride donor and Lewis base in the acidobasic pair)(Figure 10:c). Other studies mentioned the hydrogenation of  $\text{CO}_2$  into methanol<sup>14,15</sup> using FLP catalysts.

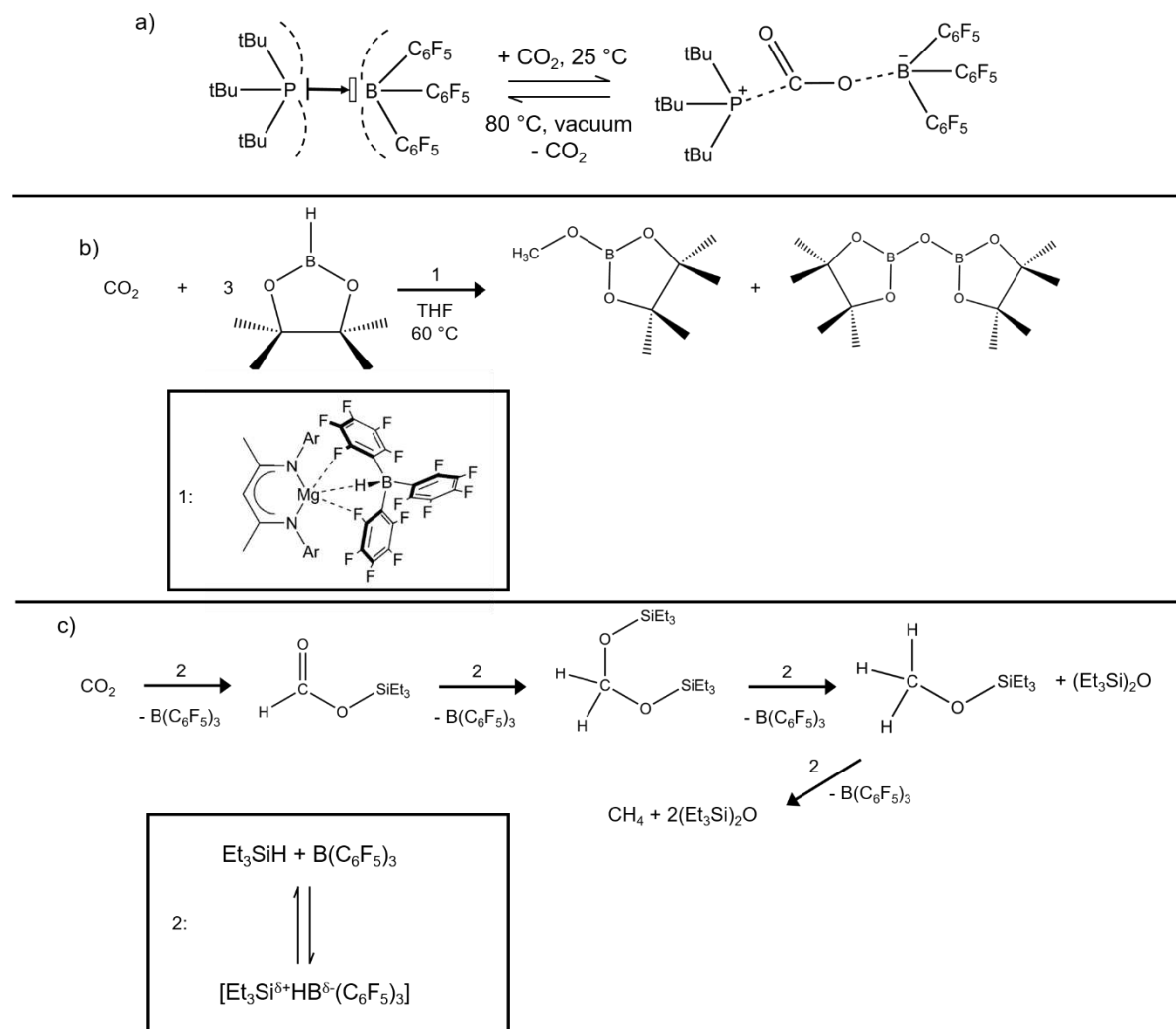


Figure 10: a) Formation of a Lewis base- $\text{CO}_2$ -Lewis acid adduct as described by Erker<sup>11</sup>, b) hydroboration of  $\text{CO}_2$  as described by Anker<sup>12</sup>, c)  $\text{CO}_2$  hydrosilylation as described by Berkefeld<sup>13</sup>.

### 3. Non-molecular FLPs

Even if the concept of FLP appeared with observations concerning molecular Lewis acids and bases, recent development showed that the concept could also be found in heterogeneous catalysis. Ma and coworkers published a review on the subject in 2018<sup>16</sup> and classified four types of non-molecular FLPs: semi solid FLP with a solid playing the role of the acid or the base and a molecular specie playing the other role, all solid FLP with a solid Lewis acidic and a solid Lewis base, and all solid FLP within one solid (Figure 11:). The rigidity of solid lattice alongside the surface cluttering was the equivalent of steric hindrance in the case of homogeneous FLP. The main systems that were worth mentioning were:

- Au nanoparticles catalysing the hydrogenation of small imines, nitriles, alkynes and aldehydes<sup>17-19</sup>. The nanoparticles played the role of Lewis acid while the imines, nitriles, phosphines, or amines played the role of molecular Lewis bases.
- Porous polymers with encumbered triphenylphosphine motifs used alongside molecular BCF activating hydrogen and capturing CO<sub>2</sub><sup>20</sup>.
- Molecular sieves combined with BCF catalysing the hydrogenation of ketones and aldehydes<sup>21</sup>.
- CeO<sub>2</sub> with high surface defect density, where oxygen atoms played the role of Lewis bases and cerium atoms played the role of Lewis acids, catalysing the hydrogenation of styrene<sup>22</sup>.

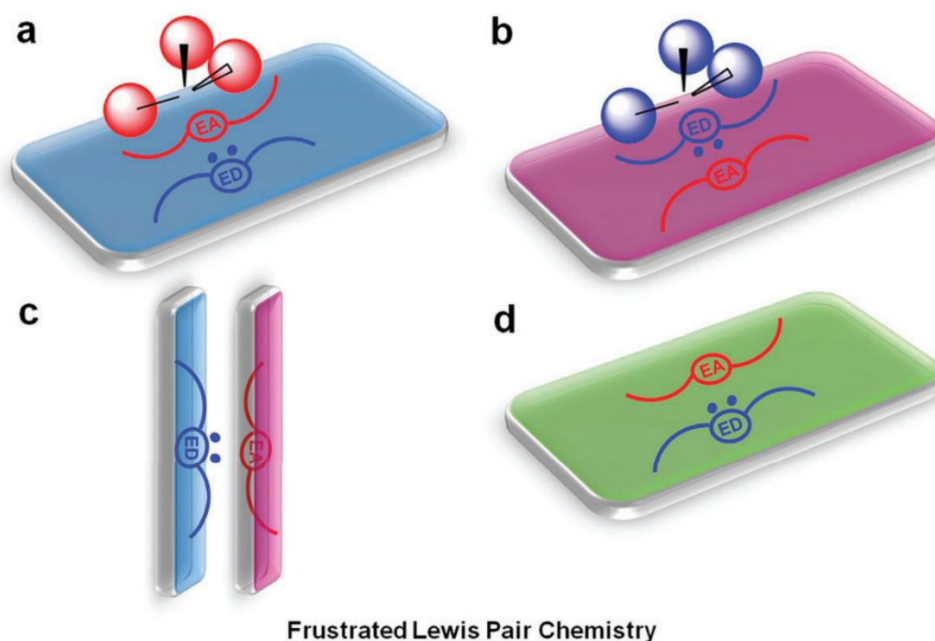


Figure 11: Schematic chemistry of semi-solid and solid FLPs: (a) semi-solid FLP catalyst with the combination of a molecular Lewis acid and a solid Lewis base; (b) semi-solid FLP catalyst with the combination of a molecular Lewis base and a solid Lewis acid; (c) all solid FLP catalyst based on a solid Lewis acid and a solid Lewis base; and (d) all solid FLP catalyst within one solid. From Ma et al.<sup>23</sup>.

### III. Forming a FLP interaction between a nanoparticle surface and its ligands to activate CO<sub>2</sub>: the NanoFLP project

This thesis was funded by the ERC NanoFLP. The goal of this project is the development and the rationalisation of semi-solid FLP catalysts. On the one hand, we will synthesize nanoparticles with either Lewis acid or Lewis base properties, and on the other hand we will chose molecular ligands as counterpart. By finely controlling the synthesis, it should be possible to fine tune the surface properties (acidity, basicity, steric hindrance) of the nanoparticles. Ligands will be chosen adequately among the vast catalogue commercially available. The idea is to create a FLP at the surface of the nanoparticles: a NanoFLP.

In this thesis we were more specifically interested in the activation/valorisation of CO<sub>2</sub>. We saw in the literature that no semi-solid FLP system was reported yet for the activation of CO<sub>2</sub>. We wanted to find a Lewis acido-basic pair capable to catalyse a CO<sub>2</sub> valorisation reaction. Of course trying all the possible nanoparticle-ligand pairs would be impossible, so we decided to strategically focus on certain materials depending on its affinity with CO<sub>2</sub>. We used the following methodology:

- choosing a material known for its interaction with CO<sub>2</sub>, either adsorption or catalysis, preferably both
- choosing a family of molecular counterparts adapted to the chosen material and known to be used in molecular FLP chemistry
- choosing a catalytic reaction for CO<sub>2</sub> valorisation that could be compatible with the chosen material and ligands



This project has received funding from the European Research Council (ERC) under the European Union's Horizon 2020 research and innovation programme (Grant agreement No. 758480).

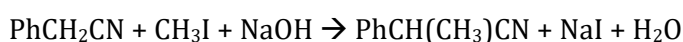


## IV. Materials known for CO<sub>2</sub> adsorption and/or activation in catalysis

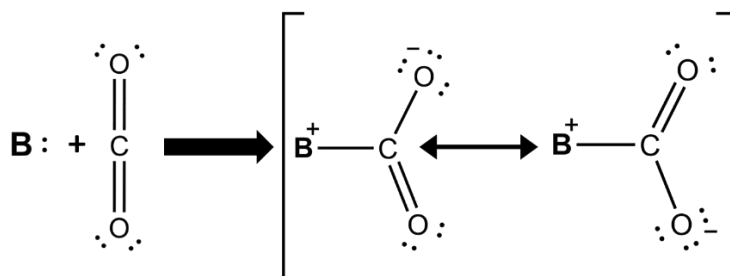
### 1. Materials with Lewis base properties: alkaline-earth oxides

#### a. Generalities on heterogeneous solid bases

As we saw previously, the carbon atom of the CO<sub>2</sub> molecule presents an electrophilic behaviour. This carbon atom can be considered as a Lewis acid and will react with Lewis bases (Scheme 1:). Bases in chemistry have been a subject of interest in catalysis for several decades due to their ability to either deprotonate<sup>24</sup> –in this case we talk about Brønsted basicity - or give an electron pair<sup>25</sup> – in this case we talk about Lewis basicity. Until the 1970s most of the used solid bases like NaOH or KOH led to the formation of secondary products in stoichiometric quantities, often inorganic salts. For example, the methylation of phenylacetonitrile with methyl iodide:



The development of heterogeneous solid base catalysts came later with the works of Tanabe<sup>26</sup>, discovering the activity of calcium oxide and magnesium oxide in the isomerisation of 1-butene. He realised that the activity of the material was strongly dependent of how it was pretreated: in this case the oxides he tested were catalytically active only when they were thermally pretreated under vacuum. Since then, many other solid bases have been discovered, especially among oxide materials, and their use in catalysis exploded<sup>27</sup>.



Scheme 1: Typical reaction between CO<sub>2</sub> and a Lewis base.

Determining the basicity of solid bases is more complex than with their homogeneous counterparts. Three factors come into play: the number of basic sites at the surface of the catalyst, the nature of the basic sites and the strength of the basic sites. If we consider the case of basic oxides, in most cases the oxygen atoms at the surface are the basic sites. The coordination number of surface oxygen atoms will be different depending on the crystallographic facet exposed and on the nature of the site (plane, corner, edge, etc.), thus their basicity will not be the same. For example, in Figure 12: the oxygen atoms in a plane surface O<sup>2-5c</sup> will have a lower basic strength than the oxygen atoms in a corner O<sup>2-3c</sup>. This is due to the fact that the second has three neighbouring Mg<sup>2+</sup> while the first has five, making them more nucleophilic. The basicity of a site

will be the outcome of the crystallographic facet, the number of neighbours, and the environment of the neighbours.

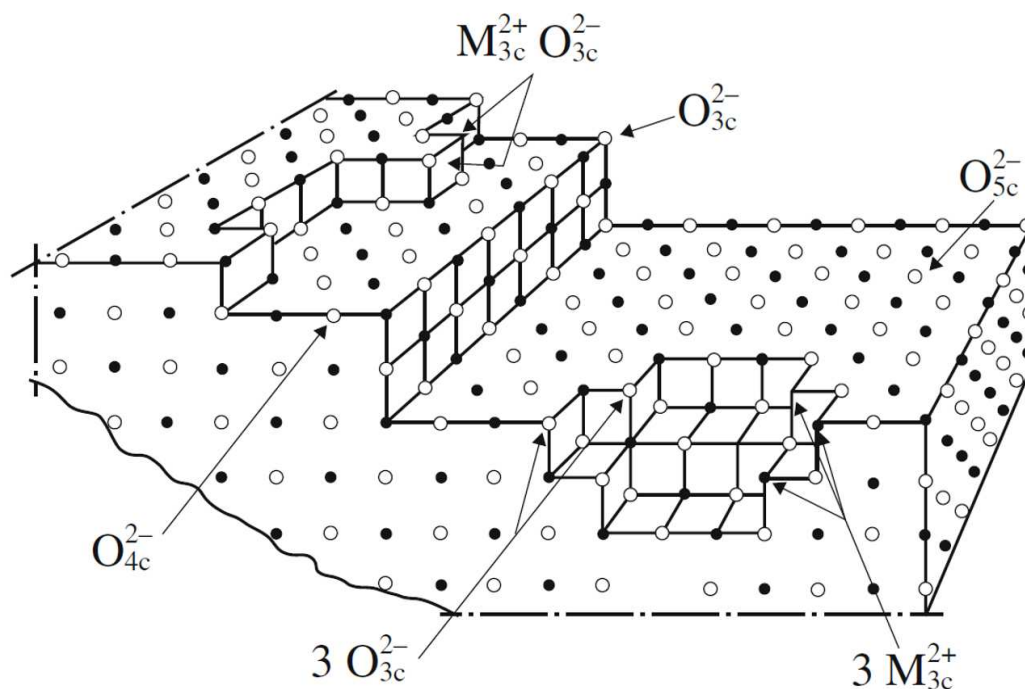


Figure 12: Ions in low coordination at the surface of MgO, reproduced from Ono et al.<sup>27</sup>.

## b. Basicity scale for heterogeneous solid bases

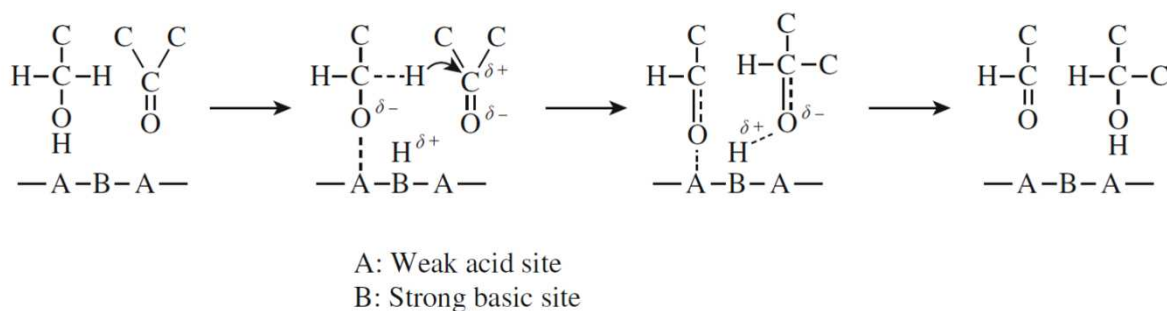
In order to quantify the basic strength of different materials, Tanabe proposed a methodology<sup>28</sup> based on the use of different colour indicator sensitive to pH. He managed to classify different material with a basicity index  $H_-$  that corresponded to the basic strength of the material (Table 1:). It was somehow an equivalent of the  $pK_a$  of organic bases but for inorganic bases: the higher the value, the stronger is the base. It was interesting to notice that depending on the way the samples were prepared (especially for MgO and CaO) the  $H_-$  value could vary. We also had to keep in mind that this indicator was not perfect for our purpose: it presented three main drawbacks. First, it did not dissociate the two components that were the number of basic sites and the basic strength of the sites. Second, the indicators were Brønsted-types acid indicators that may not inform correctly on the Lewis base properties of the material. Third, the determination of the colour-change brought some uncertainties to the method. Nevertheless, it seemed that this scale was a good first order indication of the basicity of different materials.

Solid	$H_-$ value	Remarks
Na/NaOH/Al <sub>2</sub> O <sub>3</sub>	$H_- \geq +37$ $+37 > H_- \geq +35$	
KNO <sub>3</sub> /Al <sub>2</sub> O <sub>3</sub>	$+18.4 > H_- \geq +15.0$ $H_- \geq +27$	35 wt% loading, calcined at 773 K 14 wt% loading
KI/Al <sub>2</sub> O <sub>3</sub>	$18.4 > H_- \geq +15.0$	35 wt% loading, calcined at 773 K
Na/MgO	$H_- \geq +35$	
K/MgO	$H_- \geq +35$ $+35.0 > H_- \geq +27$	K 10%, 15% K10% on MgO, prepared by aerogel method
MgO	$+35 > H_- \geq +27$ $+27 > H_- \geq +17.2$ $+26.5 > H_- \geq +22.3$ $+26.5 > H_- \geq +18.4$ $+18.4 > H_- \geq +17.2$ $+26.5 > H_- \geq +18.4$ $+17.2 > H_- \geq +15.0$	Mg(OH) <sub>2</sub> prepared by aerogel procedure, heated under vacuum at 773 K Mg(OH) <sub>2</sub> heated under vacuum at 773 K Mg(OH) <sub>2</sub> calcined at 773 K Mg(OH) <sub>2</sub> sol-gel, calcined at 1023 K Mg(OH) <sub>2</sub> calcined at 673 K basic magnesium carbonate heated at 723 K under vacuum basic magnesium carbonate calcined at 723 K
CaO	$+33.0 > H_- \geq +26.5$ $H_- \geq +26.5$ $+17.2 > H_- \geq +15.0$	Ca(OH) <sub>2</sub> calcined at 773 K CaCO <sub>3</sub> heated at 723 K under vacuum CaCO <sub>3</sub> calcined at 723 K
MgO-TiO <sub>2</sub> (9 : 1, 1 : 1)	$+18.4 > H_- \geq +17.2$	calcined at 673 K, 773 K
BaO-ZnO	$+18.4 > H_- \geq +15.0$	BaO 2.5 mmol/g, calcined at 873 K
MgO-Al <sub>2</sub> O <sub>3</sub>	$+18.0 > H_- \geq +17.2$	hydrotalcite calcined at 723 K
Hydroxyapatite	$+18.4 > H_- \geq +15.0$	calcined at 673 K
K <sub>3</sub> PO <sub>4</sub>	$+18.4 > H_- \geq +15.0$	calcined at 453 K
Ca(OH) <sub>2</sub>	$+18.4 > H_- \geq +15.0$	
Mg(OH) <sub>2</sub>	$+9.3 > H_- \geq +7.2$	
NaX	$+9.3 > H_- \geq +7.2$	
CsO <sub>x</sub> /NaX	$+18.4 > H_- \geq +17.2$ $+26.5 > H_- \geq +18.4$	Cs (0.36-1.80 mmol g <sup>-1</sup> )-loaded NaX Cs (2.60 mmol g <sup>-1</sup> )-loaded NaX
CsO <sub>x</sub> /CsX	$+18.4 > H_- \geq +17.2$	
Cs <sub>2</sub> O/Al <sub>2</sub> O <sub>3</sub>	$H_- \geq +37$	
Li <sub>2</sub> O, Na <sub>2</sub> O, K <sub>2</sub> O, Cs <sub>2</sub> O/MgO	$+26.5 > H_- \geq +18.4$	calcined at 1023 K
KF/Al <sub>2</sub> O <sub>3</sub>	$+18.4 > H_- \geq +15.0$	calcined at 773 K

Table 1:  $H_-$  values of different basic materials, from Ono et al.<sup>27</sup>.

### c. Intrinsic bifunctionality of heterogeneous basic oxides

In the case of oxides, other surface atoms can play the role of weak acidic site due their ability to accept an electron doublet. This leads to potential interesting types of activity where both the acid and the basic site play a role in the catalytic reaction. Okamoto and coworkers<sup>29</sup> proposed that the hydrogen transfer reaction between ketones and alcohol over MgO catalyst was actually due to a cooperative action of both the strong basic sites and the weak acid side at the surface. In Scheme 2;, the cleavage of the -OH bond is possible thanks to the stabilisation of the alcoolate anion by the acidic site.



Scheme 2: Hydrogen transfer reaction mechanism over a basic oxide, reproduced from Okamoto et al.<sup>29</sup>.

We can distinguish three types of cooperative effect between acid and basic sites: the simultaneous activation of the same substrate on the two sites, the simultaneous activation of two different substrates (one on each site) that will react together, or the sequential activation of the substrate on one site after the other. In all the cases the proximity of the different active sites is a real asset for the catalytic activity.

### d. Alkaline-earth oxides and their affinity toward CO<sub>2</sub>

The reactivity of the basic sites toward the acidic carbon of carbon dioxide have raised an interest since CO<sub>2</sub> capture and valorisation has become a main challenge of the 21<sup>st</sup> century<sup>1</sup>. Among the different types of solid bases, alkaline-earth oxides have shown to be promising due to their affinity with CO<sub>2</sub>. They are known to easily form surface carbonates or even bulk carbonates at room temperature in presence of CO<sub>2</sub><sup>30</sup>. These materials, especially CaO, are considered as good candidates for CO<sub>2</sub> capture technologies. Industrial processes using CaO called “Calcium looping” have been developed in the last decades<sup>31</sup> (Figure 13:). Several catalytic reactions involving alkaline-earth oxides (either as a catalyst or as a catalyst support) and CO<sub>2</sub> are reported, such as the cycloaddition of CO<sub>2</sub> on epoxides<sup>32</sup> or the CO<sub>2</sub> reforming of methane<sup>33</sup>. The basicity of the oxide increases the heavier the alkaline-earth atom is, meaning that they form a natural basicity scale starting from the less basic MgO to the most basic BaO<sup>34</sup>.

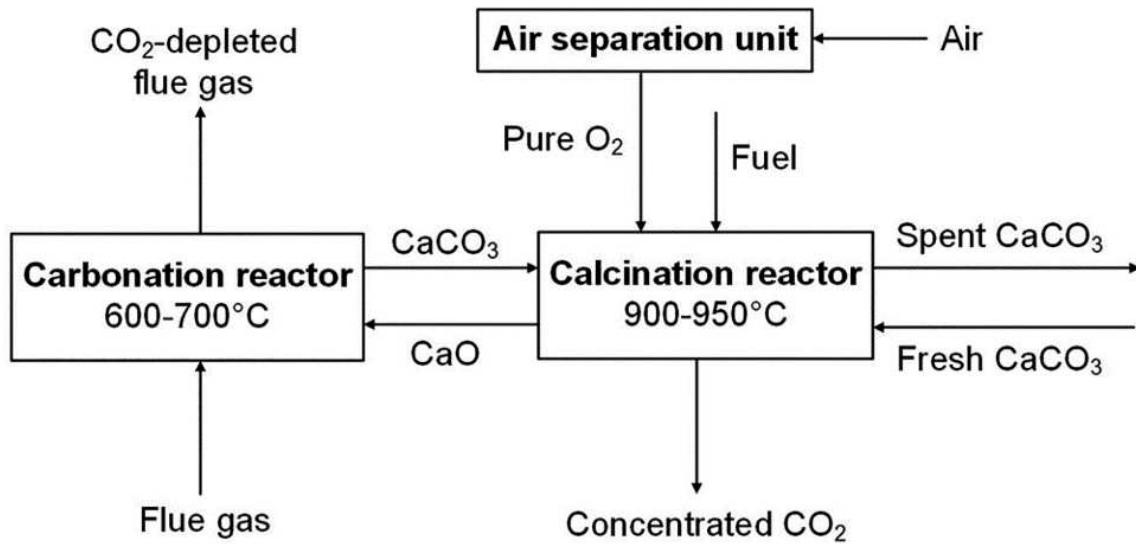


Figure 13: Calcium looping functioning, from Chen et al.<sup>31</sup>.

In our idea to develop a NanoFLP, alkaline-earth oxides seem to be good candidates. The combination of basic surface properties and affinity with the molecule that we want to activate will provide a good starting point. The control we can have over the nanoparticles size, shapes and exposed crystallographic facets will allow us to see if the NanoFLP is feasible. Since beryllium-based compounds are toxic, we decided to study alkaline-earth oxides starting from MgO.

## 2. MgO: synthesis and applications

### a. Generalities on magnesium-based materials

Magnesium is an abundant element on earth: it is the second most abundant cation in the hydrosphere and the sixth most abundant element in the lithosphere. It also plays an important role in the regulation of living organism, especially in the regulation of ATP. It is the second most present cation in most living organisms<sup>35</sup>. Magnesium is used in material science, mostly in construction materials<sup>36</sup> but also in microelectronic<sup>37</sup> and in batteries<sup>38</sup>. Magnesium oxide is a specific type of magnesium material. It is the main component of the mineral periclase, however, this mineral is quite rare in the nature due to its tendency to form brucite, which main component is magnesium hydroxide  $\text{Mg}(\text{OH})_2$ , or magnesite, which main component is magnesium carbonate  $\text{MgCO}_3$ , upon exposition to respectively water or carbon dioxide<sup>39</sup>.

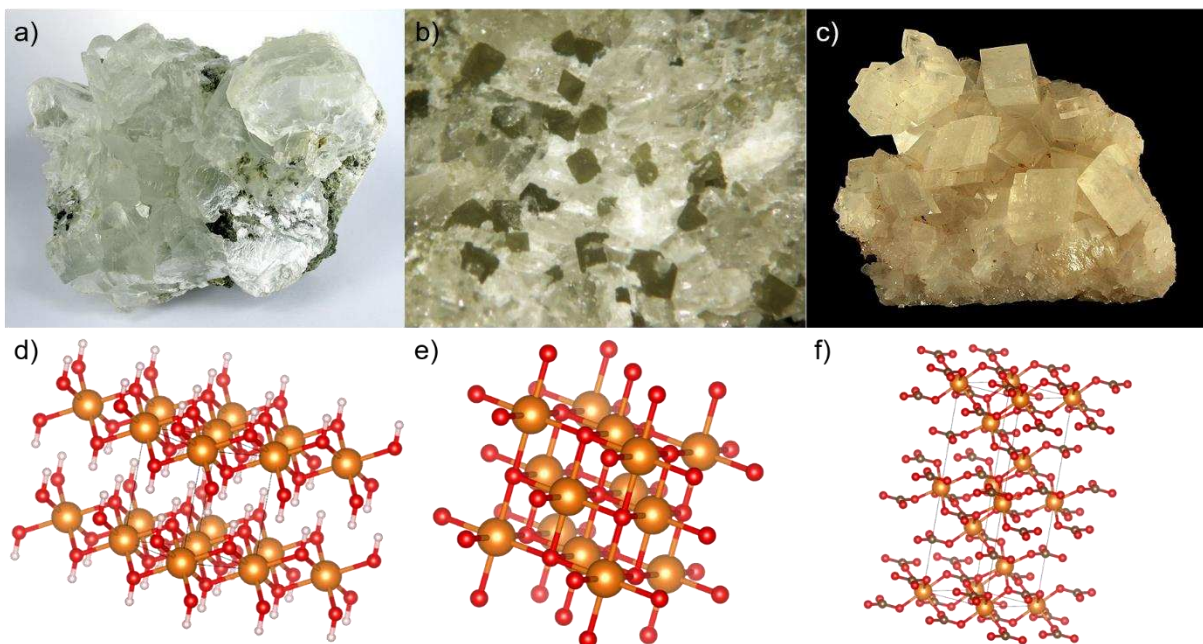


Figure 14: Natural crystals of a) brucite, b) periclase, c) calcite, and their corresponding crystallographic structure d), e) and f) (atom color: Mg=orange, O=red, H=white, C=black).

The easiest way to obtain MgO is the calcination of magnesium precursor like  $\text{Mg}(\text{OH})_2$  or  $\text{MgCO}_3$  at high temperature. Amongst the multiple synthetic pathways, almost all of them end with the calcination of one of these two precursors. When a certain type of MgO synthesis is mentioned in the literature, it most often refers to the pathway leading to either  $\text{Mg}(\text{OH})_2$  or  $\text{MgCO}_3$ , which is followed by a calcination. The properties of the final MgO particles strongly depend of the properties of the precursor.

## b. Synthesis of MgO precursor

One of the easiest pathways is precipitation-calcination in aqueous media: a magnesium salt is precipitated in basic aqueous solution to form Mg(OH)<sub>2</sub> and then calcined to form MgO<sup>40,41,42,43,44</sup>. Henrist and co-workers<sup>40</sup> showed that the use of MgCl<sub>2</sub> and Mg(NO<sub>3</sub>)<sub>2</sub> as magnesium precursors lead to the formation of platelet like magnesium hydroxide nanoparticles whereas the use of MgSO<sub>4</sub> leads to fused primary particles. They showed that the nature of the base and the temperature both have an impact on the aggregation of the particles. It is also possible to attain more complex structures with the use of templating agents, like Bain et al.<sup>45</sup> who obtained “flower like” structures by adding both poly(vinylpyrrolidone) and ethylene glycol in the synthesis.

Synthesis of Mg(OH)<sub>2</sub> is also possible through a hydrothermal pathway<sup>46,47</sup>, the main difference being that the reaction happens at temperatures higher than 100 °C in a pressurized vessel. Hydrothermal pathway tends to lead to better crystallinity of the particles<sup>40</sup>.

Sol-gel syntheses are also viable pathways to obtain Mg(OH)<sub>2</sub><sup>48</sup>, that can lead in the end to polymer-like MgO gel as shown by Matsuli et al.<sup>49</sup>.

More exotic pathways also exist, such as microwave assisted synthesis<sup>50</sup>, combustion reaction<sup>51</sup>, ultrasound assisted synthesis<sup>52</sup>, direct use of brucite<sup>53</sup> (natural mineral composed of Mg(OH)<sub>2</sub>), or hydration of magnesium oxide followed by a calcination<sup>54</sup> (the idea being to increase the crystallinity by a dissolution-recrystallization process). Pilarska and co-workers<sup>55</sup> gave a more extensive review of the variety of pathways leading to the formation of MgO and Mg(OH)<sub>2</sub> (Figure 15:).

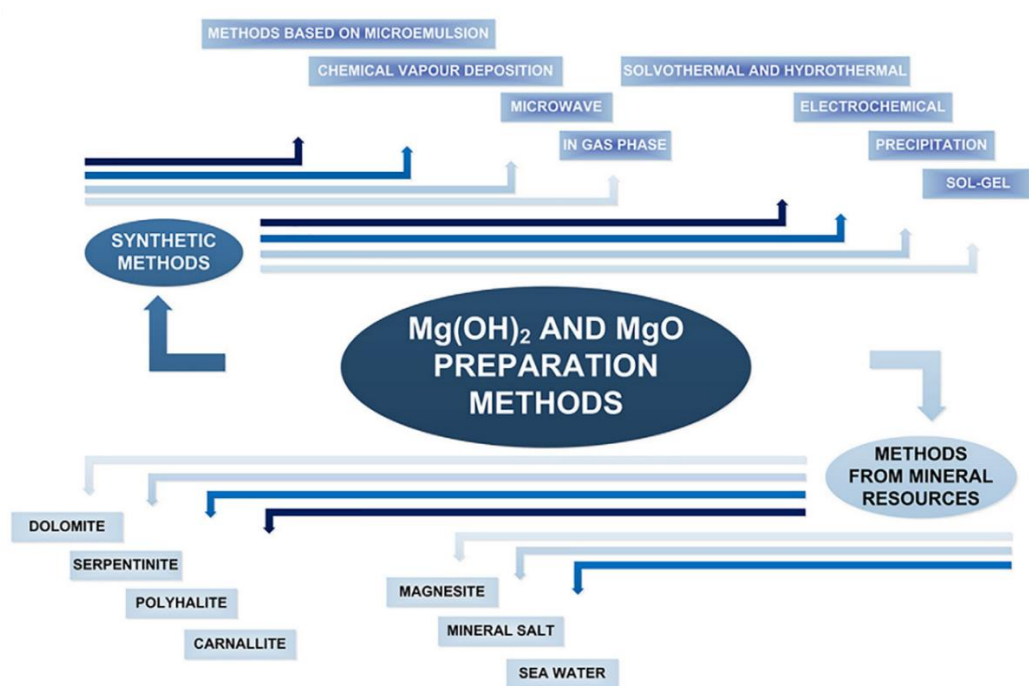


Figure 15: Methods for MgO and Mg(OH)<sub>2</sub> preparation, from Pilarska et al.<sup>55</sup>.

### c. Calcination of the precursor to form MgO

The other key part in the synthesis of MgO particles is the calcination. During this step several phenomena occur at the same time: at the atomic level there is a rearrangement of the crystalline lattice of  $\text{Mg}(\text{OH})_2$  to form MgO with  $\text{H}_2\text{O}$  leaving the crystal, at the nanoscopic level diffusion at the boundaries of the particles will fuse the objects together causing sintering.

Decomposition of  $\text{Mg}(\text{OH})_2$  has been studied since the 1960s. Gordon and coworkers<sup>56</sup> used electron microscopy and electron diffraction to study the in-situ decomposition of mineral brucite into MgO. They showed that formation of magnesium oxide could be assimilated to a nucleation and growth mechanism where the MgO nuclei form coherently with the brucite  $\text{Mg}(\text{OH})_2$  matrix causing large strains and fissuring of the original crystal (Figure 16:).

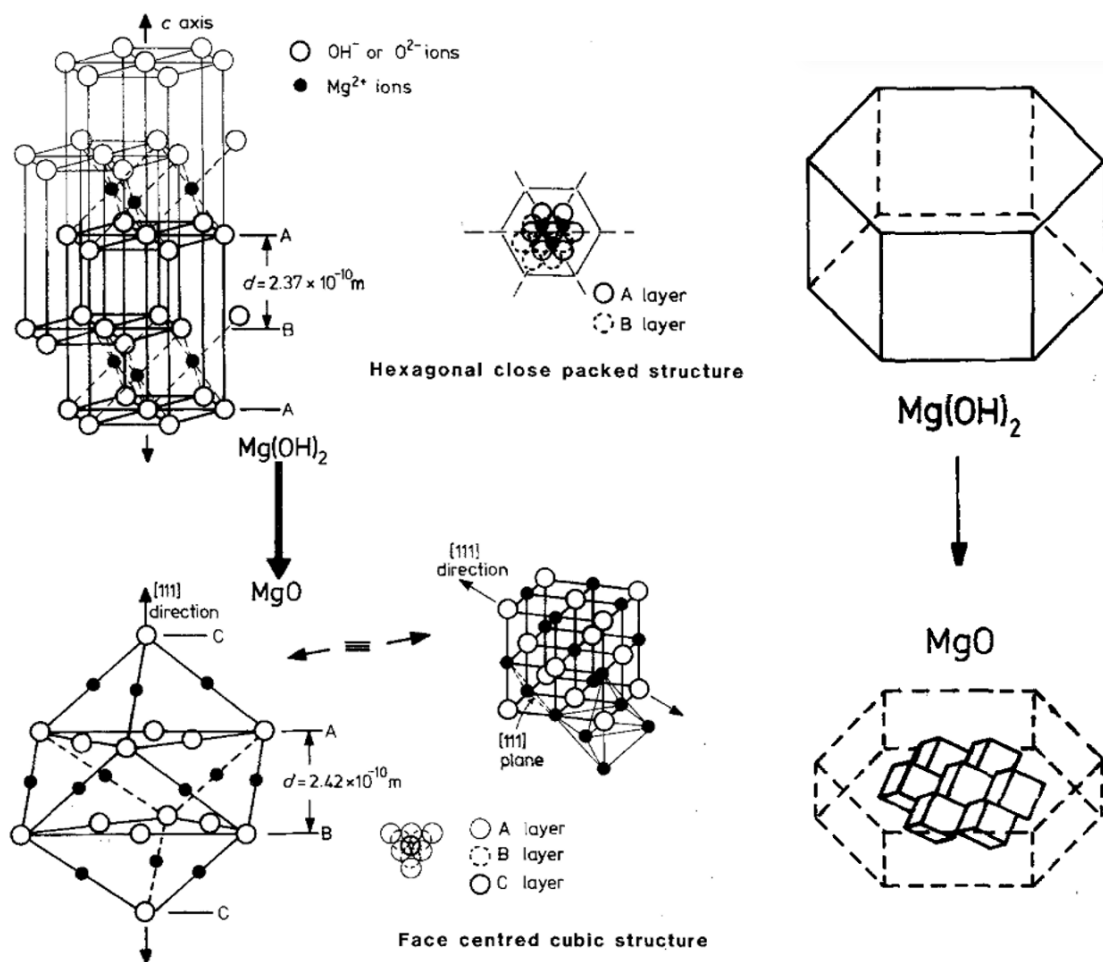


Figure 16: Relation between  $\text{Mg}(\text{OH})_2$  and MgO in terms of crystal structure (left) and nanoparticle morphology (right), from Green<sup>57</sup>.

In another study, the group of Itatina<sup>58</sup> showed that, depending on the calcination temperature, the different crystallite inside the particles would arrange differently. At 600 °C the crystallites can agglomerate and coalesce while retaining the morphological characteristic of the



initial Mg(OH)<sub>2</sub> particles. At 800 °C the nucleation and growth of MgO is similar but the morphology of the particles is not retained anymore, breaks and cracks start to appear. At 900 °C the growth of the crystallites leads to pore coalescence, but most of the pores are still in the particles. At 1200 °C the crystallites grow rapidly and the energy allows the pore to migrate and to be ejected out of the nanoparticles (Figure 17:).

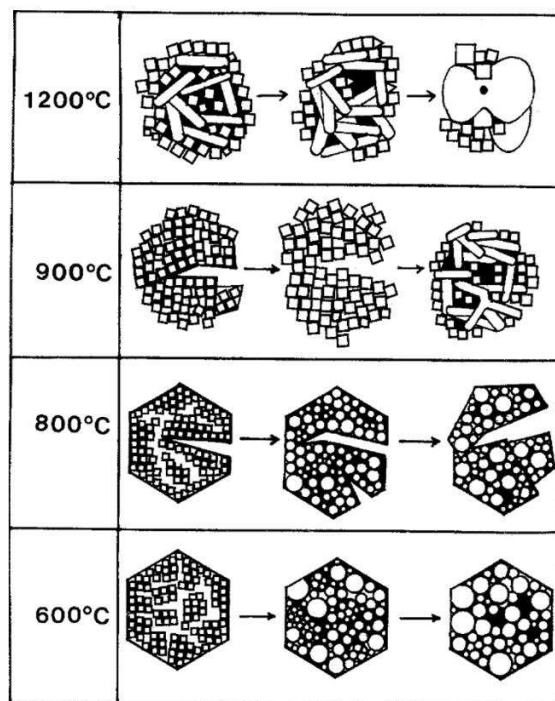


Figure 17: Evolution of the MgO crystallites during the calcination depending on the temperature, from Itatina et al.<sup>58</sup>.

Kotera and coworkers<sup>53</sup> quantified the increase of the average MgO crystallite size depending on the calcination temperature and duration. They showed that overall the crystallite size increases with time and temperature, and at fixed temperature the rate of growth follows a logarithmic law. However, at fixed calcination duration the growth rate increases exponentially with temperature.

Green<sup>57</sup> showed that the presence of impurities and surface species can also impact the nucleation. Presence of water tends to enhance nucleation of MgO, meaning that calcinations happening under vacuum will give crystallites of higher sizes at a same temperature. The presence of ionic species can either favour the grain growth, such as Fe<sup>2+</sup>, Fe<sup>3+</sup>, Si<sup>4+</sup>, Cl<sup>-</sup>, Li<sup>+</sup>, Mn<sup>3+</sup>, Mn<sup>4+</sup>, and Na<sup>+</sup>, whereas others tend to prevent grain growth and lead to smaller crystallites, such as K<sup>+</sup>, SO<sub>3</sub><sup>2-</sup>, NO<sub>3</sub><sup>-</sup> and possibly NO<sub>2</sub><sup>-</sup>.

Modifications of MgO particles are very common. For example surface functionalisation is possible after the calcination, as shown by Park and co-workers<sup>42</sup> who used capping agents like oleic acid after the synthesis in order to improve the dispersibility of the nanoparticles in organic solvents.

### d. Applications of MgO

MgO is used for a lot of applications. It can be used in the electronic industry thanks to its dielectric properties<sup>59</sup>, making it a good insulating material. The mechanical strength of the material can be of interest in construction materials<sup>60</sup>. Its thermal stability is a great advantage for the conception of refractory materials<sup>61</sup>. MgO also have antibacterial properties<sup>50</sup>, and its non-toxicity for human make it useable as acid neutraliser for gastric treatment or as source of Mg<sup>2+</sup> ions in food supplements<sup>62</sup>.

The surface properties of magnesium oxide are what is the most interesting for us in the idea to develop a NanoFLP. MgO is used as an active adsorbent for both pollutants in effluents<sup>46, 51,63</sup> and gaseous species like CO<sub>2</sub>, SO<sub>2</sub> and NO<sub>2</sub><sup>64,65,66</sup>.

It is also used either as a catalyst or a catalyst support in organic reactions. For example, Xu et al.<sup>33</sup> synthesized a Ni catalyst supported on MgO for the CO<sub>2</sub> reforming of methane, where the support increases the durability of the catalyst toward coking. Zhang et al<sup>67</sup> showed that cobalt oxide supported on MgO is a highly efficient catalyst for the degradation of organic pollutants, the support allowing the good dispersion of the cobalt oxide nanoparticles, reducing the leaching of the cobalt in solution and facilitating the formation of reactive surface species on the cobalt atoms.

### e. MgO in catalysis

There are plenty examples of MgO as catalyst support very well compiled by Julkapli et al. in their review<sup>68</sup>, the most notable reactions where it is used are dry reforming, dehydrohalogenation, dehydrogenation and hydrodesulfurisation. Magnesium oxide on its own can also be a catalyst due to its basic properties.

As mentioned above, basic oxide like MgO are active in condensation reactions like aldol condensation<sup>69</sup> and Claisen-Schmidt condensation<sup>45,70,71</sup>. Several groups showed the activity of MgO in the cycloaddition of CO<sub>2</sub> on epoxides<sup>72,73</sup>, which could be interesting for us since it involves the molecule we would like to activate. Hattori<sup>74</sup> and co-workers mentioned the activity of MgO in hydrogenation reactions when the catalyst was pretreated at high temperatures above 1000 °C. Choudary and co-workers showed that it was active in benzylation reactions<sup>75</sup> and supposed that the formation of Mg—Cl surface groups increased the acidity of the corresponding Mg atoms and drove the reaction. MgO also showed an activity in the asymmetric reactions of Henry and Michael<sup>76</sup>.

Overall, it is important to understand that the activity of MgO in a certain catalytic reaction depends both on the synthetic pathway leading to the catalyst and the pretreatment. Figure 18: illustrates the fact that certain reactions such as hydrogenation (squares) will require high temperature treatment in order to generate strong basic sites, whereas other reactions such as isomerization (circles) will require much lower temperatures. This effect of the temperature treatment brings into play the generation of strong basic sites and reduction of the surface area of the material via sintering.

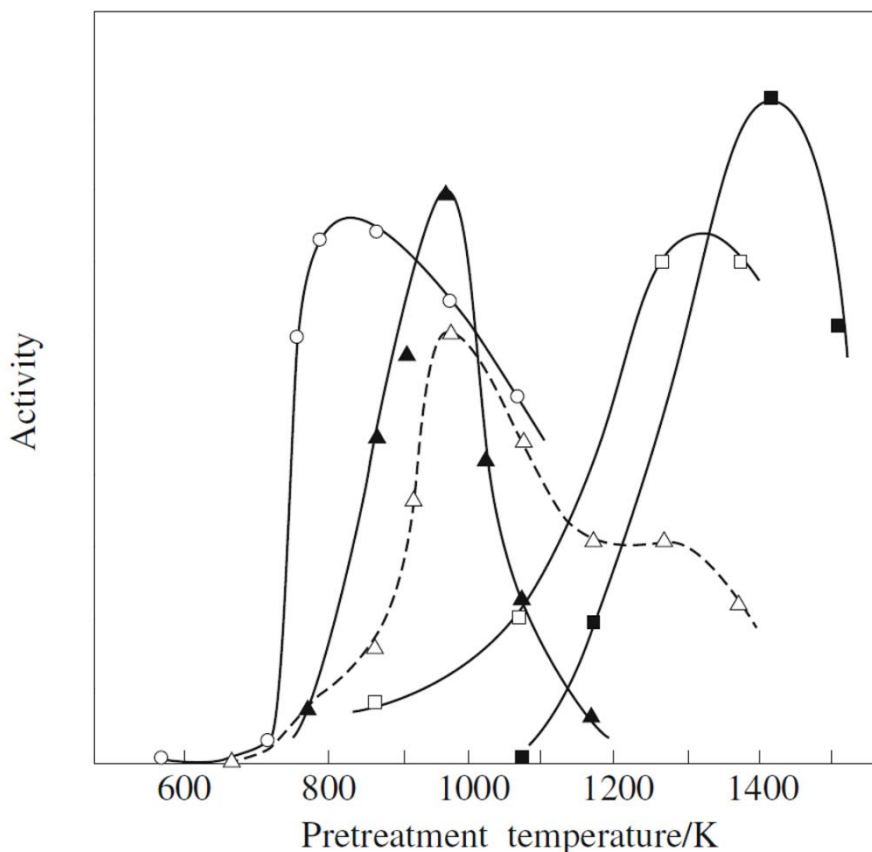


Figure 18: Variation of MgO catalytic activity for different reactions as a function of the pretreatment temperature. Reactions : circles=1-butene isomerization at 303 K, full triangles=CH<sub>4</sub>-D<sub>2</sub> exchange at 673 K, hollow triangles=amination of 1,3-butadiene with dimethylamine at 273 K, full square=ethylene hydrogenation at 523 K, hollow square=1,3-butene hydrogenation at 273 K. From Ono et al.<sup>27</sup>.

Overall, MgO is a well-rounded material, with different synthesis pathways each providing advantages and inconvenient. Depending on how the material was prepared, the reactivity of the material will not be the same. Small particles with high surface area will be used for applications such as adsorption or catalysis, while bigger crystalline objects will we used for construction or electronic materials. Following the route of alkaline-earth oxide synthesis, let's get interested in the next element in the second column: calcium.

### 3. CaO: synthesis and applications

#### a. Calcium oxide synthesis

A lot of what we previously discussed for magnesium oxide is actually also relevant for calcium oxide. The synthesis of CaO almost always ends with the calcination of a calcium precursor (often  $\text{Ca}(\text{OH})_2$  or  $\text{CaCO}_3$ ) that was obtained by methods such as precipitation<sup>77</sup> or sol-gel<sup>78</sup>. However, since calcium is an element that is more bio-abundant than magnesium, a lot of research developed syntheses using natural sources. We can think about the use of mineral sources:  $\text{CaCO}_3$  is the main component of limestone, one of the most abundant sedimentary rocks<sup>79</sup>. We can also think about bio-based sources like egg-shells<sup>80</sup> or animal bones<sup>81</sup>. Figure 19: gives an overview of the natural waste resources that could be used for the synthesis of CaO particles with a 3-step process: washing, grinding and calcination. These types of syntheses often lead to less well defined materials, with more defects and more chemical impurities than those using purified products. This can actually be an asset for the catalytic activity of the material.

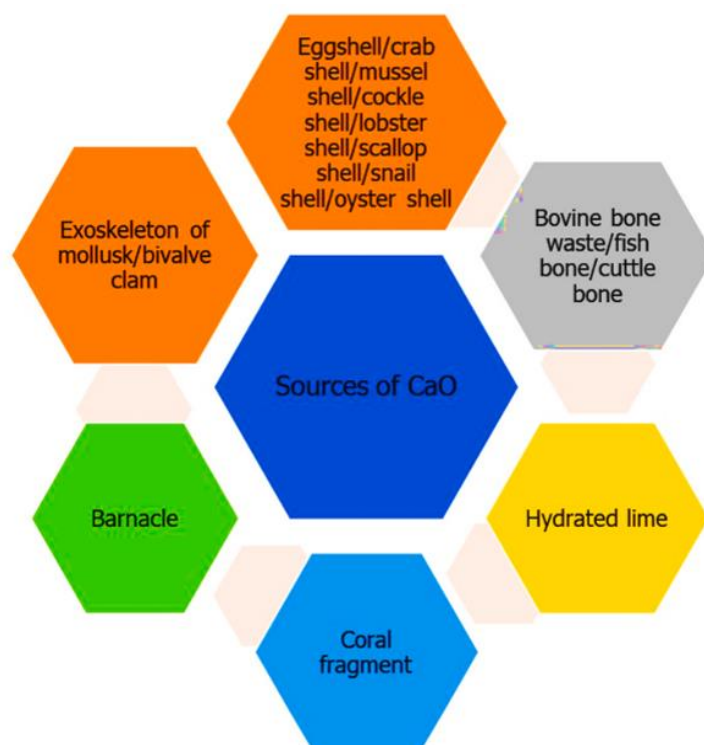
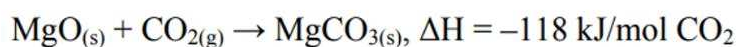
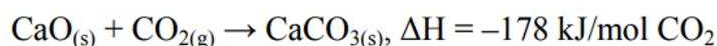
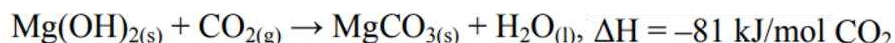
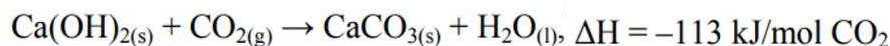


Figure 19: Natural waste sources for CaO synthesis, from Zul et al.<sup>82</sup>.

#### b. Application of CaO for CO<sub>2</sub> capture

The interaction between CO<sub>2</sub> and calcium oxide is much stronger than the one with magnesium oxide, as shown by the enthalpy of carbonation reaction in Scheme 3: This means that the formation of bulk carbonate is much faster and more exothermic. However, the calcination reaction (going from the carbonate to the oxide) costs more energy. Overall this stronger affinity with CO<sub>2</sub> and the natural availability of calcium pushed the development of CO<sub>2</sub> capture

technologies based on the formation of CaCO<sub>3</sub> from CaO called calcium looping<sup>31</sup>. This process starts to see some industrial implementations in the recent years. However, one of the disadvantages with the affinity of CaO toward CO<sub>2</sub> compared to MgO is that the calcination temperature needed to regenerate CaO from CaCO<sub>3</sub> is higher, meaning that the sintering of the nanoparticles at this temperature will also be more pronounced. This results in a progressive loss of the high surface area of the CaO sorbent and a reduction of its efficiency over time<sup>83,84</sup>.



*Scheme 3: Carbonation reactions and associated enthalpy, from Pan et al.<sup>85</sup>.*

### c. CaO in catalysis

CaO is used also in catalysis, mostly in the same reactions as MgO. However, depending on the reaction its activity can be either higher or lower than MgO. CaO is especially used in transesterification reactions for the production of bio-diesel<sup>28,79,81,82</sup>. The strong basicity of CaO allows the formation of a methoxide anion (CH<sub>3</sub>O<sup>-</sup>) which is the first step in the reaction mechanism. Due to its natural availability and its applications in carbon capture and bio-diesel production, it seems that calcium oxide is a promising material for the development of future green technologies.

## V. Classical molecular acids used in FLP: boranes

### 1. Boranes in catalysis

Boranes have been widely used in FLP chemistry since its beginning. Most of the FLPs mentioned previously uses boranes as molecular Lewis acid. Tris(pentafluorophenyl)borane ( $B(C_6F_5)_3$  or BCF) has raised interest for its catalytic properties even before the discovering of FLP chemistry<sup>86</sup>, it includes hydrometallation reactions, alkylations and tautomerizations.

Sivaev et al.<sup>87</sup> made an extensive review on the Lewis acidity of a large variety of borane and showed that BCF was among the strongest acids. Only halogenoboranes such as  $BI_3$  showed a higher Lewis acidity. The main parameters influencing the borane acidity included the electronegativity of the substituents at the boron atom, the presence of electron-withdrawing or electron-donating substituents, inclusion of the boron atom in a flat ring, etc. Figure 20: gives an acidity scale among the different types of boron compounds.

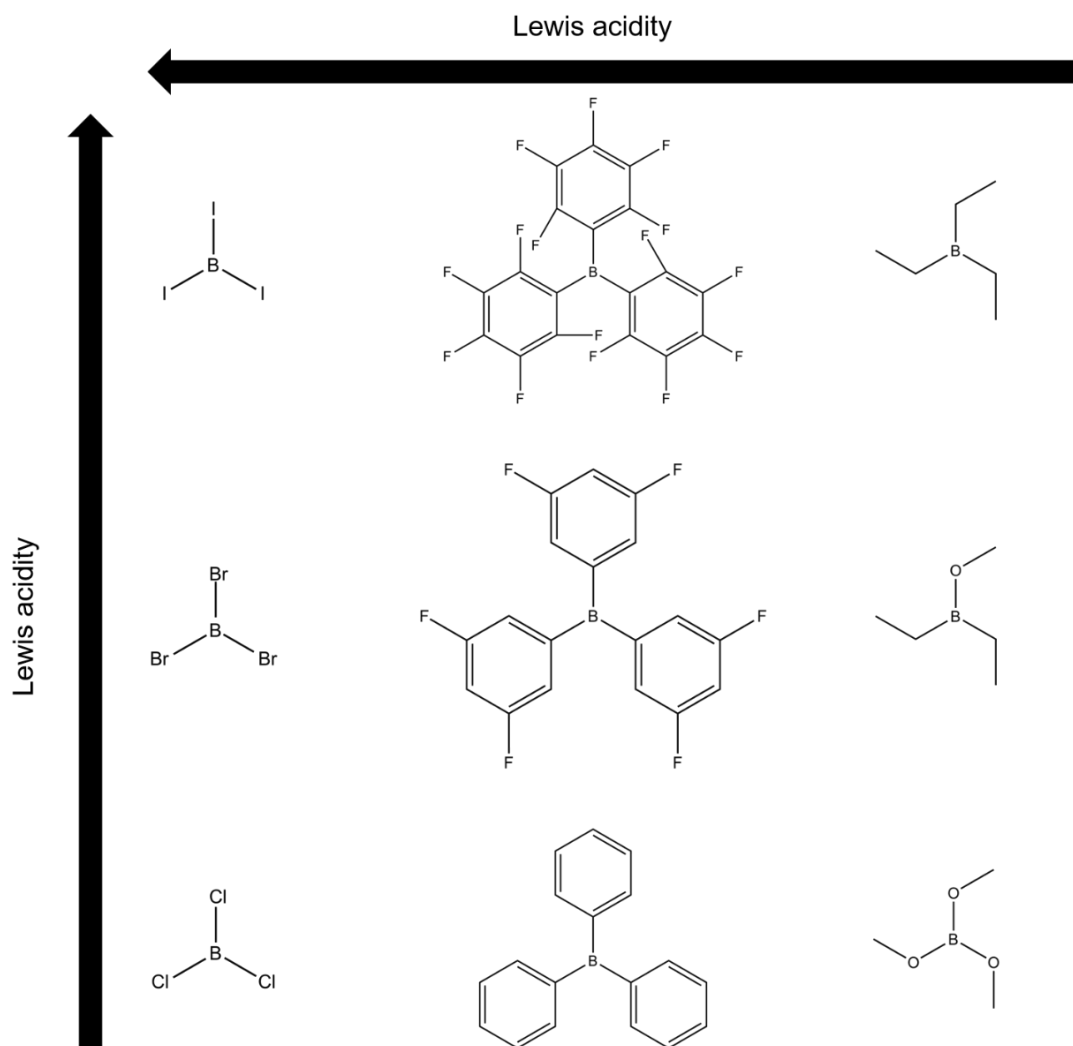


Figure 20: Trends in Lewis acidity of boron containing compounds.

## 2. Boranes for CO<sub>2</sub> activation

In addition of being a classic Lewis acid for FLP systems, boranes and boron-based materials in general have shown an activity for CO<sub>2</sub> activation<sup>88</sup>. The main reaction was the CO<sub>2</sub> reduction by hydroboranes, diboranes and silylboranes. Most of the time the reaction needed a catalyst to happen. In the example detailed in Figure 21:, a copper catalyst was used to activate the CO<sub>2</sub> molecule via a coordination of the oxygen atom on the Cu center and the formation of a C—B bond with the Bpin ligand. This lead to the formation of CO molecule and OBpin coordinated to the Cu center. The diborane B<sub>2</sub>(pin)<sub>2</sub> allows the regeneration of the IPrCu—Bpin catalyst via the formation of pinBOBpin.

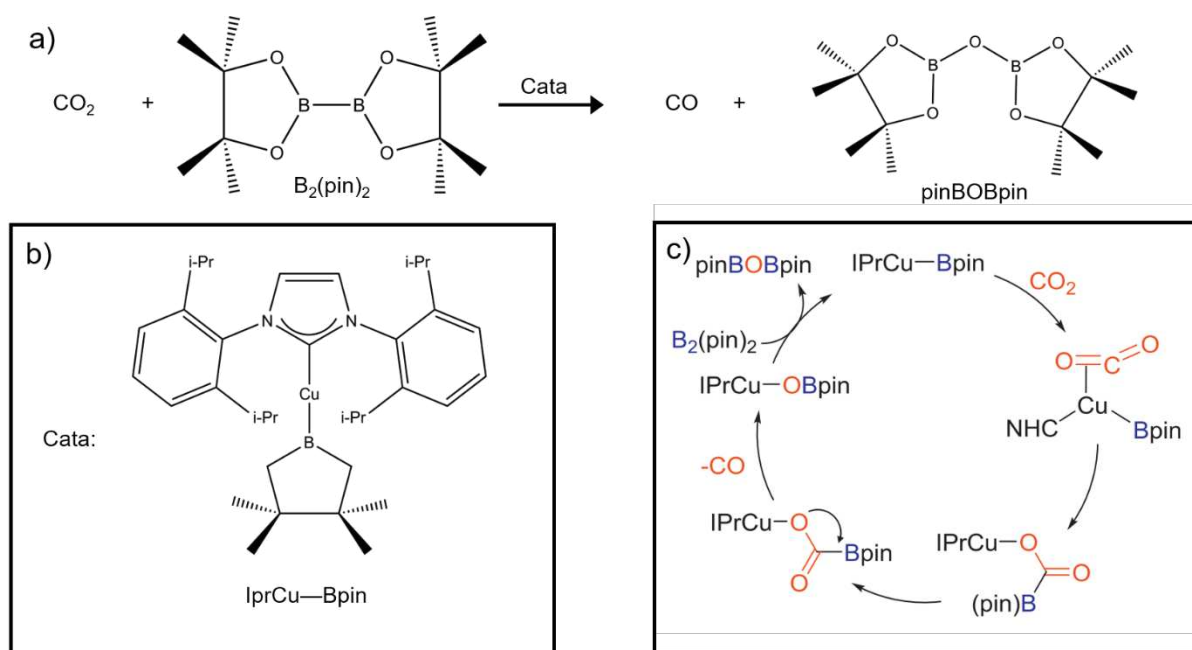


Figure 21: a) Reduction of CO<sub>2</sub> into CO by diborane B<sub>2</sub>(pin)<sub>2</sub>, b) copper-based catalyst for the reaction, c) reaction mechanism. From Bontemps et al.<sup>88</sup>.

## VI. Approach for the design of a NanoFLP for CO<sub>2</sub> activation

To our knowledge, there was no mention in the literature of semi-solid FLP catalyst able to convert CO<sub>2</sub>. There was no mention either of the study on the interaction between alkaline earth oxide nanoparticles and borane ligands. This nanoparticle-ligand pair could be promising for the activation of CO<sub>2</sub>. We decided to decompose the project in three parts:

- The study of the synthesis of alkaline earth oxide nanoparticles, starting with MgO. We will study the different pathways and try to control the surface properties of the nanoparticles.
- The study of the adsorption of CO<sub>2</sub> and borane ligands at the surface of the synthesized nanoparticles. In a first time only CO<sub>2</sub> and borane on their own, then together. We will choose a different panel of borane ligands to have some flexibility in the third part of the project.
- The study of the behaviour of the nanoparticles-ligand catalytic performances in the cycloaddition of CO<sub>2</sub> on epoxides, a reaction catalysed by alkaline earth oxides. We will first study the performances of the synthesized nanoparticles and then add boranes in the reaction. We hope to detect a variation of either the activity or the selectivity of the catalyst. We will study the impact of different parameters such as temperature, reaction duration, ligand concentration, stoichiometry, etc. If we detect a significant impact of the addition of a borane, we will try to understand the interaction between the nanoparticle and the ligand in the catalytic reaction to find if it could be attributed to NanoFLP.



- (1) Song, C. Global Challenges and Strategies for Control, Conversion and Utilization of CO<sub>2</sub> for Sustainable Development Involving Energy, Catalysis, Adsorption and Chemical Processing. *Catal. Today* **2006**, *115* (1–4), 2–32. <https://doi.org/10.1016/j.cattod.2006.02.029>.
- (2) Álvarez, A.; Borges, M.; Corral-Pérez, J. J.; Olcina, J. G.; Hu, L.; Cornu, D.; Huang, R.; Stoian, D.; Urakawa, A. CO<sub>2</sub> Activation over Catalytic Surfaces. *ChemPhysChem* **2017**, *18* (22), 3135–3141. <https://doi.org/10.1002/cphc.201700782>.
- (3) Meessen, J. Urea Synthesis. *Chemie Ing. Tech.* **2014**, *86* (12), 2180–2189. <https://doi.org/10.1002/cite.201400064>.
- (4) Wick, J. Y. Aspirin: A History, A Love Story. *Consult. Pharm.* **2012**, *27* (5), 322–329. <https://doi.org/10.4140/TCP.n.2012.322>.
- (5) Świrk, K.; Grzybek, T.; Motak, M. Tri-Reforming as a Process of CO<sub>2</sub> Utilization and a Novel Concept of Energy Storage in Chemical Products. *E3S Web Conf.* **2017**, *14*, 02038. <https://doi.org/10.1051/e3sconf/20171402038>.
- (6) Masel, R. I.; Liu, Z.; Yang, H.; Kaczur, J. J.; Carrillo, D.; Ren, S.; Salvatore, D.; Berlinguette, C. P. An Industrial Perspective on Catalysts for Low-Temperature CO<sub>2</sub> Electrolysis. *Nat. Nanotechnol.* **2021**, *16* (2), 118–128. <https://doi.org/10.1038/s41565-020-00823-x>.
- (7) Welch, G. C.; Juan, R. R. S.; Masuda, J. D.; Stephan, D. W. Reversible, Metal-Free Hydrogen Activation. *Science (80-. )*. **2006**, *314* (5802), 1124–1126. <https://doi.org/10.1126/science.1134230>.
- (8) Stephan, D. W. Frustrated Lewis Pairs. *J. Am. Chem. Soc.* **2015**, *137* (32), 10018–10032. <https://doi.org/10.1021/jacs.5b06794>.
- (9) Stephan, D. W.; Erker, G. Frustrated Lewis Pair Chemistry of Carbon, Nitrogen and Sulfur Oxides. *Chem. Sci.* **2014**, *5* (7), 2625–2641. <https://doi.org/10.1039/c4sc00395k>.
- (10) Fontaine, F.-G.; Stephan, D. W. Metal-Free Reduction of CO<sub>2</sub>. *Curr. Opin. Green Sustain. Chem.* **2017**, *3*, 28–32. <https://doi.org/10.1016/j.cogsc.2016.11.004>.
- (11) Mömning, C. M.; Otten, E.; Kehr, G.; Fröhlich, R.; Grimme, S.; Stephan, D. W.; Erker, G. Reversible Metal-Free Carbon Dioxide Binding by Frustrated Lewis Pairs. *Angew. Chemie Int. Ed.* **2009**, *48* (36), 6643–6646. <https://doi.org/10.1002/anie.200901636>.
- (12) Anker, M. D.; Arrowsmith, M.; Bellham, P.; Hill, M. S.; Kociok-Köhn, G.; Liptrot, D. J.; Mahon, M. F.; Weetman, C. Selective Reduction of CO<sub>2</sub> to a Methanol Equivalent by B(C<sub>6</sub>F<sub>5</sub>)<sub>3</sub>-Activated Alkaline Earth Catalysis. *Chem. Sci.* **2014**, *5* (7), 2826–2830. <https://doi.org/10.1039/c4sc00885e>.
- (13) Berkefeld, A.; Piers, W. E.; Parvez, M. Tandem Frustrated Lewis Pair/Tris(Pentafluorophenyl)Borane-Catalyzed Deoxygenative Hydrosilylation of Carbon Dioxide. *J. Am. Chem. Soc.* **2010**, *132* (31), 10660–10661. <https://doi.org/10.1021/ja105320c>.
- (14) Ashley, A. E.; Thompson, A. L.; O'Hare, D. Non-Metal-Mediated Homogeneous Hydrogenation of CO<sub>2</sub> to CH<sub>3</sub>OH. *Angew. Chemie Int. Ed.* **2009**, *48* (52), 9839–9843. <https://doi.org/10.1002/anie.200905466>.
- (15) Ménard, G.; Stephan, D. W. Room Temperature Reduction of CO<sub>2</sub> to Methanol by Al-Based Frustrated Lewis Pairs and Ammonia Borane. *J. Am. Chem. Soc.* **2010**, *132* (6), 1796–1797. <https://doi.org/10.1021/ja9104792>.
- (16) Ma, Y.; Zhang, S.; Chang, C. R.; Huang, Z. Q.; Ho, J. C.; Qu, Y. Semi-Solid and Solid Frustrated Lewis Pair Catalysts. *Chem. Soc. Rev.* **2018**, *47* (15), 5541–5553.

- <https://doi.org/10.1039/C7CS00691H>.
- (17) Lu, G.; Zhang, P.; Sun, D.; Wang, L.; Zhou, K.; Wang, Z.-X.; Guo, G.-C. Gold Catalyzed Hydrogenations of Small Imines and Nitriles: Enhanced Reactivity of Au Surface toward H<sub>2</sub> via Collaboration with a Lewis Base. *Chem. Sci.* **2014**, *5* (3), 1082–1090. <https://doi.org/10.1039/C3SC52851K>.
- (18) Fiorio, J. L.; López, N.; Rossi, L. M. Gold–Ligand-Catalyzed Selective Hydrogenation of Alkynes into Cis -Alkenes via H<sub>2</sub> Heterolytic Activation by Frustrated Lewis Pairs. *ACS Catal.* **2017**, *7* (4), 2973–2980. <https://doi.org/10.1021/acscatal.6b03441>.
- (19) Cano, I.; Huertos, M. A.; Chapman, A. M.; Buntkowsky, G.; Gutmann, T.; Groszewicz, P. B.; van Leeuwen, P. W. N. M. Air-Stable Gold Nanoparticles Ligated by Secondary Phosphine Oxides as Catalyst for the Chemoselective Hydrogenation of Substituted Aldehydes: A Remarkable Ligand Effect. *J. Am. Chem. Soc.* **2015**, *137* (24), 7718–7727. <https://doi.org/10.1021/jacs.5b02802>.
- (20) Trunk, M.; Teichert, J. F.; Thomas, A. Room-Temperature Activation of Hydrogen by Semi-Immobilized Frustrated Lewis Pairs in Microporous Polymer Networks. *J. Am. Chem. Soc.* **2017**, *139* (10), 3615–3618. <https://doi.org/10.1021/jacs.6b13147>.
- (21) Mahdi, T.; Stephan, D. W. Facile Protocol for Catalytic Frustrated Lewis Pair Hydrogenation and Reductive Deoxygenation of Ketones and Aldehydes. *Angew. Chemie Int. Ed.* **2015**, *54* (29), 8511–8514. <https://doi.org/10.1002/anie.201503087>.
- (22) Zhang, S.; Zhang, M.; Qu, Y. Solid Frustrated Lewis Pairs Constructed on CeO<sub>2</sub> for Small-Molecule Activation. *Wuli Huaxue Xuebao/Acta Phys. - Chim. Sin.* **2020**, *36* (9), 1–9. <https://doi.org/10.3866/PKU.WHXB201911050>.
- (23) Ma, Y.; Zhang, S.; Chang, C.-R.; Huang, Z.-Q.; Ho, J. C.; Qu, Y. Semi-Solid and Solid Frustrated Lewis Pair Catalysts. *Chem. Soc. Rev.* **2018**, *47* (15), 5541–5553. <https://doi.org/10.1039/C7CS00691H>.
- (24) Kresge, A. J. The Brønsted Relation - Recent Developments. *Chem. Soc. Rev.* **1973**, *2* (4), 475–503. <https://doi.org/10.1039/CS9730200475>.
- (25) Denmark, S. E.; Beutner, G. L. Lewis Base Catalysis in Organic Synthesis. *Angew. Chemie Int. Ed.* **2008**, *47* (9), 1560–1638. <https://doi.org/10.1002/anie.200604943>.
- (26) Tanabe, K. Solid Acids and Bases. In *Kodansha*; CRC Press, 1970.
- (27) Ono, Y.; Hattori, H. Solid Base Catalysis. *Springer Ser. Chem. Phys.* **2011**, *101*, 1–434. <https://doi.org/10.1007/978-3-642-18339-3/COVER>.
- (28) Banković-Ilić, I. B.; Miladinović, M. R.; Stamenković, O. S.; Veljković, V. B. Application of Nano CaO–Based Catalysts in Biodiesel Synthesis. *Renew. Sustain. Energy Rev.* **2017**, *72*, 746–760. <https://doi.org/10.1016/j.rser.2017.01.076>.
- (29) Okamoto, Y.; Imanaka, T.; Teranishi, S. Hydrogen-Transfer Reaction between Ketones and Alcohols over Metal Oxide Catalysts. *Bull. Chem. Soc. Jpn.* **1972**, *45* (10), 3207–3208. <https://doi.org/10.1246/bcsj.45.3207>.
- (30) Pan, S.-Y.; Chang, E. E.; Chiang, P.-C. CO<sub>2</sub> Capture by Accelerated Carbonation of Alkaline Wastes: A Review on Its Principles and Applications. *Aerosol Air Qual. Res.* **2012**, *12* (5), 770–791. <https://doi.org/10.4209/aaqr.2012.06.0149>.
- (31) Chen, J.; Duan, L.; Sun, Z. Review on the Development of Sorbents for Calcium Looping. *Energy & Fuels* **2020**, *34* (7), 7806–7836. <https://doi.org/10.1021/acs.energyfuels.0c00682>.

- (32) Bhanage, B. M.; Fujita, S.; Ikushima, Y.; Arai, M. Synthesis of Dimethyl Carbonate and Glycols from Carbon Dioxide, Epoxides, and Methanol Using Heterogeneous Basic Metal Oxide Catalysts with High Activity and Selectivity. *Appl. Catal. A Gen.* **2001**, *219* (1–2), 259–266. [https://doi.org/10.1016/S0926-860X\(01\)00698-6](https://doi.org/10.1016/S0926-860X(01)00698-6).
- (33) Xu, B.-Q.; Wei, J.-M.; Wang, H.-Y.; Sun, K.-Q.; Zhu, Q.-M. Nano-MgO: Novel Preparation and Application as Support of Ni Catalyst for CO<sub>2</sub> Reforming of Methane. *Catal. Today* **2001**, *68* (1–3), 217–225. [https://doi.org/10.1016/S0920-5861\(01\)00303-0](https://doi.org/10.1016/S0920-5861(01)00303-0).
- (34) Zhang, G.; Hattori, H.; Tanabe, K. Aldol Addition of Acetone, Catalyzed by Solid Base Catalysts: Magnesium Oxide, Calcium Oxide, Strontium Oxide, Barium Oxide, Lanthanum (III) Oxide and Zirconium Oxide. *Appl. Catal.* **1988**, *36* (C), 189–197. [https://doi.org/10.1016/S0166-9834\(00\)80114-1](https://doi.org/10.1016/S0166-9834(00)80114-1).
- (35) Wolf, F. Chemistry and Biochemistry of Magnesium. *Mol. Aspects Med.* **2003**, *24* (1–3), 3–9. [https://doi.org/10.1016/S0098-2997\(02\)00087-0](https://doi.org/10.1016/S0098-2997(02)00087-0).
- (36) Haque, M. A.; Chen, B. Research Progresses on Magnesium Phosphate Cement: A Review. *Constr. Build. Mater.* **2019**, *211*, 885–898. <https://doi.org/10.1016/j.conbuildmat.2019.03.304>.
- (37) Missoum, I.; Ocak, Y. S.; Benhaliliba, M.; Benouis, C. E.; Chaker, A. Microelectronic Properties of Organic Schottky Diodes Based on MgPc for Solar Cell Applications. *Synth. Met.* **2016**, *214*, 76–81. <https://doi.org/10.1016/j.synthmet.2016.01.004>.
- (38) Shah, R.; Mittal, V.; Matsil, E.; Rosenkranz, A. Magnesium-Ion Batteries for Electric Vehicles: Current Trends and Future Perspectives. *Adv. Mech. Eng.* **2021** (3), 1–9. <https://doi.org/10.1177/16878140211003398>.
- (39) Smithson, G. L.; Bakhshi, N. N. Kinetics and Mechanism of Carbonation of Magnesium Oxide Slurries. *Ind. Eng. Chem. Process Des. Dev.* **1973**, *12* (1), 99–106. <https://doi.org/10.1021/i260045a019>.
- (40) Henrist, C.; Mathieu, J.-P.; Vogels, C.; Rulmont, A.; Cloots, R. Morphological Study of Magnesium Hydroxide Nanoparticles Precipitated in Dilute Aqueous Solution. *J. Cryst. Growth* **2003**, *249* (1–2), 321–330. [https://doi.org/10.1016/S0022-0248\(02\)02068-7](https://doi.org/10.1016/S0022-0248(02)02068-7).
- (41) Mageshwari, K.; Mali, S. S.; Sathyamoorthy, R.; Patil, P. S. Template-Free Synthesis of MgO Nanoparticles for Effective Photocatalytic Applications. *Powder Technol.* **2013**, *249*, 456–462. <https://doi.org/10.1016/j.powtec.2013.09.016>.
- (42) Park, J. Y.; Lee, Y. J.; Jun, K. W.; Baeg, J. O.; Yim, D. J. Chemical Synthesis and Characterization of Highly Oil Dispersed MgO Nanoparticles. *J. Ind. Eng. Chem.* **2006**, *12* (6), 882–887.
- (43) Pilarska, A.; Paukszta, D.; Ciesielczyk, F.; Jesionowski, T. Physico-Chemical and Dispersive Characterisation of Magnesium Oxides Precipitated from the Mg(NO<sub>3</sub>)<sub>2</sub> and MgSO<sub>4</sub> Solutions. *Polish J. Chem. Technol.* **2010**, *12* (2), 52–56. <https://doi.org/10.2478/v10026-010-0018-x>.
- (44) Song, X.; Sun, S.; Zhang, D.; Wang, J.; Yu, J. Synthesis and Characterization of Magnesium Hydroxide by Batch Reaction Crystallization. *Front. Chem. Sci. Eng.* **2011**, *5* (4), 416–421. <https://doi.org/10.1007/s11705-011-1125-9>.
- (45) Bain, S.-W.; Ma, Z.; Cui, Z.-M.; Zhang, L.-S.; Niu, F.; Song, W.-G. Synthesis of Micrometer-Sized Nanostructured Magnesium Oxide and Its High Catalytic Activity in the Claisen–Schmidt Condensation Reaction. *J. Phys. Chem. C* **2008**, *112* (30), 11340–11344. <https://doi.org/10.1021/jp802863j>.

- (46) Camtakan, Z.; Erenturk, S. A.; Yusan, S. D. Magnesium Oxide Nanoparticles: Preparation, Characterization, and Uranium Sorption Properties. *Environ. Prog. Sustain. Energy* **2012**, *31* (4), 536–543. <https://doi.org/10.1002/ep.10575>.
- (47) Ding, Y.; Zhang, G.; Wu, H.; Hai, B.; Wang, L.; Qian, Y. Nanoscale Magnesium Hydroxide and Magnesium Oxide Powders: Control over Size, Shape, and Structure via Hydrothermal Synthesis. *Chem. Mater.* **2001**, *13* (2), 435–440. <https://doi.org/10.1021/cm000607e>.
- (48) Bueno, A. R.; Oman, R. F. M.; Jardim, P. M.; Rey, N. A.; de Avillez, R. R. Kinetics of Nanocrystalline MgO Growth by the Sol–Gel Combustion Method. *Microporous Mesoporous Mater.* **2014**, *185*, 86–91. <https://doi.org/10.1016/j.micromeso.2013.10.021>.
- (49) Mastuli, M. S.; Kamarulzaman, N.; Nawawi, M. A.; Mahat, A. M.; Rusdi, R.; Kamarudin, N. Growth Mechanisms of MgO Nanocrystals via a Sol-Gel Synthesis Using Different Complexing Agents. *Nanoscale Res. Lett.* **2014**, *9* (1), 134. <https://doi.org/10.1186/1556-276X-9-134>.
- (50) Makhluף, S.; Dror, R.; Nitzan, Y.; Abramovich, Y.; Jelinek, R.; Gedanken, A. Microwave-Assisted Synthesis of Nanocrystalline MgO and Its Use as a Bactericide. *Adv. Funct. Mater.* **2005**, *15* (10), 1708–1715. <https://doi.org/10.1002/adfm.200500029>.
- (51) Nagappa, B.; Chandrappa, G. T. Mesoporous Nanocrystalline Magnesium Oxide for Environmental Remediation. *Microporous Mesoporous Mater.* **2007**, *106* (1–3), 212–218. <https://doi.org/10.1016/j.micromeso.2007.02.052>.
- (52) Štengl, V.; Bakardjieva, S.; Maříková, M.; Bezdička, P.; Šubrt, J. Magnesium Oxide Nanoparticles Prepared by Ultrasound Enhanced Hydrolysis of Mg-Alkoxides. *Mater. Lett.* **2003**, *57* (24–25), 3998–4003. [https://doi.org/10.1016/S0167-577X\(03\)00254-4](https://doi.org/10.1016/S0167-577X(03)00254-4).
- (53) Kotera, Y.; Saito, T.; Terada, M. Crystal Growth of Magnesium Oxide Prepared by the Thermal Decomposition of Magnesium Hydroxide. *Bull. Chem. Soc. Jpn.* **1963**, *36* (2), 195–199. <https://doi.org/10.1246/bcsj.36.195>.
- (54) Yu, J. C.; Xu, A.; Zhang, L.; Song, R.; Wu, L. Synthesis and Characterization of Porous Magnesium Hydroxide and Oxide Nanoplates. *J. Phys. Chem. B* **2004**, *108* (1), 64–70. <https://doi.org/10.1021/jp035340w>.
- (55) Pilarska, A. A.; Klapiszewski, Ł.; Jesionowski, T. Recent Development in the Synthesis, Modification and Application of Mg(OH)<sub>2</sub> and MgO: A Review. *Powder Technol.* **2017**, *319*, 373–407. <https://doi.org/10.1016/j.powtec.2017.07.009>.
- (56) GORDON, R. S.; KINGERY, W. D. Thermal Decomposition of Brucite: I, Electron and Optical Microscope Studies. *J. Am. Ceram. Soc.* **1966**, *49* (12), 654–660. <https://doi.org/10.1111/j.1151-2916.1966.tb13194.x>.
- (57) Green, J. Calcination of Precipitated Mg(OH)<sub>2</sub> to Active MgO in the Production of Refractory and Chemical Grade MgO. *J. Mater. Sci.* **1983**, *18* (3), 637–651. <https://doi.org/10.1007/BF00745561>.
- (58) Itatani, K.; Koizumi, K.; Howell, F. S.; Kishioka, A.; Kinoshita, M. Agglomeration of Magnesium Oxide Particles Formed by the Decomposition of Magnesium Hydroxide - Part 2 Agglomeration at Fixed Temperatures. *J. Mater. Sci.* **1989**, *24* (7), 2603–2609. <https://doi.org/10.1007/BF01174532>.
- (59) Li, H.; Li, M.; Guo, W.; Wang, X.; Ge, C.; Yang, B. The Effect of Microstructure and Crystal Defect on Electrochemical Performances of MgO Nanobelts. *Electrochim. Acta* **2014**, *123*, 103–110. <https://doi.org/10.1016/j.electacta.2013.12.191>.

- (60) Pu, L.; Unluer, C. Investigation of Carbonation Depth and Its Influence on the Performance and Microstructure of MgO Cement and PC Mixes. *Constr. Build. Mater.* **2016**, *120*, 349–363. <https://doi.org/10.1016/j.conbuildmat.2016.05.067>.
- (61) Zhu, T.; Li, Y.; Sang, S.; Xie, Z. Formation of Nanocarbon Structures in MgO–C Refractories Matrix: Influence of Al and Si Additives. *Ceram. Int.* **2016**, *42* (16), 18833–18843. <https://doi.org/10.1016/j.ceramint.2016.09.029>.
- (62) Chow, E. H. H.; Strobridge, F. C.; Friščić, T. Mechanochemistry of Magnesium Oxide Revisited: Facile Derivatisation of Pharmaceuticals Using Coordination and Supramolecular Chemistry. *Chem. Commun.* **2010**, *46* (34), 6368. <https://doi.org/10.1039/c0cc01337d>.
- (63) Wang, T.; Xu, Y.; Su, Q.; Yang, R.; Wang, L.; Liu, B.; Shen, S.; Jiang, G.; Chen, W.; Wang, S. Hierarchical Porous Nanosheet-Assembled MgO Microrods with High Adsorption Capacity. *Mater. Lett.* **2014**, *116*, 332–336. <https://doi.org/10.1016/j.matlet.2013.11.053>.
- (64) Bhagiyalakshmi, M.; Lee, J. Y.; Jang, H. T. Synthesis of Mesoporous Magnesium Oxide: Its Application to CO<sub>2</sub> Chemisorption. *Int. J. Greenh. Gas Control* **2010**, *4* (1), 51–56. <https://doi.org/10.1016/j.ijggc.2009.08.001>.
- (65) Guo, Y.; Tan, C.; Sun, J.; Li, W.; Zhang, J.; Zhao, C. Biomass Ash Stabilized MgO Adsorbents for CO<sub>2</sub> Capture Application. *Fuel* **2020**, *259*, 116298. <https://doi.org/10.1016/j.fuel.2019.116298>.
- (66) Duong, T. H. Y.; Nguyen, T. V. T. N.; Oanh, H. T.; Dang Thi, T. A.; Giang, L. N. T.; Phuong, H. T.; Anh, N. T.; Nguyen, B. M.; Quang, V. T.; Le, G. T.; Nguyen, T. V. T. N.; Tran Quang, V.; Le, G. T.; Nguyen, T. V. T. N. Synthesis of Magnesium Oxide Nanoplates and Their Application in Nitrogen Dioxide and Sulfur Dioxide Adsorption. *J. Chem.* **2019**, *2019*, 1–9. <https://doi.org/10.1155/2019/4376429>.
- (67) Zhang, W.; Tay, H. L.; Lim, S. S.; Wang, Y.; Zhong, Z.; Xu, R. Supported Cobalt Oxide on MgO: Highly Efficient Catalysts for Degradation of Organic Dyes in Dilute Solutions. *Appl. Catal. B Environ.* **2010**, *95* (1–2), 93–99. <https://doi.org/10.1016/j.apcatb.2009.12.014>.
- (68) Julkapli, N. M.; Bagheri, S. Magnesium Oxide as a Heterogeneous Catalyst Support. *Rev. Inorg. Chem.* **2016**, *36* (1), 1–41. <https://doi.org/10.1515/revic-2015-0010>.
- (69) Díez, V. K.; Apesteguía, C. R.; Di Cosimo, J. I. Aldol Condensation of Citral with Acetone on MgO and Alkali-Promoted MgO Catalysts. *J. Catal.* **2006**, *240* (2), 235–244. <https://doi.org/10.1016/j.jcat.2006.04.003>.
- (70) Choudary, B. M.; Kantam, M. L.; Ranganath, K. V. S.; Mahendar, K.; Sreedhar, B. Bifunctional Nanocrystalline MgO for Chiral Epoxy Ketones via Claisen–Schmidt Condensation–Asymmetric Epoxidation Reactions. *J. Am. Chem. Soc.* **2004**, *126* (11), 3396–3397. <https://doi.org/10.1021/ja038954n>.
- (71) Drexler, M. T.; Amiridis, M. D. The Effect of Solvents on the Heterogeneous Synthesis of Flavanone over MgO. *J. Catal.* **2003**, *214* (1), 136–145. [https://doi.org/10.1016/S0021-9517\(02\)00013-1](https://doi.org/10.1016/S0021-9517(02)00013-1).
- (72) Tu, M.; Davis, R. J. Cycloaddition of CO<sub>2</sub> to Epoxides over Solid Base Catalysts. *J. Catal.* **2001**, *199* (1), 85–91. <https://doi.org/10.1006/jcat.2000.3145>.
- (73) Dai, W. L.; Luo, S. L.; Yin, S. F.; Au, C. T. The Direct Transformation of Carbon Dioxide to Organic Carbonates over Heterogeneous Catalysts. *Appl. Catal. A Gen.* **2009**, *366* (1), 2–12. <https://doi.org/10.1016/j.apcata.2009.06.045>.

- (74) Hattori, H.; Tanaka, Y.; Tanabe, K. HYDROGENATION OF OLEFINS CATALYZED BY ALKALINE EARTH METAL OXIDES. *Chem. Lett.* **1975**, 4 (7), 659–660. <https://doi.org/10.1246/cl.1975.659>.
- (75) Choudary, B. M.; Mulukutla, R. S.; Klabunde, K. J. Benzylation of Aromatic Compounds with Different Crystallites of MgO. *J. Am. Chem. Soc.* **2003**, 125 (8), 2020–2021. <https://doi.org/10.1021/ja0211757>.
- (76) Choudary, B. M.; Ranganath, K. V. S.; Pal, U.; Kantam, M. L.; Sreedhar, B. Nanocrystalline MgO for Asymmetric Henry and Michael Reactions. *J. Am. Chem. Soc.* **2005**, 127 (38), 13167–13171. <https://doi.org/10.1021/ja0440248>.
- (77) Jensen, M. B.; Pettersson, L. G. M.; Swang, O.; Olsbye, U. CO<sub>2</sub> Sorption on MgO and CaO Surfaces: A Comparative Quantum Chemical Cluster Study. *J. Phys. Chem. B* **2005**, 109 (35), 16774–16781. <https://doi.org/10.1021/jp052037h>.
- (78) Patel, G.; Pal, U.; Menon, S. Removal of Fluoride from Aqueous Solution by CaO Nanoparticles. *Sep. Sci. Technol.* **2009**, 44 (12), 2806–2826. <https://doi.org/10.1080/01496390903014425>.
- (79) Ngamcharussrivichai, C.; Meechan, W.; Ketcong, A.; Kangwansaichon, K.; Butnark, S. Preparation of Heterogeneous Catalysts from Limestone for Transesterification of Vegetable Oils—Effects of Binder Addition. *J. Ind. Eng. Chem.* **2011**, 17 (3), 587–595. <https://doi.org/10.1016/j.jiec.2011.05.001>.
- (80) Habte, L.; Shiferaw, N.; Mulatu, D.; Thenepalli, T.; Chilakala, R.; Ahn, J. Synthesis of Nano-Calcium Oxide from Waste Eggshell by Sol-Gel Method. *Sustainability* **2019**, 11 (11), 3196. <https://doi.org/10.3390/su11113196>.
- (81) Smith, S. M.; Oopathum, C.; Weeramongkhonlert, V.; Smith, C. B.; Chaveanghong, S.; Ketwong, P.; Boonyuen, S. Transesterification of Soybean Oil Using Bovine Bone Waste as New Catalyst. *Bioresour. Technol.* **2013**, 143, 686–690. <https://doi.org/10.1016/j.biortech.2013.06.087>.
- (82) Zul, N. A.; Ganesan, S.; Hamidon, T. S.; Oh, W.-D.; Hussin, M. H. A Review on the Utilization of Calcium Oxide as a Base Catalyst in Biodiesel Production. *J. Environ. Chem. Eng.* **2021**, 9 (4), 105741. <https://doi.org/10.1016/j.jece.2021.105741>.
- (83) Karami, D.; Mahinpey, N. Highly Active CaO-Based Sorbents for CO<sub>2</sub> Capture Using the Precipitation Method: Preparation and Characterization of the Sorbent Powder. *Ind. Eng. Chem. Res.* **2012**, 51 (12), 4567–4572. <https://doi.org/10.1021/ie2024257>.
- (84) Zhu, Y.; Wu, S.; Wang, X. Nano CaO Grain Characteristics and Growth Model under Calcination. *Chem. Eng. J.* **2011**, 175 (1), 512–518. <https://doi.org/10.1016/j.cej.2011.09.084>.
- (85) Pan, S.-Y.; Chang, E. E.; Chiang, P.-C. CO<sub>2</sub> Capture by Accelerated Carbonation of Alkaline Wastes: A Review on Its Principles and Applications. *Aerosol Air Qual. Res.* **2012**, 12 (5), 770–791. <https://doi.org/10.4209/aaqr.2012.06.0149>.
- (86) Erker, G. Tris(pentafluorophenyl)borane: A Special Boron Lewis Acid for Special Reactions. *Dalt. Trans.* **2005**, No. 11, 1883. <https://doi.org/10.1039/b503688g>.
- (87) Sivaev, I. B.; Bregadze, V. I. Lewis Acidity of Boron Compounds. *Coord. Chem. Rev.* **2014**, 270–271 (1), 75–88. <https://doi.org/10.1016/j.ccr.2013.10.017>.
- (88) Bontemps, S. Boron-Mediated Activation of Carbon Dioxide. *Coord. Chem. Rev.* **2016**, 308, 117–130. <https://doi.org/10.1016/j.ccr.2015.06.003>.



**Chapter III**  
**Synthesis of basic alkaline-earth oxides  
nanoparticles and activity in the  
Claisen-Schmidt condensation**





# Table of contents

<b>I. Experimental section .....</b>	<b>67</b>
<b>II. Synthesis of simple and mixed oxide nanoparticles by precipitation-calcination .....</b>	<b>69</b>
<b>1. Synthesis of MgO .....</b>	<b>69</b>
<b>a. Precipitation-calcination synthesis .....</b>	<b>69</b>
<b>b. Modification of the calcination temperature .....</b>	<b>71</b>
<b>c. Modification of the washing step .....</b>	<b>72</b>
<b>2. Synthesis of CaO .....</b>	<b>74</b>
<b>3. Attempts to synthesise MgO-CaO mixed oxides.....</b>	<b>76</b>
<b>4. Attempts to synthesize MgO-M (M = Co, Ni, Cu) .....</b>	<b>80</b>
<b>III. Surface state of MgO nanoparticles.....</b>	<b>86</b>
<b>1. Ageing of MgO nanoparticles under ambient air .....</b>	<b>86</b>
<b>2. IR spectrum of MgO nanoparticles .....</b>	<b>86</b>
<b>3. Repeatability of the MgO synthesis .....</b>	<b>88</b>
<b>IV. MgO nanoparticles as catalyst in the Claisen-Schmidt condensation .....</b>	<b>89</b>
<b>1. The Claisen-Schmidt condensation .....</b>	<b>89</b>
<b>2. Activity of the synthesized MgO nanoparticles .....</b>	<b>90</b>
<b>a. First catalytic test.....</b>	<b>91</b>
<b>b. Comparison to Bain study .....</b>	<b>93</b>
<b>3. Activity of the pair MgO+BPh<sub>3</sub>.....</b>	<b>94</b>
<b>4. Conclusion .....</b>	<b>95</b>
<b>V. Conclusion.....</b>	<b>96</b>
<b>VI. Annexes.....</b>	<b>97</b>

In this chapter we summarized the work we did on the synthesis of alkaline-earth oxide nanoparticles. We focused on a NanoFLP with nanoparticles playing the role of the Lewis base and ligands playing the role of the Lewis acid. We made it clear in Chapter 2 that alkaline-earth oxides were good candidates due to their Lewis base and good CO<sub>2</sub> adsorption properties. We decided to start with MgO synthesis. Among the variety of synthetic paths available to obtain alkaline-earth oxide nanoparticles we chose the precipitation-calcination. It was easy to implement in our lab, scalable to obtain grams of material in one synthesis and it was possible to modify the synthesis to obtain mixed oxides by co-precipitation of inorganic salts. This last point was relevant especially when we considered that the presence of different reactive sites at the surface of our nanoparticles could allow new reaction pathways in catalysis. The nanoparticles were mainly characterized by XRD, TEM and IR spectroscopy, with N<sub>2</sub> adsorption measurements on some samples.

The last part of this chapter concerned the first activity test of the synthesized nanoparticles in catalysis. We wanted to be sure that they have a comparable activity with these in the literature. For sake of simplicity we decided to focus here on the activity of pure MgO nanoparticles, and in general it will be the case in the rest of the project. Among the different reactions reported to be catalysed by alkaline-earth oxide nanoparticles we chose the Claisen-Schmidt condensation, mainly because it involved the activation of C=O double bonds. At last we tried our first acid-base pair in the same reaction using triphenylborane alongside the MgO nanoparticles.

## I. Experimental section

*Note: all the details concerning the suppliers and the purity of chemical products were given in the Appendix section.*

### Synthesis of MgO nanoparticles

Magnesium oxide nanoparticles were obtained by a three step process inspired from the work of Park and coworkers<sup>1</sup>. First  $\text{Mg}(\text{NO}_3)_2 \cdot 6\text{H}_2\text{O}$  (10 mmol, 2.56 g) was dissolved in 100 mL of deionized water in a 250 mL borosilicate bottle. NaOH (20 mmol, 1.6 g) was also dissolved in 100mL of deionized water in another 250 mL borosilicate bottle. The solution of NaOH was then slowly added to the solution of  $\text{Mg}(\text{NO}_3)_2$ , while stirring at 600 rpm, in approximately 1 minute. After 2 hours of stirring, the solution was a white suspension. It was centrifuged at 9000 rpm for 10 minutes. The supernatant was eliminated and the solid was redispersed in four centrifugation tubes for a total volume of 80 mL of ethanol and the solution was centrifuged again at 9000 rpm for 10 minutes. The supernatant was eliminated, the white solid was put on an alumina crucible and dried at 110 °C for 12 hours in a muffle furnace. The dry solid was then finely grinded with a mortar and pestle before the final calcination in a muffle furnace under ambient air. We used the following heating program: heating from 20 °C to 500 °C in one hour, plateau at 500 °C for 3 hours and cooling at room temperature in 2 hours. The powder was stored in an inert glove box.

### Synthesis of CaO nanoparticles

Calcium oxide nanoparticles were obtained following the same three step process used to synthesize MgO nanoparticles. First  $\text{Ca}(\text{NO}_3)_2 \cdot 4\text{H}_2\text{O}$  (10 mmol, 2.56 g) was dissolved in 100 mL of deionized water in a 250 mL borosilicate bottle. NaOH (20 mmol, 1.6 g) was also dissolved in 100mL of deionized water in another 250 mL borosilicate bottle. The solution of NaOH was then slowly added to the solution of  $\text{Ca}(\text{NO}_3)_2$ , while stirring at 600 rpm, in approximately 1 minute. After 2 hours of stirring, the solution was a white suspension. It was centrifuged at 9000 rpm for 10 minutes. The supernatant was eliminated and the solid was redispersed in four centrifugation tubes for a total volume of 80 mL of ethanol and the solution was centrifuged again at 9000 rpm for 10 minutes. The supernatant was eliminated, the white solid was put on an alumina crucible and dried at 110 °C for 12 hours in a muffle furnace. The dry solid was then finely grinded with a mortar and pestle before the final calcination in a muffle furnace under ambient air. We used the following heat program: heating from 20 °C to 500 °C in one hour, plateau at 650 °C for 3 hours and cooling at room temperature in 2 hours. The powder was stored in an inert glove box. We chose different calcination temperature in certain syntheses.

### Synthesis of $\text{Mg}_{95}\text{X}_{05}\text{O}$ (X = Ca, Co, Ni, Cu) mixed oxide nanoparticles

MgO-based mixed oxide nanoparticles were obtained by the same three step process. First  $\text{Mg}(\text{NO}_3)_2 \cdot 6\text{H}_2\text{O}$  (9.5 mmol, 2.43 g) and  $\text{X}(\text{NO}_3)_2 \cdot n\text{H}_2\text{O}$  (X was another element amongst: Ca (n=4), Co (n=6), Ni (n=6), Cu (n=3)) (0.5 mmol, mass depending on the salt) were dissolved in 100 mL of

deionized water in a 250 mL borosilicate bottle. NaOH (20 mmol, 1.6 g) was also dissolved in 100 mL of deionized water in another 250 mL borosilicate bottle. The solution of NaOH was then slowly added to the solution of  $\text{Mg}(\text{NO}_3)_2$ , while stirring at 600 rpm, in approximately 1 minute. After 2 hours of stirring, the solution was a colored suspension: white for X=Ca, blue for X=Cu and green for X=Ni and Co. It was centrifuged at 9000 rpm for 10 minutes. The supernatant was eliminated and the solid was redispersed in four centrifugation tubes for a total volume of 80 mL of ethanol and the solution was centrifuged again at 9000 rpm for 10 minutes. The supernatant was eliminated, the solid was put on an alumina crucible and dried at 110 °C for 12 hours in a muffle furnace. The dry solid was then finely grinded with a mortar and pestle before the final calcination in a muffle furnace under ambient air. We used the following heat program: heating from 20 °C to 500 °C in one hour, plateau at 500 °C for 3 hours and cooling at room temperature in 2 hours. The powder was stored in an inert glove box.

### **Catalysis of the Claisen-Schmidt condensation of acetophenone on benzaldehyde with MgO**

The reaction was performed under  $\text{N}_2$  atmosphere in a 25 mL three-necked round flask with a refrigerant connected to a Schlenk ramp. All the glassware was dried for one night in a 120 °C oven before usage. Dry toluene (10 mL) was first introduced, then acetophenone (3 mmol, 0.35 mL, 1.2 eq.) and benzaldehyde (2.5 mmol, 0.26 mL, 1 eq.) were added, finally the MgO catalyst (2.5 mmol, 0.1 g, 1 eq.) and eventually triphenylborane (0.3 mmol, 38 mg, 0.12 eq.) were introduced in the flask. The MgO catalyst corresponded to the nanoparticles obtained by precipitation-calcination with no supplementary washing steps and calcined at 500 °C. The solution was then heated at 110 °C with a heating mantle for 8 hours. Magnetic stirring at 500 rpm ensured the homogeneity of the solution. At the end of the reaction the solution was centrifuged at 7000 rpm for 15 min, the supernatant and the nanoparticles were separated for further analyses. NMR tubes were prepared by diluting one droplet of reaction crude in 0.5 mL of  $\text{CDCl}_3$ .

### **Catalysis of the Claisen-Schmidt condensation of acetophenone on benzaldehyde with MgO+BPh<sub>3</sub>**

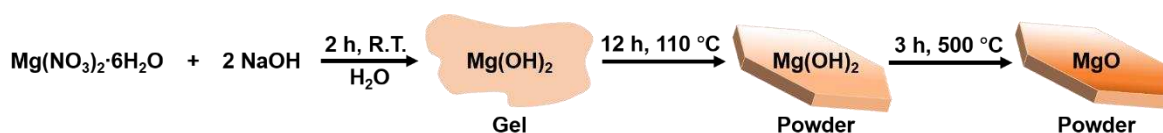
The reaction was the same as the previous one with some modification of the amount of catalyst. The MgO catalyst (1 mmol, 40 mg, 0.33 eq.) and triphenylborane (0.3 mmol, 38 mg, 0.12 eq.) were introduced in the flask after the reactants.

## II. Synthesis of simple and mixed oxide nanoparticles by precipitation-calcination

### 1. Synthesis of MgO

#### a. Precipitation-calcination synthesis

As a starting point for the synthesis of MgO nanoparticles, we decided to reproduce the experiments described by Park et al<sup>1</sup>. The authors found that it was possible to form MgO nanoparticles by precipitating magnesium nitrate in basic aqueous solution and calcining it at 500 °C afterward. This straight forward route led to the formation of nanoparticles identified as pure MgO by XRD. The Scherrer formula gave an average crystallite size of 20 nm. Their SEM images showed the formation of spherical objects with a size in the range of 30 to 500 nm corresponding to the agglomeration of primary MgO nanoparticles. The nitrogen adsorption using the BET method showed a specific surface of 91.4 m<sup>2</sup>/g. Their IR spectrum showed the presence of both carbonates and hydroxides at the surface of the particles. The synthesis was summarized in Scheme 1:



*Scheme 1: Synthesis of MgO nanoparticles by precipitation-calcination.*

When we reproduced the experiment, we observed the solution containing Mg(NO<sub>3</sub>)<sub>2</sub> turning white as soon as we added the basic solution. The Mg(OH)<sub>2</sub> nanoparticles formed immediately. After the centrifugation, a white gel sedimented at the bottom of the centrifugation tubes while the supernatant was transparent, indicating that no particles were left in suspension (this assertion was confirmed by TEM micrographs of the supernatant). Once the gel was dried at 110 °C, we obtained bulky white solids that were easily grinded into a fine powder. TEM micrographs and XRD pattern of this intermediate powder indicated that it was composed of hexagonal nano-platelets of Mg(OH)<sub>2</sub> with a thickness of 5 nm and a radius between 10 and 40 nm (Figure 1:). This anisotropy could also be retrieved in the XRD pattern thanks to the Scherrer formula: peaks with high width to mid-height indicated smaller characteristic length in the corresponding crystallographic direction (Table 1:).

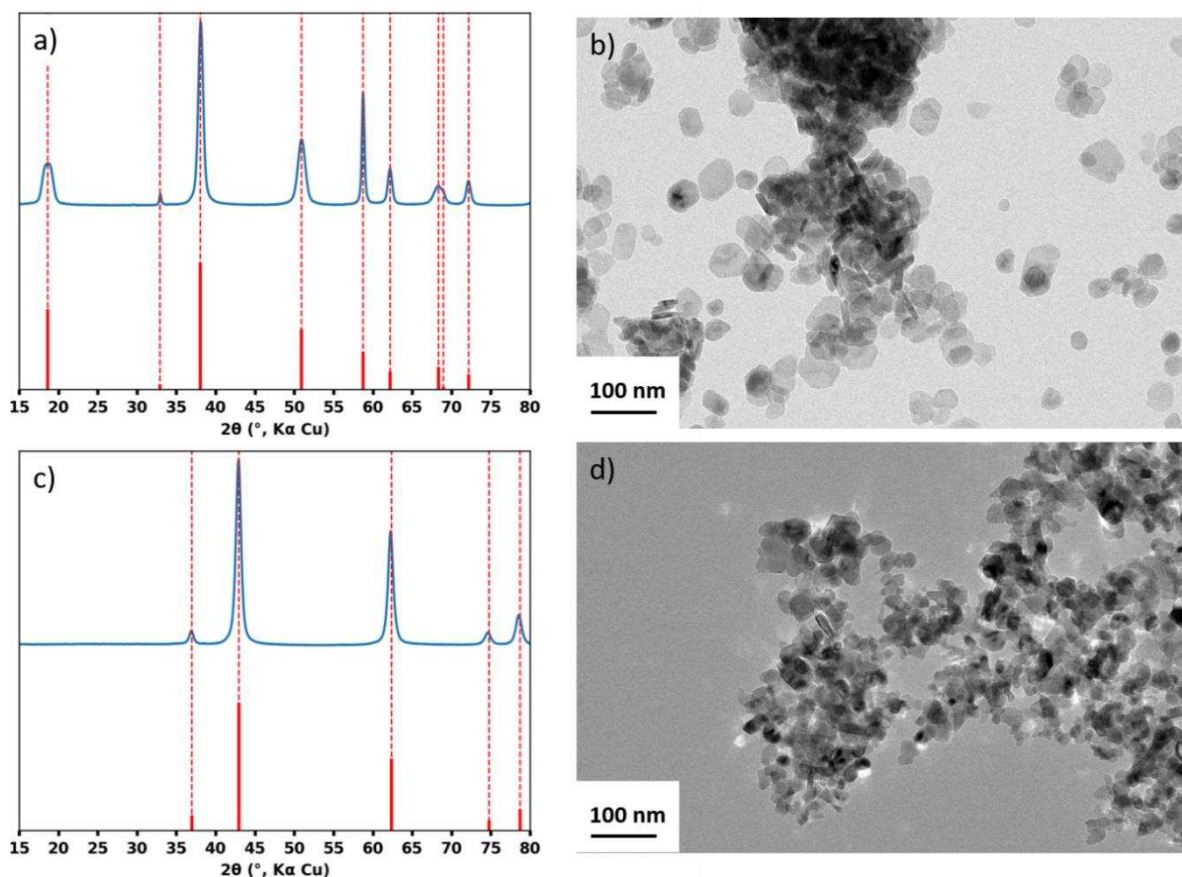
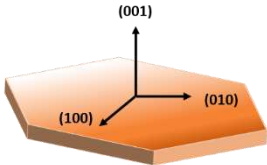


Figure 1: a) XRD pattern of  $Mg(OH)_2$  nanoparticles (reference is given by the red bars, PDF Card n°01-071-5972), b) corresponding TEM micrograph. c) XRD pattern of  $MgO$  nanoparticles (reference is given by the red bars, PDF Card n°00-004-0829), d) corresponding TEM micrograph.

The  $Mg(OH)_2$  nanoparticles were then further calcined at 500 °C. No visual modification of the white powder was observed at a macroscopic level. However, the XRD pattern showed clearly that  $Mg(OH)_2$  completely transformed into  $MgO$ . The TEM micrographs showed that the powder was composed of aggregates of primary nanoparticles of around 15 nm radius with no well-defined shape. The Scherrer formula gave average crystallite sizes of 11 to 13 nm for all the peaks. The nitrogen adsorption using the BET method gave a surface area of 93 m<sup>2</sup>/g (details on the nitrogen adsorption experiment were given in the experimental section). All these results were coherent with what obtained Parks. The difference in aggregate sizes could be attributed to difference in the grinding method (grinding was not mentioned in the original protocol and we added that step).

a)



b)

Mg(OH) <sub>2</sub> XRD peak	Scherrer crystallite size	MgO XRD peak	Scherrer crystallite size
001	6 nm	111	13 nm
010	27 nm	200	11 nm
011	12 nm	220	12 nm
102	8 nm	311	11 nm
110	29 nm	222	12 nm
111	16 nm		
103	7 nm		
201	16 nm		

Table 1: a) Schematic view of a typical Mg(OH)<sub>2</sub> nanoparticle with the main crystallographic directions, b) Average crystallite sizes calculated from the width of the XRD peaks of Mg(OH)<sub>2</sub> and MgO with the Scherrer formula.

Since we had in hand a protocol that yields MgO nanoparticles, we thought it would be interesting to see what parameters we could play with in order to have some control on their properties like their size, the exposed crystallographic facets or the surface state. We focused on the calcination temperature and the post-synthesis washing steps of the Mg(OH)<sub>2</sub> nanoparticles.

## b. Modification of the calcination temperature

Calcination temperature was a key parameter that had a strong impact on the final properties of the nanoparticles<sup>2</sup>. It was shown that the calcination process starts at 350 °C but the crystallization of the MgO phase starts only at 400 °C<sup>3,4</sup>, and the higher the temperature the more crystalline the final particles will be. At relatively low temperature (500 °C) the MgO nanoparticles will keep some of the morphological properties of the initial Mg(OH)<sub>2</sub>, whereas at higher temperature (1000 °C) the atom will have more energy to rearrange themselves<sup>5</sup>. It was also important to note that at higher temperature there will be less residual hydroxides and carbonates at the surface of the particles. This will impact the surface state of the nanoparticles.

In order to have the two extreme types of material we did the synthesis with a calcination temperature of 1000 °C. In the following, MgO calcined at 500 °C will be referred as 'MgO<sub>500</sub>' or 'MgO' and MgO calcined at 1000 °C will be referred as 'MgO<sub>1000</sub>'. The TEM images clearly showed a different morphology with cubic nanoparticles with characteristic sizes between 50 and 200 nm for MgO<sub>1000</sub> (Figure 2:c). When we compared these to the particles calcinated at 500 °C (Figure 2:d), we could see on one hand some retention of the hexagonal pellet structure and in the other hand the rearrangement into cubic nanoparticles. The XRD (Figure 2:a) still showed a pure MgO phase. However, the average Scherrer crystallite size was around 40 nm, much higher than for MgO<sub>500</sub> but still smaller than the size of the particles observed in TEM. All these results were coherent the study of Itatani et al.<sup>2</sup>. Having both the more crystalline MgO<sub>1000</sub> and the low calcination temperature MgO<sub>500</sub> will be interesting for further catalytic studies.



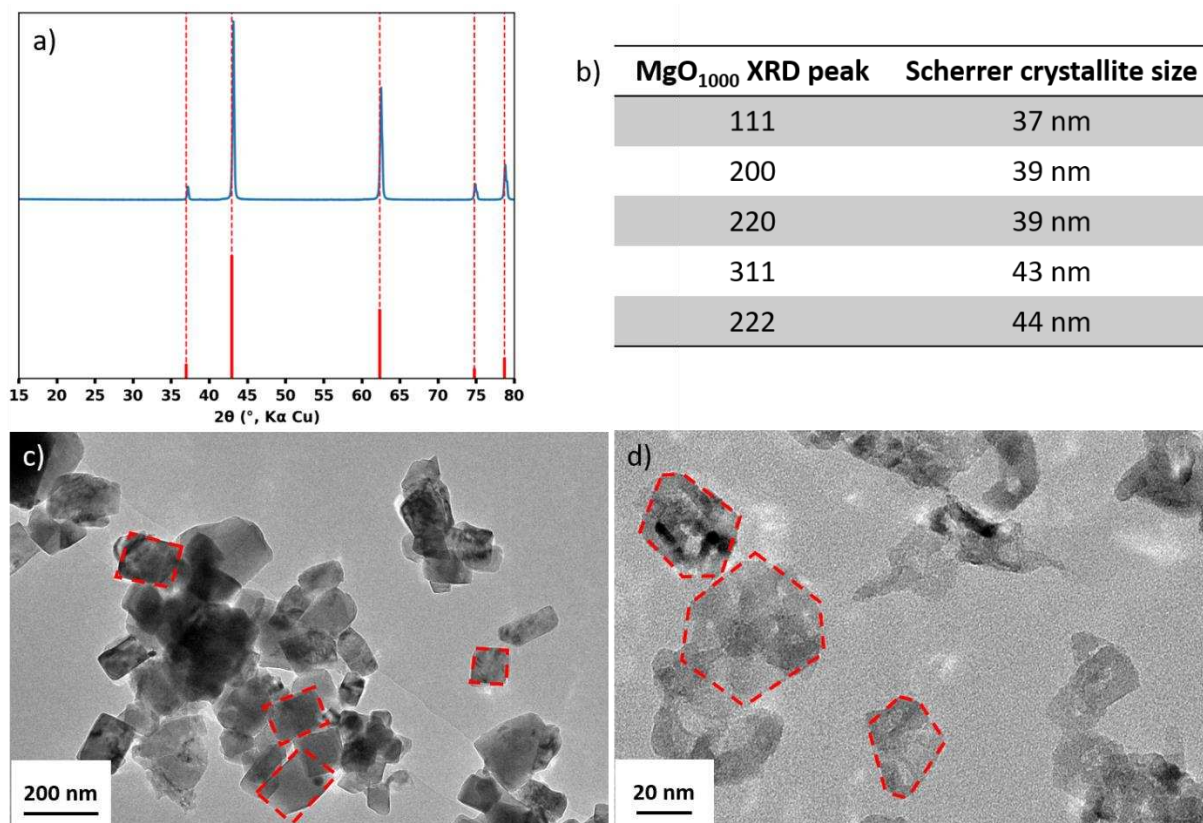


Figure 2: a) XRD pattern of MgO calcined at 1000 °C, b) corresponding Scherrer average crystallite sizes, c) TEM micrograph of MgO calcined at 1000 °C (red dashes are a guide to see the cubic morphology), d) TEM micrograph of MgO calcined at 500 °C (red dashes are a guide to see the retention of the hexagonal pelet morphology).

### c. Modification of the washing step

Another key parameter in the synthesis was the washing step after the precipitation of Mg(OH)<sub>2</sub> before the drying at 110 °C<sup>1</sup>. Depending on the solvent, ions from the reactants like Na<sup>+</sup>, K<sup>+</sup>, or Cl<sup>-</sup> could stay adsorbed on the surface of the Mg(OH)<sub>2</sub> nanoparticles, thus influencing the calcination<sup>6</sup>. For example, presence of Na<sup>+</sup> was shown to favour sintering.

Since we used NaOH as the Brønsted base and Mg(NO<sub>3</sub>)<sub>2</sub> as the magnesium precursor in the synthesis, we could expect to have remaining Na<sup>+</sup> and NO<sub>3</sub><sup>-</sup> ions adsorbed on the surface of Mg(OH)<sub>2</sub> particles. Actually, it happened in certain synthesis that traces of NaNO<sub>3</sub> were detected by XRD (Figure 3:a). To see if removing these species would have an impact on the final MgO nanoparticles, we decided to wash the Mg(OH)<sub>2</sub> gel five times with water instead of one time with ethanol. The calcination was still at 500 °C for 3 hours. The corresponding sample was referred as 'MgO<sub>washed</sub>'.

We did not see in XRD nor in TEM any impact on the intermediate Mg(OH)<sub>2</sub> nanoparticles after the drying step, however we saw differences on the final MgO nanoparticles. TEM micrographs (Figure 3:d) showed that the nanoparticles were less sintered than in the original

synthesis (Figure 3:c), and we could see even more clearly the hexagonal pellet shape inherited from the  $\text{Mg}(\text{OH})_2$  NPs. XRD measurement (Figure 3:a), showed a pure MgO phase, but the Scherrer crystallite sizes (Figure 3:b) were around 8 to 10 nm instead of the 11 to 13 nm, which was a significant difference.

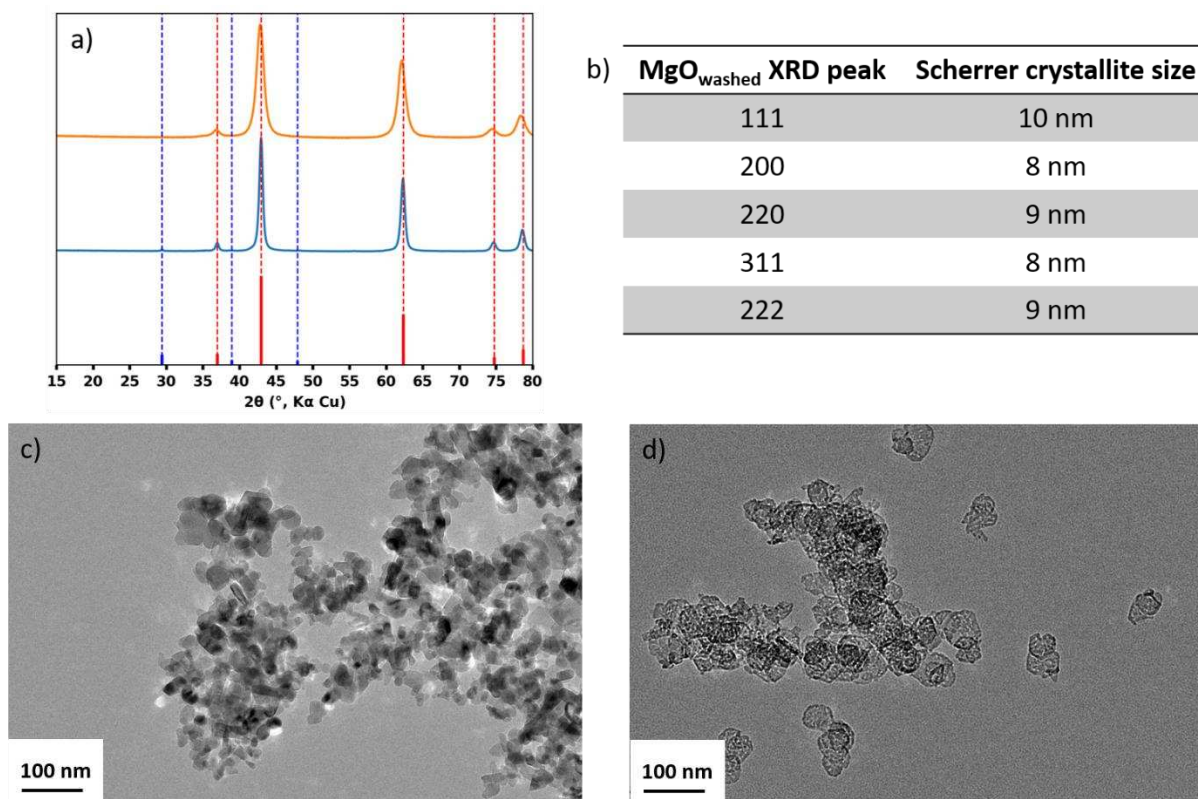


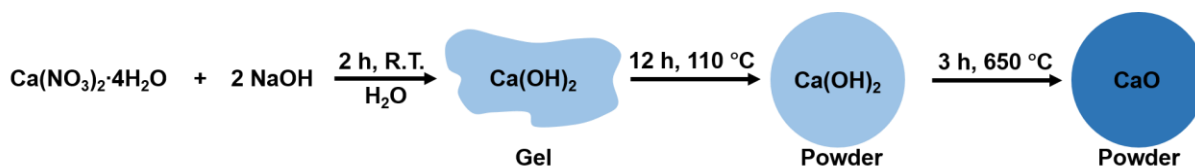
Figure 3: a) XRD pattern of (bottom) MgO containing traces of  $\text{NaNO}_3$  and (top)  $\text{MgO}_{\text{washed}}$  (MgO reference is given by the red bars and  $\text{NaNO}_3$  reference is given by the blue bars, PDF Card n°00-036-1474), b)  $\text{MgO}_{\text{washed}}$  Scherrer average crystallite sizes, c) TEM micrograph of MgO, d) TEM micrograph of  $\text{MgO}_{\text{washed}}$ .

The two parameters that we varied were not the only ones that would impact on the final properties of the nanoparticles. We could also mention the chemical nature of the magnesium source, the chemical nature of the base, the temperature during the precipitation, the concentration of the initial solutions or the presence of a templating agent<sup>6,7,8</sup>. Our three samples MgO,  $\text{MgO}_{1000}$  and  $\text{MgO}_{\text{washed}}$  would help us understand the impact of the surface state on the nanoparticle ligand interaction.

Now that we successfully managed to synthesize MgO nanoparticles using the precipitation calcination method, we wanted to synthesize other alkaline-earth oxide nanoparticles. They were known to have different basicity (Lewis basicity scale:  $\text{MgO} < \text{CaO} < \text{SrO} < \text{BaO}$ ) that would be interesting for testing the impact of the basicity in the nanoparticle-ligand interaction. We decided to synthesize CaO nanoparticles next using the same precipitation-calcination process.

## 2. Synthesis of CaO

We synthesized CaO nanoparticles with a similar protocol than MgO nanoparticles. We just switched the  $\text{Mg}(\text{NO}_3)_2 \cdot 6\text{H}_2\text{O}$  reactant by  $\text{Ca}(\text{NO}_3)_2 \cdot 4\text{H}_2\text{O}$  while keeping the stoichiometry. We increased the calcination temperature to  $650\text{ }^\circ\text{C}$  since  $\text{Ca}(\text{OH})_2$  require higher temperatures to form the corresponding oxide<sup>10</sup> (Scheme 2:).



*Scheme 2: Synthesis of CaO nanoparticles by precipitation-calcination.*

The experiment went almost identically as the synthesis of MgO, except for one detail: when adding the basic solution to the alkaline-earth solution, it took approximately 10 seconds to become white (whereas it was immediate in the case of Mg). This could indicate that either the early stages in the formation of hydroxide particles or the kinetics of growth were not the same.

XRD analysis of the powder after the drying step (12h,  $110\text{ }^\circ\text{C}$ ) showed the main crystallized phase to be  $\text{Ca}(\text{OH})_2$ , but traces of  $\text{CaCO}_3$  were also detected. We hoped that the carbonate phase would disappear during the calcination, however XRD analysis of the final particles still showed the presence of  $\text{CaCO}_3$ . Interestingly, this carbonate phase was really hard to remove and required calcination temperatures higher than  $1000\text{ }^\circ\text{C}$ . This was also observed by Mirghiasi and coworkers<sup>10</sup>, they attributed this residual carbonate phase to a rapid carbonation of the material by atmospheric  $\text{CO}_2$ .

The TEM images (Figure 4:b) of the intermediate powder showed the presence of two kinds of objects: thin sheets of approximately 30-100 nm diameter, and rods of several hundreds of nanometers length and roughly 50 nm diameter. We could not measure the thickness of the sheets since all these that we managed to observe were parallel to the observation plan and so thin that tomography did not help either. We did not perform High Resolution TEM to identify the phases of each kind of objects, however since hydroxides were known to form lamellar structures (just like the  $\text{Mg}(\text{OH})_2$  platelets) we believed that the thin sheets were composed of  $\text{Ca}(\text{OH})_2$  whereas the rods were composed of  $\text{CaCO}_3$ . Further analysis would be required to confirm this assumption. The TEM images of the final powder (Figure 4:d) showed primary nanoparticles of approximately 10 to 30 nm fused together in aggregates. Higher temperature, required to calcine  $\text{Ca}(\text{OH})_2$ , also favoured the sintering of CaO particles. The Scherrer average crystallite sizes did not show sign of any anisotropy and gave values between 40 and 50 nm for both  $\text{Ca}(\text{OH})_2$  and CaO.

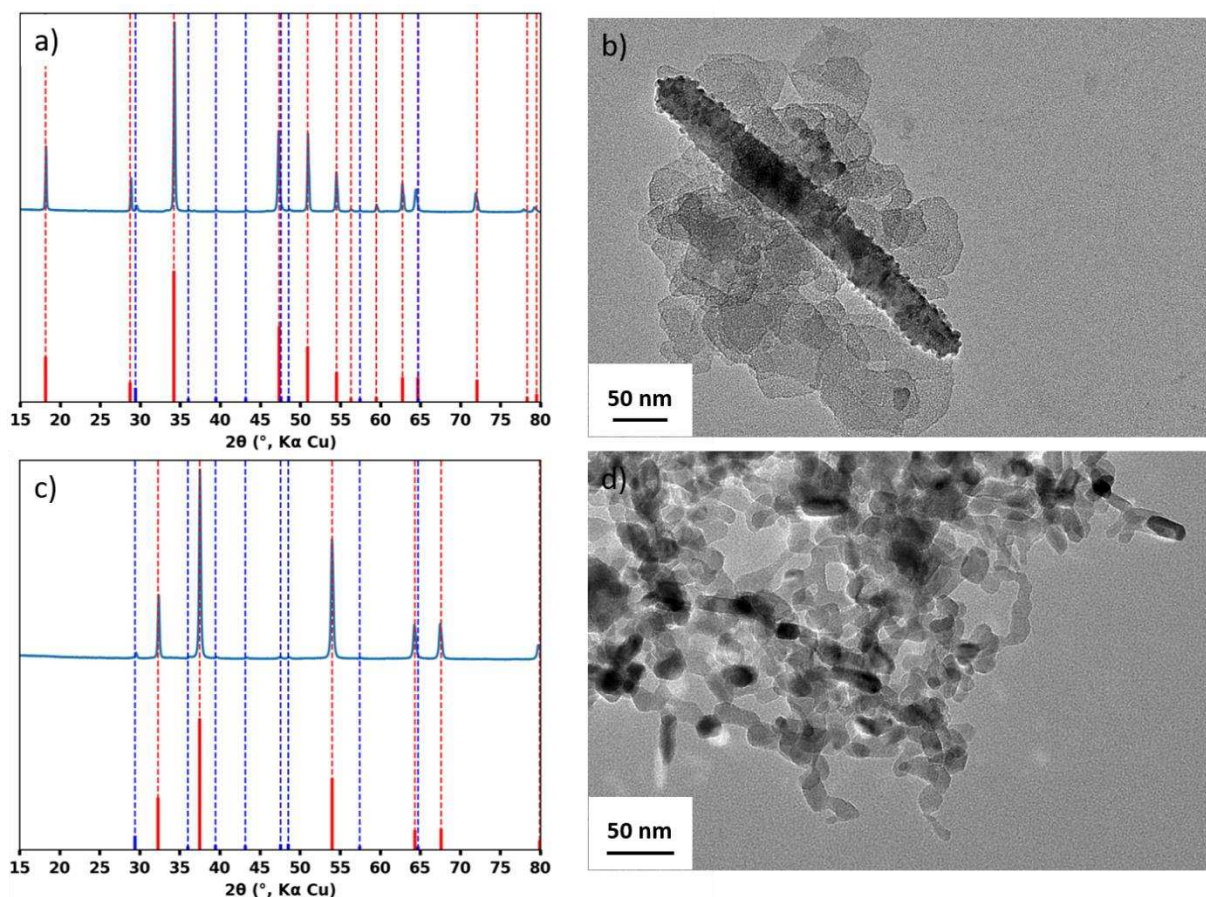
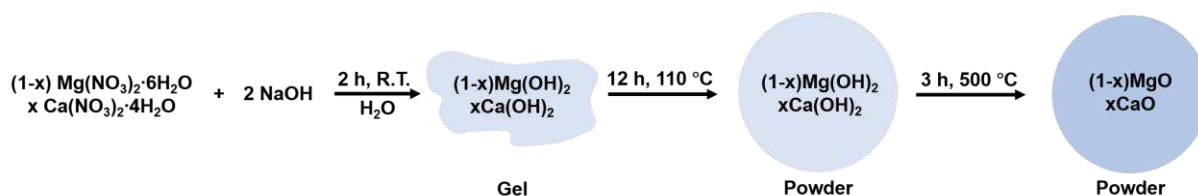


Figure 4: a) XRD pattern of  $\text{Ca(OH)}_2$  nanoparticles (references are given by the red bars for  $\text{Ca(OH)}_2$ , PDF Card n°00-044-1481, and blue bars for  $\text{CaCO}_3$ , PDF Card n°00-005-0586), b) corresponding TEM micrograph. c) XRD pattern of  $\text{CaO}$  nanoparticles (reference is given by the red bars for  $\text{CaO}$ , PDF Card n°00-037-1497, and blue bars for  $\text{CaCO}_3$ ), d) corresponding TEM micrograph.

We successfully managed to synthesize  $\text{CaO}$  nanoparticles, and from this point we had to choose a plan of action. The first idea was to try to synthesize the next alkaline-earth oxides in our list,  $\text{SrO}$  and  $\text{BaO}$ , in order to compare their activity in the formation of a NanoFLP. A problem that we may encounter in this case would be the comparison between our different pairs since not only the chemical nature of the particle will be different but also the morphologies, surface area and surface state. The second idea was to take  $\text{MgO}$  as our reference material and apply small modifications to see the impact in catalysis and in the interaction with the borane. For example, if we wanted to see the impact of the strength of the basic sites we could compare  $\text{MgO}$  and  $\text{MgO-CaO}$  mixed oxides instead of comparing  $\text{MgO}$  and  $\text{CaO}$ , since it was known that  $\text{MgO-CaO}$  mixed oxides were more basic than  $\text{MgO}$ <sup>11</sup>. We hoped that small addition of  $\text{Ca}$  atoms would not impact to greatly the morphology of the reference  $\text{MgO}$  nanoparticles so comparison would be possible. This idea was selected.

### 3. Attempts to synthesize MgO-CaO mixed oxides

Just like for the synthesis of pure CaO nanoparticles, we decided to synthesize MgO-CaO mixed oxides using close parameters to those of the synthesis of MgO nanoparticles. We just switched  $x$  equivalent of  $\text{Mg}(\text{NO}_3)_2 \cdot 6\text{H}_2\text{O}$  by  $x$  equivalent of  $\text{Ca}(\text{NO}_3)_2 \cdot 4\text{H}_2\text{O}$  (Scheme 3:). We decided to keep a calcination at  $500\text{ }^\circ\text{C}$  since it was reported that MgO-CaO mixed oxides could be formed at such temperature<sup>11</sup>. In our analyses, we did not study the hydroxide intermediate and only were interested in the nanoparticles after the calcination.



*Scheme 3: Expected synthesis of MgO-CaO mixed oxide nanoparticles by precipitation-calcination.*

At the end of the precipitation phase, we obtained a white gel that was dried and grinded into a fine hydroxide powder, then further calcined into an oxide powder. We decided to vary the amount of Ca incorporated from 0 to 50 % and see how the final diffractogram would be impacted (Figure 5:).

We observed different regimes depending of the value of  $x$ :

- at low Ca/Mg ratio ( $x < 0.1$ ) we observed a main MgO phase with traces of  $\text{CaCO}_3$ . This phase was probably the same mentioned earlier, corresponding to a fast carbonation of calcium exposed to ambient air. It was not clear at the time if all the calcium atoms were forming this carbonate phase or if some of them were incorporated in the MgO phase.
- at intermediate Ca/Mg ratio ( $0.1 < x < 0.2$ ) we still had a main phase of MgO but the intensity of the  $\text{CaCO}_3$  peaks increased.
- at high Ca/Mg ratio ( $x > 0.3$ ) we saw that MgO was not the main phase anymore, a drastic increase of the carbonate peaks was observed, along with the appearance of a CaO phase and even a  $\text{Ca}(\text{OH})_2$  phase for  $x > 0.4$ . This meant that when the concentration was too high, pure  $\text{Ca}(\text{OH})_2$  domains were able to form. Since the calcination of  $\text{Ca}(\text{OH})_2$  nanoparticles was not complete at  $500\text{ }^\circ\text{C}$ , it led to a mix of  $\text{Ca}(\text{OH})_2$ ,  $\text{CaCO}_3$  and CaO.

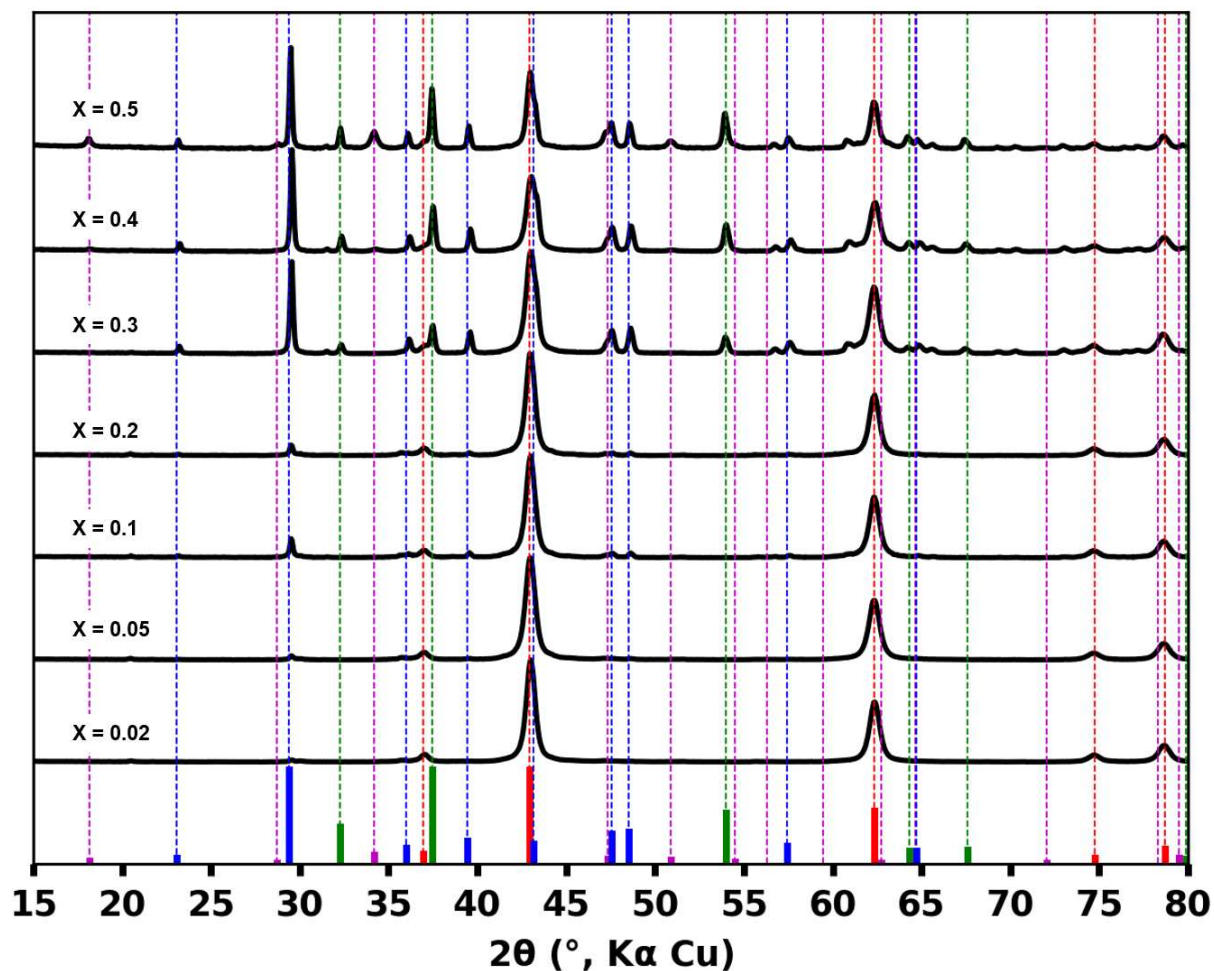


Figure 5: XRD pattern of the final powder of  $(1-x)\text{MgO}-x\text{CaO}$  for different  $x$  values. References are the following: red =  $\text{MgO}$ , blue =  $\text{CaCO}_3$ , green =  $\text{CaO}$ , magenta =  $\text{Ca}(\text{OH})_2$ .

The TEM images of these objects showed morphology similar to pure  $\text{MgO}$  nanoparticles for  $x < 0.2$  (Figure 6:a to c), and the apparition of bigger objects for  $x > 0.2$  (Figure 6:d to g), and finally big spheres for  $x = 0.5$  (Figure 6:h). Since TEM provided local analysis, even if we did not see any rods that could correspond to the ones seen in  $\text{CaO}$  synthesis, it did not mean that they were not present. Overall, our samples contained several phases: it was quite difficult to identify which type of particles corresponded to which phases with certainty without elemental analysis. We decided to perform STEM-EDX measurements on the  $x = 0.1$  sample.

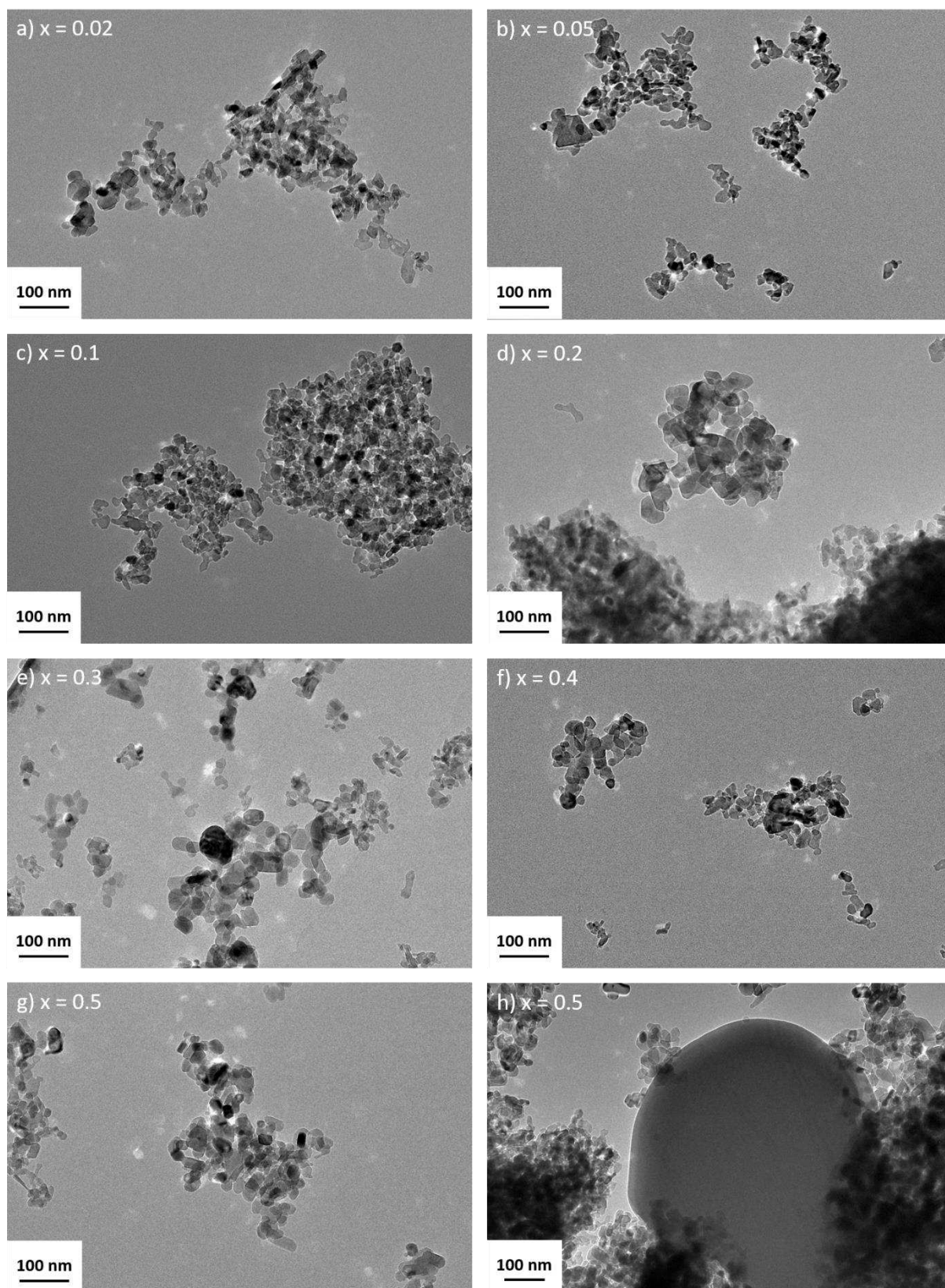


Figure 6: TEM images of the final nanoparticles obtained in the Mg-Ca mixed oxide synthesis for different values of  $x = \text{Ca/Mg}$ .

Figure 7: presented the results of the elemental analysis of the 0.9MgO-0.1CaO sample. First thing we noticed was that the atomic ratio in the analysed area was far from what we expected. Ideally, we expected a 50 % oxygen, 45 % magnesium and 5 % calcium atomic ratio, but instead we obtained 55.88 % oxygen, 44.01 % magnesium and 0.11 % calcium. This meant that the amount of calcium in the sample was far lower than expected. The elemental mapping however indicated that it was homogeneously dispersed in the scanned area, at least given the precision of the measurement. This difference could be explained by the presence of the  $\text{CaCO}_3$  phase detected in XRD. Maybe the majority of the calcium was contained in a  $\text{CaCO}_3$  phase and only a small fraction was incorporated in the MgO. We did not perform the same STEM-EDX measurements on the other MgO-CaO samples, but we could expect a similar result. For sake of simplicity, we will keep mentioning the MgO-CaO samples using the introduced ratio instead of the real ratio.

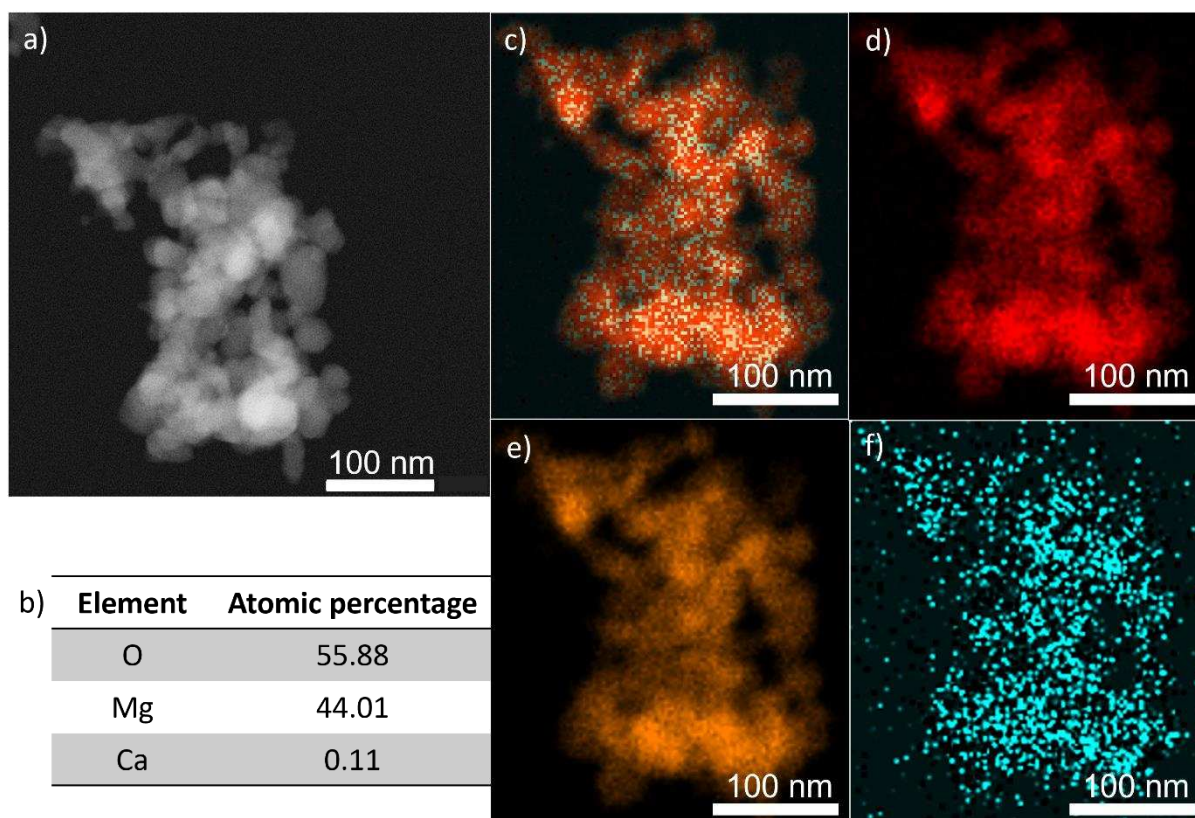


Figure 7: a) HAADF of the 0.9MgO-0.1CaO sample. b) elemental composition of the scanned zone, c) superposition of the elemental mappings of the different elements, d) oxygen elemental mapping, e) magnesium elemental mapping, f) calcium elemental mapping.

In the end, it appeared that synthesis of MgO-CaO mixed oxide with controlled homogeneous dispersion of the Ca atoms in the MgO lattice was not easily attainable via precipitation-calcination synthesis. More in depth study would be needed, especially on the precipitation part: impact of temperature, on the alkaline earth precursors, on the base and on the order of addition (precipitation of  $\text{Mg}(\text{OH})_2$  then addition of Ca precursor), etc. However, the material we synthesized with phase segregation between MgO, CaO and  $\text{CaCO}_3$  might still be interesting to study in catalysis.



As mentioned in Chapter 2, intercalation of transition metal ions in the MgO lattice could increase its catalytic activity by creating new acidic sites at its surface. We wondered if such metal addition would be possible by coprecipitation. It was reported that it was possible to form mixed oxides with MgO and transition metals such as Fe, Zn, Ni, Cu or Co<sup>12</sup>. For example, we hoped to form MgO-NiO particles that could further transform into MgO-Ni particles with a correct reduction treatment.

#### **4. Attempts to synthesize MgO-M (M = Co, Ni, Cu)**

To try to limit as much as possible phase segregation, we decided to work at a low M/Mg ratio with  $x = M/Mg = 5\%$ . For simplicity's sake, we decided to keep the same synthesis as before, just replacing the calcium source  $\text{Ca}(\text{NO}_3)_2$  by either  $\text{Co}(\text{NO}_3)_2$ ,  $\text{Ni}(\text{NO}_3)_2$  or  $\text{Cu}(\text{NO}_3)_2$ . The rest of the reaction was the same as described in the experimental part.

When doing the experiment, we could from the beginning observe a difference in the colour of the nanoparticles after the drying step (hydroxide powder) and after the calcination (oxide powder) (Table 2:). The hydroxide powder containing nickel was yellow and turned light brown after the calcination. The hydroxide powder containing cobalt was light brown and turned dark brown after the calcination. The hydroxide powder containing copper was blue and turned dark yellow after the calcination.

The origin of the different colours came from the presence of transition metal ions in the material making it absorb certain length waves in the visible spectrum. The adsorption depended on the metal and its electronic environment. Modification of the crystal lattice during the calcination might have caused a colour change.







Material	Ni	Co	Cu
Hydroxide powder			
Oxide powder			

Table 2: Magnesium based mixed oxides/hydroxides and their corresponding colors.

The XRD pattern of the different powders were displayed in Figure 8:, as well as the TEM micrographs of the final powder after the calcination. In the case of nickel (Figure 8:a), the hydroxide powder showed the presence of a pure  $\text{Mg}(\text{OH})_2$  phase. However, we could observe a linear background underneath it. Such backgrounds were characteristic of a fluorescent sample. Our explanation was that the final powder contained nickel. The XRD measurement could not allow to know what quantity of the introduced nickel was in the sample, nor if it was inserted in the  $\text{Mg}(\text{OH})_2$  lattice or if it formed an amorphous phase (not detectable in XRD). After the calcination, the XRD pattern showed the presence of a pure MgO phase. The diffractogram also showed fluorescence indicating that some nickel was still in the sample. The TEM micrograph of the final powder after calcination (Figure 8:b) were not different from the MgO nanoparticles. Same analysis, both in terms of XRD and TEM, applied for cobalt insertion (Figure 8:c and d) and for copper insertion (Figure 8:e and f).

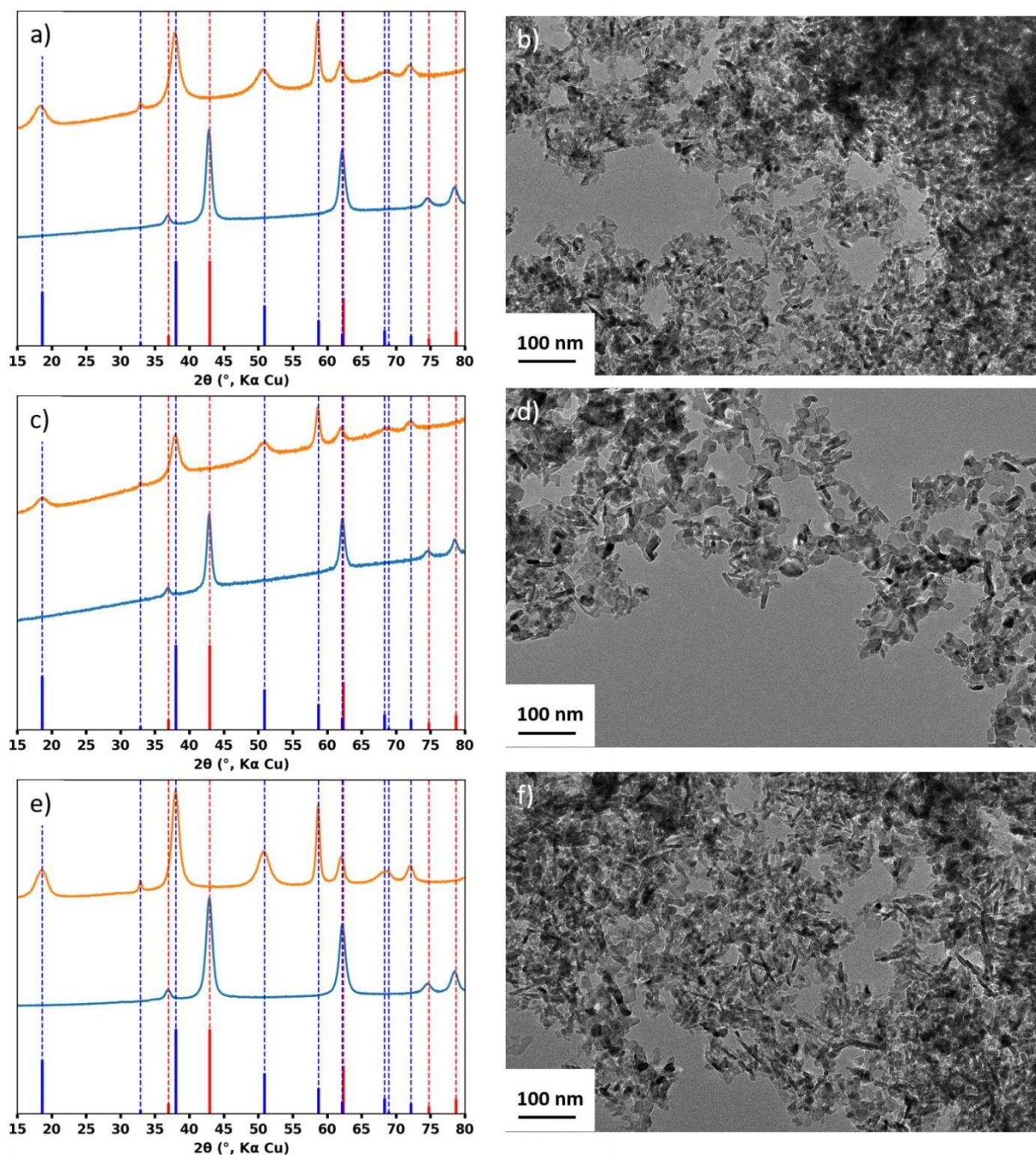


Figure 8: a) XRD patterns of  $Mg(OH)_2$ -Ni (orange) and  $MgO$ -Ni (blue) (reference of  $MgO$  is given by the red bars and of  $Mg(OH)_2$  by the blue), b) TEM micrograph of  $MgO$ -Ni nanoparticles, c) XRD pattern of  $Mg(OH)_2$ -Co (orange) and  $MgO$ -Co (blue), d) TEM micrograph of  $MgO$ -Co nanoparticles, e) XRD pattern of  $Mg(OH)_2$ -Cu (orange) and  $MgO$ -Cu (blue), f) TEM micrograph of  $MgO$ -Cu nanoparticles.

Just like with the  $MgO$ - $CaO$  sample, we decided to perform STEM-EDX measurements on the samples in order to evaluate the amount of transition metal inserted and its dispersion in the  $MgO$  nanoparticles. Figure 9: presented the results of the STEM-EDX measurements on the  $MgO$ -Ni sample. We could see that the atomic ratio of the scanned zone was close to the one expected. We expected a 50 % oxygen, 47.5 % magnesium, 2.5 % nickel and obtained respectively 56.66 %, 47.5 %, 2.5 %.

40.87 % and 2.47 %. It was not clear if the dispersion of the nickel on the sample was homogeneous, we decided to select a zone with a high apparent nickel density (in the elemental mappings Figure 9:c to f) and measured the atomic ratio in this specific zone (red squares in Figure 9:). We obtained ratio close to the previous ones: 57.46 % oxygen, 39.74 % magnesium and 2.80 % nickel. Nickel insertion in the MgO nanoparticles was successful according to these information.

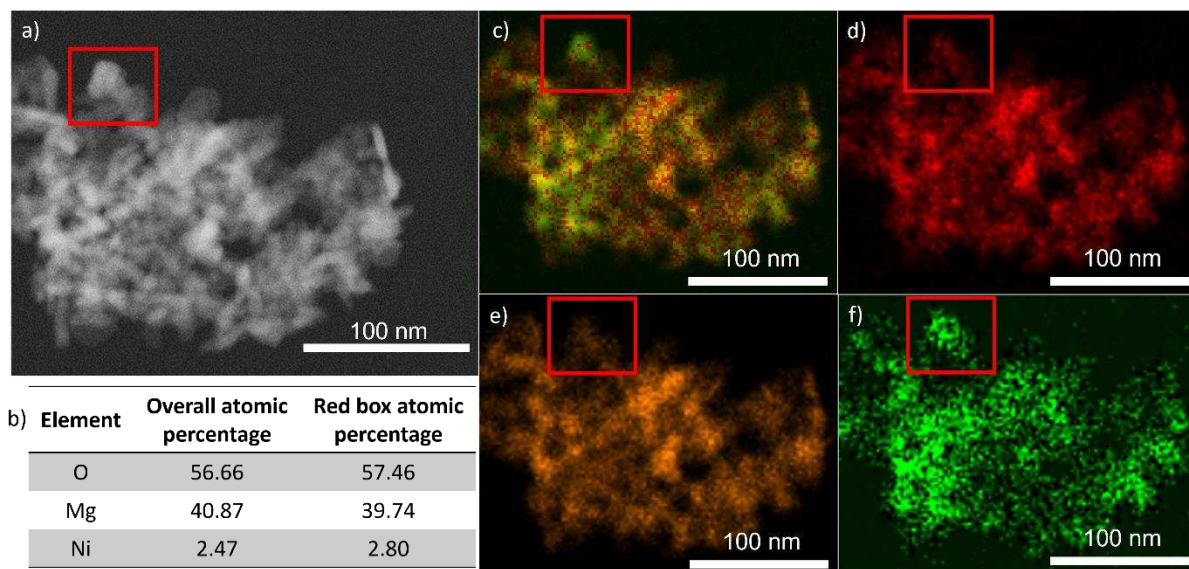


Figure 9: a) HAADF of the MgO-Ni sample. b) elemental composition of the scanned zone, c) superposition of the elemental mappings of the different elements, d) oxygen elemental mapping, e) magnesium elemental mapping, f) nickel elemental mapping. Red boxes show the area scanned for a smaller scale measurement.

Figure 10: showed the STEM-EDX measurements of the MgO-Co sample. Just like with nickel, we obtained atomic ratio close to the expected ones: 56.50 % oxygen, 40.34 % magnesium and 3.17 % cobalt. However, when we did the measurement on a zone with a high apparent cobalt density, we observed a modification of the ratio: 59.56 % oxygen, 31.63 % magnesium and 8.82 % cobalt. The cobalt concentration was significantly higher in this area than in the entire zone. We managed to incorporate cobalt inside the MgO nanoparticles but its repartition was not homogeneous.

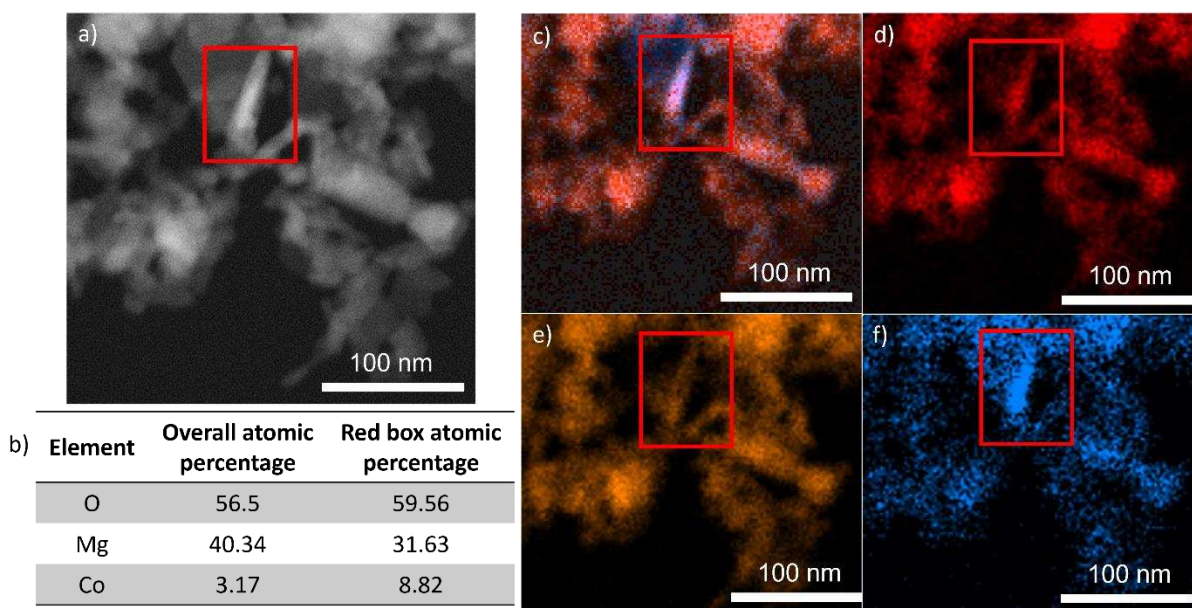


Figure 10: a) HAADF of the MgO-Co sample. b) elemental composition of the scanned zone, c) superposition of the elemental mappings of the different elements, d) oxygen elemental mapping, e) magnesium elemental mapping, f) cobalt elemental mapping. Red boxes show the area scanned for a smaller scale measurement.

Results of the STEM-EDX experiment on the MgO-Cu sample were displayed in Figure 11:. We could observe on the HAADF micrograph the presence of small white dots. These dots corresponded to clusters with higher contrast that we associated to copper clusters that grew on the MgO nanoparticles. The elemental analysis gave a copper content a bit higher than expected: 55.98 % oxygen, 39.82 % magnesium and 4.21 copper. This could be due to the fact that the samples were deposited on copper grids for the analysis, thus leading to contamination. We tried to make an elemental analysis on a zone with a copper cluster, but we did not obtain significantly different result: 56.86 % oxygen, 39.73 % magnesium, 3.81 % copper. We concluded that the copper cluster were too small to be detected with this technique without having 10 hours long measurements.

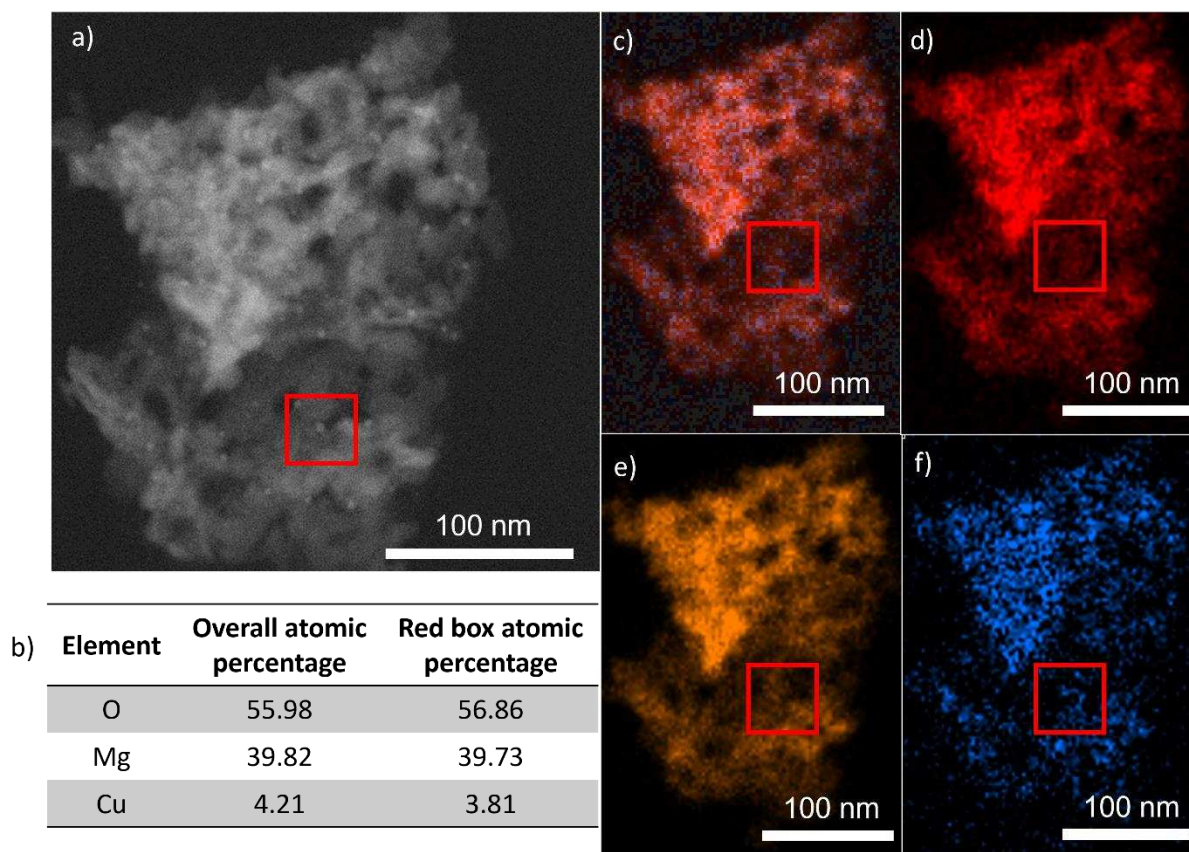


Figure 11: a) HAADF of the MgO-Cu sample. b) elemental composition of the scanned zone, c) superposition of the elemental mappings of the different elements, d) oxygen elemental mapping, e) magnesium elemental mapping, f) copper elemental mapping. Red boxes show the area scanned for a smaller scale measurement.

We now have different type of materials that could be good candidates for our NanoFLP. Synthesis of MgO nanoparticles by precipitation-calcination was the cornerstone of our materials and we could see how variation of the initial synthesis led to modification of the future catalyst. The impact of temperature on the crystallographic facets, the influence of the washing step on the sintering during the calcination and the incorporation of other elements through coprecipitation were the main features explored.

We talked a lot about the bulk nature of the nanoparticles, but we did not talk much about the surface, a crucial part in the activity of particles in catalysis. Thus, we wondered: how could we correctly describe the surface of our particles?

### III. Surface state of MgO nanoparticles

#### 1. Ageing of MgO nanoparticles under ambient air

As mentioned in Chapter II, alkaline-earth oxides were known to react with  $\text{CO}_2$  and water to form respectively carbonates and hydroxides at their surface. A sample of MgO nanoparticles (synthesized by precipitation-calcination with no additional washing treatments and calcined at  $500\text{ }^\circ\text{C}$ ) and a sample of CaO nanoparticles were let at ambient air for 3 weeks, XRD was performed again (Figure 12:). It showed the formation of both  $\text{Ca}(\text{OH})_2$  and  $\text{CaCO}_3$  and the total disappearance of the CaO phase. However, the diffractogram of the MgO nanoparticles did not change. We could see that CaO nanoparticles were more sensitive to both hydration and carbonation than MgO nanoparticles despite their bigger size. All our samples were stored under inert atmosphere to reduce their exposition to  $\text{H}_2\text{O}$  and  $\text{CO}_2$ .

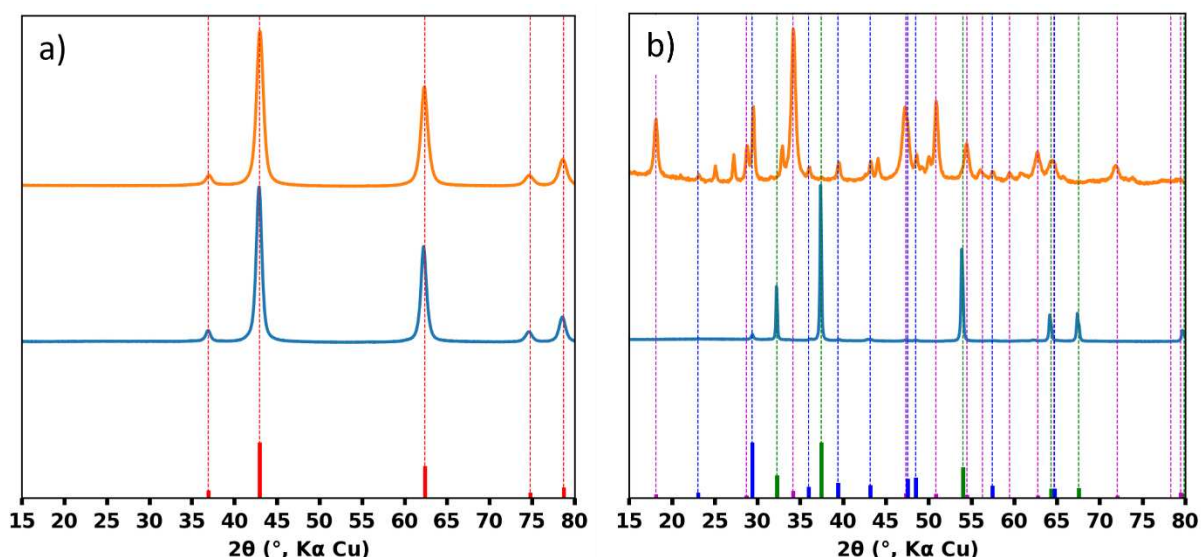


Figure 12: XRD pattern of alkaline earth oxides nanoparticles after the synthesis (blue) and after ageing under ambient air (orange). a) MgO nanoparticles (MgO reference is given by the red bars). b) CaO nanoparticles (CaO reference: green bars,  $\text{Ca}(\text{OH})_2$  reference: magenta bars,  $\text{CaCO}_3$  reference: blue bars).

Even if bulk magnesium hydroxide and carbonate did not form upon air exposition, we expected the formation of hydroxyls and carbonates at the surface of the nanoparticles. XRD was a characterisation technique only informing on the presence of bulk crystalline phases; we needed a technique sensitive to surface properties. We decided to use Fourier Transform Infrared Spectroscopy (FTIR).

#### 2. IR spectrum of MgO nanoparticles

To better understand the surface state of the nanoparticles during precipitation-calcination synthesis (no additional washing steps, calcination at  $500\text{ }^\circ\text{C}$ ), we measured the IR spectrum of the nanoparticles in ATR mode using a spectrometer inside the inert glovebox for both the

hydroxide and the final oxide powders (Figure 13:). The hydroxide IR spectrum (in blue) featured a fine band at  $3695\text{ cm}^{-1}$  and a large superposition of bands between  $1200$  and  $1400\text{ cm}^{-1}$ . The first one was characteristic of the O—H vibration of the hydroxide group, and the other was characteristic of surface carbonates. The oxide spectrum presented a small band at  $3764\text{ cm}^{-1}$  and a large superposition of bands between  $1200$  and  $1400\text{ cm}^{-1}$ . The first could be attributed to surface hydroxyls, and the second to surface carbonates. The zone around  $1800\text{ cm}^{-1}$  due to the spectrometer, the blank spectrum presents the same feature and we never managed to erase it. And finally, the big band that we start to see at  $600\text{ cm}^{-1}$  was due the Mg—O bond.

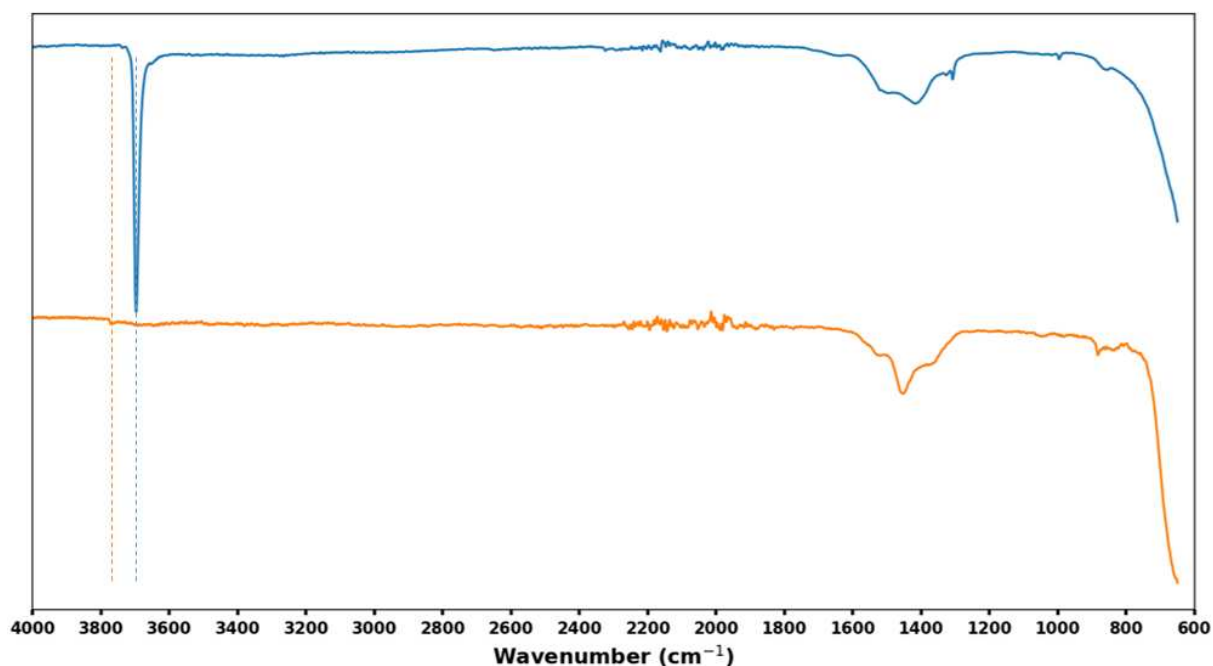


Figure 13: IR spectra of MgO nanoparticles (orange) and Mg(OH)<sub>2</sub> nanoparticles (blue), dotted lines are a guide to see the O—H band in each material.

We measured the IR spectrum of the nanoparticles that aged under air to see the impact on the bands associated to O—H and carbonate vibrations (Figure 14:). We could see on the spectrum of the aged particles that a large band appeared between  $3000$  and  $3400\text{ cm}^{-1}$ , and that the shape of the superposition of bands between  $1200$  and  $1400\text{ cm}^{-1}$  also changed. It indicated a modification of the surface hydroxyls and carbonate groups. More in depth analysis of these spectra will be given in Chapter IV.



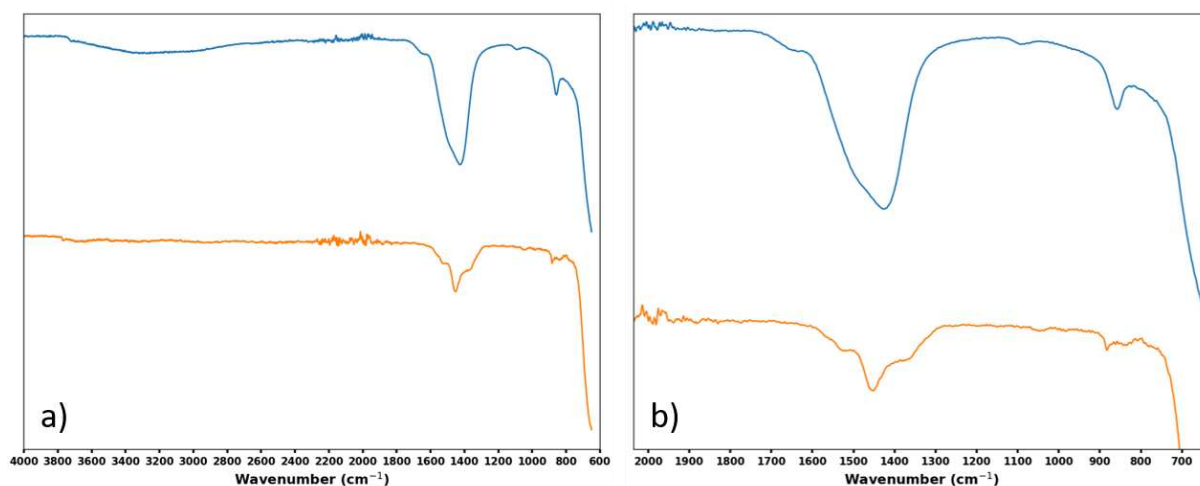


Figure 14: a) IR spectra of MgO nanoparticles just after the synthesis (orange) and after 3 weeks in air (blue), b) zoom in the zone where carbonates are visible.

### 3. Repeatability of the MgO synthesis

MgO synthesis via precipitation-calcination was repeated several times during the project. Surprisingly enough, even if XRD and TEM measurements gave the same results from one synthesis to another, we observed variation in the IR spectra. This was especially true in the carbonate signal between 1200 and 1400 cm<sup>-1</sup> (Figure 10:). More in depth analysis of this variability will be made in Chapter IV.

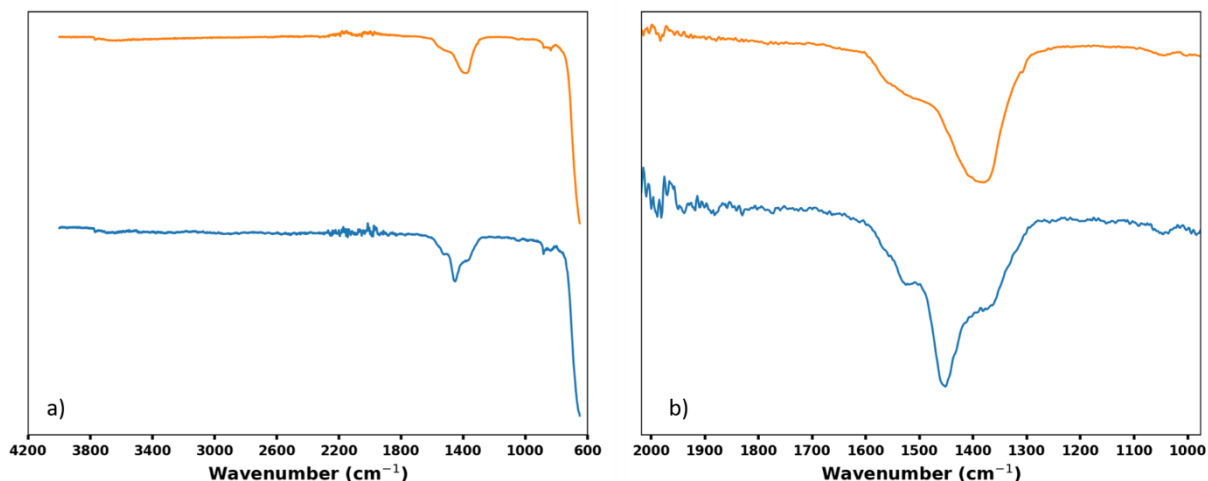
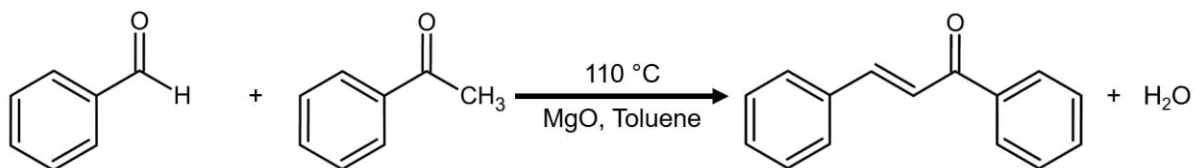


Figure 15: IR spectra of two different MgO synthesis by precipitation-calcination (no additional washings, calcination at 500 °C). a) Full spectra, b) zoom on the carbonate signal.

## IV. MgO nanoparticles as catalyst in the Claisen-Schmidt condensation

### 1. The Claisen-Schmidt condensation

For practical reasons, we decided to test the activity of the synthesized MgO nanoparticles in a catalytic reaction that did not involve gaseous reactants like CO<sub>2</sub>. Among the different reactions mentioned in chapter 2, we chose the Claisen-Schmidt condensation since it involved the activation of a C=O double bond (Scheme 4:).



*Scheme 4: Claisen-Schmidt condensation reaction between benzaldehyde and acetophenone leading to the formation of chalcone and water, conditions from Bain et al<sup>8</sup>.*

The Claisen-Schmidt condensation was discovered in the 1880s by R.L. Claisen and J.G. Schmidt. It recently gained interest since it can lead to the formation of flavonoids and chalcones used as flavours, colorants or medicines.<sup>13</sup> This reaction is a condensation reaction similar to aldol condensation. The main difference is that it specifically concerns the reaction between an aldehyde or a ketone with an  $\alpha$ -hydrogen and an aromatic carbonyl compound lacking an  $\alpha$ -hydrogen.

### Mechanism

The Claisen-Schmidt condensation starts with the addition of the ketone on the aldehyde followed by the dehydration of the intermediate. This reaction can actually be catalysed either by an acid or a base. As described in Figure 16:, the base-catalysed reaction consists of three steps: the activation of the ketone to form an enolate, the addition of the enolate on the aldehyde, and the dehydration of the intermediate to form chalcone and water. The acid-catalysed reaction also follows three steps: protonation of the ketone, formation of an enol, addition on the aldehyde and dehydration. Lots of heterogeneous catalysts were reported to be active for the Claisen-Schmidt condensation: alkaline-doped activated carbons, zeolites, magnesium oxide, hydroxyapatite, alumina, or natural phosphates. The list was not exhaustive, but more details were given in Yadav's review on the subject<sup>13</sup>.

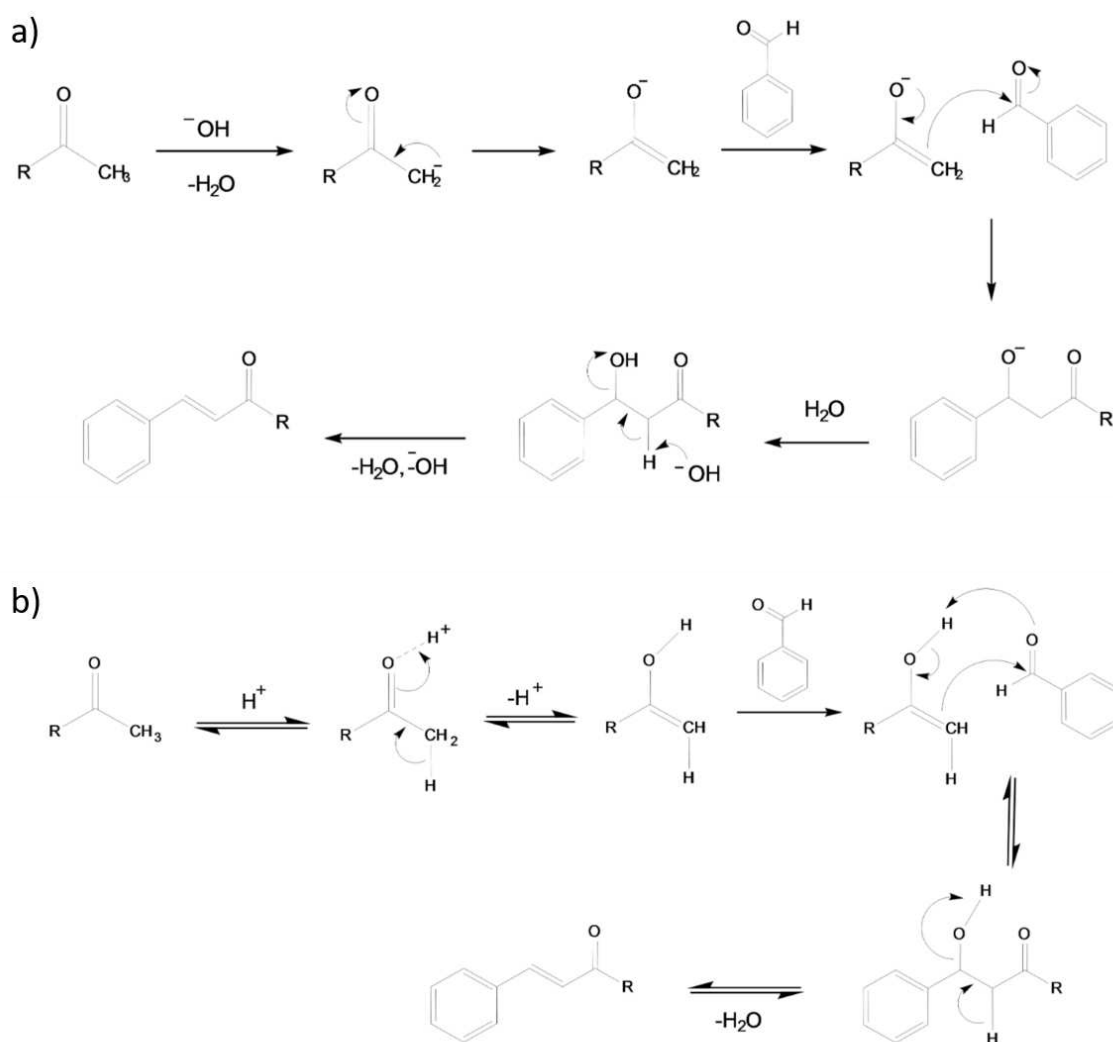


Figure 16: Mechanism of the Claisen-Schmidt condensation a) catalyzed by a base, b) catalyzed by an acid, from Yadav et al.<sup>13</sup>

## 2. Activity of the synthesized MgO nanoparticles

Several studies mention MgO as an active catalyst for the Claisen-Schmidt condensation<sup>8,14,15</sup>. In these studies, they used organic solvents such as toluene, DMSO, nitrobenzene or benzonitrile. Drexler and co-workers<sup>14</sup> especially showed an interesting effect of the addition of small quantities of DMSO in other solvents. It increased the catalytic activity of MgO due to the formation of sulphate groups at its surface. These sulphates helped the adsorption of benzaldehyde at the surface of the MgO catalyst. In all these studies, the temperatures ranged between 100 °C and 160 °C. Here, we decided to use similar parameters as Bain et al. in their study<sup>8</sup>. The detailed experimental protocol was detailed in the experimental part of the chapter.

**a. First catalytic test**

After a 15h reaction, we calculated the NMR yield of the reaction (formula used for the calculation of the peaks was given in Annexe 4.). Detailed spectra of the different reactants were given in Annexe. Benzaldehyde was easily recognized by its aldehyde peak around 10 ppm (Annexe 1), acetophenone was recognized by its  $-CH_3$  signal at 2.6 ppm (Annexe 2), and ethylenic protons in chalcone were visible around 7.8 and 7.6 ppm (Annexe 3). The aromatic peaks were harder to use to calculate NMR yields due to overlapping. Since we did not isolate the product, the most intense peaks detected were attributed to toluene (solvent of the reaction) and water (by-product of the reaction and traces in  $CDCl_3$ ) (Figure 17:a). When we zoomed in we could see the peaks corresponding to benzaldehyde, acetophenone and chalcone (Figure 17:b). We could also detect a small peak at 4.7 ppm, but its integration was negligible compared to the one of chalcone (Table 3:). With these data we could calculate the NMR yield of the reaction.

Since benzaldehyde was the limiting reactant (1 eq. of benzaldehyde for 1.2 eq. of acetophenone), we followed its consumption to calculate the NMR yields and conversions (Table 3:). Interestingly, at the end of the reaction we had a 1.29 ratio between the area of acetophenone peak at 2.6 ppm and the area of benzaldehyde peak at 10 ppm instead of the expected 1.2. Uncertainties on the introduced quantities of reactant were estimated to 5 % and could explain this difference. Using the water peak at 1.5 ppm, we calculated that 5.32 equivalents of water was formed during the reaction. This was more than what could be expected (one equivalent of water for one equivalent of chalcone). This was due to the residual water contained in  $CDCl_3$  used for the measurement. The water peak could not be used for NMR yield calculations. The peaks of chalcone gave an NMR yield of 45 % with a selectivity of 93 %. We confirmed that the nanoparticles synthesized by precipitation-calcination were active catalysts for the Claisen-Schmidt condensation.

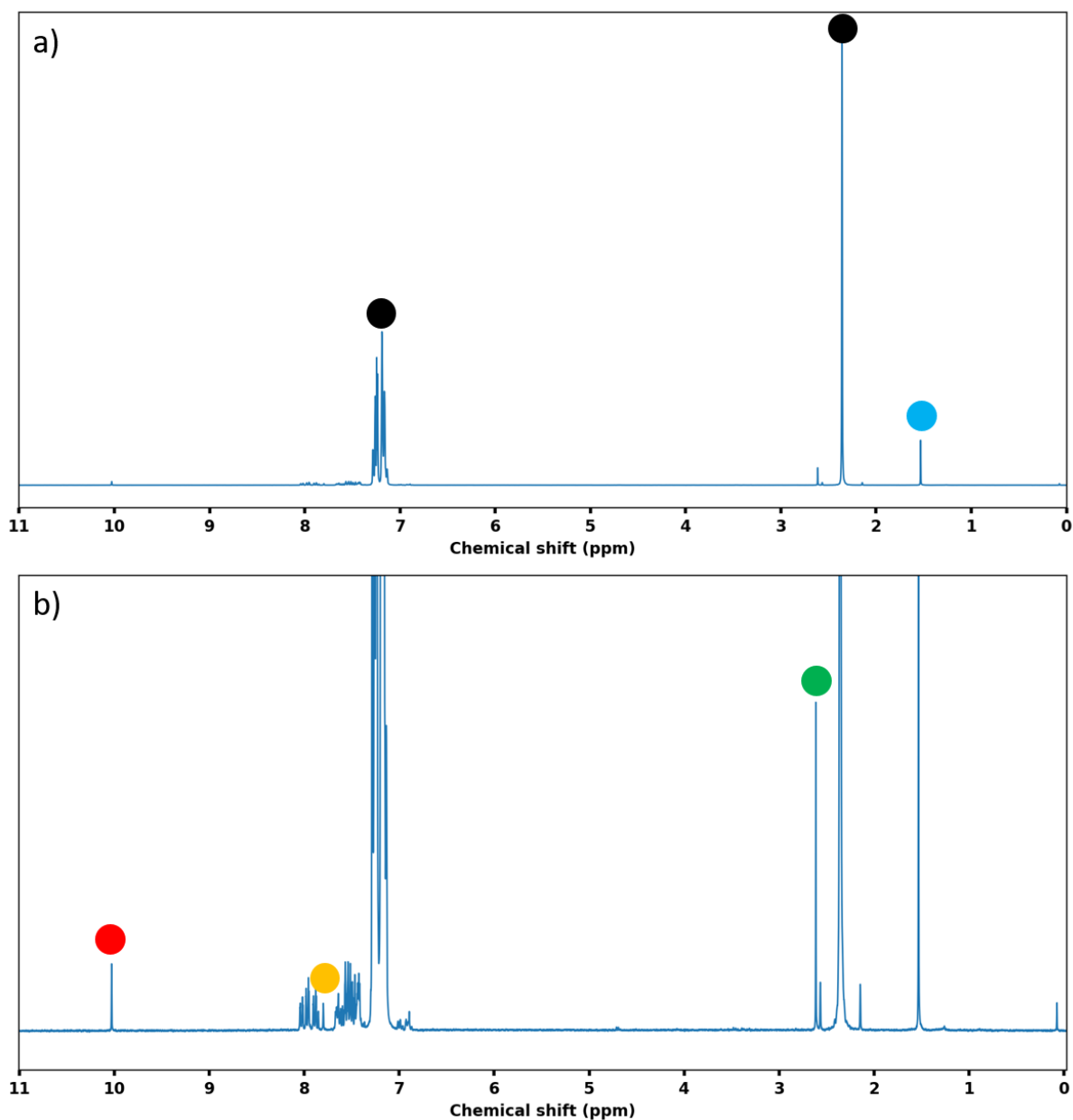


Figure 17: <sup>1</sup>H NMR spectrum of the crude after the Claisen-Schmidt condensation in CDCl<sub>3</sub> a) full view where mostly toluene (black dots) and water (blue dots) are visible, b) zoom where we see benzaldehyde (red dot), acetophenone (green dot) and chalcone (yellow dot).

Species	Integration	Equivalents	NMR conversion	NMR yield	NMR selectivity
Benzaldehyde	1	1	52 %	-	-
Acetophenone	3.88	1.29	-	-	-
Chalcone	0.87	0.87	-	45 %	93 %
Water	10.63	5.32	-	*	-
By-product 4.7	0.07	0.07	-	3 %	0.07 %

Table 3: Results of the Claisen-Schmidt condensation. Integrations are calculated directly from the proton NMR spectrum. Equivalents result from the normalisation of the integrations. NMR conversions, yields and selectivity are calculated as described in Annexe 4.

### b. Comparison to Bain's study

We compared our results to the work of Bain and co-workers. Our catalyst was not quite as active as their "flower-like" MgO but more active than the commercial one (Table 4:). This might be explained by the fact that they synthesized particles with a specific shape using ethylene glycol and poly(vinylpyrrolidone). The authors stated that this morphology eased the access to catalytic sites. This could explain why the activity of their catalyst was higher despite having a lower surface area.

Catalyst	Catalyst surface area	Benzaldehyde consumption
Bain's flower like MgO	45 m <sup>2</sup> /g	97 %
Bain's commercial MgO	27 m <sup>2</sup> /g	20 %
Precipitation-calcination MgO	100 m <sup>2</sup> /g	52 %

Table 4: Comparison of the benzaldehyde consumption in the Claisen-Schmidt condensation between our work and the work of Bain et al.. They calculated the yield using gas chromatography and not NMR.

We verified that our MgO nanoparticles were active in catalysis, even if they were less active than the one presented in Bain's work.

### 3. Activity of the pair MgO+BPh<sub>3</sub>

In this last part, we wanted to test the impact of borane addition on the catalytic activity of MgO nanoparticles. Even before the test, we knew that the Claisen-Schmidt condensation was not the most suited reaction to observe a MgO-borane effect for two reasons:

- The reaction produced water that could react with the borane (hydrolysis)
- The reaction was catalysed by Lewis acids so we could expect the borane to catalyse the reaction. We did not find reference of borane catalysed Claisen-Schmidt condensation in the literature

Furthermore, we did not find any record of Claisen-Schmidt condensation catalysed by a FLP in the literature.

Even if we did not have a specific FLP mechanism in mind, we could imagine that the tandem interaction between the Lewis acid and the Lewis base could help stabilise the first anionic intermediate forming after the C—H bond cleavage (Figure 18:). This could lead to an enhancement of the activity of the catalyst. These were *a priori* ideas, proving the existence of such intermediates could actually be complicated.

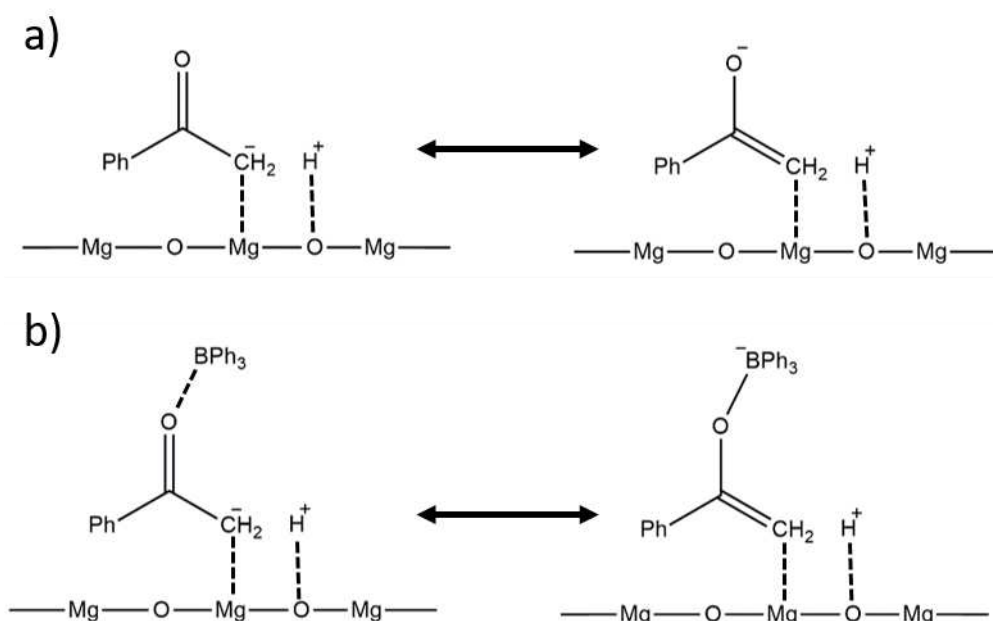


Figure 18: Propositions for the stabilisation of the enolate intermediate a) by a MgO surface, b) by the pair MgO+BPh<sub>3</sub>.

In order to reduce the probability to form strong borane-water adducts, we decided to use a weak Lewis acid in the reaction: BPh<sub>3</sub>. We feared that the traditionally used B(C<sub>6</sub>F<sub>5</sub>)<sub>3</sub> (BCF) would react too strongly with water and not be available to interact with the MgO surface. Since acids could catalyse Claisen-Schmidt condensation, it was important to first measure the activity

of BPh<sub>3</sub> alone as a catalyst before trying the pair MgO+BPh<sub>3</sub>. We reduced the amount of catalyst in the solution from 2.5 mmol (1 equivalent versus benzaldehyde) to 1 mmol (0.33 equivalent versus benzaldehyde). With these parameters we ensured to be at low consumption rates. We wanted to see the impact of the borane on the early stages of the reaction before it could react with the produced H<sub>2</sub>O. We used 0.12 equivalents of BPh<sub>3</sub> compared to benzaldehyde. The results of the catalysis in these conditions with MgO, BPh<sub>3</sub> and MgO+BPh<sub>3</sub> were given in Table 5:

MgO (eq. compared to benzaldehyde)	BPh <sub>3</sub> (eq. compared to benzaldehyde)	Benzaldehyde consumption
0.33	0	5 %
0	0.12	9 %
0.33	0.12	5 %

Table 5: Comparison of the benzaldehyde consumption in the Claisen-Schmidt condensation catalysed by MgO, BPh<sub>3</sub> and MgO+BPh<sub>3</sub>.

In these conditions, we obtained a 5 % consumption of the benzaldehyde with MgO nanoparticles alone. BPh<sub>3</sub> alone was a catalyst for the reaction, leading to a 9 % consumption of benzaldehyde. This activity was not reported in the literature, but we were not surprised since Claisen-Schmidt condensation was catalysed by Lewis acids. The most interesting part however concerned the use of MgO+BPh<sub>3</sub>. When using MgO+BPh<sub>3</sub>, we obtained a consumption of 5 %, the same value as MgO alone. In these conditions the use of MgO and BPh<sub>3</sub> actually reduced the catalytic activity of both catalysts. Explanation could be that the interaction between MgO and BPh<sub>3</sub> was too strong, thus poisoning the active sites of MgO and preventing BPh<sub>3</sub> to act as a catalyst. This result hinted toward the fact that MgO and BPh<sub>3</sub> interacted even if it did not increase the catalytic activity.

## 4. Conclusion

The result of these first catalytic tests were the following:

- the MgO nanoparticles we synthesized were active in catalysis but with a lower activity than the ones presented in the reference study of Bain
- the use of BPh<sub>3</sub> reduced the catalytic activity of our MgO catalyst

It appeared that the study of the interaction between the Lewis base inorganic nanoparticles and the Lewis acid ligand was of paramount importance. We had to study this interaction first before trying catalytic tests if we wanted to understand the catalytic activity of the MgO-borane pair.



## V. Conclusion

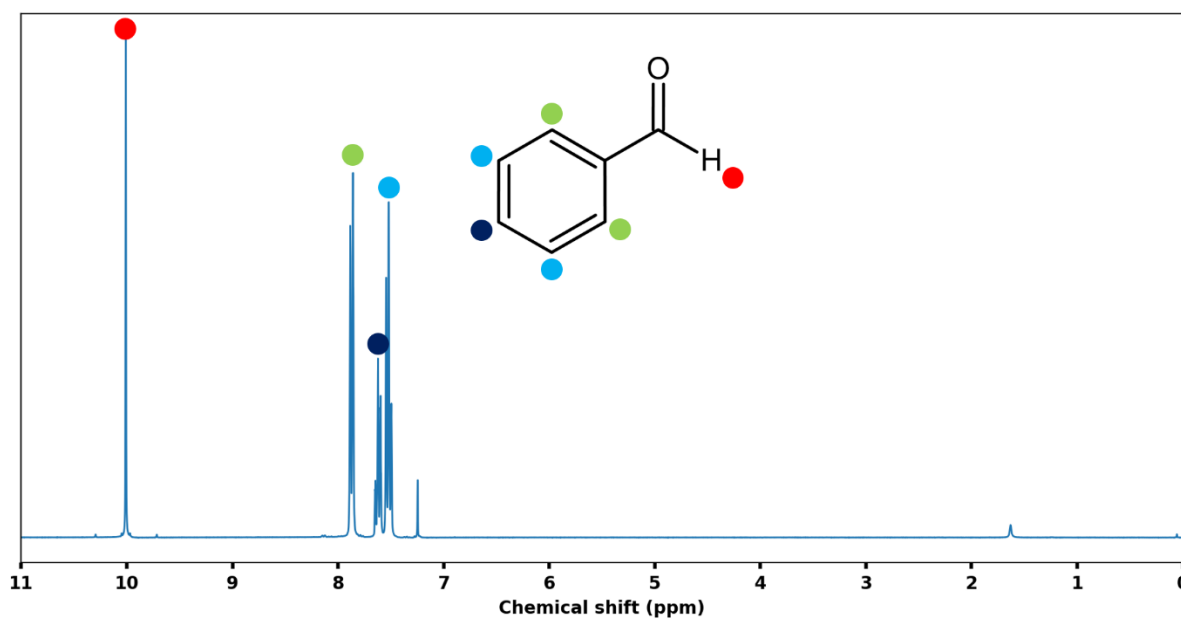
We managed to synthesize different alkaline earth oxide nanoparticles for the continuation of the project. We managed to synthesize them by precipitation-calcination of nitrate precursors in basic aqueous conditions.

- For the MgO synthesis, we studied the impact of two main parameters that were the calcination temperature and the washing of the hydroxide intermediate. They influenced the shape and the size of the final nanoparticles.
- We synthesized CaO nanoparticles and showed that they were more sensitive to carbonation and hydration than the MgO ones. A residual CaCO<sub>3</sub> was always present in the samples.
- We synthesized MgO-CaO mixed oxide nanoparticles by coprecipitation and studied the influence of Mg/Ca ratio. Calcium was hard to incorporate inside the MgO nanoparticles and tended to nucleate on its own forming calcium containing phases such as CaCO<sub>3</sub>, Ca(OH)<sub>2</sub> and CaO.
- We synthesized MgO-M (M = Co, Ni and Cu) mixed oxides nanoparticles by coprecipitation and showed different end results depending on the transition metal. Nickel was introduced successfully and homogeneously in the MgO nanoparticles. Cobalt was introduced successfully but we observed zones with higher cobalt concentration. Copper formed small clusters on the MgO nanoparticles and we could not determine if all the copper was contained in these clusters or if a part of it was incorporated in the MgO lattice.
- We tested the MgO nanoparticles in the Claisen-Schmidt condensation and showed that they were active catalysts. Nanoparticles calcined at 1000 °C were less active than the one calcined at 500 °C.
- We made a first attempt at MgO-borane catalytic synergy by adding triphenyl borane in the reaction medium for the Claisen-Schmidt condensation. We showed an unreported activity of the borane alone for the reaction and showed that the combination of MgO nanoparticles and BPh<sub>3</sub> ligands was less active than the sum of the individual activity. We suggested that BPh<sub>3</sub> was coordination on MgO nanoparticles surface, thus blocking both active sites.

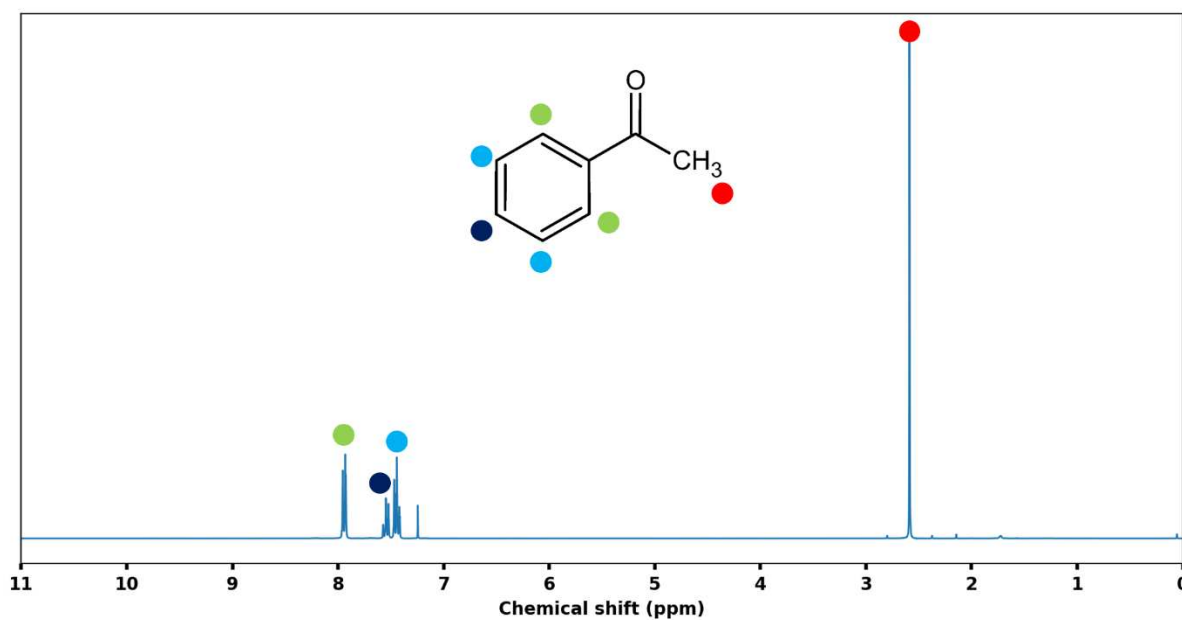
We decided to study MgO nanoparticles surface and its interaction with both CO<sub>2</sub> and boranes more in detail in the next chapter.

## VI. Annexes

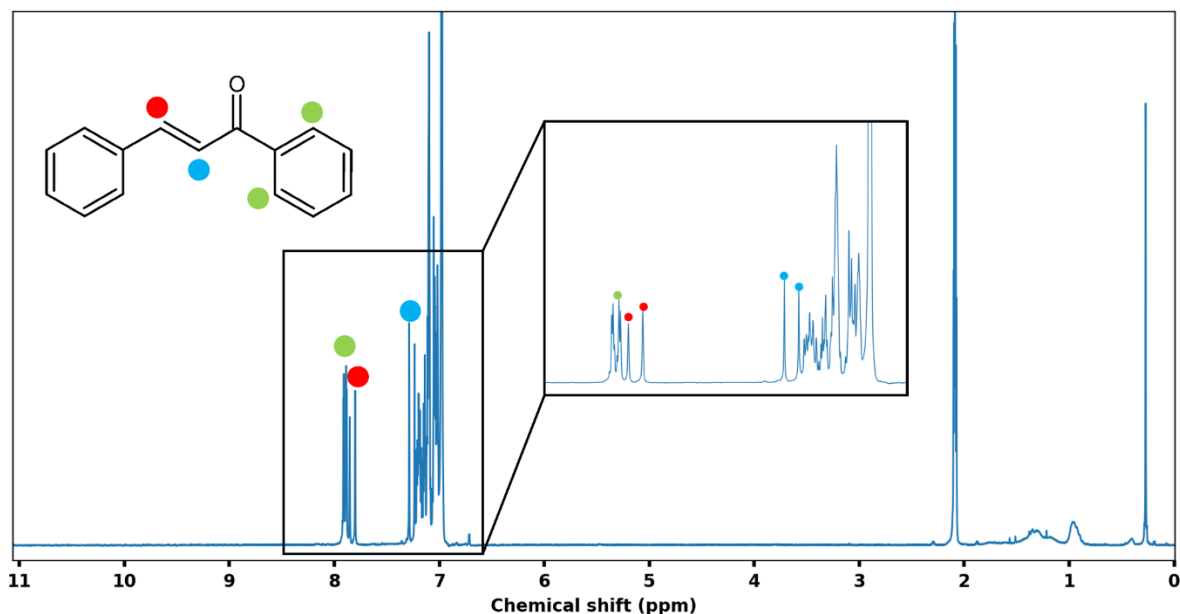
## NMR references



Annexe 1. NMR reference of benzaldehyde in CDCl<sub>3</sub>



Annexe 2. NMR reference of acetophenone in CDCl<sub>3</sub>



Annexe 3. NMR reference of chalcone in toluene- $d_8$

## Calculation of NMR yields

We used NMR in order to follow the evolution of the reaction. If we consider one proton in a reactant, we follow its evolution to see where it will be at the end of the reaction. This proton could either: not have reacted (initial reactant still present), be in the main product, or be in a by-product. When there are no/few by-products, NMR conversions are really easy to handle and do not need the addition of internal standards that could bring repeatability issues. When there was by-products we decided to always consider that the corresponding main peak accounted for one proton. This means that we over-estimate the quantity of by-products in most cases.

$$\text{NMR yield} = \frac{\text{area of H in the product}}{\text{area of H in the reactant} + \text{area of H in the product} + \text{area of H in the byproducts}}$$

$$\text{NMR conversion} = \frac{\text{area of H in the reactant}}{\text{area of H in the reactant} + \text{area of H in the product} + \text{area of H in the byproducts}}$$

$$\text{NMR selectivity} = \frac{\text{area of H in the product}}{\text{area of H in the product} + \text{area of H in the byproducts}}$$

Annexe 4. Equations used to calculate the NMR yields, conversions, and selectivities

- (1) Park, J. Y.; Lee, Y. J.; Jun, K. W.; Baeg, J. O.; Yim, D. J. Chemical Synthesis and Characterization of Highly Oil Dispersed MgO Nanoparticles. *J. Ind. Eng. Chem.* **2006**, *12* (6), 882–887.
- (2) Itatani, K.; Koizumi, K.; Howell, F. S.; Kishioka, A.; Kinoshita, M. Agglomeration of Magnesium Oxide Particles Formed by the Decomposition of Magnesium Hydroxide - Part 2 Agglomeration at Fixed Temperatures. *J. Mater. Sci.* **1989**, *24* (7), 2603–2609. <https://doi.org/10.1007/BF01174532>.
- (3) GORDON, R. S.; KINGERY, W. D. Thermal Decomposition of Brucite: I, Electron and Optical Microscope Studies. *J. Am. Ceram. Soc.* **1966**, *49* (12), 654–660. <https://doi.org/10.1111/j.1151-2916.1966.tb13194.x>.
- (4) Pilarska, A.; Paukszta, D.; Ciesielczyk, F.; Jesionowski, T. Physico-Chemical and Dispersive Characterisation of Magnesium Oxides Precipitated from the  $Mg(NO_3)_2$  and  $MgSO_4$  Solutions. *PJCT* **2010**, *12* (2), 52–56. <https://doi.org/10.2478/v10026-010-0018-x>.
- (5) Ding, Y.; Zhang, G.; Wu, H.; Hai, B.; Wang, L.; Qian, Y. Nanoscale Magnesium Hydroxide and Magnesium Oxide Powders: Control over Size, Shape, and Structure via Hydrothermal Synthesis. *Chem. Mater.* **2001**, *13* (2), 435–440. <https://doi.org/10.1021/cm000607e>.
- (6) Green, J. Calcination of Precipitated  $Mg(OH)_2$  to Active MgO in the Production of Refractory and Chemical Grade MgO. *J. Mater. Sci.* **1983**, *18* (3), 637–651. <https://doi.org/10.1007/BF00745561>.
- (7) Henrist, C.; Mathieu, J.-P.; Vogels, C.; Rulmont, A.; Cloots, R. Morphological Study of Magnesium Hydroxide Nanoparticles Precipitated in Dilute Aqueous Solution. *J. Cryst. Growth* **2003**, *249* (1–2), 321–330. [https://doi.org/10.1016/S0022-0248\(02\)02068-7](https://doi.org/10.1016/S0022-0248(02)02068-7).
- (8) Bain, S.-W.; Ma, Z.; Cui, Z.-M.; Zhang, L.-S.; Niu, F.; Song, W.-G. Synthesis of Micrometer-Sized Nanostructured Magnesium Oxide and Its High Catalytic Activity in the Claisen–Schmidt Condensation Reaction. *J. Phys. Chem. C* **2008**, *112* (30), 11340–11344. <https://doi.org/10.1021/jp802863j>.
- (9) Zhang, G.; Hattori, H.; Tanabe, K. Aldol Addition of Acetone, Catalyzed by Solid Base Catalysts: Magnesium Oxide, Calcium Oxide, Strontium Oxide, Barium Oxide, Lanthanum (III) Oxide and Zirconium Oxide. *Appl. Catal.* **1988**, *36* (C), 189–197. [https://doi.org/10.1016/S0166-9834\(00\)80114-1](https://doi.org/10.1016/S0166-9834(00)80114-1).
- (10) Mirghiasi, Z.; Bakhtiari, F.; Darezereshki, E.; Esmailzadeh, E. Preparation and Characterization of CaO Nanoparticles from  $Ca(OH)_2$  by Direct Thermal Decomposition Method. *J. Ind. Eng. Chem.* **2014**, *20* (1), 113–117. <https://doi.org/10.1016/j.jiec.2013.04.018>.
- (11) Suttibut, P.; Suriye, K.; Prasertdam, P.; Panpranot, J. Synthesis and Characteristics of CaO/MgO Mixed Oxides for the Double Bond Isomerization of 1-Butene. *J. Nanosci. Nanotechnol.* **2018**, *18* (1), 439–444. <https://doi.org/10.1166/jnn.2018.14574>.
- (12) Silva, M.; Murzin, V.; Zhang, L.; Baltrus, J.; Baltrusaitis, J. Transition Metal-Doped MgO Nanoparticles for Nutrient Recycling: An Alternate Mg Source for Struvite Synthesis from

- Wastewater. *Environ. Sci. Nano* **2020**, 7 (11), 3482–3496.  
<https://doi.org/10.1039/D0EN00660B>.
- (13) Yadav, G. D.; Wagh, D. P. Claisen-Schmidt Condensation Using Green Catalytic Processes: A Critical Review. *ChemistrySelect* **2020**, 5 (29), 9059–9085.  
<https://doi.org/10.1002/slct.202001737>.
- (14) Drexler, M. T.; Amiridis, M. D. The Effect of Solvents on the Heterogeneous Synthesis of Flavanone over MgO. *J. Catal.* **2003**, 214 (1), 136–145. [https://doi.org/10.1016/S0021-9517\(02\)00013-1](https://doi.org/10.1016/S0021-9517(02)00013-1).
- (15) Choudary, B. M.; Kantam, M. L.; Ranganath, K. V. S.; Mahendar, K.; Sreedhar, B. Bifunctional Nanocrystalline MgO for Chiral Epoxy Ketones via Claisen–Schmidt Condensation–Asymmetric Epoxidation Reactions. *J. Am. Chem. Soc.* **2004**, 126 (11), 3396–3397. <https://doi.org/10.1021/ja038954n>.

**Chapter IV**  
**Adsorption of CO<sub>2</sub> and boranes on**  
**MgO surfaces**



# Table of contents

<b>I.</b>	<b>Carbonate formation on MgO surface .....</b>	<b>105</b>
	1. IR spectroscopy theory and experimental works .....	105
	2. Modelling the adsorption of CO <sub>2</sub> on surfaces.....	106
<b>II.</b>	<b>Experimental section .....</b>	<b>108</b>
<b>III.</b>	<b>Surface carbonates on MgO nanoparticles.....</b>	<b>110</b>
	1. MgO nanoparticles after the synthesis and impact of air exposition.....	110
	2. Variability in MgO IR spectrum .....	111
	3. IR spectra of MgO <sub>washed</sub> and MgO <sub>1000</sub> .....	113
	4. Carbonation of MgO nanoparticles under pure CO <sub>2</sub> .....	114
<b>IV.</b>	<b>Adsorption of boranes.....</b>	<b>117</b>
	1. Adsorption of BPh <sub>3</sub> on MgO in toluene.....	117
	a. Impact of BPh <sub>3</sub> addition on colloidal stability of MgO suspension.....	117
	b. Infrared study of the adsorption of BPh <sub>3</sub> on MgO.....	118
	c. Infrared study of the adsorption of BPh <sub>3</sub> and CO <sub>2</sub> on MgO .....	120
	2. Borane screening .....	122
	3. Adsorption of BCl <sub>2</sub> Ph on MgO .....	125
<b>V.</b>	<b>Conclusion .....</b>	<b>129</b>
<b>VI.</b>	<b>Annexes .....</b>	<b>130</b>



In this chapter, we were interested in the study of MgO nanoparticles surface. Both nanoparticles at the end of their synthesis and after exposition to CO<sub>2</sub> and/or molecular boranes were studied. As we saw in Chapter III, we needed better comprehension of the surface state of MgO nanoparticles before investigating catalytic reactions. The first part of the chapter was a reminder of the literature on surface carbonates forming on alkaline-earth oxides. The second part focused on the analysis of the synthesized MgO nanoparticles in terms of carbonate formation, and the last part focused on the adsorption of boranes.

Using IR spectroscopy, we found that carbonates were naturally present after the precipitation-calcination synthesis. Both the calcination temperature and the washing steps impacted the number and the types of carbonates present on the surface of the nanoparticles. Exposition of the MgO nanoparticles to CO<sub>2</sub> increased the intensity of the carbonate signal but did not modify consistently the position of the bands.

Since we studied the impact of BPh<sub>3</sub> addition on MgO nanoparticles for the Claisen-Schmidt condensation in Chapter III, we started to study the MgO-BPh<sub>3</sub> as the first MgO borane interaction. We used both colloidal stability tests and IR spectroscopy to determine if the borane were adsorbed on the surface of the nanoparticles. We also added CO<sub>2</sub> after the borane adsorption to see if it led to the apparition of new IR bands corresponding to potential MgO-CO<sub>2</sub>-borane adducts. Finally, we observed surprising results when adsorbing the chloroborane BCl<sub>2</sub>Ph on MgO nanoparticles that we interpreted as a cleavage of the B—Cl bonds to form MgO—B bonds.

## I. Carbonate formation on MgO surface

As explained in Chapter 2, basic alkaline earth oxide such as MgO formed carbonates due to a negative enthalpy associated to the carbonatation reaction<sup>1</sup>. In this first section, we gave a brief overview of the IR studies allowing to differentiate carbonate adsorption on MgO surfaces.

### 1. IR spectroscopy theory and experimental works

Different types of carbonates have different IR signature. Evans et al.<sup>2</sup> showed that adsorbed carbonates IR bands could be determined from the IR spectrum of the carbonate ion  $\text{CO}_3^{2-}$ . Carbonate ion belong to the point group  $D_{3h}$ , and the adsorption on a surface would decrease the symmetry of the ion, thus splitting certain degenerated bands and modifying the dipolar moment variation associated to certain vibrations. For example, a monodentate adsorption forming the  $-\text{O}-\text{CO}_2$  specie would belong to the  $C_{2v}$  point group. The initial asymmetric stretching of the carbonate ion would split into two components: the  $\text{CO}_2$  asymmetric stretching mode, and the  $\text{CO}_2$  symmetric stretching mode (Figure 1:). Furthermore, the symmetric stretching mode did not modify the dipolar moment of the  $\text{CO}_3^{2-}$  ion, it was not detectable in IR. This was no longer the case in monodentate adsorption, making the vibration visible in IR.

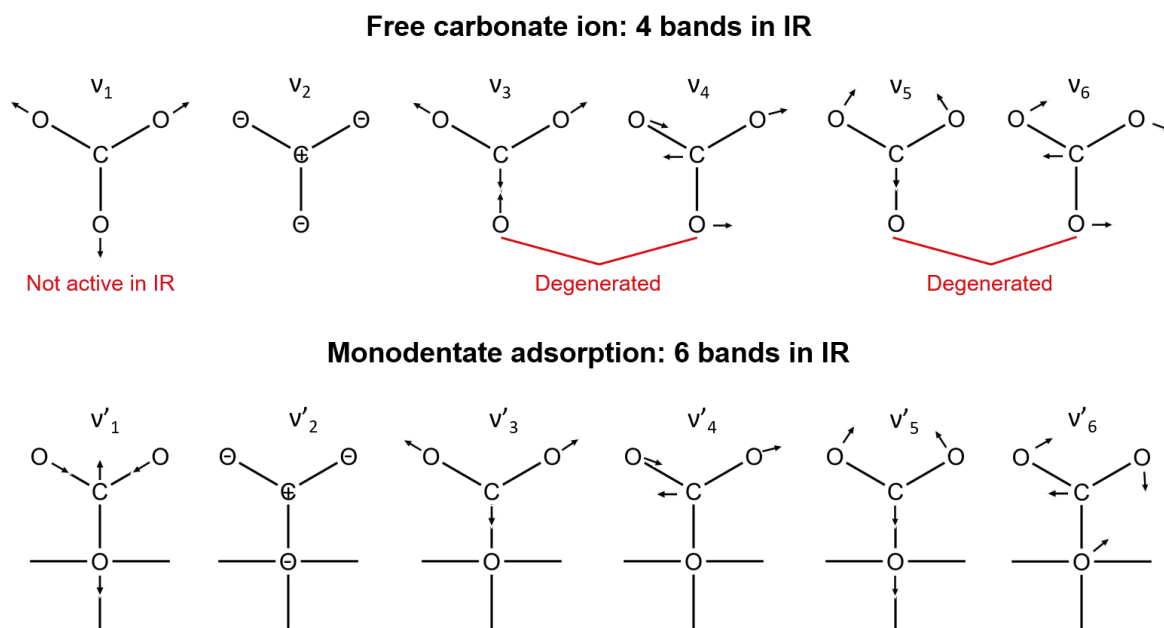


Figure 1: Vibration modes of the free carbonate ion and monodentate adsorbed carbonate. Adapted from Solis et al.<sup>3</sup>.

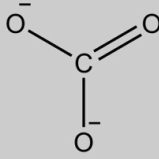
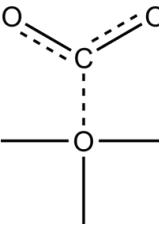
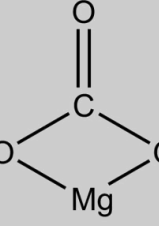
Wavenumber (cm <sup>-1</sup> )	Attribution	Vibration	
1420-1470	Carbonate ion	$\nu_3 + \nu_4$	
1020-1090		( $\nu_1$ not active in IR)	
860-880		$\nu_2$	
680-750		$\nu_5 + \nu_6$	
1470-1530	Monodentate carbonate	$\nu'_4$	
1300-1370		$\nu'_3$	
1040-1080		$\nu'_1$	
850-880		$\nu'_2$	
750-820		$\nu'_5$	
670-690		$\nu'_6$	
1590-1630	Bidentate carbonate		
1260-1270			
1020-1030			
830-840			
740-760			
660-680			

Table 1: IR wavelength of carbonate vibrations, adapted from Evans et al.<sup>2</sup> Vibrations are referring to Figure 1.

## 2. Modelling the adsorption of CO<sub>2</sub> on surfaces

Progress made in the field of modelling in the 90s allowed for better accuracy concerning the prediction of carbonate formation on surfaces. The latest were not considered like immovable anchors anymore, and the adsorption on different sites could be analysed. Most of the time it was still simple cases like perfect planes, perfect edges or perfect corners that were considered. But it still gave a better understanding on the adsorption modes of CO<sub>2</sub> on oxide surfaces. For example, Jensen et al.<sup>4</sup> showed that the monodentate adsorption on perfect MgO (100) planes was not energetically favourable, corners and edges were necessary to have a stable adsorption. The author acknowledged the fact that comparison between computed wavenumbers and experimental data was often impossible due to the fact that adsorption properties revolved around the presence of defects in the material.

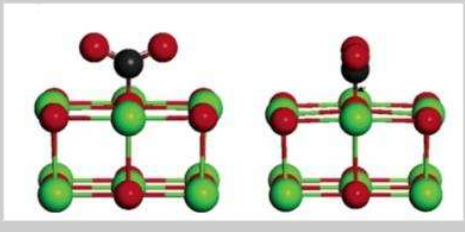
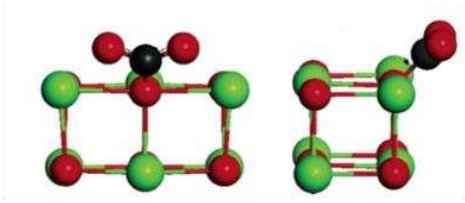
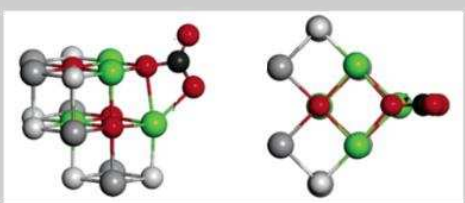
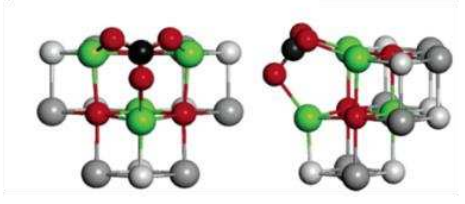
Wavenumber (cm <sup>-1</sup> )	Attribution	
1784	Monodentate carbonate, terrace	
1288		
827		
821		
1703		
1327	Monodentate carbonate, edge	
1011		
847		
1778	Bidentate carbonate, corner	
1243		
932		
847		
1451	Tridentate carbonate, corner	
1084		
906		

Table 2: IR wavelength of carbonate vibrations depending on the adsorption mode on a MgO surface, adapted from Jensen et al.<sup>4</sup>. Green and dark grey spheres corresponds to Mg atoms, red and light grey spheres to O atoms and black spheres to C atoms.

## II. Experimental section

*Note: all the details concerning the suppliers and the purity of chemical products are given in the Appendix.*

### Adsorption of CO<sub>2</sub> on nanoparticles

The reaction was performed in a 25 mL glass autoclave. All the glassware was dried for one night in a 120 °C oven before usage. Inside an argon glovebox, MgO (20 mg, 0.5 mmol, 1 equivalent) was introduced. We closed the autoclave and got it out of the glovebox. We connected the autoclave to a vacuum-gas system where we made two vacuum/CO<sub>2</sub> (1 bar) cycles before putting 7 bars of CO<sub>2</sub> (10 mmol, 20 equivalents) in the autoclave. The autoclave was then put in an oil bath and heated at the desired temperature. We let the reaction going overnight. Once the reaction was finished, we opened the autoclave in the glovebox and analysed the powder using ATR. The nanoparticles were not exposed to air in the process.

### Colloidal stability tests in solvents

The reaction was made in 2 mL vials. All the glassware was dried for one night in a 120 °C oven before usage. Inside an argon glovebox, toluene (0.5 mL, 4.5 mmol, 19 equivalents), MgO (10 mg, 0.2 mmol, 1 equivalent) and BPh<sub>3</sub> (1.2 mg, 9.4E-3 mmol, 0.04 equivalents) were introduced. The solution was heated at 80 °C under a heating plate for 10 minutes. The solution was then sonicated for 30 seconds and let to rest. We observed regularly the dispersion of the nanoparticles in the solution to estimate the time it took to sediment.

### Adsorption of BPh<sub>3</sub> on nanoparticles with evaporation of the solvent

The reaction was performed in a 25 mL glass autoclave. All the glassware was dried for one night in a 120 °C oven before usage. Inside an argon glovebox, toluene (1 mL, 9 mmol, 19 equivalents), MgO (20 mg, 0.5 mmol, 1 equivalent) and BPh<sub>3</sub> (2.4 mg, 1.9E-2 mmol, 0.04 equivalents) were introduced. We closed the autoclave and got it out of the glovebox. The autoclave was then put in an oil bath and heated at 60 °C. We let the reaction going for 1 hour. Once the reaction was finished, we evaporated the toluene by putting the autoclave under vacuum for 1 hour. Once the toluene was evaporated, we opened the autoclave in the glove box and analysed the powder using ATR.

### Adsorption of borane on nanoparticles with centrifugation of the nanoparticles

The reaction was performed in a 25 mL glass autoclave. All the glassware was dried for one night in a 120 °C oven before usage. Inside an argon glovebox, toluene (1 mL, 9 mmol, 19 equivalents), MgO (20 mg, 0.5 mmol, 1 equivalent) and the borane (1.9E-2 mmol, 0.04 equivalents) were introduced. Borane tested were BPh<sub>3</sub>, tris(pentafluorophenyl)borane, BEt<sub>3</sub>, BCl<sub>2</sub>Ph and B(OH)<sub>2</sub>Ph. We closed the autoclave and got it out of the glovebox. We let the reaction going for 1 hour. Once the reaction was finished, centrifuged the solution at 9000 rpm for

10 minutes. We isolated the precipitated nanoparticles and let them to dry under inert atmosphere overnight. Once the nanoparticles were dried, we analysed the powder using ATR.

### **Adsorption of CO<sub>2</sub> on MgO+borane powders**

The reaction was the same as the adsorption of CO<sub>2</sub> on MgO nanoparticles, but we only put 10 mg of the nanoparticles-borane powder in the autoclave.

### III. Surface carbonates on MgO nanoparticles

#### 1. MgO nanoparticles after the synthesis and impact of air exposition

In Chapter III, we observed the modification of the IR spectrum of MgO nanoparticles stored under ambient air. This was mainly due to the interaction with CO<sub>2</sub> and H<sub>2</sub>O. We were interested in understanding how our MgO nanoparticles and CO<sub>2</sub> interacted since it could be interesting for future catalytic studies. We started by studying MgO nanoparticles synthesized by precipitation-calcination without extra washing steps and calcined at 500 °C. We analysed more precisely the evolution of the IR spectrum to see what was the type of surface carbonates forming on the surface of the nanoparticles. To do so, we deconvoluted the part of the IR spectrum associated to carbonate vibration most sensitive to the adsorption mode, i.e. the region between 1250 and 1650 cm<sup>-1</sup>. As shown above, it was in this region that the difference between different types of carbonates was the most visible. The other zones were easier to analyse and we decided not to spend too much time in their deconvolution. We deconvoluted the using pseudo-Voigt functions, as it was done by Reilly et al.<sup>5</sup>.

First, we analysed the two IR spectra presented in Chapter III: the one corresponding to fresh MgO nanoparticles and the one measured after 3 weeks exposition to air (Figure 2:a). Figure 2:b and c showed the result of the deconvolution, with a table summarizing the position and the intensity of the bands in Figure 2:d. We kept the acquisition parameter constants so that the measurement of the intensity of the different bands could be compared from one measurement to another. Most of the time, we only used it to determine which were the main bands in a spectrum.

We could see first that the intensity of the main bands increased after the carbonation under ambient air. More interestingly, we could see that the positions of the bands were not the same. For the nanoparticles right after the synthesis, we found 3 components at 1382, 1454 and 1526 cm<sup>-1</sup>. From what we understood in the introduction of the chapter, a free carbonate ion should only have one band in the domain while adsorbed carbonates would have two bands (with the notable exception of tridentate carbonate on corner sites). The two bands at 1382 and 1526 cm<sup>-1</sup> could correspond to monodentate carbonates, while the peak at 1454 cm<sup>-1</sup> could correspond to either free carbonate ions (residual from the synthesis, basic conditions favoured the formation of CO<sub>3</sub><sup>2-</sup> in solution) or tridentate carbonates adsorbed on corners.

After ambient air exposition, two main bands were detected at 1409 and 1493 cm<sup>-1</sup>, and a minor band was detected at 1659 cm<sup>-1</sup>. The main bands could correspond to monodentate carbonates, and the minor one could be attributed to bidentate carbonates. If bidentate carbonates were present, we should have also detected a minor vibration band around 1260 cm<sup>-1</sup>. Since the contribution would have been minor, it was possible that this band was hidden under the main band at 1493 cm<sup>-1</sup>.

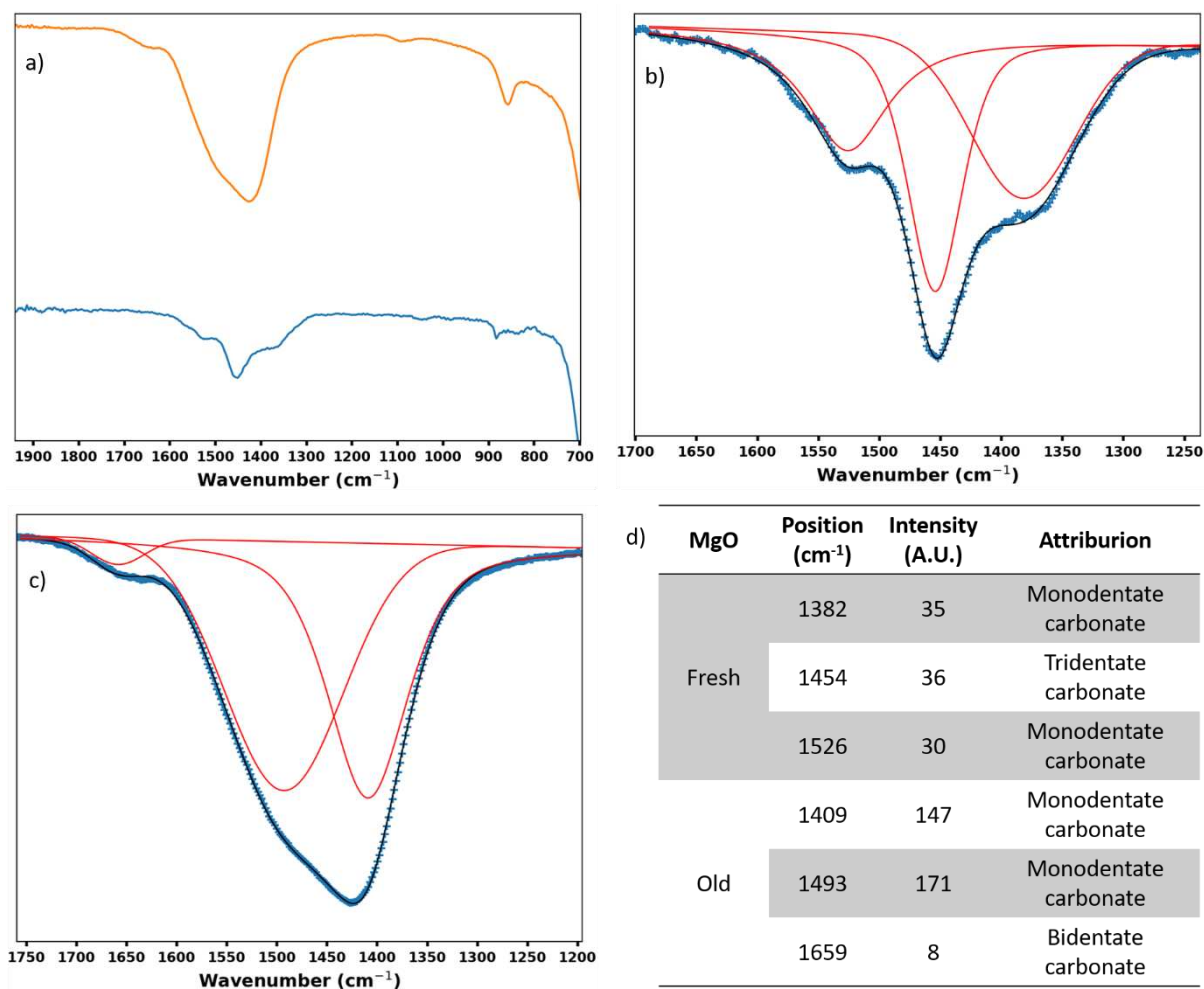


Figure 2: a) IR spectra of the nanoparticles freshly synthesized (blue) and after 3 weeks under air (orange), b) deconvolution of the carbonate band (1250 cm<sup>-1</sup>-1700 cm<sup>-1</sup>) of the fresh MgO IR spectrum, c) deconvolution of the carbonate band (1250 cm<sup>-1</sup>-1700 cm<sup>-1</sup>) of the aged MgO IR spectrum, d) table with the information concerning the different bands.

Air exposition increased the amount of bidentate carbonates on MgO nanoparticles due to the CO<sub>2</sub> present in ambient air. The band at 1454 cm<sup>-1</sup> that we associated to tridentate carbonate disappeared or was hidden behind the monodentate carbonate signal. We could make the following hypothesis: less sites were available for tridentate carbonate formation so the corresponding band could not increase much and was hidden under the monodentate carbonate signal.

## 2. Variability in MgO IR spectrum

As mentioned in the Chapter III, we observed a variability in the shape of the carbonate signal (1250 cm<sup>-1</sup>-1700 cm<sup>-1</sup>) between the different batches of MgO we synthesized. To understand if this was due to different types of carbonates present at the surface of the particles,



we applied the same methodology and deconvoluted the different spectra (Annexe 1). We observed that even if the spectra were different, there was a similar pattern in most of them (Figure 3:). The signal was composed of three main bands which position varied between the samples. The most intensive bands were located between 1400 and 1450  $\text{cm}^{-1}$ , and the two others were respectively positioned between 1360 and 1395  $\text{cm}^{-1}$  for the first one and between 1510 and 1540  $\text{cm}^{-1}$  for the second one.

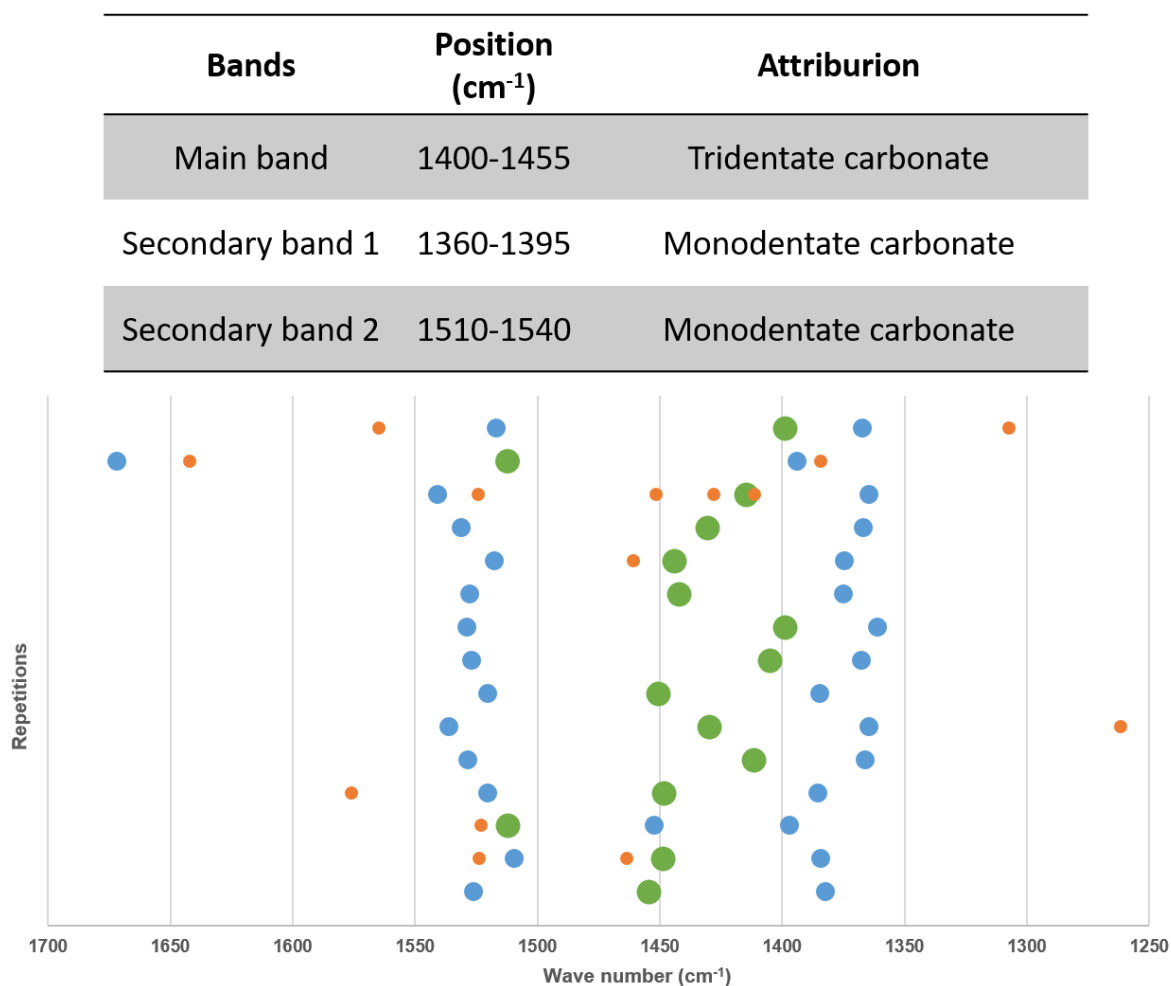


Figure 3: a) Position and attribution of the three most intense IR carbonate bands in MgO after synthesis, b) Representation of the position of the different IR bands in the carbonate signal for the different repetitions. The most intensive band were shown by the green dots, the second and the third most intensive bands were represented by blue dots, and the other bands were represented by orange dots.

Just like in Figure 2:b, these main bands could be attributed to monodentate carbonates (1360-1395  $\text{cm}^{-1}$  and 1510-1540  $\text{cm}^{-1}$ ) and to either free carbonate ion or tridentate carbonate (1400-1450  $\text{cm}^{-1}$ ) according to the literature. Minor bands were sometimes present, but they often represented less than 3 % of the intensity of the main band of the spectrum (Annexe 2). No clear trend was found concerning the position of these minor bands, but we could assume they corresponded to different types of monodentate or bidentate adsorption.

### 3. IR spectra of MgO<sub>washed</sub> and MgO<sub>1000</sub>

Since we believed that the IR spectrum of the MgO nanoparticles was related to the surface state through the formation of different type of carbonates, we wanted to compare the different MgO nanoparticles we had to if any difference was visible. We applied the same methodology to both MgO<sub>1000</sub> and MgO<sub>washed</sub> (Figure 4:). Interestingly, the IR carbonate band were weaker in MgO<sub>1000</sub> and MgO<sub>washed</sub> than in the previous MgO samples (Figure 4:a). The carbonate signal in MgO<sub>1000</sub> was broad and could be deconvoluted in two bands at 1508 and 1416 cm<sup>-1</sup> (Figure 4:b). They could be associated to the presence of monodentate carbonates. The carbonate signal in MgO<sub>washed</sub> was more defined and could be deconvoluted in seven bands as described in Figure 4:c. These bands could be attributed to a mix of monodentate, bidentate and tridentate carbonates.

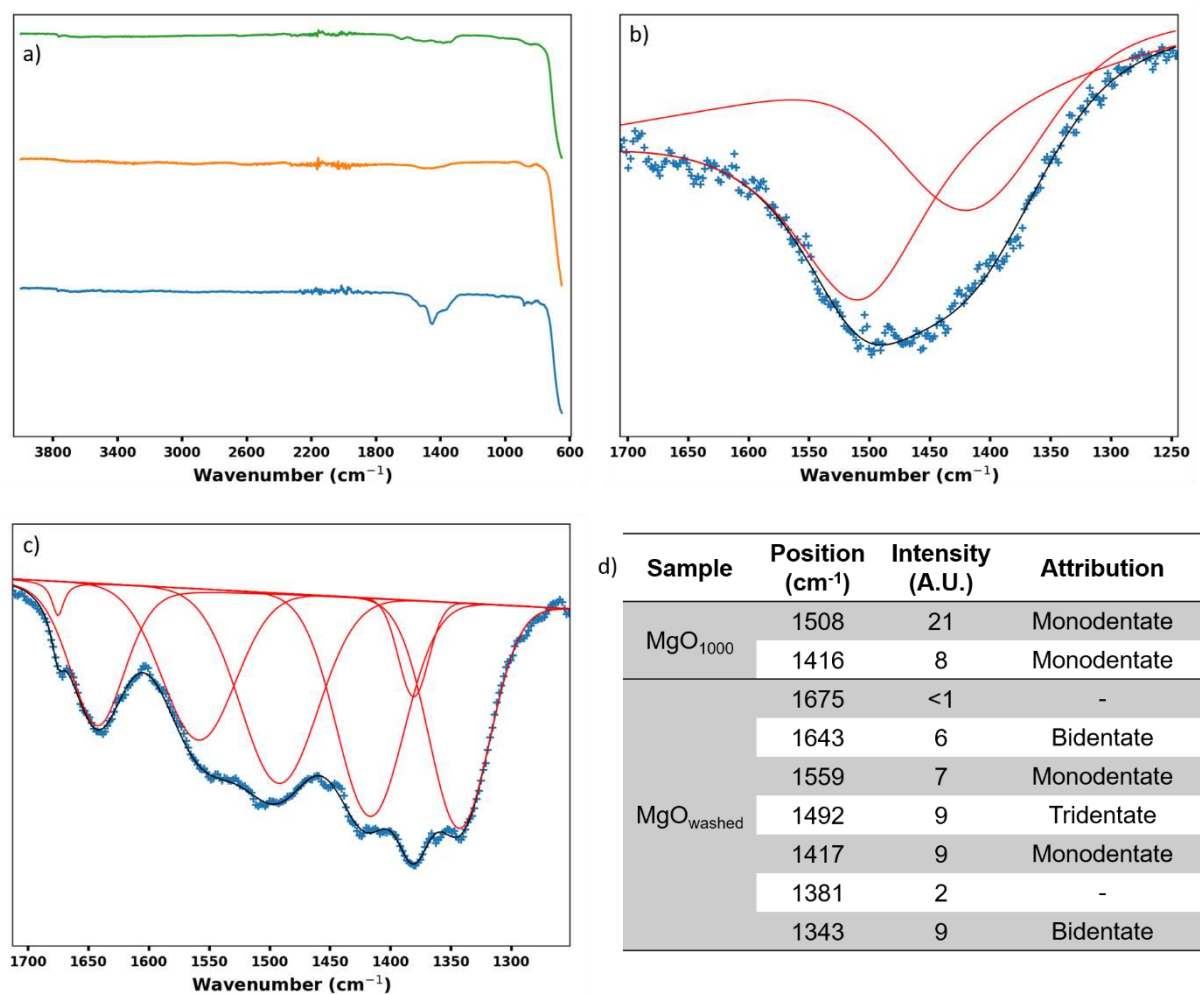


Figure 4: a) IR spectra of MgO (blue), MgO<sub>1000</sub> (orange) and MgO<sub>washed</sub> (green). b) Deconvolution of the carbonate band (1250 cm<sup>-1</sup>-1700 cm<sup>-1</sup>) of MgO<sub>1000</sub> IR spectrum. c) Deconvolution of the carbonate band (1250 cm<sup>-1</sup>-1700 cm<sup>-1</sup>) of MgO<sub>washed</sub> IR spectrum. d) Table with the positions, intensities and attributions of the different IR carbonate bands.

The fact that the carbonate signal was weaker in MgO<sub>1000</sub> than in MgO<sub>500</sub> could be explained by the lower surface area of the nanoparticles. Since there was less available surface, less surface

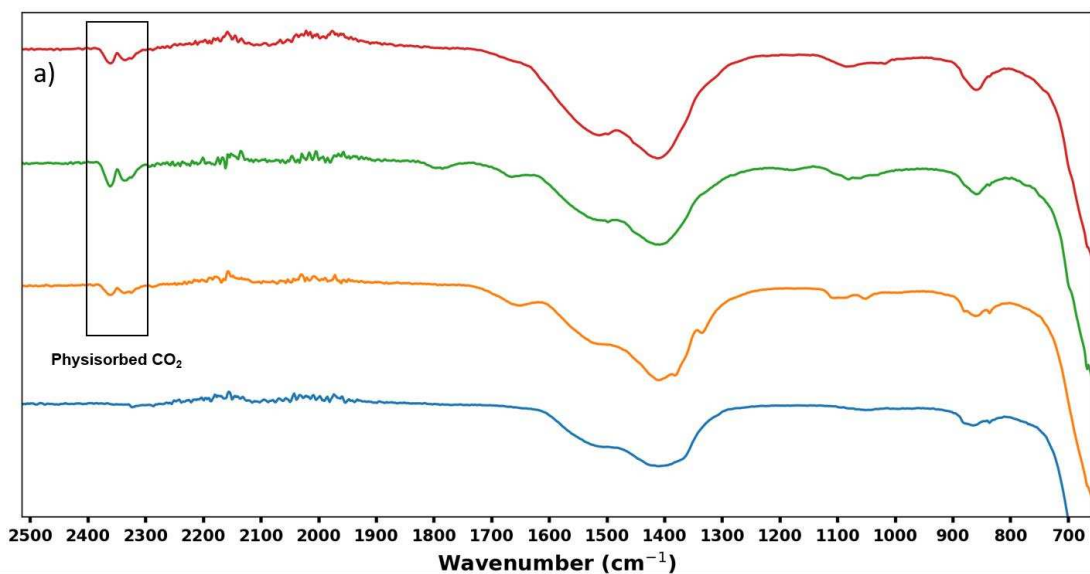
carbonates were formed. When we compared the position of the bands, the two detected in  $\text{MgO}_{1000}$  could correspond to two of the main bands in  $\text{MgO}_{500}$ . We could make the following hypothesis: calcining at low temperatures (500 °C) favoured the formation of corner sites where a tridentate adsorption was possible.

For  $\text{MgO}_{\text{washed}}$ , the surface area of the nanoparticles could not explain the difference in carbonate intensity (we expected the surface area of  $\text{MgO}_{\text{washed}}$  to be higher than the one of MgO). The difference of surface state could influence the carbonation rate of the nanoparticles during the calcination. The cleaner surfaces of  $\text{Mg}(\text{OH})_{2\text{washed}}$  nanoparticles were less subject to sintering and maybe to carbonation. The carbonate signal of  $\text{MgO}_{\text{washed}}$  was more complex than the one of MgO. The detected bands could be attributed to a mix of monodentate, bidentate and tridentate carbonates. These differences could be explained by cleaner surfaces allowing different types of carbonates to be present on the surface of the nanoparticles.

#### 4. Carbonation of MgO nanoparticles under pure $\text{CO}_2$

After these experiments, we had a better understanding of the types of carbonates present on the surface of the MgO nanoparticles right after their synthesis. However, as we saw with the nanoparticles that were carbonated due to storage in ambient air, the carbonates that formed when the nanoparticles were exposed to  $\text{CO}_2$  were not the same (no more tridentate adsorption). We decided to study the impact of  $\text{CO}_2$  exposition on the carbonate signal of MgO nanoparticles. We still studied in detail the zone between 1250 and 1700  $\text{cm}^{-1}$  since it was the zone where changes were the most visible.

We exposed the MgO powder to  $\text{CO}_2$  without any solvent, as described in the experimental part. We used 7 bar of  $\text{CO}_2$  and did the experiment at room temperature, at 80 °C, and at 150 °C. Results were shown in Figure 5:. Each experiment was repeated three times and we obtained repeatable results. Deconvolution was used to identify the position of the main bands, but the smaller ones were pointed directly on the spectra to reduce the time required to analyse the data.



b)	Sample	Position( $\text{cm}^{-1}$ )	Attribution
	MgO	1528	Monodentate
		1412	Tridentate
		1366	Monodentate
		1658	Bidentate
	MgO+CO <sub>2</sub> RT	1533	Monodentate
		1407	Tridentate
		1382	-
		1376	Monodentate
	MgO+CO <sub>2</sub> 80 °C	1336	Bidentate
		1789	-
		1667	Bidentate
		1526	Monodentate
		1498	-
		1405	Tridentate
	MgO+CO <sub>2</sub> 150 °C	1303	Monodentate
		1676	Bidentate
		1524	Monodentate
		1498	-
		1403	Tridentate
		1321	Monodentate

Figure 5: a) IR spectra of the zone of interest of MgO (blue), MgO+CO<sub>2</sub> at RT (orange), MgO+CO<sub>2</sub> at 80 °C (green) and MgO+CO<sub>2</sub> at 150 °C (red). b) Table of the position and attribution of the different bands in the carbonate zone between 1250 and 1800  $\text{cm}^{-1}$  (green color indicated the most intense band and blue color indicated the the second and third most intense bands).

The experiments made at different temperatures had similarities: we could see the apparition of new bands while the main ones already present were retained. We detected physisorbed CO<sub>2</sub> with its bands at 2362 and 2335 cm<sup>-1</sup> in all the experiments (Figure 5:a). The initial main band at 1412 cm<sup>-1</sup> was still detected with a slight shift toward the lower wave numbers (Figure 5:b). The band initially at 1528 cm<sup>-1</sup> was still detected at approximately the same position. The band at 1366 cm<sup>-1</sup> reduced in intensity and was displaced toward smaller wavenumbers at high temperature. We also observed the apparition of new secondary bands with the exposition of CO<sub>2</sub>. Some were common to the experiment at RT and 80 °C, or at 80 °C and 150 °C, and some others only were present at certain temperatures. We proposed the an attribution in Figure 5:b.

This measurement method had its limits since we were not making the measurements in situ. We only could detect carbonates forming at a certain temperature and stable when returning to room temperature. Making the study using techniques such as Diffuse Reflectance infrared Fourier Transform spectroscopy (DRIFT) would bring an even greater understanding of the MgO carbonatation process.

## IV. Adsorption of boranes

The second part of this chapter was focused on the adsorption of boranes on the surface of MgO nanoparticles. First, we wanted to see if borane molecules could adsorb on the surface of MgO, and then we wondered if the carbonate formation at the surface of the nanoparticles would be impacted by the presence of borane ligands.

### 1. Adsorption of BPh<sub>3</sub> on MgO in toluene

#### a. Impact of BPh<sub>3</sub> addition on colloidal stability of MgO suspension

To have a qualitative information on the affinity of borane ligands toward MgO we did a colloidal stability test. We decided to start with BPh<sub>3</sub> since it was a borane often used in FLP chemistry with steric hindrance and moderate Lewis acidity (see Chapter 2). We mixed MgO nanoparticles with and without BPh<sub>3</sub> in different toluene and observed the time it took for the colloidal suspension to sediment. The exact protocol was described in the experimental part.

We could see that 10 minutes after we made the suspension, the suspension without BPh<sub>3</sub> already sedimented whereas the suspension with BPh<sub>3</sub> was stable (Figure 6:a). This suspension was stable for 2 hours before we saw the nanoparticles sediment. When we looked at the TEM grids made with these suspensions, we could see that the nanoparticles in toluene without the borane were aggregated in big objects with a characteristic size of the order of 1  $\mu\text{m}$  (Figure 6:b). When BPh<sub>3</sub> was present, the aggregates were much smaller with a characteristic size of 100 nm (Figure 6:c). Even if TEM micrographs were not always representative of the dispersion state of the nanoparticles in suspension due to aggregation during the grid preparation (evaporation of the solvent), we believed that these different aggregate sizes were representative of the solutions and explained the different colloidal stability. DLS measurements could help provide a more accurate answer.

This result indicated that BPh<sub>3</sub> helped to stabilize MgO suspension in toluene, probably through surface coordination (Figure 6:d).

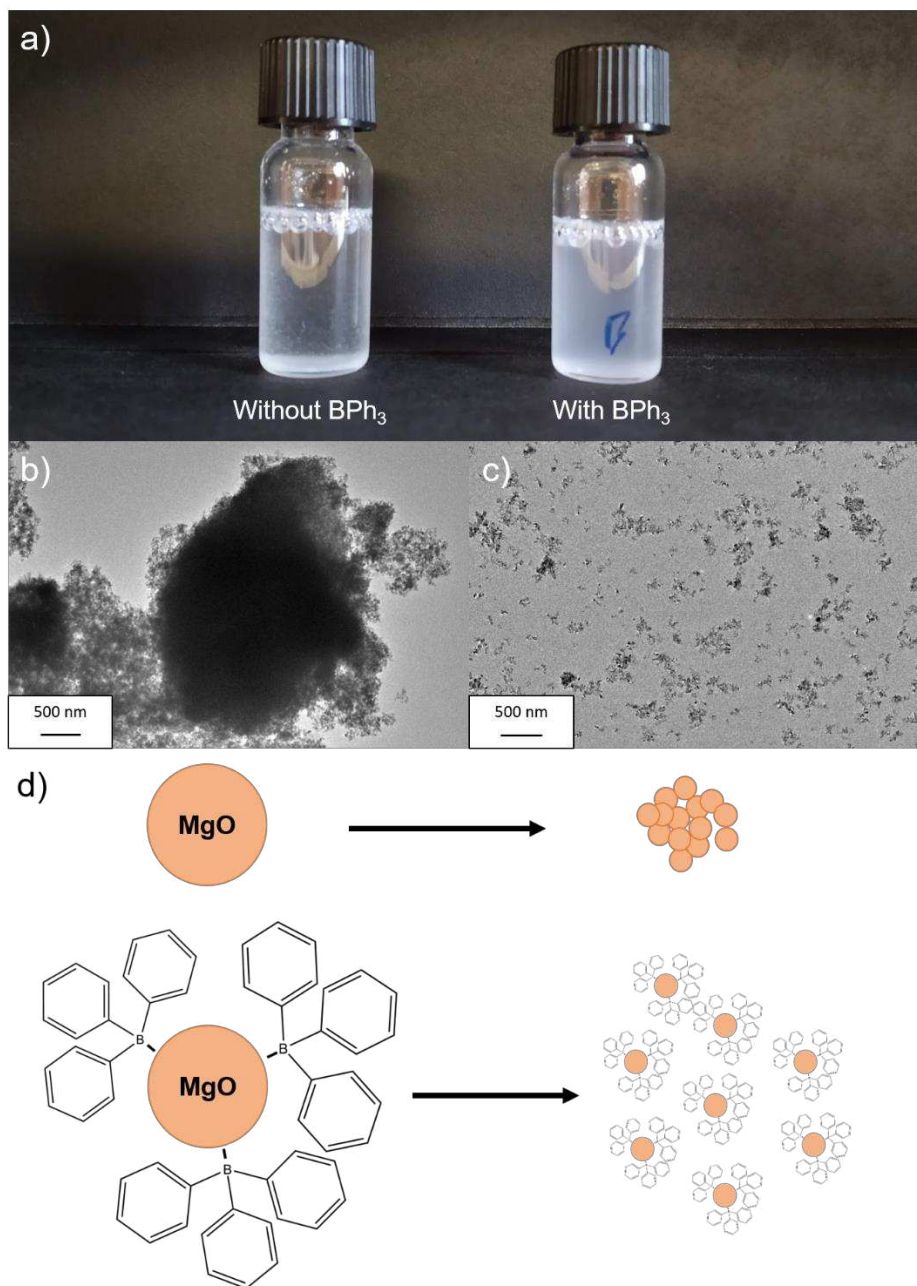


Figure 6: a) Colloidal stability of the MgO suspension in toluene with and without BPh<sub>3</sub> after 10 minutes. b) TEM micrograph of the suspension without BPh<sub>3</sub>. c) TEM micrograph of the suspension with BPh<sub>3</sub>. d) Hypothesis of BPh<sub>3</sub> coordination on MgO surface explaining the improved colloidal stability in toluene.

## b. Infrared study of the adsorption of BPh<sub>3</sub> on MgO

Now that we had a good indication that BPh<sub>3</sub> coordinated MgO nanoparticles in toluene, we wanted to see if IR spectroscopy could provide us information on the type of coordination: was there formation of a B—O bond? Were there Van der Waals interactions? etc.

We decided to prepare the suspension of  $\text{MgO}+\text{BPh}_3$  in the same way we did previously. The toluene was then evaporated and we analysed the residual powder via IR-spectroscopy. The measurement was made in the inert glovebox, the samples were not exposed to air in the process. Detailed protocol was described in the experimental part. We expected to observe the signal of the  $\text{MgO}$  nanoparticles and of  $\text{BPh}_3$  since the evaporation of the solvent did not remove the borane. We hoped to see the apparition of new IR band that we could attribute either to a B—O vibration or to a loss of symmetry of the  $\text{BPh}_3$  molecule due to its adsorption on  $\text{MgO}$  nanoparticles (detailed  $\text{BPh}_3$  reference IR spectrum was given in Annexe 3).

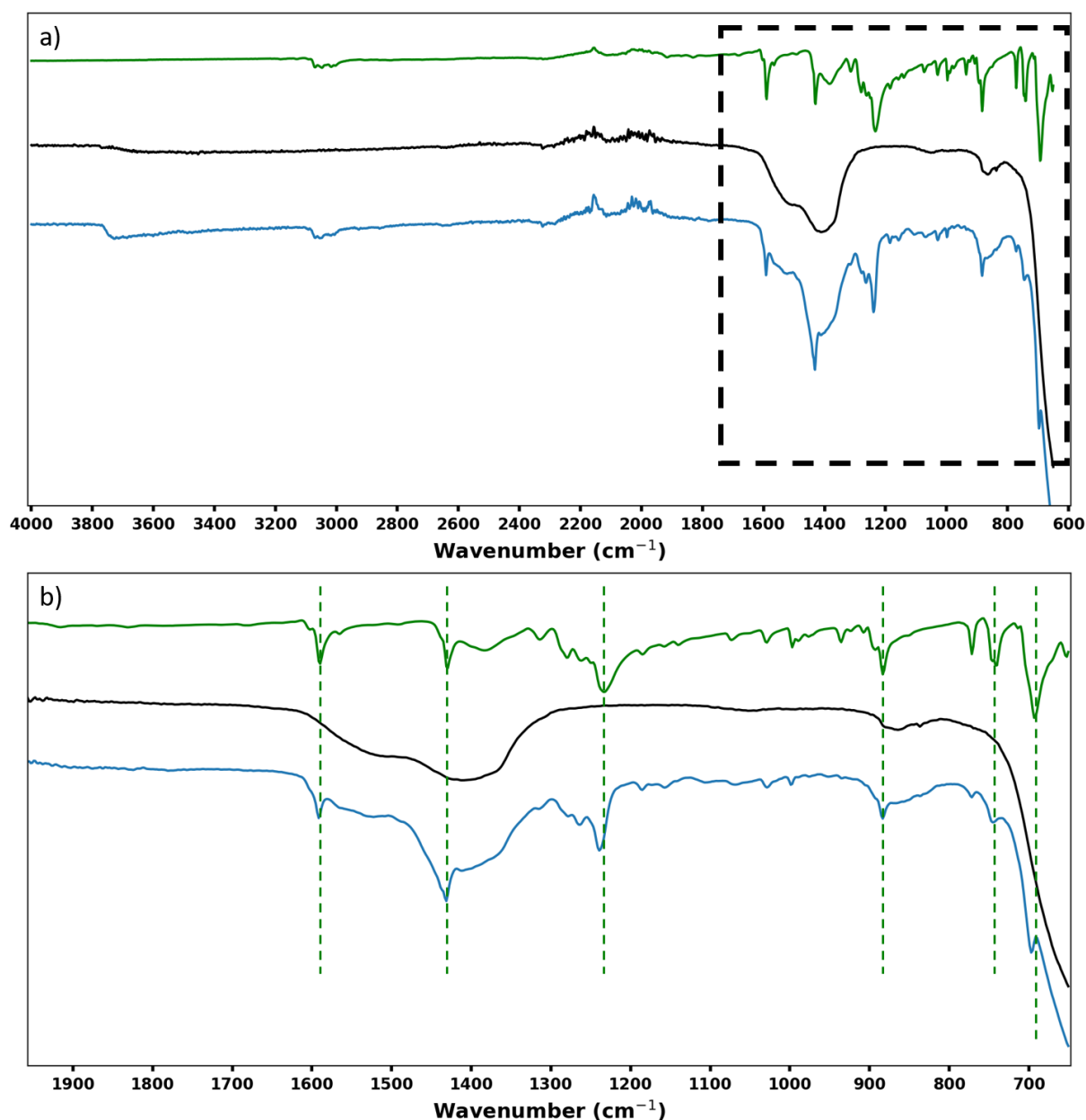


Figure 7: IR spectra of the powder  $\text{MgO}+\text{BPh}_3$  after toluene evaporation (green:  $\text{BPh}_3$  reference, black:  $\text{MgO}$  reference, blue:  $\text{MgO}+\text{BPh}_3$ ). a) Full spectrum. b) Zoom on the 600-1700  $\text{cm}^{-1}$  zone. Green dotted lines indicate the main bands of molecular  $\text{BPh}_3$ .



Figure 7: showed the IR spectra resulting of the adsorption. Due to the complexity of the IR spectra, we did not manage to deconvolute them. Instead, we used classical peak picking to analyse the data. We observed that the spectrum of the final powder after the adsorption of BPh<sub>3</sub> on MgO was the sum of the spectrum of MgO and the spectrum of BPh<sub>3</sub>. We only saw two differences:

- the apparition of a broad band at 3700 cm<sup>-1</sup> that might correspond to O—H elongation vibration
- a slight shift of the B—C elongation band toward higher wavenumbers (a 5 cm<sup>-1</sup> shift) that might not be significant.

IR spectroscopy did not allow to detect the adsorption of the borane in these conditions. Maybe the coordination of the borane was enhanced by the apolar solvent: after toluene evaporation the bond between MgO and BPh<sub>3</sub> became weaker and undetectable. Or maybe the interaction between BPh<sub>3</sub> and MgO was too weak to be detected in the first place.

### c. Infrared study of the adsorption of BPh<sub>3</sub> and CO<sub>2</sub> on MgO

To conduct the study to its end, we decided to expose the powder containing MgO+BPh<sub>3</sub> (after toluene evaporation in the adsorption experiment) to 6 bar of CO<sub>2</sub> at room temperature for one night (15 hours). Even if the adsorption of BPh<sub>3</sub> on MgO was not detected, maybe the addition of CO<sub>2</sub> would cause the formation of a MgO—CO<sub>2</sub>—BPh<sub>3</sub> specie that might have an IR signature. Figure 8: showed the IR spectra of the MgO+BPh<sub>3</sub> powder after its exposition to CO<sub>2</sub>. The spectrum was very similar to the one obtained after the previous experiment (adsorption of BPh<sub>3</sub> on MgO). However, we spotted four differences:

- the apparition of the physisorbed CO<sub>2</sub> bands at 2362 cm<sup>-1</sup> and 2335 cm<sup>-1</sup>
- a shift of the C—C phenyl elongation bands toward higher wavenumbers (13 cm<sup>-1</sup> difference)
- the apparition of a large band between 1250 and 1400 cm<sup>-1</sup> (red square in Figure 8:b)
- the disappearing of the B—C band at 1240 cm<sup>-1</sup>

We decided to deconvolute these new peaks between 1250 and 1400 cm<sup>-1</sup>, assuming a linear background, to have a rough estimation of how many new bands appeared and what their respective wavenumbers were (Figure 9:a and b). We found 5 new bands with similar intensities at wavenumbers between 1383 and 1307 cm<sup>-1</sup>. This range of wavenumbers could correspond to C—O carbonate vibrations, B—C vibrations or B—O vibrations. These new bands were not present in the blanc reaction where we exposed BPh<sub>3</sub> to CO<sub>2</sub> under the same conditions.

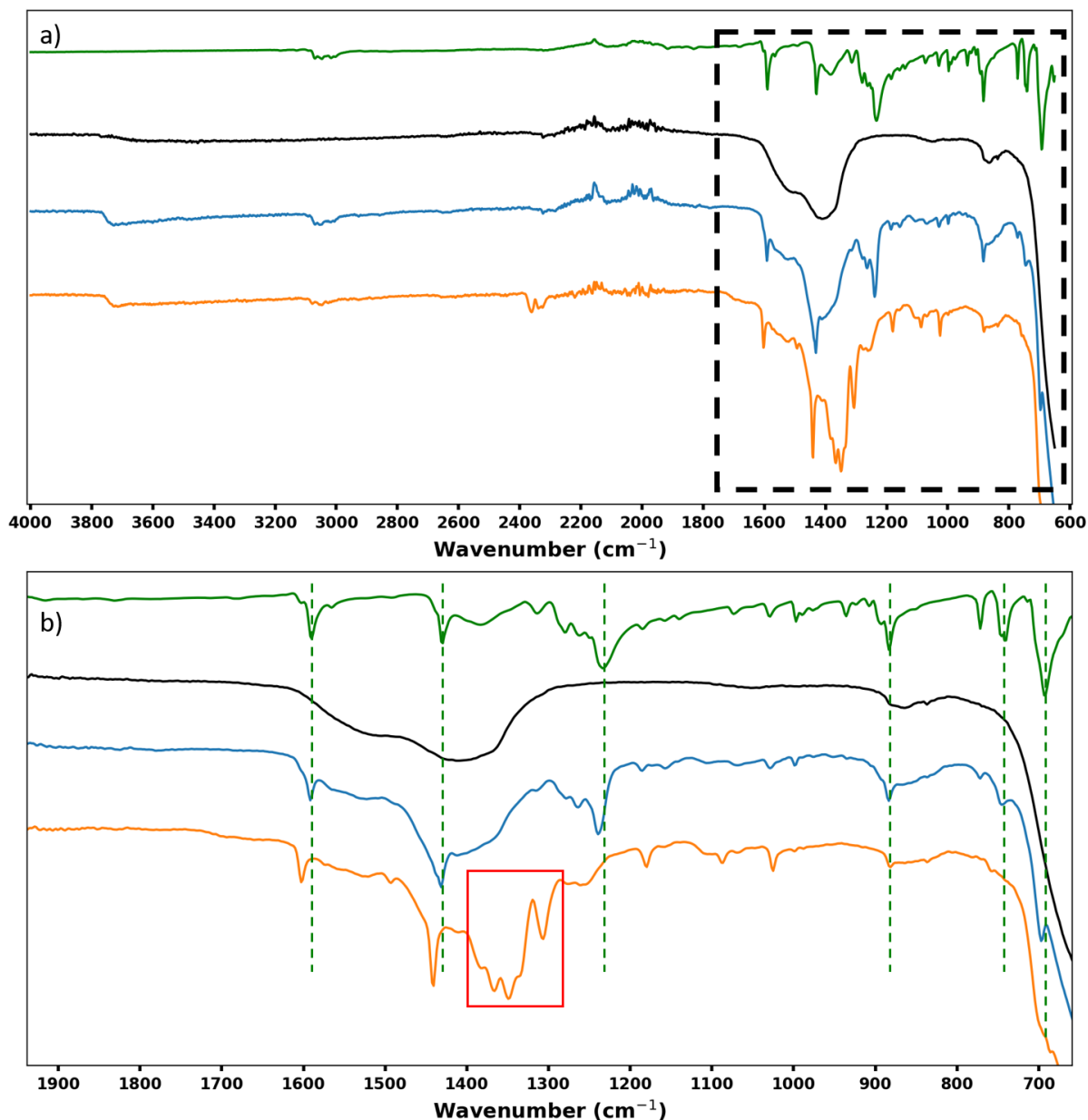


Figure 8: IR spectra of the powder  $\text{MgO}+\text{BPh}_3+\text{CO}_2$  (green:  $\text{BPh}_3$  reference, black:  $\text{MgO}$  reference, blue:  $\text{MgO}+\text{BPh}_3$ , orange:  $\text{MgO}+\text{BPh}_3+\text{CO}_2$ ). a) Full spectrum. b) Zoom on the 600-1700  $\text{cm}^{-1}$  zone. Green dotted lines indicate the pics of molecular  $\text{BPh}_3$ .

It appeared that the exposition of the  $\text{MgO}+\text{BPh}_3$  powder to  $\text{CO}_2$  modified the B—C vibration of  $\text{BPh}_3$  molecules. The fact that the blank with only  $\text{BPh}_3$  and  $\text{CO}_2$  did not react indicated that this modification was due to the presence of  $\text{MgO}$ . The disappearing of the B—C band and the apparition of the new peaks between 1300 and 1400  $\text{cm}^{-1}$  were probably linked. Maybe the presence of  $\text{CO}_2$  allowed the formation of a  $\text{MgO}-\text{CO}_2-\text{BPh}_3$  specie where the borane was more strongly adsorbed than in the case of its adsorption on  $\text{MgO}$  alone. The phenyl vibrations would also be impacted by the B—O bands, explaining their shift.

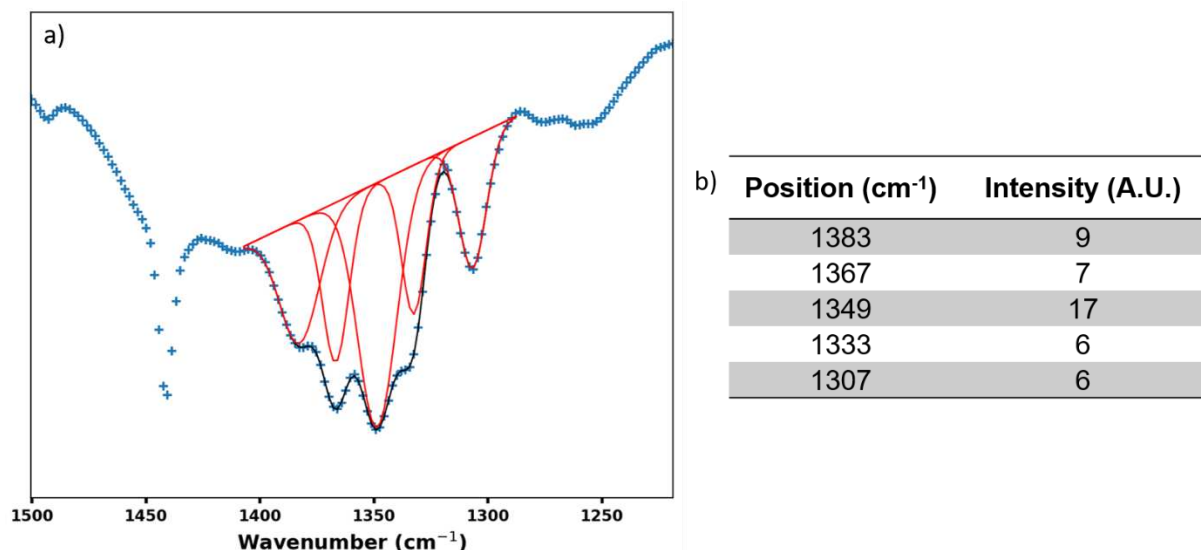


Figure 9: a) Deconvolution of the zone between 1285 and 1405 cm<sup>-1</sup> where new peaks appeared.  
b) Position and intensity of the new peaks.

## 2. Borane screening

Given the results we obtained with BPh<sub>3</sub>, we decided to do a screening over different borane and boron containing species to see if we observed similar results. We modified a little bit the experimental protocol as explained in the experimental part. Overall, the experiment stayed the same: adsorption of the boron containing species on MgO in toluene, isolation of the nanoparticles and finally exposition to CO<sub>2</sub> overnight. The only difference was the isolation of the nanoparticles by centrifugation instead of solvent evaporation. In this case we expected a weaker signal of the borane since some of it would be evacuated with the supernatant. We tested this new protocol with BPh<sub>3</sub>, BCF, BEt<sub>3</sub> and B(OH)<sub>2</sub>Ph. We also did the experiment with BCl<sub>2</sub>Ph but we will discuss these results in the next section. Results were displayed in Figure 10:

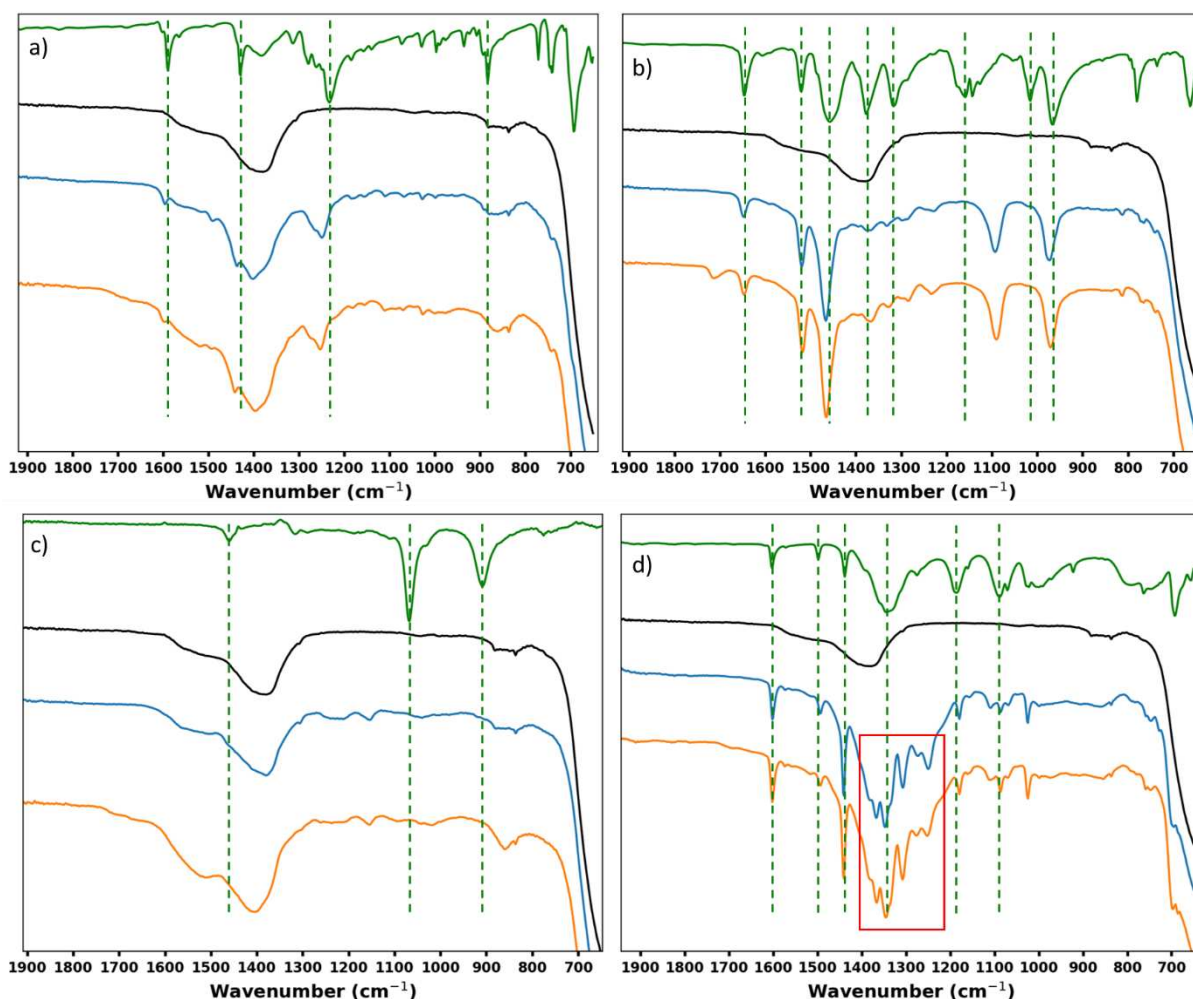


Figure 10: IR spectra of reference borane (green), reference MgO (black), MgO+borane (blue) and MgO+borane+CO<sub>2</sub> (orange), with a) BPh<sub>3</sub>, b) BCF, c) BEt<sub>3</sub> and d) B(OH)<sub>2</sub>Ph.

The reaction with BPh<sub>3</sub> did not yield new bands like previously (Figure 10:a). Maybe the remaining boranes after the solvent evaporation in the previous experiments played a role in the apparition of these IR bands. Here we only saw the adsorption of BPh<sub>3</sub> on the MgO surface with a slight shift of the BPh<sub>3</sub> bands.

The reaction with BCF (Figure 10:b) gave an interesting result where some of the bands were maintained, but the ones corresponding to B—C vibrations disappeared. When we added CO<sub>2</sub>, we observed the apparition of a new band at 1713 cm<sup>-1</sup> that could correspond to a C=O vibration.

The experiment with BEt<sub>3</sub> (Figure 10:c) showed only weak peaks, it was not obvious that the borane was still present on the MgO surface.

The experiment with B(OH)<sub>2</sub>Ph (Figure 10:d) showed the apparition of a signal around 1200 to 1400 cm<sup>-1</sup> that looked like the one observed with MgO+BPh<sub>3</sub>+CO<sub>2</sub> in the previous section. But these bands already appeared when we just mixed MgO and B(OH)<sub>2</sub>Ph without the CO<sub>2</sub>. Addition

of  $\text{CO}_2$  changed the intensities of certain of these bands. It could be that these peaks corresponded to a certain adsorption mode of the borane. Figure 11: showed propositions for the adsorption of either  $\text{BPh}_3 + \text{CO}_2$  or  $\text{B(OH)}_2\text{Ph}$ . We considered that the similarities of the IR spectrum in the zone between  $1200$  and  $1400\text{ cm}^{-1}$  could be due to the formation of a  $\text{Ph-B-O}_2\text{X}$  specie, with  $\text{B-O}_2\text{X}$  forming a four members ring. In the first case  $\text{X}=\text{C}$  and in the second case  $\text{X}=\text{Mg}$ . These were hypothetical propositions.

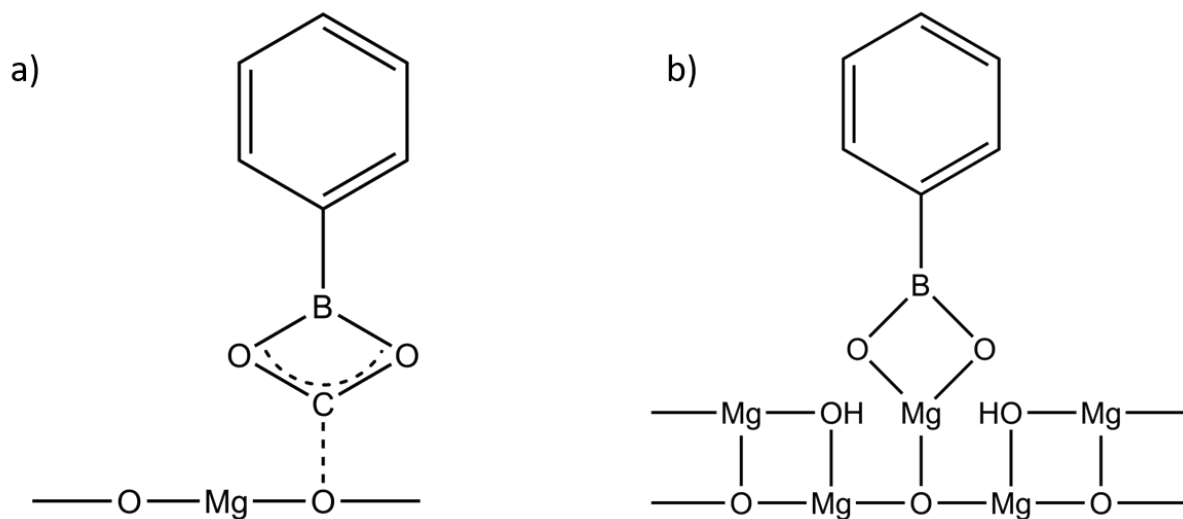


Figure 11: Proposition for the adsorption of: a)  $\text{CO}_2 + \text{BPh}_3$ , and b)  $\text{B(OH)}_2\text{Ph}$  on MgO surface.

### 3. Adsorption of $\text{BCl}_2\text{Ph}$ on $\text{MgO}$

We did the same experiment with the chloroborane  $\text{BCl}_2\text{Ph}$ . To our surprise, we observed a direct reaction between  $\text{MgO}$  nanoparticles and  $\text{BCl}_2\text{Ph}$ . When they were put in contact in toluene, the colour of the nanoparticles changed from white to dark brown (Figure 12:). At the end of the reaction, we centrifuged the solution and saw the supernatant was transparent while the sedimented nanoparticles were dark brown. We realised that the colour of the nanoparticles was air sensitive: when exposed to air they became light brown.

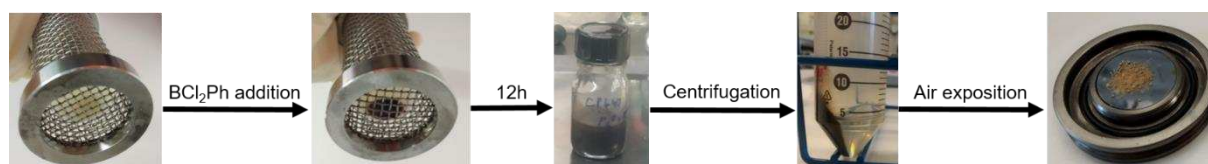


Figure 12: *MgO nanoparticles colour changes after exposition to  $\text{BCl}_2\text{Ph}$ .*

To understand the phenomenon, we decided to make IR and XRD analyses of the nanoparticles before and after exposition to air. IR results were displayed in Figure 13: and XRD results in Figure 13:.. The IR spectrum before the air exposition showed differences compared to the spectra of reference  $\text{BCl}_2\text{Ph}$  (Annexe) and  $\text{MgO}$ :

- shift of the C—H phenyl bands toward higher wavenumbers
- disappearance of the B—C band at  $1221\text{ cm}^{-1}$
- apparition of new peaks between  $1300$  and  $1400\text{ cm}^{-1}$

This was really similar to what we obtained for the adsorption of  $\text{BPh}_3+\text{CO}_2$  on  $\text{MgO}$  previously. When we exposed the nanoparticles to air, we saw the apparition of a broad signal between  $3000$  and  $3700\text{ cm}^{-1}$ , a zone usually characteristic to O—H vibrations. We also saw the modification of the zone between  $1000$  and  $1800\text{ cm}^{-1}$  where we observed a broad signal with bands at  $1420$  and  $1620\text{ cm}^{-1}$ .

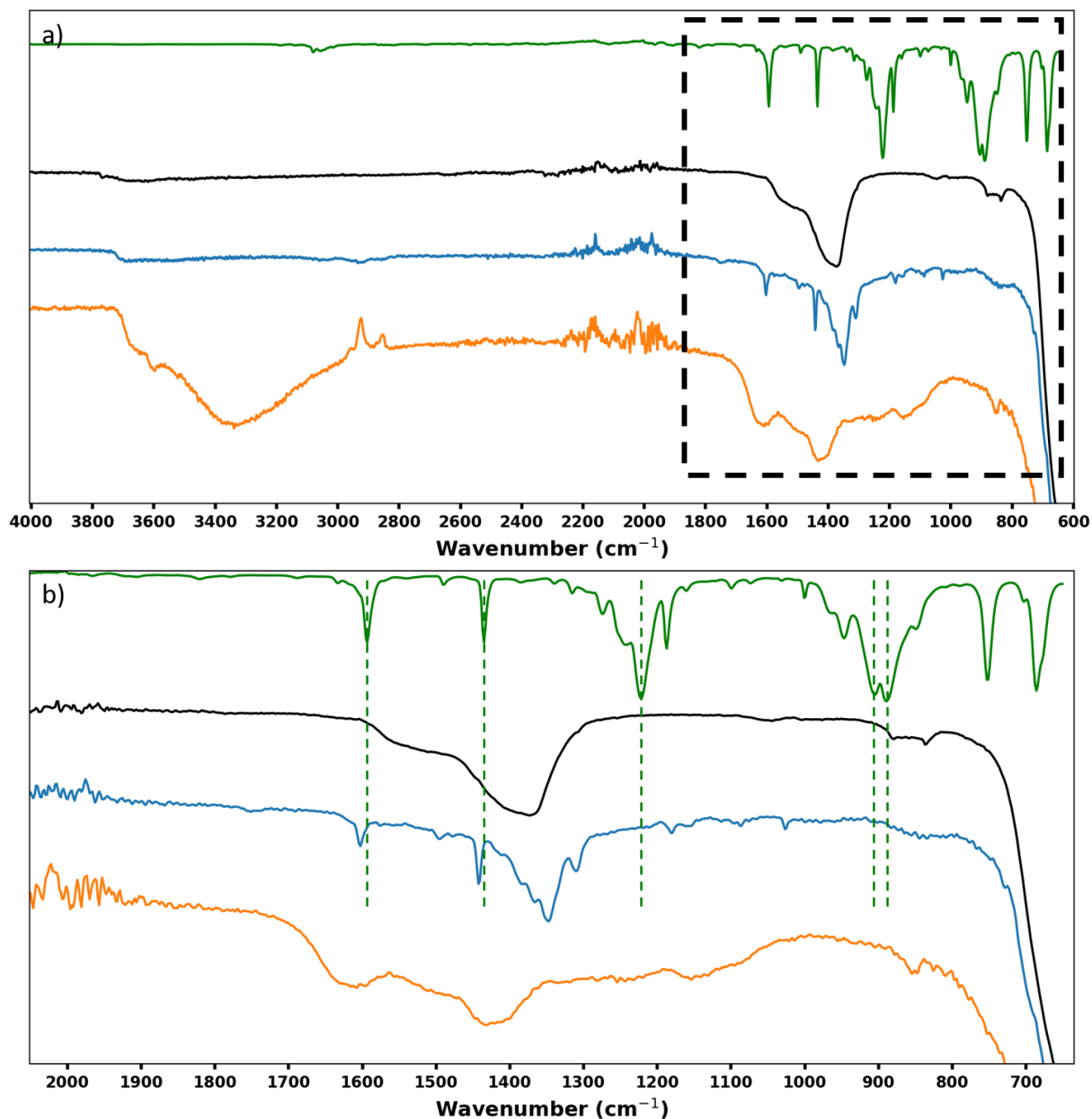


Figure 13: IR spectra of reference  $\text{BCl}_2\text{Ph}$  (green), reference  $\text{MgO}$  (black),  $\text{MgO}+\text{BCl}_2\text{Ph}$  before air exposition (blue),  $\text{MgO}+\text{BCl}_2\text{Ph}$  after air exposition (orange). a) Full spectra. b) Zoom on the 700-2000  $\text{cm}^{-1}$  zone.

XRD results were shown in Figure 14. When we measured the diffractogram of the nanoparticles under inert conditions, we only observed  $\text{MgO}$  peaks. The broad signal between 15 and 25  $^\circ$  was due to the plastic dome ensuring that the sample was not exposed to air. When we removed the dome, we observed the colour change from dark to light brown in about 20 seconds. We did the XRD measurement with the dome to compare with the previous measurement. We observed the apparition of a phase that we attributed to  $\text{NaCl}$ .

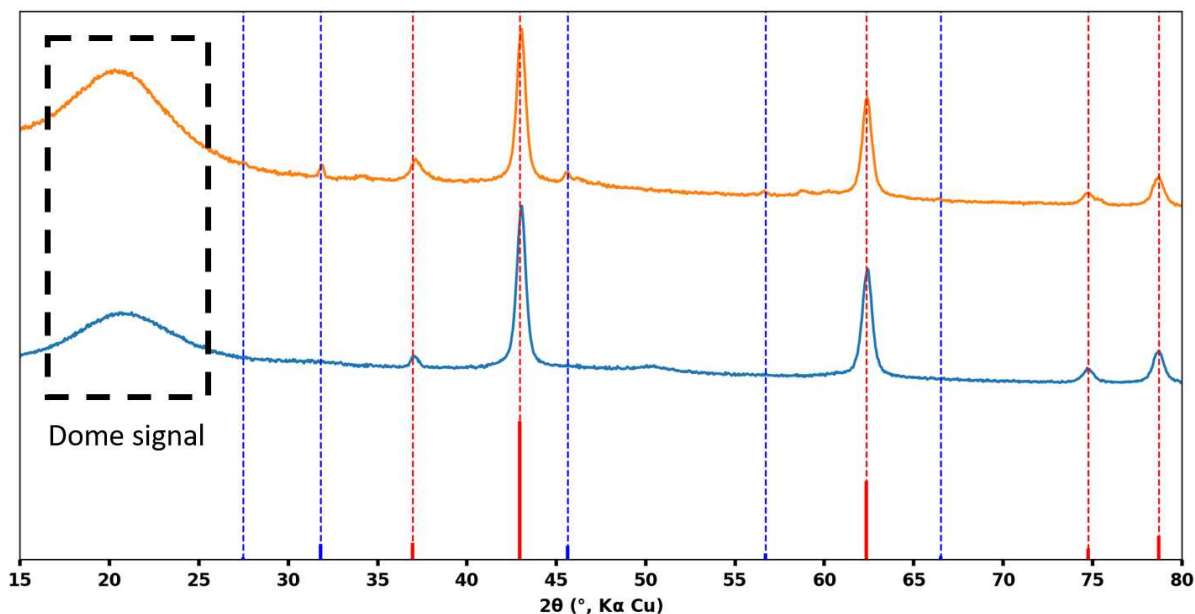


Figure 14: XRD diffractogram of  $MgO+BCl_2Ph$  before (blue) and after (orange) air exposition,  $MgO$  reference (red bars, PDF Card n°00-004-0829) and  $NaCl$  reference (blue bars, PDF Card n°00-005-0628).

The presence of  $NaCl$  in the final powder could be explained in the following way:

- $Na^+$  cations were present on the surface of  $MgO$  nanoparticles due to the use of  $NaOH$  during their synthesis. It was actually this result that encouraged us to increase the number of washings for the synthesis of  $MgO_{washed}$
- $Cl^-$  anions were present on the surface due to a cleavage of the  $B-Cl$  bond to form  $B-O$  and  $Mg-Cl$  bonds at the surface

Figure 15: presented a hypothetic adsorption of  $BCl_2Ph$  on  $MgO$ . Since the nanoparticles were synthesized using  $NaOH$  as a base, residual  $Na^+$  ions were probably present on the surface. This would explain the presence of  $NaCl$  in XRD and both the modification of  $B-C$  bands and the apparition of potential  $B-O$  bands in IR spectroscopy. Yet we still had to understand why air exposition had this effect on the  $MgO$  surface. We tried exposing the  $MgO+BCl_2Ph$  nanoparticles to either dry air, pure  $CO_2$  or  $H_2O$ , and waited to see if the nanoparticles changed colour (Annexe 5). We observed that nanoparticles exposed to  $H_2O$  immediately changed colour, but the ones exposed to either dry air or  $CO_2$  did not change colour after one day. We concluded that it was water present in the ambient air that caused the colour change.

We came to the following hypothesis: presence of water allowed the ions at the surface of  $MgO$  nanoparticles to move. This mobility allowed the  $Na^+$  and  $Cl^-$  ions to migrate and crystallize to form a  $NaCl$  phase detectable in XRD. Boranes adsorbed on the surface might also be sensitive to moisture, forming  $B(OH)_2Ph$  or  $B(OH)_3$  at the surface, thus resulting in a modification of the IR



spectrum of the nanoparticles and in the apparition of a broad O—H band between 3000 and 3700  $\text{cm}^{-1}$ . Potential remaining  $\text{BCl}_2\text{Ph}$  would also react with  $\text{H}_2\text{O}$  forming  $\text{B(OH)}_2\text{Ph}$ .

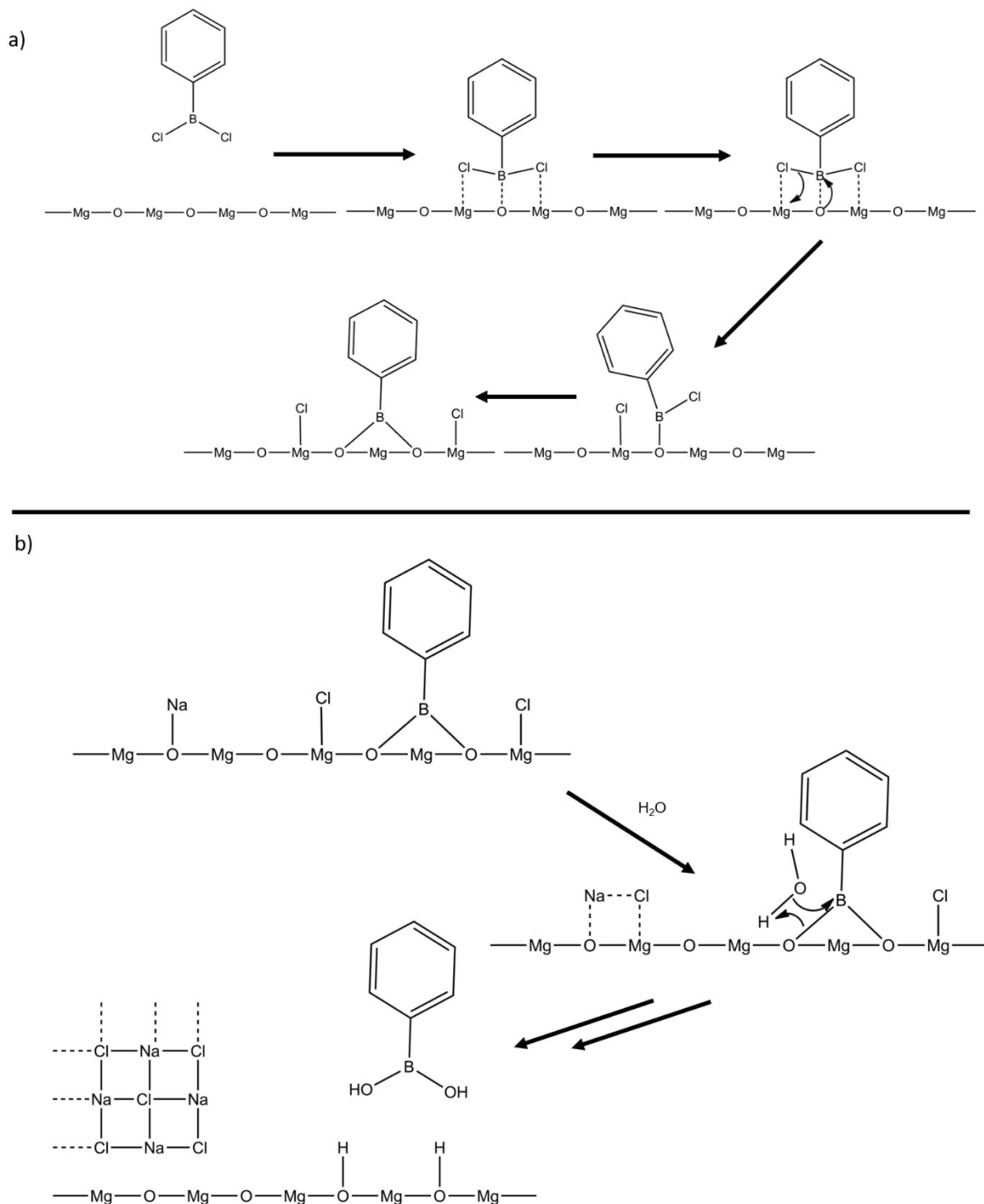


Figure 15: Mechanism proposition for: a) the adsorption of  $\text{BCl}_2\text{Ph}$  on  $\text{MgO}$ , b) the impact of water.

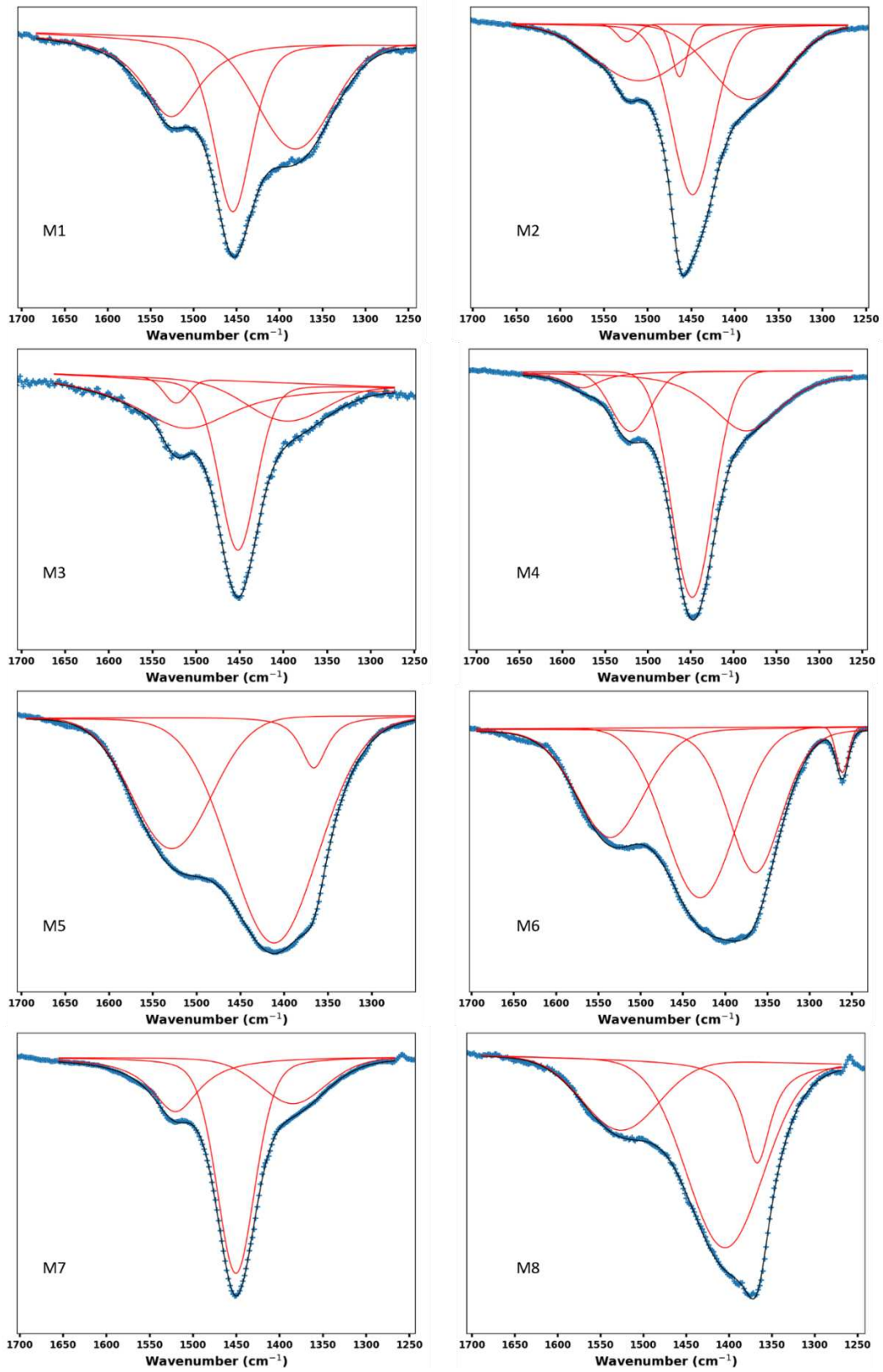
## V. Conclusion

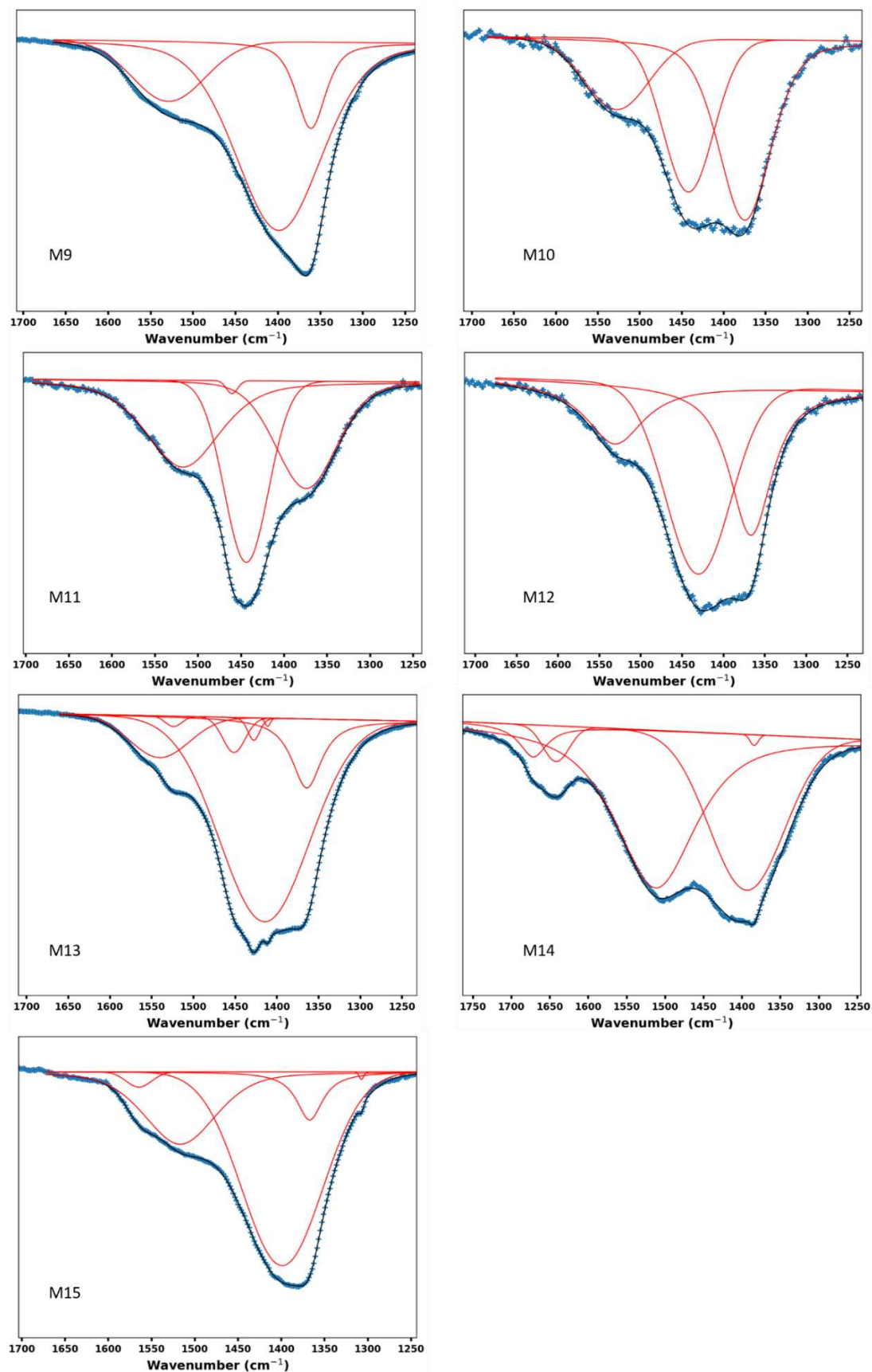
In this chapter, we investigated on the adsorption of CO<sub>2</sub> and boranes on the surface of MgO nanoparticles. We showed that the precipitation-calcination synthesis mostly yielded tridentate and monodentate carbonates at the surface of the nanoparticles. Modification of the protocol, either by increasing the calcination temperature or by increasing the number of washing, decreased the intensity of the carbonate bands and modified the present bands. Exposition of the nanoparticles to CO<sub>2</sub> did not drastically changed the nature of the adsorbed carbonates.

The experiments on borane adsorption showed that weak interactions between MgO nanoparticles and BPh<sub>3</sub> allowing the stabilisation of colloidal dispersion in toluene. This MgO+borane mix was sensitive to CO<sub>2</sub> exposure: modifications of the B—C bonds were observed along with the apparition of potential new B—O bonds. Similar phenomenon was observed with B(OH)<sub>2</sub>Ph.

Lastly, we observed an unprecedented reactivity between MgO nanoparticles and BCl<sub>2</sub>Ph molecules. We observed the formation of NaCl after air exposition of the MgO+BCl<sub>2</sub>Ph powder, clearly indicating the cleavage of the B—Cl borane bonds. We proposed an adsorption mechanism of the chloroborane on MgO surfaces.

## VI. Annexes



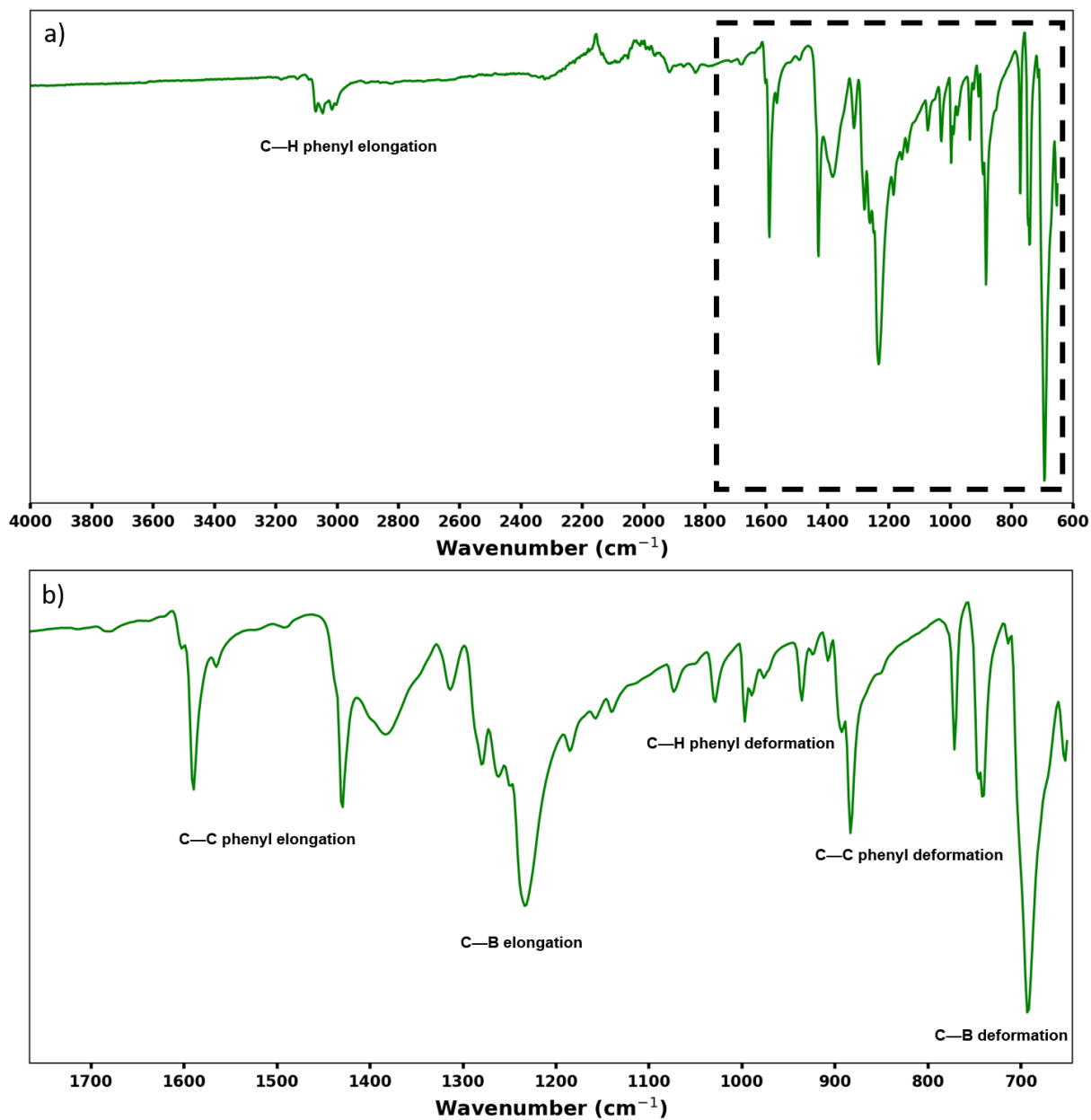


Annexe 1. IR spectra deconvolution of the carbonate band ( $1250\text{ cm}^{-1} - 1700\text{ cm}^{-1}$ ) of different batches of MgO nanoparticles. Blue crosses: measured data, black line: overall fit, red lines: different components of the fit.

Adsorption of borane on MgO surfaces

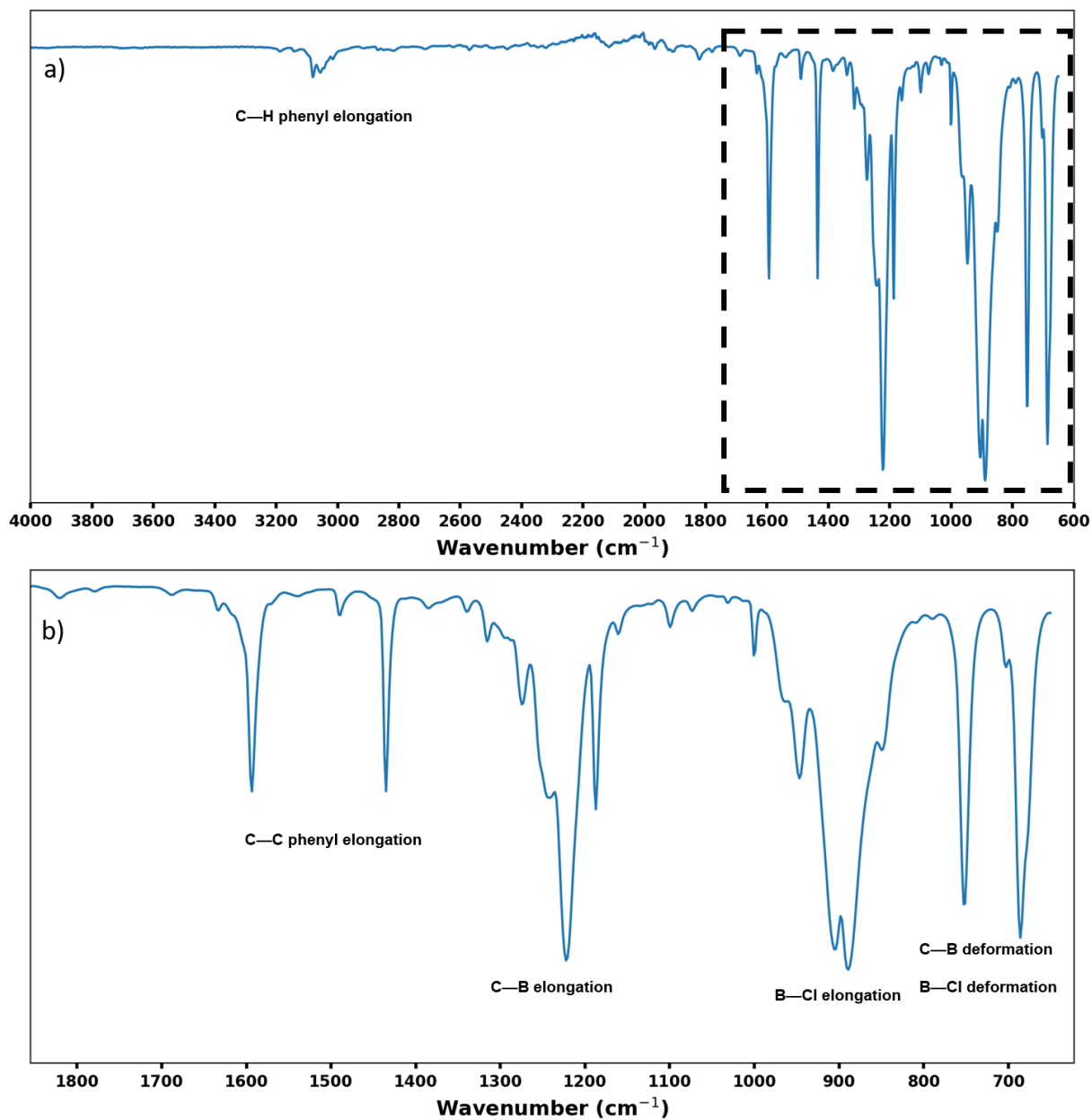
Sample	Position (cm <sup>-1</sup> )	Intensity (A.U.)	Sample	Position (cm <sup>-1</sup> )	Intensity (A.U.)	Sample	Position (cm <sup>-1</sup> )	Intensity (A.U.)
M1	1526	30	M6	1536	32	M12	1531	33
	1454	36		1430	46		1430	74
	1382	35		1364	35		1367	54
M2	1524	2		1261	2	1541	17	
	1509	28	1520	28	1524	1		
	1463	5	M7	1450	67	1451	5	
M3	1449	41	1385	25	M13	1415	130	
	1384	31	1527	26	1364	21		
	1523	3	M8	1405	70	1428	2	
M4	1512	40	1367	20	1411	1		
	1452	36	1529	26	1672	4		
	1397	15	M9	1399	106	1642	3	
M5	1576	5	1361	19	M14	1512	51	
	1520	13	1528	12	1394	34		
	1448	51	M10	1442	20	1384	1	
M6	1385	31	1375	28	1565	1		
	1528	42	1518	27	1517	21		
	1412	85	1461	1	M15	1399	53	
M7	1366	8	M11	1444	27	1367	6	
	1374	25	1374	25	1307	1		

*Annexe 2. Position and intensity of the different IR carbonate bands of MgO nanoparticles determined after the deconvolution of the 1250-1700 cm<sup>-1</sup> zone.*



Annexe 3. IR spectrum of BPh<sub>3</sub>. a) Full spectrum. b) zoom on the 600-1700 cm<sup>-1</sup> zone.

## Adsorption of borane on MgO surfaces



Annexe 4. IR spectrum of BCl<sub>2</sub>Ph. a) Full spectrum. b) zoom on the 600-1800 cm<sup>-1</sup> zone.

Exposition to	Time lapse to observe colour change
Ambiant air	20 seconds
Dry air	No colour change observed
CO <sub>2</sub>	No colour change observed
H <sub>2</sub> O	Immediat

Annexe 5. Exposition of MgO+BCl<sub>2</sub>Ph powder to several molecules to observe colour change.

## Bibliography

- (1) Song, C. Global Challenges and Strategies for Control, Conversion and Utilization of CO<sub>2</sub> for Sustainable Development Involving Energy, Catalysis, Adsorption and Chemical Processing. *Catal. Today* **2006**, *115* (1–4), 2–32. <https://doi.org/10.1016/j.cattod.2006.02.029>.
- (2) Evans, J. V.; Whateley, T. L. Infra-Red Study of Adsorption of Carbon Dioxide and Water on Magnesium Oxide. *Trans. Faraday Soc.* **1967**, *63* (0), 2769. <https://doi.org/10.1039/tf9676302769>.
- (3) Solis, B. H.; Cui, Y.; Weng, X.; Seifert, J.; Schauer mann, S.; Sauer, J.; Shaikhutdinov, S.; Freund, H.-J. Initial Stages of CO<sub>2</sub> Adsorption on CaO: A Combined Experimental and Computational Study. *Phys. Chem. Chem. Phys.* **2017**, *19* (6), 4231–4242. <https://doi.org/10.1039/C6CP08504K>.
- (4) Jensen, M. B.; Pettersson, L. G. M.; Swang, O.; Olsbye, U. CO<sub>2</sub> Sorption on MgO and CaO Surfaces: A Comparative Quantum Chemical Cluster Study. *J. Phys. Chem. B* **2005**, *109* (35), 16774–16781. <https://doi.org/10.1021/jp052037h>.
- (5) Reilly, J. T.; Walsh, J. M.; Greenfield, M. L.; Donohue, M. D. Analysis of FT-IR Spectroscopic Data: The Voigt Profile. *Spectrochim. Acta Part A Mol. Spectrosc.* **1992**, *48* (10), 1459–1479. [https://doi.org/10.1016/0584-8539\(92\)80154-0](https://doi.org/10.1016/0584-8539(92)80154-0).





**Chapter V**  
**MgO-based catalysts in the**  
**cycloaddition of CO<sub>2</sub> on**  
**(2,3-epoxypropyl)benzene**



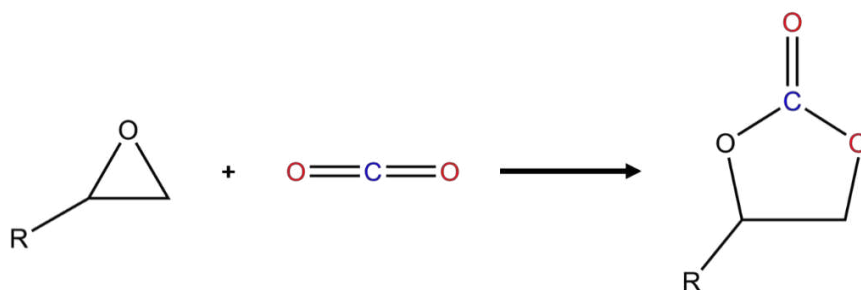
# Table of contents

<b>I.</b>	<b>Cycloaddition of CO<sub>2</sub> on epoxides as a valorisation pathway .....</b>	<b>142</b>
1.	The cycloaddition reaction.....	142
2.	Reaction mechanism .....	143
3.	Reported catalysts.....	144
a.	Homogeneous catalysts.....	144
b.	Heterogeneous catalysts.....	144
c.	Use of a heterogeneous Lewis acid catalyst with a homogeneous Lewis base co-catalyst.....	145
4.	Reported reaction between boranes and epoxides.....	146
5.	Objectives of the chapter .....	148
<b>II.</b>	<b>Experimental section .....</b>	<b>149</b>
<b>III.</b>	<b>Cycloaddition in neat conditions .....</b>	<b>150</b>
1.	Performances of MgO nanoparticles.....	151
a.	First catalytic test.....	151
b.	Kinetic study.....	153
c.	Temperature study.....	154
d.	Tests with other catalysts .....	155
2.	Polymerization of epoxide .....	157
a.	Tests with tris(pentafluorophenyl)borane .....	157
b.	Tests with triphenylborane.....	158
3.	Combining the Lewis base nanoparticles and the Lewis acid ligands .....	162
a.	First attempt with MgO+BPh <sub>3</sub> .....	162
b.	Repeatability of the experiment .....	163
c.	Impact of the temperature .....	164
d.	Impact of borane concentration.....	165
e.	Attempts with other catalysts +BPh <sub>3</sub> .....	166
4.	Inverting the NanoFLP .....	169
a.	Phosphines as molecular Lewis bases.....	169
b.	Impact of the temperature.....	171
5.	Conclusion .....	172
<b>IV.</b>	<b>Cycloaddition in DMF.....</b>	<b>173</b>
1.	Reported impact of DMF in the cycloaddition of CO <sub>2</sub> on epoxides.....	173
2.	Cycloaddition of CO <sub>2</sub> on EpBz in DMF catalysed by MgO+BPh <sub>3</sub> .....	174
a.	Impact of the reaction temperature.....	176
b.	Impact of BPh <sub>3</sub> concentration .....	178
3.	Conclusion .....	179

<b>V.</b>	<b>Cycloaddition in toluene.....</b>	<b>180</b>
	1. Performance of MgO+BPh <sub>3</sub> .....	182
	2. Dimerization of cyclic carbonate .....	186
	a. Identification of the secondary product .....	186
	b. Impact of the borane concentration .....	189
	c. Impact of the NMR tube concentration on chemical displacements.....	190
	d. Impact of the temperature.....	191
	e. Conclusion .....	192
	3. Performances of modified MgO nanoparticles.....	193
	a. Calcium containing MgO nanoparticles .....	193
	b. Transition metal containing MgO nanoparticles .....	195
	4. Borane screening.....	196
<b>VI.</b>	<b>Understanding the interaction between MgO and BCl<sub>2</sub>Ph.....</b>	<b>199</b>
	1. Parameter variation .....	200
	a. Blanc reaction .....	200
	b. Kinetic study.....	201
	c. Impact of the borane loading .....	202
	d. Impact of temperature .....	204
	2. Supernatant activity test.....	206
	3. Post mortem analysis .....	209
	4. Mechanism proposition.....	210
	a. One component experiments .....	211
	b. Two components experiments .....	212
	c. Three components experiments .....	218
	d. Four components experiment .....	224
	e. Mechanism proposition .....	226
<b>VII.</b>	<b>Conclusion .....</b>	<b>231</b>
<b>VIII.</b>	<b>Annexes .....</b>	<b>232</b>

In this chapter, we detailed our results on the activity of MgO-based catalysts in the cycloaddition of CO<sub>2</sub> on epoxides. Since we had a better understanding of the interaction between MgO nanoparticles and borane ligands, we decided to see how the pair behaved in catalysis. As mentioned in Chapter II, we had to choose a catalytic reaction to study: we could either choose a reaction known to be catalysed by molecular FLP and see if our MgO-borane pair could catalyse it, or we could choose a reaction known to be catalysed by either MgO or boranes and see how our MgO-borane pair would behave.

Nothing ensured that NanoFLP would be possible on any reactions we would choose, so we decided to study a reaction that was already catalysed by MgO nanoparticles and see how the addition of borane ligands would impact the activity (just like we did in Chapter III with the Claisen-Schmidt condensation). We decided to focus on a reaction that involved CO<sub>2</sub> since its activation via a NanoFLP mechanism was one of the initial goals of the project. We detailed in Chapter II the main reactions catalysed by MgO. The cycloaddition of CO<sub>2</sub> on epoxides was chosen (Scheme 1:).



*Scheme 1: Cycloaddition of CO<sub>2</sub> on epoxide.*

# I. Cycloaddition of CO<sub>2</sub> on epoxides as a valorisation pathway

## 1. The cycloaddition reaction

As mentioned in Chapter II, the main strategies for CO<sub>2</sub> valorisation are: the use of high amount of energy (heat, light or electricity mainly) to perform a transformation, the use of high-energy starting molecule such as H<sub>2</sub>, or the synthesis of low energy target molecules<sup>1</sup>. In the case of the cycloaddition of CO<sub>2</sub> on epoxides, it is a mix of the two last strategies that is at stakes. Epoxides are constrained heterocycles that can react with CO<sub>2</sub> when activated by a catalyst to form cyclic carbonates (Scheme 1:). Cyclic carbonate molecules have been commercialized since the 1950s and can be used as polar aprotic solvents, electrolytes for lithium-ion batteries, precursor for polycarbonate synthesis, additive in oil or paints<sup>2-5</sup>. Cyclic carbonates can also be used as intermediates for the synthesis of fine chemicals since it can react with compounds such as amines, alcohols, or carboxylic acids (Figure 1:).

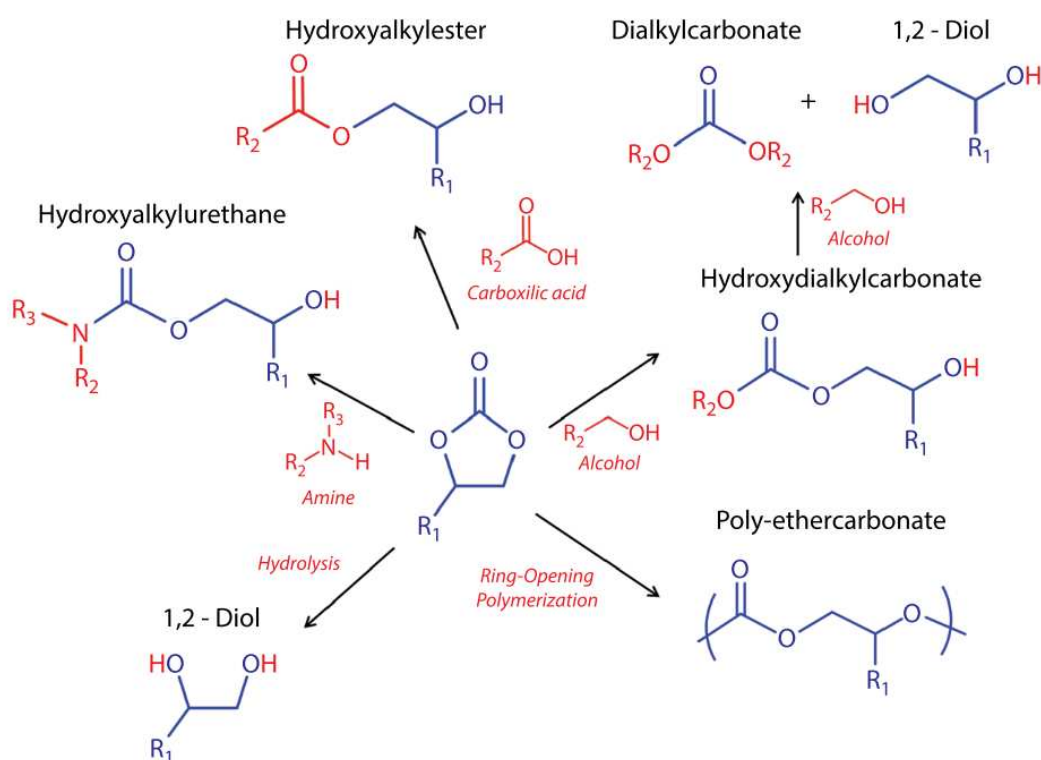


Figure 1: Reactivity of cyclic carbonates, from Bobadilla et al.<sup>5</sup>.

CO<sub>2</sub> valorisation for better carbon capture economic viability, development of Li-ion batteries for the decarbonation of vehicles and use of renewable carbon feedstock for chemical synthesis have been three main challenges of the last decades. We understood why the

cycloaddition of CO<sub>2</sub> on epoxides has drawn increasing interest recently<sup>6</sup>. Adding the fact that the reaction is atom-economic, thus not producing any by-product, cyclic carbonate synthesis using CO<sub>2</sub> seemed even more attractive. Actually, it was one of the few CO<sub>2</sub> valorisation pathways that has been industrialised<sup>7,8</sup>.

## 2. Reaction mechanism

Different mechanisms were reported for the catalytic reaction. They almost always included the action of both a nucleophile agent and a Lewis acid for the activation of either the CO<sub>2</sub> molecule, the epoxide or both at the same time<sup>5</sup>. Figure 2: showed the proposition of two different mechanisms proposed by Kiatkittipong et al.<sup>3</sup>. In the first one the nucleophile activates the CO<sub>2</sub> molecule, and the Lewis acid facilitates the opening of the epoxide by interacting with its oxygen atom. Then the five membered ring closes giving the cyclic carbonates. In the second proposed mechanism the Lewis acid activates the epoxide so that the nucleophile agent can open the cycle. Then the electrophilic carbon of the CO<sub>2</sub> molecule interacts with the oxygen atom of the opened epoxide to finally lead to the closure of the five membered ring.

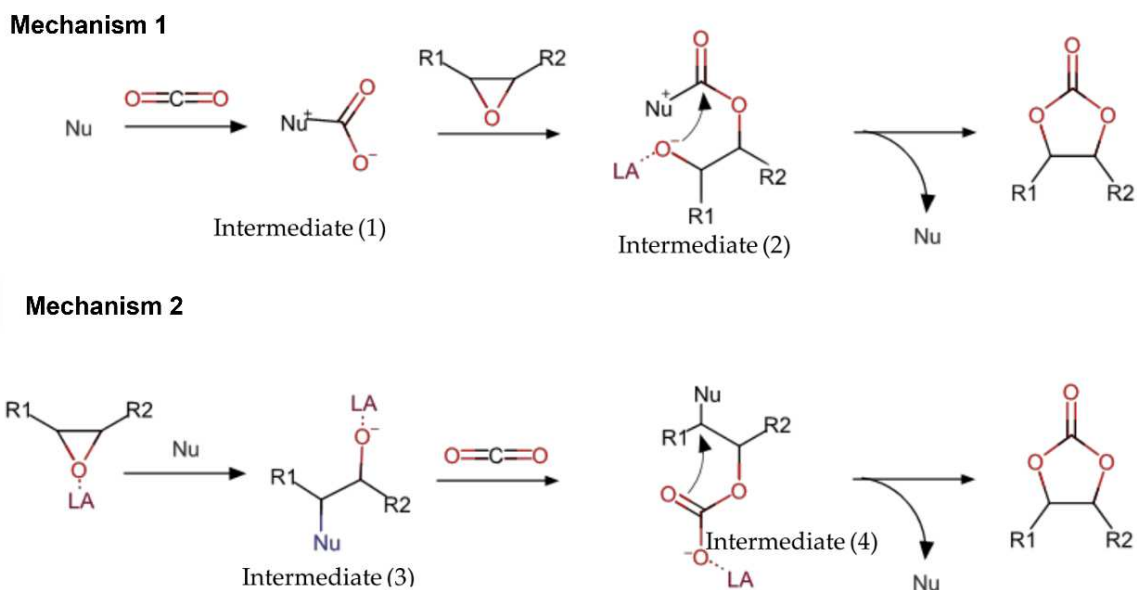


Figure 2: Two proposed mechanisms for the cycloaddition of CO<sub>2</sub> on epoxides, from Kiatkittipong et al.<sup>3</sup>.

Both the epoxide and the CO<sub>2</sub> have a nucleophilic oxygen atom that can interact with a Lewis acid, and an electrophilic carbon atom that can interact with a nucleophile agent. Even if the steric hindrance did not seem to enter into account here, this kind of reactions where both a Lewis acid and a Lewis base (acting as a nucleophile) had a role to play were good candidates to attempt NanoFLP.



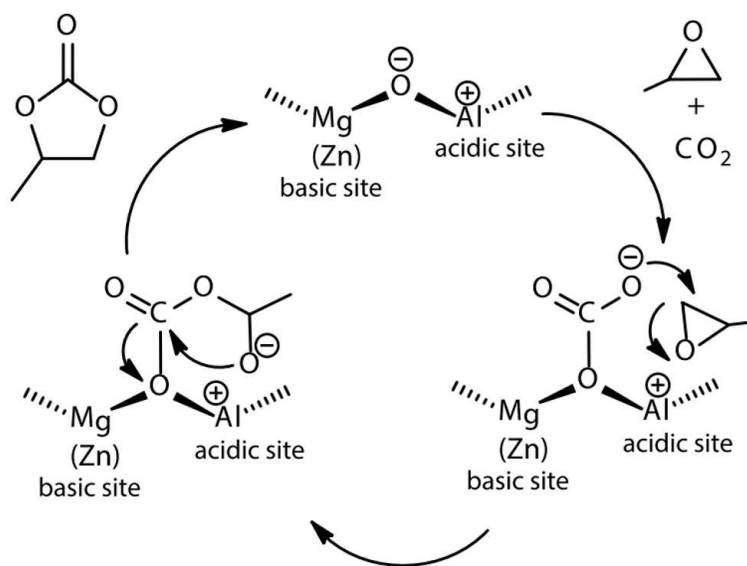
### 3. Reported catalysts

#### a. Homogeneous catalysts

Reported catalysts for the cycloaddition of CO<sub>2</sub> on epoxides are numerous and being exhaustive would be difficult. We could classically divide two families of catalysts: homogeneous and heterogeneous. On the homogeneous side we had notably ionic liquids, amines and other organic bases, deep eutectic solvents, metal salts, organometallic complexes<sup>3</sup>. These types of catalysts were really efficient and could operate under mild conditions. For example, Wang et al.<sup>9</sup> used 2,6-pyridinedimethanol in ionic liquids (TBACl, TBAB, TBAI) at 25 °C under 1 bar of CO<sub>2</sub> and managed to get up to 92 % ethylene carbonate yield in a 24 hours reaction. Castro-Osma et al.<sup>10</sup> showed that the use aluminium scorpionate could catalyse the reaction at room temperature under 10 bar of CO<sub>2</sub> to achieve a 100 % conversion of ethylene oxide in 24 hours. Some other catalysts required higher temperature and CO<sub>2</sub> pressure, like Aresta et al.<sup>11</sup> that had to work at 150 °C for their Nb(V) complex catalyst to reach 80 % styrene oxide yield in 12 hours.

#### b. Heterogeneous catalysts

Several heterogeneous catalysts are also reported to be active in the cycloaddition of CO<sub>2</sub> on epoxides. Bobadilla et al.<sup>5</sup> made an extensive review on the subject. The first class of materials that was found to be active in the reaction was oxides and mixed oxides. Yamaguchi et al.<sup>12</sup> showed that Mg-Al mixed oxides were active at 120 °C under 5 bars of CO<sub>2</sub> to yield 88 % of propylene carbonate in 24 hours. Interestingly enough, they emphasized that the efficiency of the catalyst came from the cooperative interaction of Mg—O basic sites and Al acidic sites (Scheme 2:). This mechanism would correspond to the Mechanism 1 described in Figure 2; where the nucleophile (basic site) activated the CO<sub>2</sub> molecule and the acidic sites activated the epoxide. Several oxides were reported to be active in the cycloaddition of CO<sub>2</sub> on epoxides: MgO, CaO, ZnO, ZrO<sub>2</sub>, La<sub>2</sub>O<sub>3</sub>, CeO<sub>2</sub>, Al<sub>2</sub>O<sub>3</sub>, K<sub>2</sub>CO<sub>3</sub>, Nb<sub>2</sub>O<sub>5</sub>, Fe<sub>3</sub>O<sub>4</sub>. Basic zeolites also showed to be active in the reaction through the incorporation of alkali metal oxide clusters (Na, K, Cs)<sup>13</sup>. Dorskocil and coworkers managed to obtain 33 % ethylene carbonate yield at 150 °C under 100 bar of CO<sub>2</sub> in 3 hours. More recently, some organic materials were discovered to be active in the reaction such as chitosan, resins and polymers<sup>14-17</sup>.



Scheme 2: Cyloaddition of  $\text{CO}_2$  on propylene oxide mechanism over Mg-Al mixed oxide, adapted from Dai et al.<sup>2</sup>.

### c. Use of a heterogeneous Lewis acid catalyst with a homogeneous Lewis base co catalyst

A specific case caught our attention: the catalysis of the reaction by a zinc-based hydroxyapatite (Zn-HAP) combined with a molecular Lewis base. Mori et al.<sup>18</sup> showed that this pair was active at 100 °C under 5 bar of  $\text{CO}_2$  and yielded styrene carbonate up to 79 % in 20 hours in solvent-free conditions. The catalytic activity was strongly dependent of the base used in the reaction (Figure 3:b). When no base was used, the Zn-HAP only yielded traces of carbonates. When molecular bases were added, the activity increased drastically, up to 79 % yield. The activity varied depending on the base: 57 % for pyridine, 60 % for 1,8-diazabicyclo[5.4.0]-7-undecene (DBU), 63 % for triethylamine (TEA), and 79 % for 4-(dimethylamino)pyridine (DMAP).

Blank reaction was only performed with DMAP and it showed that the base alone was active in catalysis. However, the authors clearly showed that there was a synergetic effect between Zn-HAP and the bases. They also showed that the use of solvents (DMF and  $\text{CH}_2\text{Cl}_2$ ) reduced the catalytic activity of the Zn-HAP + TEA pair. The synergy probably came from the cooperative activation of  $\text{CO}_2$  and of the epoxide involving both the acidic Zn sites of the Zn-HAP and the Lewis bases (Figure 3:). In this case the proposed mechanism corresponded to the Mechanism 2 described in Figure 2:, where the Lewis acid and the nucleophile activated the epoxide.

This study was interesting to us since it showed an activation similar to the one we would like to achieve with NanoFLP. In our case MgO would play the role of the Lewis base and boranes the role of the Lewis acid.

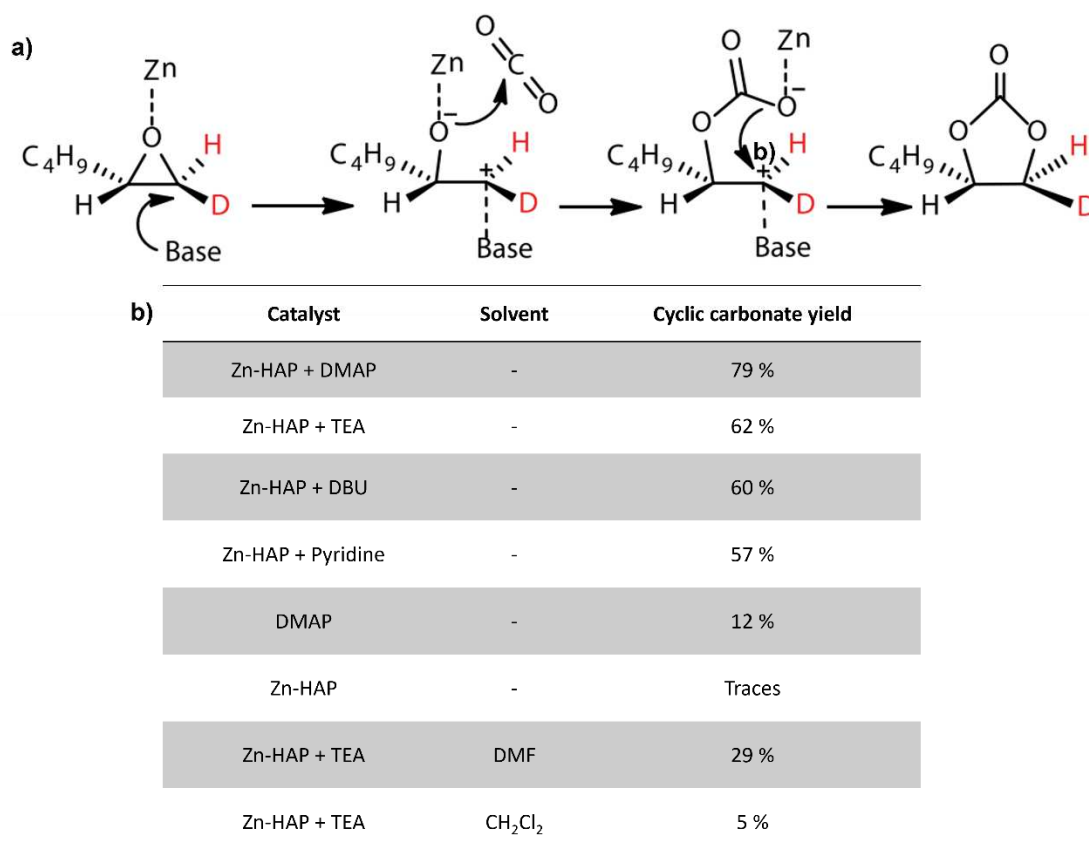


Figure 3: a) Proposed mechanisms for the cycloaddition of CO<sub>2</sub> on *trans*-1-deuterio-1,2-hexene oxide catalysed by Lewis base assisted Zn-HAP, b) performance of Lewis base assisted Zn-HAP in the cycloaddition of CO<sub>2</sub> on styrene oxide (100 °C, 5 bar CO<sub>2</sub>, 20 h), adapted from Mori et al.<sup>18</sup>.

#### 4. Reported reaction between boranes and epoxides

We searched reported reactions occurring between epoxides and boranes. It appeared that boranes and other Lewis acids were known to activate the opening of epoxide cycles as well as epoxide polymerisation. Andrea and coworkers<sup>19</sup> published a review on the ring-opening polymerisation (ROP, polymerisation of the epoxide on itself) and copolymerisation (ROCOP, polymerisation of epoxide and other molecules like CO<sub>2</sub>) activated by boron and aluminium catalysts. ROP of epoxides was reported to be activated by boranes. Chen and coworkers<sup>20</sup> reported that a variety of organoboranes were active in the ROP reaction and that the yield depended on the acidity of the boranes. Weakly acid boranes like BPh<sub>3</sub> or B(OC<sub>6</sub>F<sub>5</sub>)<sub>3</sub> did not yield isolable amount of polypropylene oxide, but stronger acids like BCF did. The presence of a hydroxyl-containing initiator (such as H<sub>2</sub>O, EtOH or glycerine) helped to obtain longer polymer chains and accelerated the reaction. On its own, BCF only produced short oligomers (dimer, trimer or tetramer). In the presence of CO<sub>2</sub>, boron catalysed ROCOP was possible, leading to the formation of either polycarbonates or copolymers containing both ether and carbonate moieties (Figure 4:).

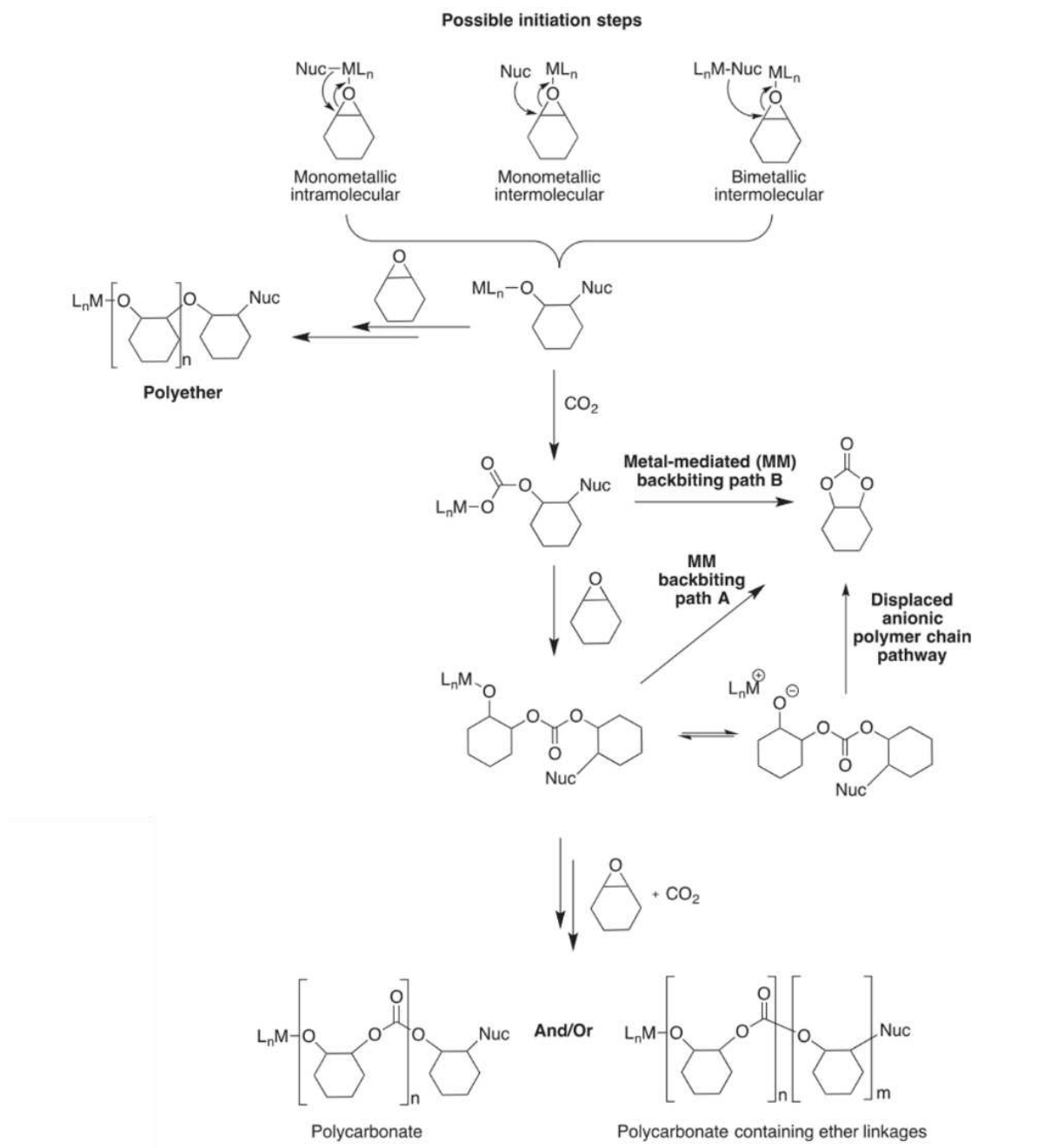


Figure 4: General mechanism for the polymerisation of cyclohexene oxide and the copolymerisation of  $CO_2$  and cyclohexene oxide, from Andrea et al.<sup>19</sup>.

These were crucial information that had to keep in mind when we started to study the impact of the borane ligands in the activity of our MgO-borane pair.

## 5. Objectives of the chapter

All things considered, it seemed that the cycloaddition of CO<sub>2</sub> on epoxides was a good candidate to attempt NanoFLP. The fact that it involved the activation of small molecules like CO<sub>2</sub> and even epoxides in some extent, that MgO nanoparticles were already catalysts of the reaction, that the mechanism involved both a Lewis acid and a nucleophile species were encouraging. In our case the basic sites of the MgO nanoparticles would play the role of the nucleophile species and the boranes would be the Lewis acid. We would have to be careful not using boranes with too strong acidity since we did not want the epoxide to polymerise. It could be interesting in future steps of the NanoFLP project, but at this point we wanted to study the cycloaddition and not the copolymerisation reaction.

Since some epoxides like ethylene oxide and propylene oxide were flammable and explosive, we chose to work with one specific epoxide that was (2,3-epoxypropyl)benzene (EpBz) for safety reasons. This epoxide was not used really often and seemed more difficult to activate than less bulky epoxides like ethylene oxide, as shown by Tu and coworkers<sup>21</sup>. Their experiments were the starting point of our study. They showed that EpBz was harder to activate than ethylene oxide: their MgO catalyst only yielded 4 % cyclic carbonate with EpBz against 19 % with ethylene oxide. The study also showed that MgO was one of the least active catalysts: the authors obtained a 41 % carbonate yield for the cycloaddition on EpBz when they used the homogeneous [N(C<sub>2</sub>H<sub>5</sub>)<sub>4</sub>]Br catalyst.

We wanted to see if our NanoFLP strategy could lead to higher catalytic activity of MgO nanoparticles in the cycloaddition of CO<sub>2</sub> on (2,3-epoxypropyl)benzene.

## II. Experimental section

*Note: all the details concerning the suppliers and the purity of chemical products are given in the Appendix.*

### Cycloaddition catalysed by MgO in neat conditions

The reaction was performed in a 25 mL glass autoclave. All the glassware was dried for one night in a 120 °C oven before usage. Inside an argon glovebox, MgO (20 mg, 0.5 mmol, 0.13 equivalent) was introduced, then EpBz (0.5 mL, 3.8 mmol, 1 equivalent), and finally borane (1.9E-2 mmol, 0.005 equivalent, mass depending on the borane) when it was used. We closed the autoclave and took it out of the glovebox. We connected the autoclave to a vacuum-gas system where we made two vacuum/CO<sub>2</sub> (1 bar) cycles before putting 7 bars of CO<sub>2</sub> (10 mmol, 2.6 equivalents) in the autoclave. The autoclave was then put in an oil bath and heated at 150 °C. We let the reaction going for a duration that varied from 3 hours to 5 days. After that we got the autoclave out of the oil bath and let it cool at room temperature. Depending on the cases we would either degas and open the autoclave under ambient air or in the glovebox if we feared the products to be air sensitive. NMR analyses were made by diluting one droplet (for <sup>1</sup>H NMR) or 0.1 mL (for <sup>11</sup>B NMR) of the crude reaction in 0.5 mL of either CDCl<sub>3</sub> or toluene-d<sub>8</sub>.

### Cycloaddition catalysed by MgO with DMF

When conducting the cycloaddition with DMF we used the following stoichiometry: EpBz (0.5 mL, 3.8 mmol, 1 equivalent), DMF (0.5 mL, 6.5 mmol, 1.7 equivalents), MgO (20 mg, 0.5 mmol, 0.13 equivalent), borane (1.9E-2 mmol, 0.005 equivalent, mass depending on the borane) when it was used. The experimental procedure was the same as the reaction in neat conditions with the extra step where we added the DMF right after MgO and before the epoxide.

### Cycloaddition catalysed by MgO in other solvents

When using a solvent, we modified the stoichiometry of the reactions: solvent (4 mL), EpBz (0.4 mL, 3.0 mmol, 1 equivalent), MgO (80 mg, 2 mmol, 0.66 equivalent), borane (7.5E-2 mmol, 0.02 equivalent, mass depending on the borane). However, procedure was the same with the extra step where we added 4 mL of the desired solvent right after MgO and before the epoxide.

### Blanc reaction at room temperature without CO<sub>2</sub>

We use the term “blanc reaction” when we did a reaction without one of the reactants or the catalyst. In most cases the experimental procedure was the same. The only exception was when we carried experiments without CO<sub>2</sub> at room temperature: in this case the reactions were performed in 15 mL glass vial directly in the glove box.

### III. Cycloaddition in neat conditions

From the studies we mentioned above, neat (or solvent-free) reactions were often performed for the cycloaddition of CO<sub>2</sub> on epoxides. This was probably due to several reasons: the low solubility of CO<sub>2</sub> in usual solvents, the high concentration of epoxide in neat conditions, the easier isolation of the product, or the reduction of waste at the end of the reaction. Both the reference paper we chose as a starting point<sup>21</sup> and the paper mentioning the Lewis base assisted Zn-HAP catalyst showed higher results in neat conditions. We decided to start in this direction.

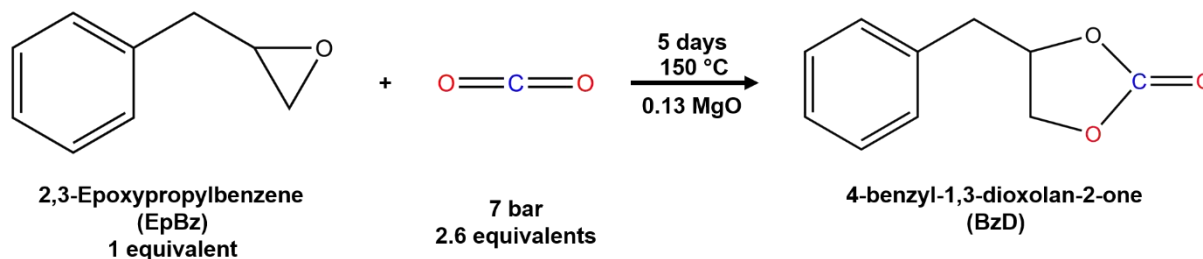
However, working in neat conditions also have shown some limitations<sup>22</sup>. These included among others: the solubility or miscibility of the different reagents, the necessity to use excess of some reactants, the formation of side product, a low control over the selectivity, and a faster poisoning of the catalyst. In our case, this could be problematic especially when we would use boranes since they could trigger the polymerisation of the epoxide. Working in neat condition could increase the rate of polymerisation, so we had to be really careful to which borane we chose in order not to entirely consume the epoxide.

We adapted the protocol described in the work of Tu and coworkers<sup>21</sup>, and tried to make the cycloaddition of CO<sub>2</sub> on EpBz in neat conditions. In their work, they obtained a 4.0 % cyclic carbonate yield under 50 bar of CO<sub>2</sub> at 150 °C during 3 hours with a catalyst loading of 25 %. At the time we could not go as high in pressure, so we decided to work at lower pressure (7 bar). We had to keep in mind that the reaction parameters were not exactly the same when we compared the results.

## 1. Performances of MgO nanoparticles

### a. First catalytic test

As a first attempt, we wanted to have a high advancement of the reaction to have the cyclic carbonate in decent amount for our analyses. The cyclic carbonate 4-benzyl-1,3-dioxolan-2-one (BzD) was not found commercially, so we could not have spectral references. We let the reaction run for 5 days using the stoichiometry detailed in the experimental section (also summed up in Scheme 3:).



Scheme 3: Cycloaddition of CO<sub>2</sub> on 2,3-Epoxypropylbenzene catalysed by MgO in neat conditions.

After making the <sup>1</sup>H NMR analysis of the reaction crude in CDCl<sub>3</sub>, we obtained the spectrum showed in Figure 5:. By using the same method than in the Chapter III, we calculated the NMR epoxide consumption and the NMR cyclic carbonate selectivity. We obtained 75 % consumption of the epoxide and 74 % selectivity toward the cyclic carbonate.

Secondary products were essentially detected by the triplet at 4.3 ppm, the peaks around 6.5 ppm and the broad signal around 3.5 ppm. We did not find in the literature any precise description of the secondary products possible in the cycloaddition of CO<sub>2</sub> on epoxides. We guessed that they would come from the epoxide ring-opening activated by the MgO catalyst. The considered secondary products were given in Figure 6:. After simulating the different <sup>1</sup>H NMR spectra using the ChemDraw software, we found that the signal at 6.5 ppm could come from the secondary product **5**, and the triplet at 4.3 ppm could come from the secondary product **1** (see Annexe 2 for the attribution proposition).

This was interesting since it gave information on the mechanism of the cycloaddition reaction. It was the C—O bond with the most sterically hindered carbon atom that was cleaved. However, it was a little bit surprising to see the secondary product **1** since it requires a hydrogenation step to be formed. It was also surprising that we detected the enol **5** but not the corresponding aldehyde **3**. Usually, the aldehyde form would be the more favoured in a tautomeric keto-enolic equilibrium. It was possible that in these conditions the enol form was more stable, or that the transformation of **5** into **3** was not possible.

Due to the chemical displacement and the shape of the peaks at 3.5 ppm, we could suppose that the broad signal was due to a partial polymerisation of the epoxide. This will be more discussed in the latter when we will introduce boranes in the reaction. These were just propositions based on <sup>1</sup>H NMR analysis only, and on the hypothesis that the secondary products



came from the epoxide ring-opening. Further studies would have to be made, using different techniques like gas chromatography or mass spectroscopy, to confirm these propositions.

We verified that the blanc reaction with no catalyst did not yield any cyclic carbonate. MgO was necessary for both the formation of the cyclic carbonate and the secondary products (Annexe 3).

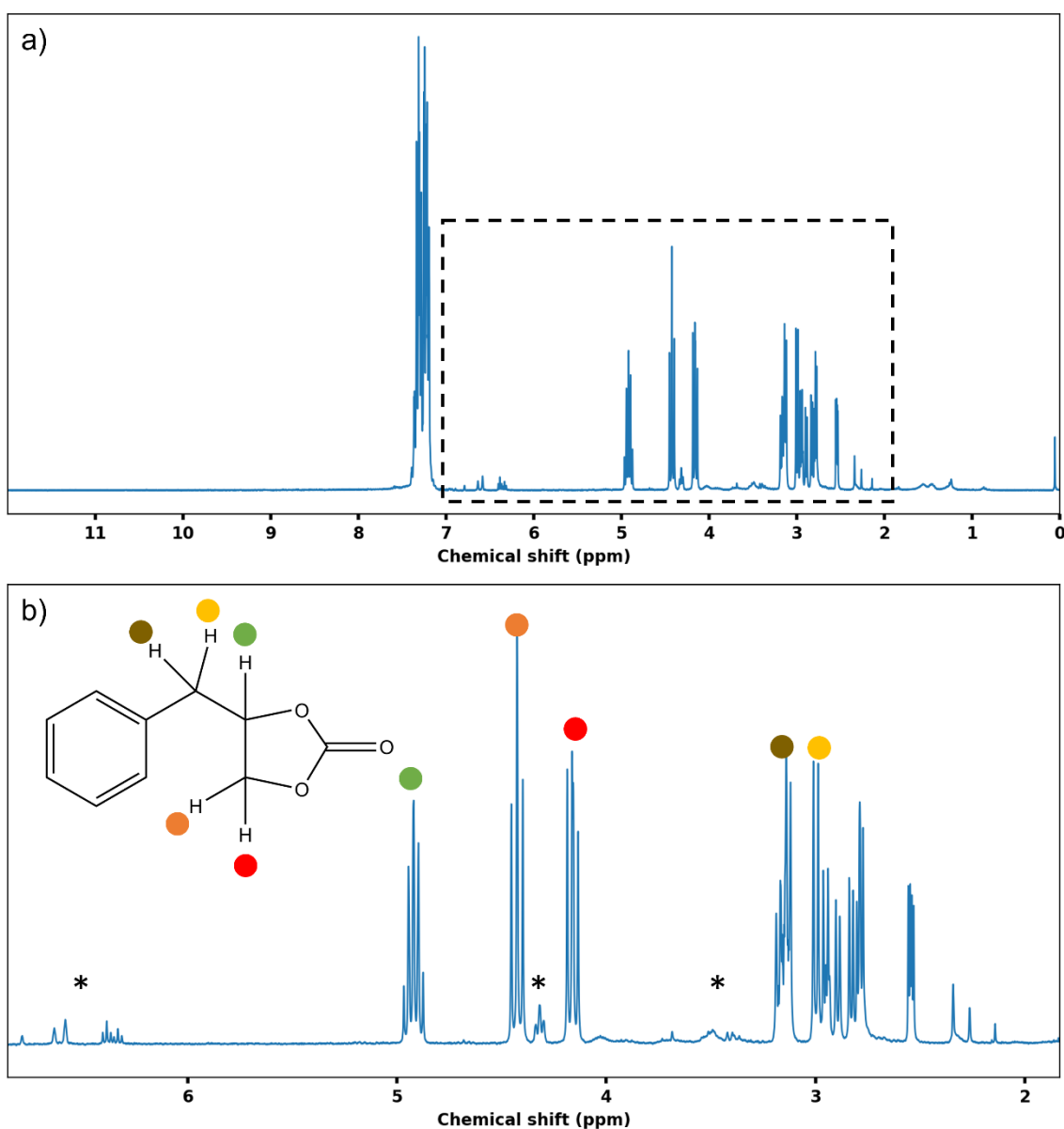


Figure 5: <sup>1</sup>H NMR spectrum of the crude after the cycloaddition. a) full spectrum, the dotted box corresponds to the zone in b). Identification of the cyclic carbonate peaks. Secondary products are marked by a star.

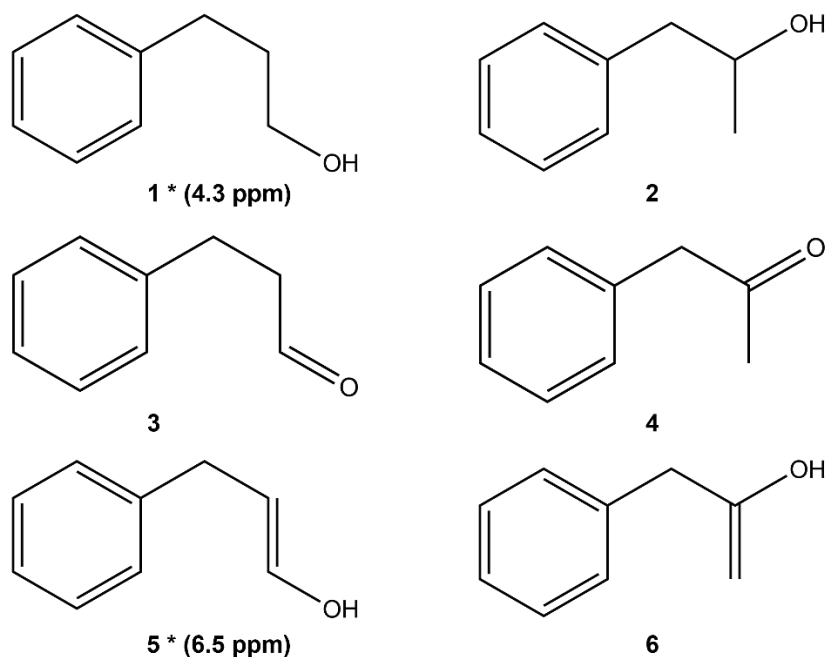


Figure 6: Considered secondary products originating from the epoxide ring-opening, those detected in the reaction crude of the cycloaddition reaction are marked with a star and associated chemical displacement are given in parenthesis.

We managed to obtain a consumption of the epoxide into the desired cyclic carbonate allowing the identification of its NMR peaks. This result was not comparable with the one of the original paper since our reaction lasted 5 days and not 3 hours. However, we were intrigued by the formation of these secondary products that were not mentioned by Tu and co-workers in their study. Actually, they did not give selectivity results at all. We could not know if this was expected.

## b. Kinetic study

The low selectivity was maybe due to the formation of secondary products at long reaction times. To answer this question, and to be able to compare our results to those of Tu, we decided to do a kinetic study of the reaction. We varied the duration of the experiment from 3 hours to 5 days (120 hours), while keeping the other parameters constant. Evolution of the NMR epoxide consumption and of the NMR cyclic carbonate selectivity were shown in Figure 7:. This study showed that the selectivity of the reaction was low even at small reaction duration. The number of equivalents of the different species depending on the duration were given in Annexe 4. Before 72h, the only secondary product was the polymeric specie. The two other secondary products were not detected before 72 h, and in negligible quantities afterward. We estimated the cyclic carbonate selectivity to be between 60 and 80 %. The point at 3 hour gave a lower selectivity, but the low consumption increased the uncertainties.

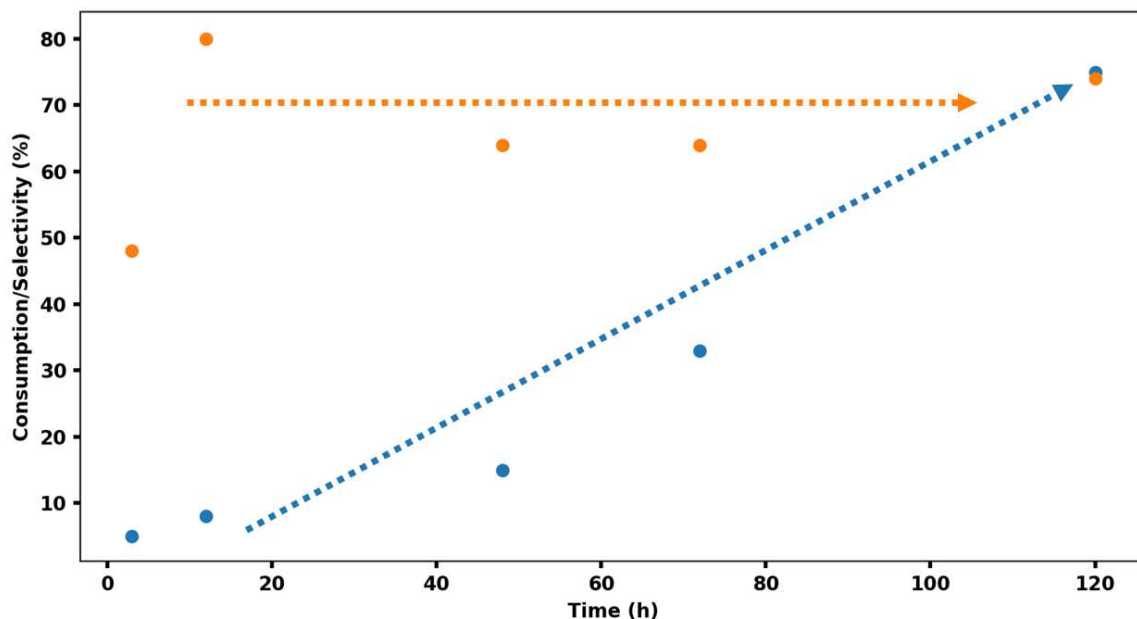


Figure 7: Evolution of the epoxide consumption (blue) and the cyclic carbonate selectivity (orange) depending on the duration of the reaction. Dotted arrows of corresponding colors are here to guide the eye.

If we compared the reaction that lasted 3 hours like in the study of reference, we could see that we obtained a lower cyclic carbonate yield: 2 % instead of 4. On the one hand, considering the low quantities we were dealing with, we could wonder if this 2 % difference was significant; on the other hand, we had to remember that we conducted the experiment at only 7 bar of CO<sub>2</sub> pressure, while they used 50 bar. This could explain the difference in consumption.

In order to get better cyclic carbonate selectivity, we decided to modify the temperature of the reaction. It would allow us to see if the secondary products could form at temperatures where the cycloaddition was not possible, or if the two reactions were inherently linked to each other.

### c. Temperature study

We decided to vary the temperature from room temperature (RT) to 150 °C (the temperature we used until now) while fixing the duration at 48 hours. The lowest temperature reported for the catalytic reaction with MgO-based catalyst was 120 °C<sup>12</sup>. We expected that below this temperature we would not see any reactivity. The results of the study were summed up in Table 1.: No cycloaddition was detected up to 60 °C. However, at 80 °C traces of cyclic carbonate were detected at the end of the reaction even if it was hard to quantify (less than 1 % yield). We also evidenced that the reaction producing the polymeric species took place at temperatures as low as 40 °C. The amount of secondary product formed did not vary when the temperature increased until 150 °C. However, since the uncertainty on the calculation of the NMR

measurements was approximately 1 %, it was hard to be quantitative. We could say for sure that the polymeric product was detectable.

Species	RT	40 °C	60 °C	80 °C	150 °C
Epoxide	1	0.99	0.99	0.99	0.85
Cyclic carbonate	0	0	0	< 0.01	0.09
Sec. Product 3.5ppm	0	0.01	0.01	0.01	0.05
Sec. Product 4.2 ppm	0	0	0	0	0.01
Sec. Product 6.5 ppm	0	0	0	0	0

*Table 1: Evolution of the quantities (in equivalent) of the different species in the cycloaddition of CO<sub>2</sub> on epoxides in neat condition at the end of the reaction depending of the reaction temperature.*

#### d. Tests with other catalysts

Since no reference studies used the exact same reaction conditions as ours, we wanted to have an idea of the efficiency of our MgO catalyst compared to other types of MgO. We decided to conduct the catalytic experiment with MgO<sub>com</sub> (commercial MgO) and MgO<sub>1000</sub> (MgO calcined at 1000 °C). We performed the reaction with the same stoichiometry at 150 °C for 48 hours. We also decided to try other catalysts: the synthesized CaO nanoparticles and the hydroxides Mg(OH)<sub>2</sub> and Ca(OH)<sub>2</sub>. These last two materials were not reported as active catalysts for the reaction. We maintained the ratio epoxide vs alkaline-earth atom constant between the different catalytic experiments, without any normalisation with the surface area of the materials. Results were given in Table 2:.

We noted that the synthesized MgO calcined at 500 °C was the most active of the MgO nanoparticles we tested. This was probably due to the points mentioned in Chapter III: higher surface area and more active exposed facets. It was also the material with the best selectivity. The other MgO nanoparticles mostly lead to the formation of the polymeric secondary product. CaO was almost inactive for the cycloaddition but lead to the formation of the polymer. The hydroxides lead to different results depending on the alkaline-earth atom: Mg(OH)<sub>2</sub> was active in catalysis with properties exceeding those of CaO but inferior to MgO, and Ca(OH)<sub>2</sub> was totally inactive.

Catalyst	Epoxide consumption	Cyclic carbonate selectivity	Cyclic carbonate yield
MgO	15 %	64 %	9 %
MgO <sub>com</sub>	2 %	40 %	1 %
MgO <sub>1000</sub>	1 %	13 %	< 1 %
CaO	10 %	14 %	1 %
Mg(OH) <sub>2</sub>	13 %	41 %	5 %
Ca(OH) <sub>2</sub>	0 %	/	0 %

Table 2: Comparison of different catalysts for the cycloaddition of CO<sub>2</sub> on EpBz at 150 °C for 48 hours.

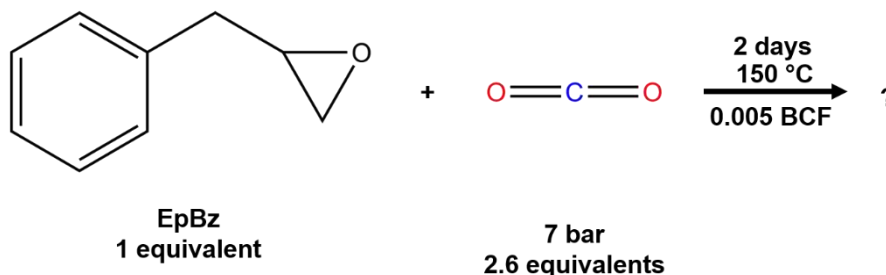
These results were coherent with what we found in the literature. MgO nanoparticles treated at high temperatures can lose reactivity for certain reactions (cf. Chapter II) and the cycloaddition of CO<sub>2</sub> on epoxide appeared to be one of them. Commercial MgO exhibited larger particle sizes, probably leading to lower surface area and lower catalytic activity for a given mass. CaO was reported to be a catalyst for the reaction with properties much inferior compared to MgO<sup>5</sup>. However, the results we obtained concerning magnesium hydroxide was not reported to our knowledge. Even if it was lower, Mg(OH)<sub>2</sub> showed an activity comparable to the one of MgO both in terms of epoxide consumption and cyclic carbonate selectivity. Post mortem analysis would be necessary to verify that Mg(OH)<sub>2</sub> nanoparticles did not undergo strong morphological or crystallographic changes. It could be interesting to see if the activity was due to the Lewis basicity of the sites or if the hydroxide function plays a role. To do so, we could study the catalytic activity of MgO nanoparticles with different hydroxyl coverage obtained by exposition with water. We could also study the activity of partially calcined MgO/Mg(OH)<sub>2</sub> nanoparticles, where both bulk oxide and hydroxide phases would be present. However, we did not believe that this investigation was worth to do, and we preferred to move further in our plan toward the NanoFLP.

After these studies, we had a first understanding of the catalytic reaction and the efficiency of the different catalysts that we used. The next step was to see if the addition of a Lewis acidic borane could modify activity of our MgO catalyst, either in terms of epoxide consumption or cyclic carbonate selectivity.

## 2. Polymerization of epoxide

### a. Tests with tris(pentafluorophenyl)borane

As mentioned in the introduction of the chapter, we knew that the interaction between borane Lewis acid species and epoxides could lead to polymerisation. This was especially true since we were working in neat conditions. The Lewis acidity of the boranes was the most critical factor to control if we wanted to avoid polymerisation. Since tris(pentafluorophenyl)borane (BCF) was the most used borane in FLP chemistry, we decided to use it as a first test. The stoichiometry of the reaction is described in the experimental part of the chapter (summed up in the Scheme 4:).



*Scheme 4: Attempt at the cycloaddition of CO<sub>2</sub> on EpBz catalysed by BCF in neat conditions.*

As soon as the borane was added to the mixture three phenomenon occurred simultaneously: the emission of a white smoke, the heating of the solution and the increase of the viscosity of the solution. All these signs clearly indicated that the epoxide polymerised immediately when in contact with BCF.

We did the <sup>1</sup>H NMR spectra of the crude of reaction (Figure 8:) to see what the signal of the polymerised epoxide would be. A broad signal was detected from 2.5 ppm to 4 ppm with some sharper peaks on top of it. It was at this moment that we associated the broad signals around 3.5 ppm obtained in previously to polymerised species. The large signal with some sharp peaks on top seemed to be characteristic of polymeric species. However, the shape of the signal was not the same when repeating the reaction (Annexe 5). Both the area of the broad peaks and the position/intensity of the sharp ones varied. A finer analysis of the polymeric species was difficult only using proton NMR. No signal was detected in <sup>11</sup>B NMR, potentially because polymerised species were harder to detect. Moreover, since we were using an echo on the <sup>11</sup>B measurement, the borane would be even harder to detect if it was incorporated in polymeric species.

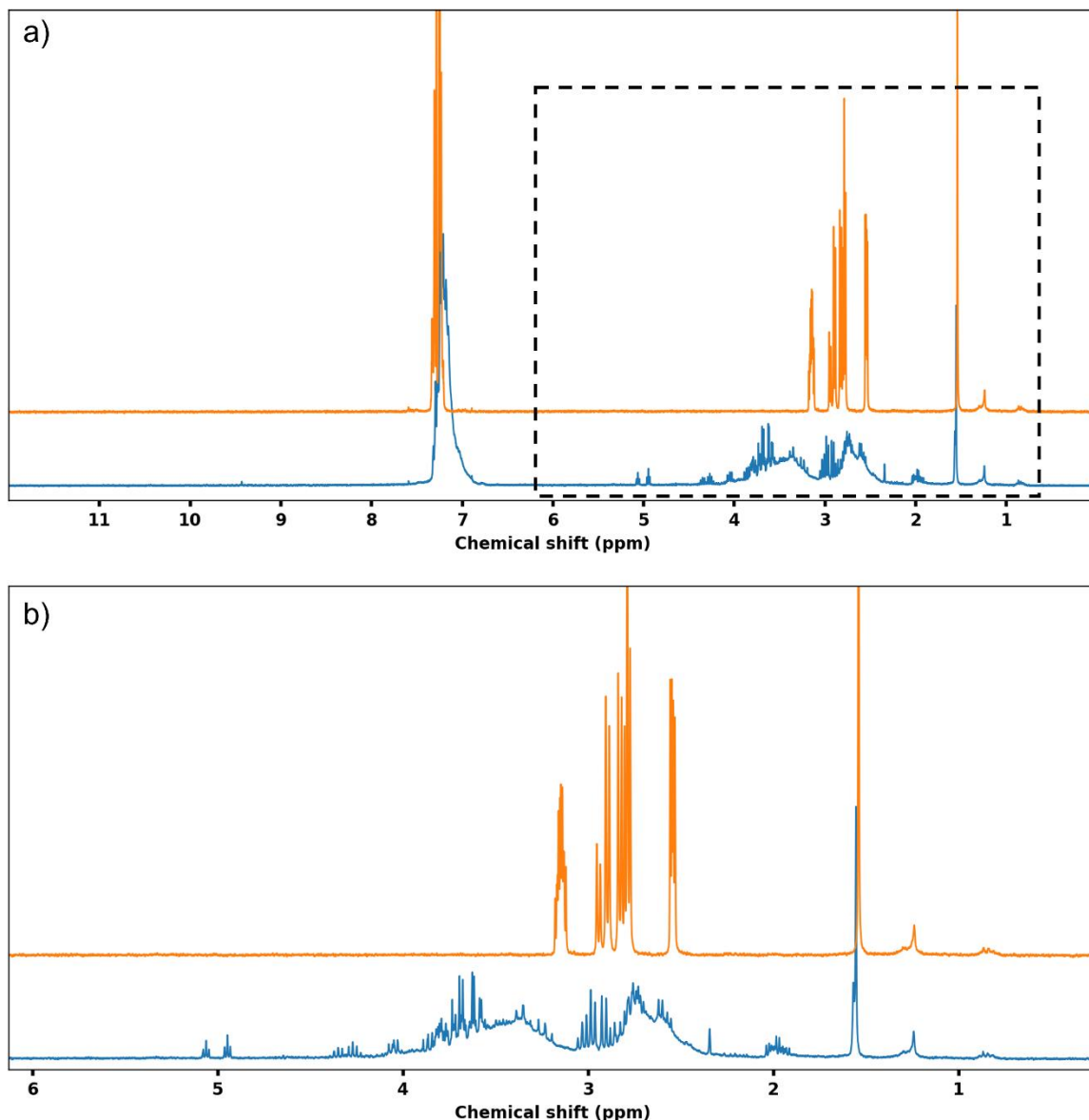


Figure 8: <sup>1</sup>H NMR spectrum after the addition of BCF to the epoxide (blue) and the reference of EpBz (orange). a) Full spectrum, b) zoom on the dotted box.

## b. Tests with triphenylborane

BCF was too acidic for us to use without polymerising the epoxide. We decided to try another less acidic borane: triphenylborane (BPh<sub>3</sub>). We did the reaction in the same condition (keeping the borane stoichiometry) and we did not observe any smoke formation, heating nor increase of the viscosity. It seemed that the epoxide did not polymerize.

To confirm this, we did the <sup>1</sup>H NMR of the crude of reaction like with BCF (Figure 9:). We did see a modification of the initial epoxide spectrum, but unlike with BCF the epoxide was still visible here. The appearance of the broad signal occurred at room temperature but was more important at higher temperatures. The signal was also more intense when more borane was

introduced at room temperature. Just like with BCF, the signal of the polymerised product varied from one experiment to the other. Its interpretation was complex.

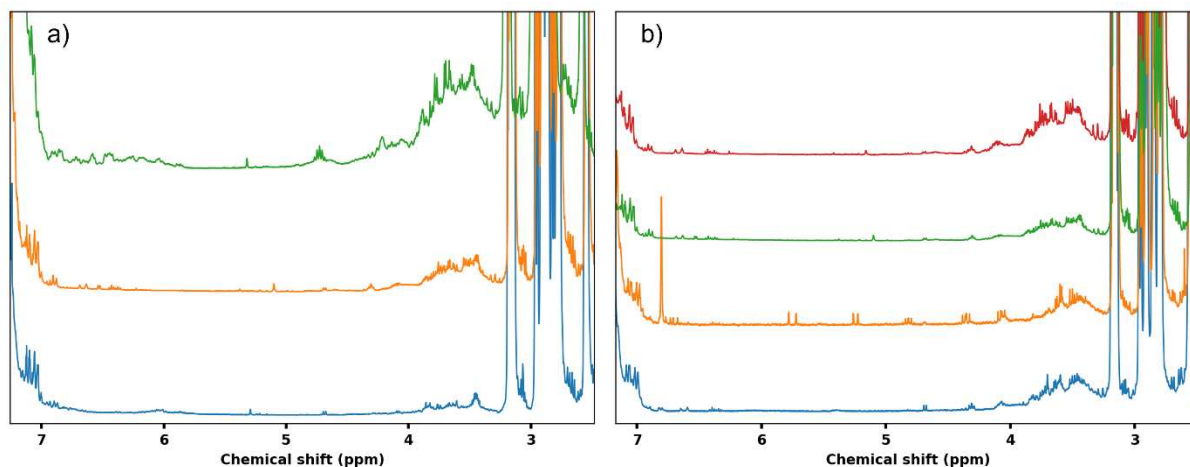


Figure 9:  $^1\text{H}$  NMR spectrum of the mixture with EpBz and  $\text{BPh}_3$ . a) At room temperature (blue), at  $150\text{ }^\circ\text{C}$  (orange), at room temperature with 10 times more borane (green). b) Four repetitions of the reaction at  $150\text{ }^\circ\text{C}$ .

We also did the  $^{11}\text{B}$  NMR of these reactions (Figure 10:). It was surprising for us that BCF in the same concentrations was not detectable by NMR whereas  $\text{BPh}_3$  was. This was probably linked to the fact that polymerised species were harder to detect. In the case of  $\text{BPh}_3$  the polymerisation was only partial, so most of the borane was detectable. We could see in Figure 10:a that when the reaction was conducted at room temperature, we only observed a peak at 46 ppm. This corresponded to  $\text{BPh}_2\text{OR}$  compounds, meaning that the borane probably entirely reacted with the epoxide to form one of the product **1** or **2** described in Figure 11:.. The small peak at 29 ppm corresponded to a  $\text{BPh}(\text{OR})_2$  specie, like products **3** or **4**. This was also the case for the reaction conducted with a high concentration of boranes (Figure 10:a green). However, in the reaction at  $150\text{ }^\circ\text{C}$ , we could see the apparition of 3 peaks with variable intensities (Figure 10:b) at 32 ppm, 23 ppm and 20 ppm. The peak at 32 ppm would correspond to another  $\text{BPh}(\text{OR})_2$  type specie, whereas the peaks at 23 ppm and 20 ppm would correspond to  $\text{B}(\text{OR})_3$  species like the products **5** and **6**.



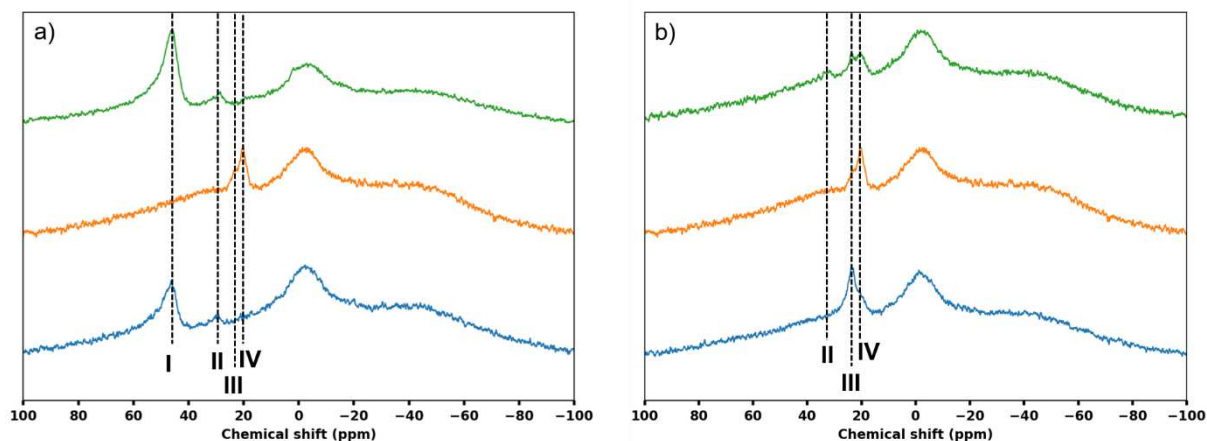


Figure 10: <sup>11</sup>B NMR spectrum of the mixture with EpBz and BPh<sub>3</sub>. a) At room temperature (blue), at 150 °C (orange), at room temperature with 10 times more borane (green). b) Three repetitions of the reaction at 150 °C. Peak I: 46 ppm, peak II: 32 ppm, peak III: 23 ppm, peak IV: 20 ppm.

It seemed that at room temperature BPh<sub>3</sub> interacted with the epoxide allowing the replacement of one of the phenyl groups and two of them in some molecules. Even at high borane concentration no BPh<sub>3</sub> signal (65 ppm) was detectable. The high epoxide/borane ratio favoured the total transformation of the borane. When increasing the temperature to 150 °C the apparition of the new peaks could be due to a stronger interaction between the borane and the epoxide. The value of the chemical displacements hinted toward species like BPh(OR)<sub>2</sub> and B(OR)<sub>3</sub>, hypotheses were given in Figure 11: for what could be the corresponding species. <sup>11</sup>B NMR spectra were harder to predict than usual <sup>1</sup>H and <sup>13</sup>C NMR spectra, so it was not possible to verify by simulation the chemical displacement associated to these boron species. None of these species were detectable in <sup>1</sup>H NMR, probably due to their low concentration (0.01 equivalent of borane compared to the epoxide). It could be also due to the fact that the peaks were covered in the broad polymer signal.

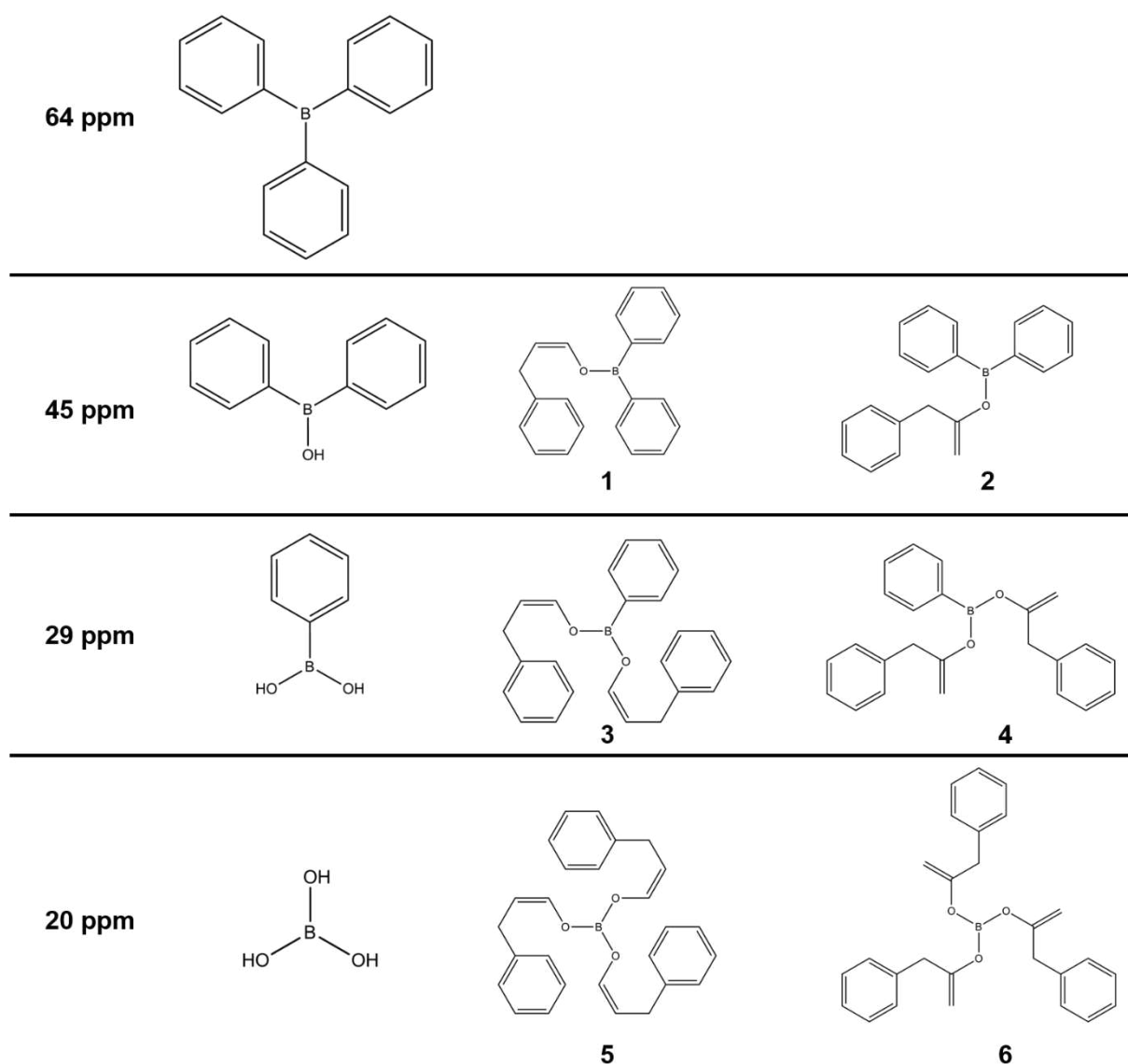


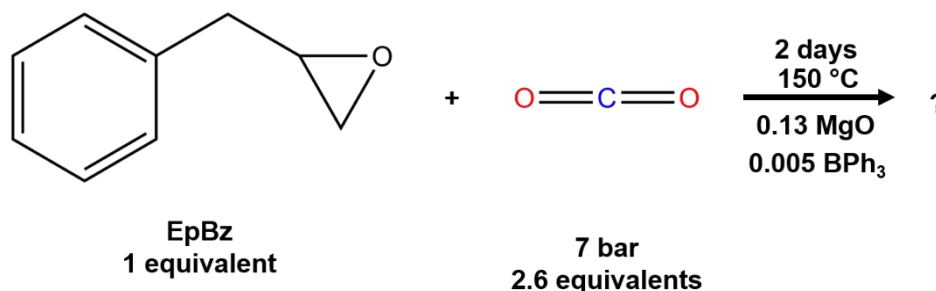
Figure 11: Boron compounds possibly present in the reaction. Chemical displacement of the  $BPh_n(OH)_{3-n}$  species are given on the left.

We were starting to see one of the limitations of neat reaction with our system. Even if the activity of MgO was higher, neat conditions also favoured other undesired side reactions such as the polymerisation of the epoxide in presence of a borane (and even with MgO). But still we wanted to see if the use of both MgO and  $BPh_3$  would lead to the simple addition of the effect of the two species (catalytic activity of MgO + polymerisation with  $BPh_3$ ), or if there was an additional effect due to a synergy between the nanoparticles and the ligands.

### 3. Combining the Lewis base nanoparticles and the Lewis acid ligands

#### a. First attempt with MgO+BPh<sub>3</sub>

In this part we investigated on the effect of the combination of MgO and BPh<sub>3</sub> in catalysis. We decided to keep the previous stoichiometry, as described in Scheme 5:



Scheme 5: Attempt at the cycloaddition of CO<sub>2</sub> on EpBz catalysed by MgO+BPh<sub>3</sub> in neat condition.

We conducted a first experiment at 150 °C for 2 days to see if the main and secondary products of the reaction were the same as with MgO and BPh<sub>3</sub> alone (Figure 12:). We could see that the <sup>1</sup>H NMR gave no new species (Figure 12:a), we still had formation of the cyclic carbonate and of secondary products (polymeric, and traces of the product at 6.5 ppm). However, the <sup>11</sup>B NMR spectrum was different from the one with BPh<sub>3</sub> only. Here we had three peaks at 32 ppm, 23 ppm and 7 ppm, and no peak at 20 ppm. Apparently, the presence of MgO prevented the formation of the 20 ppm species and instead allowed the formation of the 7 ppm species.

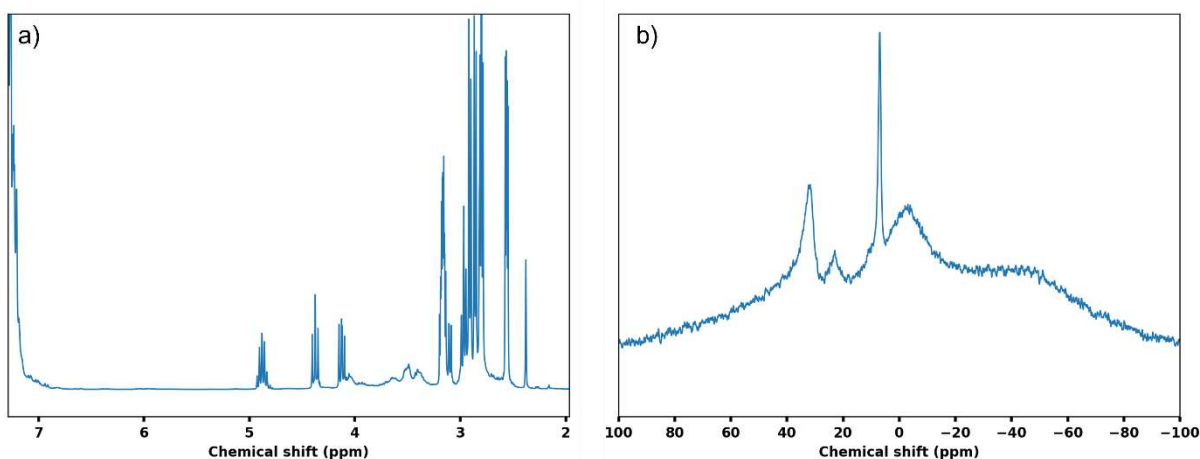


Figure 12: NMR spectra of the crude of reaction using MgO+BPh<sub>3</sub> as a catalyst, a) <sup>1</sup>H NMR, b) <sup>11</sup>B NMR.

The sharpness of the new peak in <sup>11</sup>B NMR and the chemical displacement inferior to 10 ppm were characteristic of tetravalent boron species. This signal could correspond to a

BPh<sub>3</sub>-epoxide adduct (Figure 13:). It would be surprising that this species could form in this reaction whereas it could not in the reaction with BPh<sub>3</sub> alone. This might be due to the fact that MgO nanoparticles and its surface species managed to stabilise the BPh<sub>3</sub>-EpBz adducts.

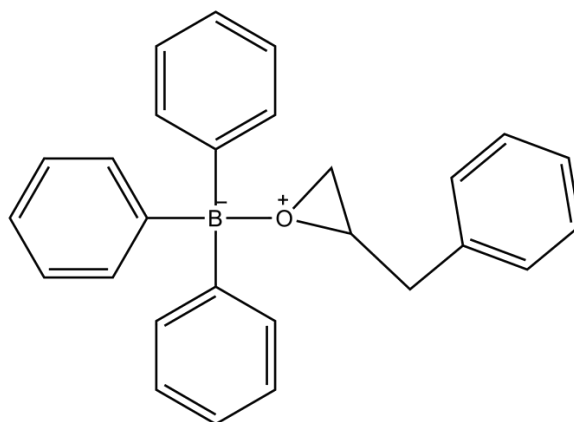


Figure 13: Possible adduct formed by BPh<sub>3</sub> and EpBz.

#### b. Repeatability of the experiment

Just like in the case of MgO and BPh<sub>3</sub> alone, we had some questions concerning the repeatability of the experiment in terms of secondary products, epoxide consumption, carbonate selectivity, and boron species present in the final solution. We decided to reproduce the experiment 5 times to evaluate its repeatability. As showed in Figure 14:a, depending on the repetitions the broad signal of the polymeric species could overlap with the signal of the cyclic carbonate, making the integration of certain peaks challenging. The production of cyclic carbonate varied a lot from one experiment to another. This was confirmed when we made the calculations (Figure 14:b). The carbonate yield varied from 1 % to 18 %, with an average of 6 % and a standard deviation of 6 %. This reflected a very high variability, and the experiment with a 18 % carbonate yield could be considered as suspicious point when using the Grubbs method (see Annexe 6). If we removed this point, the average was 3 % and the standard deviation was 1 %. It seemed that overall, the presence of the borane reduced the activity of the MgO catalyst, who alone gave a 9 % yield toward the cyclic carbonate.

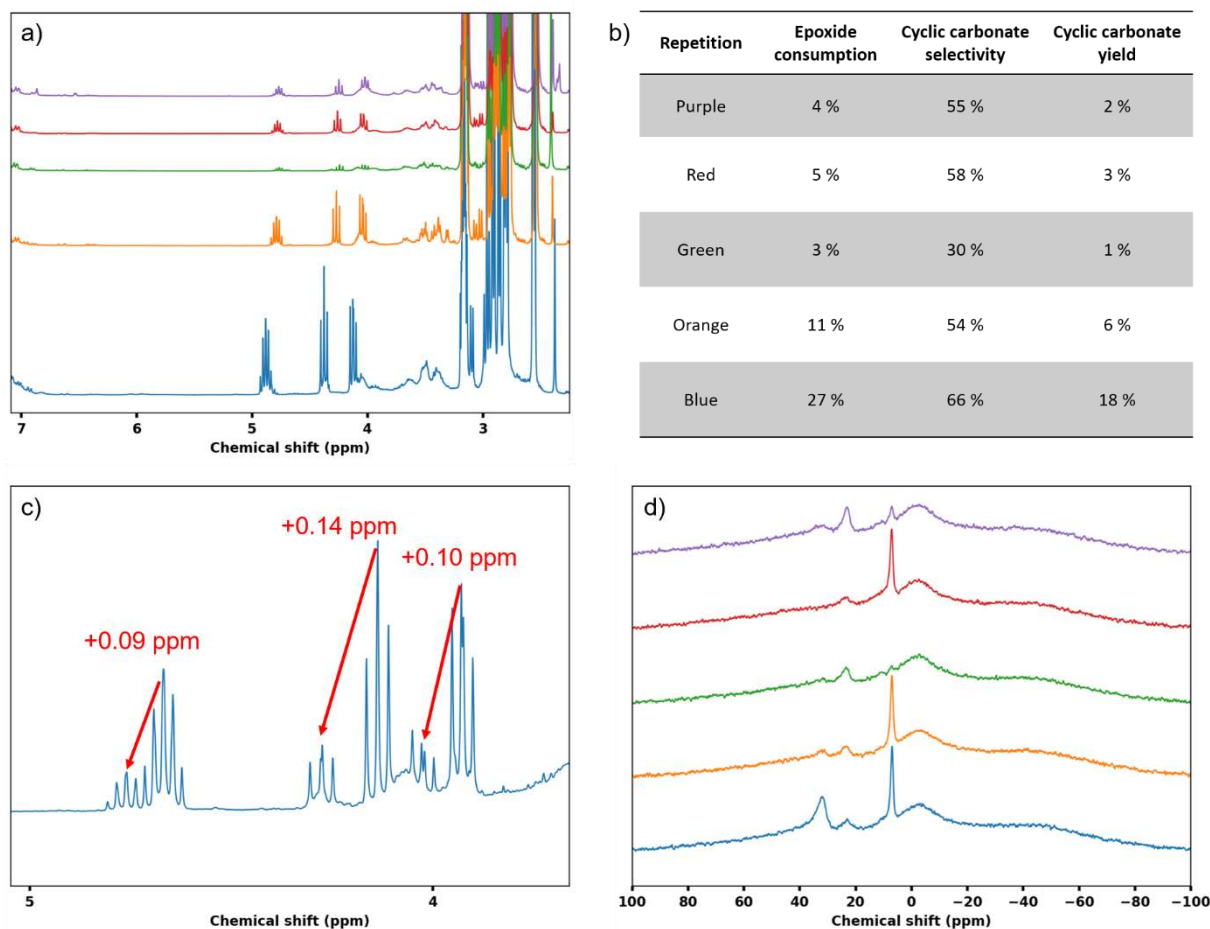


Figure 14: Repeatability of the catalytic experiment with MgO+BPh<sub>3</sub> a) <sup>1</sup>H NMR spectra of the 5 repetitions of the catalytic experiments, b) corresponding calculations of the NMR consumptions, NMR selectivities and NMR yields, c) local <sup>1</sup>H NMR spectra showing the apparition of the supposed dimer product (the experiment was conducted only one day instead of two), d) <sup>11</sup>B NMR spectra of the 5 repetitions of the catalytic experiments (the colors of a) and d) correspond to matching experiments).

Worth mentioning, in one of the experiments we saw the apparition of another secondary product with a peak structure similar to the one of the cyclic carbonate BzD, but with shifted chemical displacement (Figure 14:b). These peaks were likely to come from a dimer of the cyclic carbonate; it will be discussed more in detail later in the chapter. As shown in Figure 14:d, in the different repetitions we had between 2 and 4 peaks in boron NMR: at 32 ppm, 23 ppm, 18 ppm and 7 ppm with variations of the relative intensity of the peaks from one experiment to another. We could not find any links between the variable intensities of these peaks and the corresponding epoxide consumptions or cyclic carbonate selectivity.

### c. Impact of the temperature

Even if we had repeatability issues, we decided to investigate on the effect of the reaction temperature. We wanted to see if there were different trends of the effect of MgO+BPh<sub>3</sub> in other

conditions (for example an activation of the reaction at lower temperature). Results were given in Figure 15:a. Like when we used MgO alone as catalyst, the cycloaddition did not occur at room temperature nor at 40 °C. However, whereas MgO did not yield any cyclic carbonate at 60 °C, we detected traces when we tested MgO+BPh<sub>3</sub>. It was hard to quantify, but it was detectable. It was possible that even though BPh<sub>3</sub> reduced the catalytic activity of MgO at 150 °C, it decreased the activation temperature of the reaction. This could be explained by a pre-activation of the epoxide by the borane for example. The species detected in <sup>11</sup>B NMR corresponding to BPh<sub>2</sub>(OR) and BPh(OR)<sub>2</sub> could be these pre-activated epoxide species.

When we looked at the evolution of the <sup>11</sup>B NMR spectra with the temperature, we could clearly see a trend: the main peak at 45 ppm at room temperature was progressively replaced by the peak at 32 ppm the more the reaction temperature increased. There was no detection of the peaks at 23 ppm, 18 ppm nor 7 ppm that were present in the reaction at 150 °C. This was interesting to see and we made several hypotheses: maybe the borane species responsible for the activation of the epoxide corresponded to the peak at 32 ppm, and maybe the species responsible for the decrease of the MgO activity were among the ones at 23, 18 and 7 ppm. However, we had to keep in mind that if the reduction of MgO activity was due to surface species blocking the reactive sites, the corresponding boron species should not be detectable by liquid NMR. Liquid NMR only informed us on the molecular species present in solution.

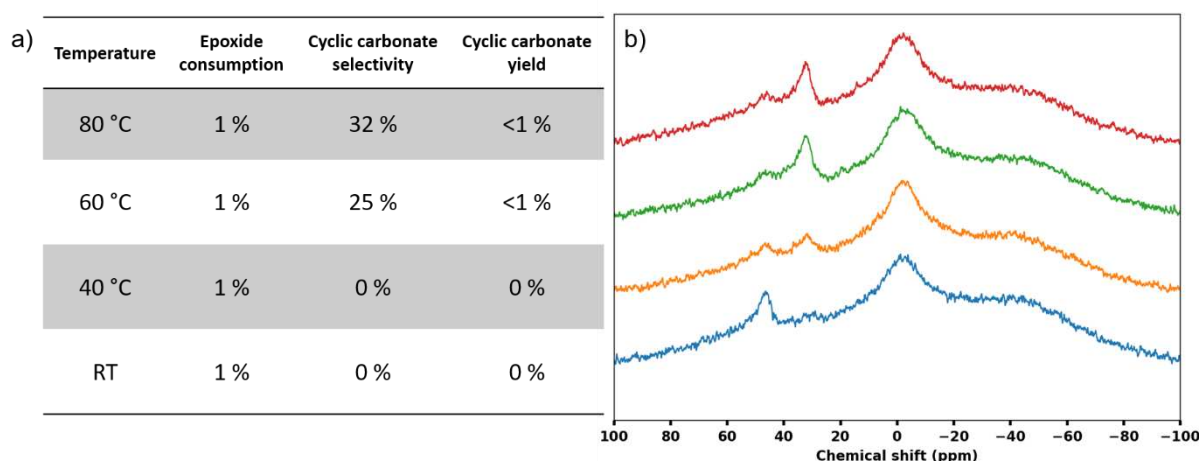


Figure 15: a) Performances of MgO+BPh<sub>3</sub> as a catalyst in the cycloaddition of CO<sub>2</sub> on epoxide at low temperatures, b) <sup>11</sup>B NMR spectra of the corresponding experiments (blue: RT, orange: 40 °C, green: 60 °C, red: 80 °C).

#### d. Impact of borane concentration

Another test we wanted to make was modifying the borane concentration. We increased the borane stoichiometry by a factor of 10 to see if it was possible to completely hinder the catalytic activity of MgO nanoparticles. We did the experiment both at 150 °C and 80 °C to see if there was also a hindering of the formation of carbonate at low temperatures. The <sup>1</sup>H NMR spectra (Figure 16:a) showed a high formation of polymeric species. The broad signal was so important that it was difficult to estimate the NMR yield of cyclic carbonate in the two reactions. If estimations had to

be given, it would be 0 % formation at 80 °C and less than 1 % at 150 °C. It seemed that the high concentration of borane indeed prevented the formation of cyclic carbonate and favoured the formation of polymeric species, which was in accordance with the results obtained in part III.2. The <sup>11</sup>B NMR spectra indicated the apparition of a new boron species at the chemical shift of 2 ppm. At 80 °C we could see a pic at 45 ppm and a smaller one at 32 ppm. The ratio was not the same for the reaction with lower borane concentration, meaning that it took time/energy to convert the 45 ppm specie into the 32 ppm one. At 150 °C we could see the peak at 32 ppm, but no peaks at 23 ppm, 18 ppm nor 7 ppm. This could be due to a repeatability issue, or to the formation of the 2 ppm specie that prevented the formation of other boron species.

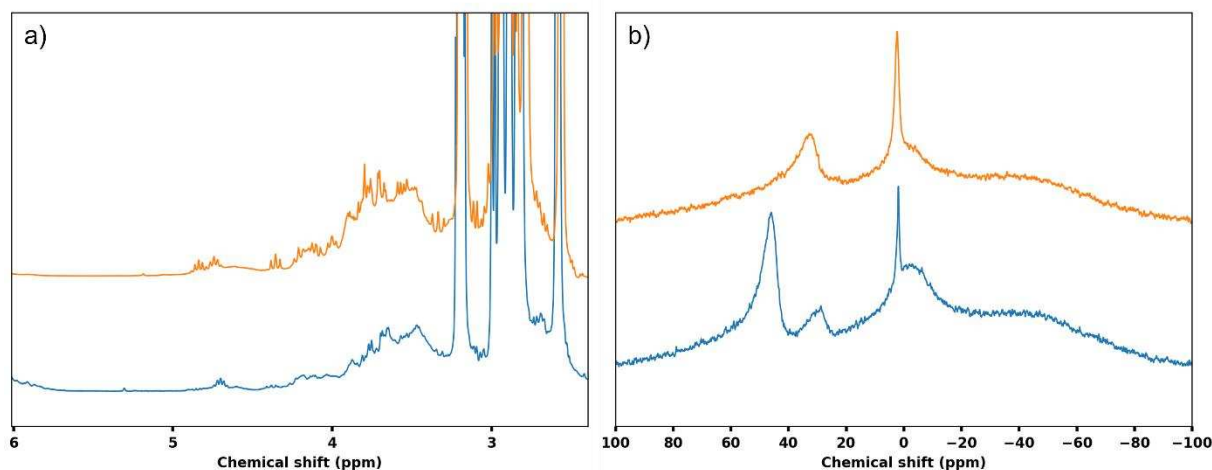
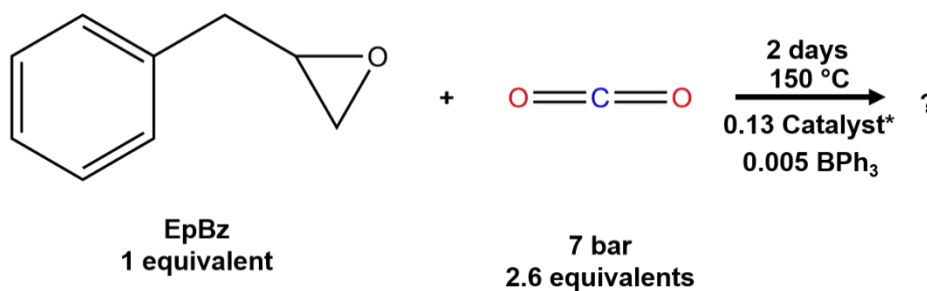


Figure 16: a) <sup>1</sup>H NMR spectra of the catalytic reaction conducted with a high borane concentration at 80 °C (blue) and 150 °C (orange), b) corresponding <sup>11</sup>B NMR spectra.

This new peak at 2 ppm could be attributed to a tetravalent boron species like the one presented in Figure 13. However, due to the high formation of polymeric species in these reactions and the low carbonate yield, we did not try a more precise identification. We observed that the increase of borane stoichiometry prevented the cyclic carbonate formation.

#### e. Attempts with other catalysts +BPh<sub>3</sub>

The last experiments we conducted in this part of the project were catalytic experiments using other catalysts paired with BPh<sub>3</sub>. We tried commercial MgO, CaO, Mg(OH)<sub>2</sub> and Ca(OH)<sub>2</sub>. We kept the other parameters constant (Scheme 6:).



Scheme 6: Attempt at the cycloaddition of  $\text{CO}_2$  on EpBz catalysed by different catalysts+BPh<sub>3</sub> in neat condition. \* catalysts: MgO<sub>com</sub>, CaO, Mg(OH)<sub>2</sub>, Ca(OH)<sub>2</sub>.

As shown in Figure 17:, we could see that in almost all the cases the presence of BPh<sub>3</sub> reduced the consumption of the epoxide. We already discussed the case of the MgO<sub>500</sub> nanoparticles. For commercial MgO<sub>com</sub>, the addition of BPh<sub>3</sub> did not have any effect. In the case of CaO, the epoxide consumption decreased from 9 % to 3 % whereas the production of cyclic carbonate did not vary. In fact, the selectivity toward the cyclic carbonate increased due to a reduction of the formation of the polymeric product. The same phenomenon occurred in the case of Mg(OH)<sub>2</sub>. Ca(OH)<sub>2</sub> initially was not active at all in the reaction (no product was formed during the reaction). However, the addition of the borane seemed to help both the cycloaddition and the secondary reactions to start. This could be due to the pre-activation of the epoxide by the borane as mentioned above. Post mortem analyses would be necessary to verify that the Ca(OH)<sub>2</sub> catalyst did not undergo strong morphological or crystallographic changes.

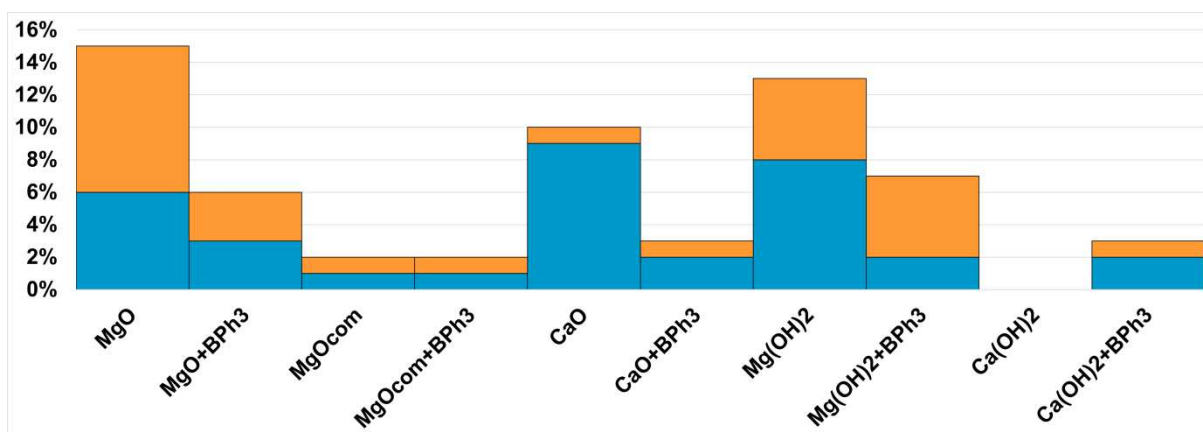


Figure 17: Performances of the different catalysts with and without BPh<sub>3</sub> in terms of epoxide consumption (blue+orange) and cyclic carbonate yield (orange).

In terms of boron NMR, all the reactions gave peaks at 32 ppm and 23 ppm (Figure 18:), with the notable exception of Ca(OH)<sub>2</sub>+BPh<sub>3</sub> that also gave a peak at 20 ppm. This boron specie could be responsible of the activation of the reaction; further studies would have to be made in order to better understand the mechanism at stakes here. The peak at 7 ppm that we assigned to



a tetravalent boron specie was never seen in these experiments. This peak specifically came from an interaction involving MgO nanoparticles synthesised by the precipitation-calcination method.

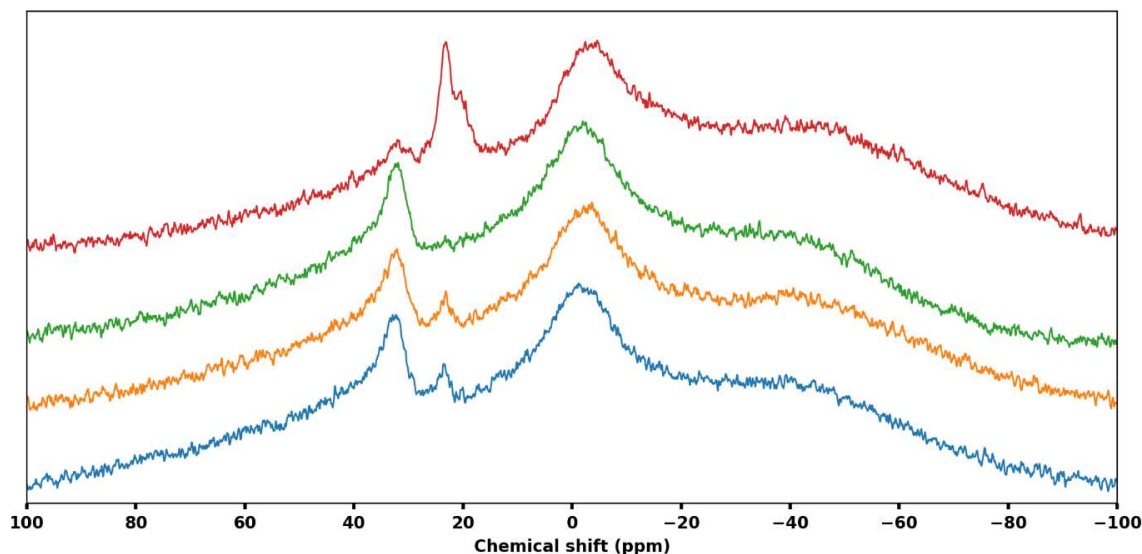


Figure 18: <sup>11</sup>B NMR of the crude of reaction after the cycloaddition using BPh<sub>3</sub> and MgO<sub>com</sub> (blue), CaO (orange), Mg(OH)<sub>2</sub> (green) and Ca(OH)<sub>2</sub> (red).

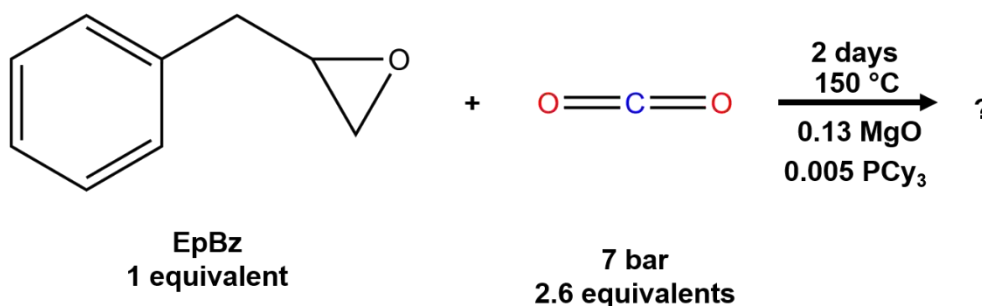
Most of these results were not reported in the literature. The combination of MgO<sub>500</sub> and BPh<sub>3</sub> reduced the catalytic activity of the nanoparticles, but the reaction was initiated at lower temperature. BPh<sub>3</sub> played three roles: it preactivated the epoxide making the cycloaddition reaction happen at lower temperature, it poisoned the MgO surface at higher temperature, and it initiated the epoxide polymerisation. When allied with other catalysts than MgO<sub>500</sub>, it modified either the activity or the selectivity of the reaction. We believed that the inconvenients of the borane usage (MgO poisoning and epoxide polymerisation) could be get rid of by working in solvent.

However, before getting to the reactions in solvent, we tried a completely different strategy: we tried to consider the MgO nanoparticles as Lewis acids and combined them with molecular Lewis base. Even though the strength of MgO basic sites was high, we saw in chapter III (and even in this chapter) that MgO nanoparticles also have weak Lewis acidic sites that were actually important in the cycloaddition reaction. So, we wondered: could MgO play the role of the acid in our NanoFLP?

## 4. Inverting the NanoFLP

### a. Phosphines as molecular Lewis bases

Phosphines were often used as Lewis bases in molecular FLP. Plus, recent studies in our lab showed promising NanoFLP-like systems where phosphines played the role of molecular Lewis base ligands<sup>23</sup>. To simplify the study, we decided to keep the previous parameters, but replaced the borane with a phosphine (**Erreur ! Source du renvoi introuvable.**). Since MgO surfaces were reported to have weak acidic sites, we wanted to use a strong base to increase the probability to have a Lewis acid-base interaction between the MgO surface and the phosphine. Hence, we chose tri(cyclohexyl)phosphine (PCy<sub>3</sub>) which was reported to be a stronger Lewis base than other phosphines usually used in FLP chemistry such as PPh<sub>3</sub><sup>24</sup>. Some reports in the literature mentioned that phosphines could be involved in the catalysis of the cycloaddition of CO<sub>2</sub> (as a ligand of a metallic complex, or as a cocatalyst)<sup>25-27</sup>. However, we did not find any consistent study on the role of phosphines as catalyst of the reaction.



*Scheme 7: Attempt at the cycloaddition of CO<sub>2</sub> on EpBz catalysed by MgO+PCy<sub>3</sub> in neat conditions.*

With that in mind we did the cycloaddition with PCy<sub>3</sub> alone before trying with MgO+PCy<sub>3</sub> and analysed the <sup>1</sup>H NMR spectra (Figure 19:). The reaction with PCy<sub>3</sub> and MgO+PCy<sub>3</sub> gave very similar products than the one with MgO alone: the cyclic carbonate, peaks around 3.5 ppm (polymeric species), a doublet around 4.3 ppm (it was a triplet at the same chemical displacement in catalytic reaction with MgO only), and multiplet at 6.5 ppm (see Annexe 7). When looking closer to the different species, we could confirm that the 6.5 ppm signal was the same for MgO and PCy<sub>3</sub>. This peak was associated to the secondary product **5** in Figure 6:.. The signal at 4.3 ppm was different depending on the catalyst: a triplet in the case of MgO and a doublet in the case of PCy<sub>3</sub>. This could mean that we obtained the secondary product **6** (attribution proposed in Annexe 8). Finally, we noted the presence of a singlet signal at 3.7 ppm in the spectrum associated to the reaction with PCy<sub>3</sub>. This signal was not present in the reaction with MgO+PCy<sub>3</sub>. It could be attributed to secondary product **4** (attribution proposed in Annexe 8).

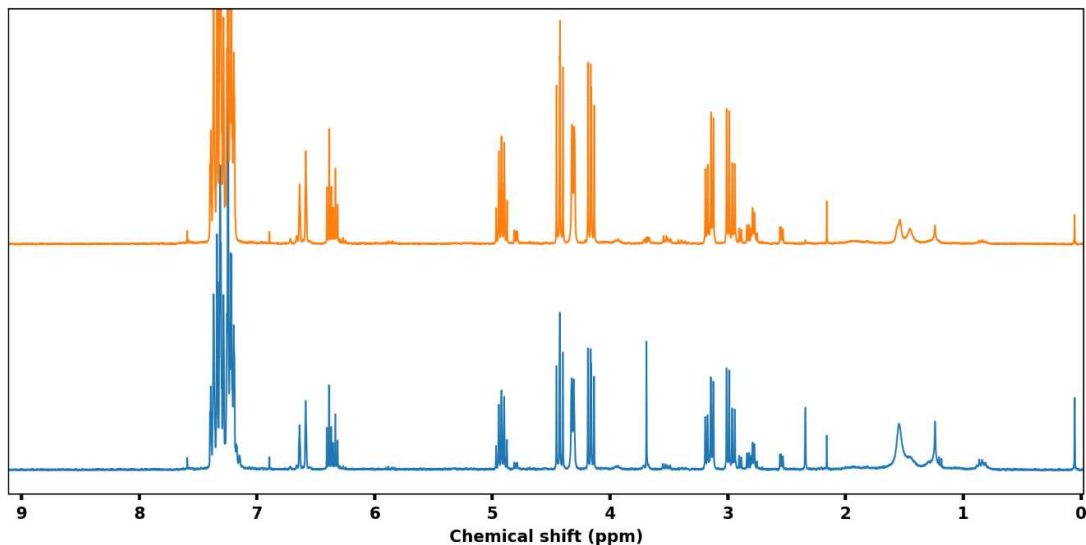


Figure 19: <sup>1</sup>H NMR spectra of the reaction using PCy<sub>3</sub> (blue) and MgO+PCy<sub>3</sub> (orange) as catalyst.

The ratio between the different species was quite different compared to the reaction with MgO alone (Table 3:). The overall epoxide consumption was almost complete (96 % consumption). The polymeric specie and the 3.7 ppm product, when present, were minor compared to the other products. The production of cyclic carbonate, 4.3 ppm product and 6.3 ppm product were almost the same. This meant that under these conditions, the selectivity of the reaction using PCy<sub>3</sub> and MgO were radically different, and that the efficiency of PCy<sub>3</sub> in terms of epoxide consumption was much higher than the one of MgO. The later was almost playing no role in the catalytic reaction, even if we could attribute the slightly higher carbonate yield in MgO+PCy<sub>3</sub> to the activity of MgO. To be more precise it could be that MgO increased the selectivity toward cyclic carbonate by preventing the formation of the 3.7 ppm product. However, studies on the significance of these results would have to be made to confirm these propositions.

Species	Epoxide	Cyclic carbonate	Sec. Product 3.5 ppm	Sec. Product 3.7 ppm	Sec. Product 4.2 ppm	Sec. Product 6.5 ppm
MgO	0.85	0.09	0.05	0	0.01	0
PCy <sub>3</sub>	0.04	0.29	0.03	0.7	0.36	0.21
MgO+PCy <sub>3</sub>	0.04	0.33	0.03	0	0.39	0.21

Table 3: Quantities (in equivalent) of the different species at the end of the 2 days cycloaddition of CO<sub>2</sub> on epoxides catalysed by MgO, PCy<sub>3</sub> or MgO+PCy<sub>3</sub>.

## b. Impact of the temperature

In these conditions it was quite hard to see if MgO+PCy<sub>3</sub> had any interest compared to PCy<sub>3</sub> alone, so we decided to reduce the reaction duration to go back to lower epoxide consumption rates. Then we decided to study the impact of the temperature on both the epoxide consumption and the selectivity (Table 4:). At 80 °C, it seemed that there was no difference between the reaction with the phosphine alone and the reaction with MgO and the phosphine. The epoxide consumption was very low, and we only detected traces of cyclic carbonate. Despite being a better catalyst than MgO, phosphines could not quantitatively catalyse the cycloaddition reaction at such low temperatures. At 120 °C, there was a slight difference when MgO was used. The experiment with MgO+PCy<sub>3</sub> yielded 10 % cyclic carbonate against 7 % for the reaction using PCy<sub>3</sub> alone. At 150 °C the two experiments gave almost the same results, we could not consider the 1 % difference to be significant since we did not repeatability studies here.

It was interesting to see that the 3 hours reaction almost did not produce any 4.2 ppm nor 6.5 ppm secondary products. This hinted toward two possibilities: the fact that cyclic carbonates further evolved toward these secondary products after a certain time, or that the formation of these secondary products was slower than the cycloaddition and was detectable only after a certain time. Given our proposition for the identification of the secondary products, it was not obvious that the two reactions were coupled. The second hypothesis seemed more plausible.

Temperature	Catalyst	Epoxide	Cyclic carbonate	Sec. Product 3.5ppm	Sec. Product 4.2 ppm	Sec. Product 6.5 ppm
80 °C	PCy <sub>3</sub>	0.99	< 0.01	0.01	0	0
	MgO+PCy <sub>3</sub>	0.99	< 0.01	0.01	0	0
120 °C	PCy <sub>3</sub>	0.91	0.07	0.02	0	0
	MgO+PCy <sub>3</sub>	0.88	0.10	0.01	0	0
150 °C	PCy <sub>3</sub>	0.58	0.39	0.02	0.01	0
	MgO+PCy <sub>3</sub>	0.57	0.40	0.01	0.02	0

Table 4: Quantities (in equivalent) of the different species at the end of the 3 hours cycloaddition of CO<sub>2</sub> on epoxides catalysed by PCy<sub>3</sub> or MgO+PCy<sub>3</sub> depending on the temperature.

Our attempt at seeing a synergetic effect between MgO nanoparticles and phosphines was not successful. However, we realised that phosphines were underestimated catalysts for the cycloaddition of CO<sub>2</sub> on epoxides. It would be interesting to make an in depth study to better understand what were the key parameters (basicity, steric hindrance) that influenced the epoxide consumption and the selectivity toward the different products. It would be also interesting to compare its efficiency with other homogeneous catalysts, both for the formation of cyclic

carbonate, or the formation of the 6.3 ppm product. We did not go further with our studies on phosphine activities since what interested us was the development of a NanoFLP catalyst.

## 5. Conclusion

In this first part, we studied the activity of MgO nanoparticles in the cycloaddition of CO<sub>2</sub> on EpBz in neat condition. We realised that the nanoparticles were active catalysts of the reaction with an activity comparable to the one of the reference paper of Tu and coworkers<sup>21</sup>. We detected formation of secondary products that were not mentioned in the reference study and tried to identify them. Impact of the reaction duration and temperature were studied in an attempt to improve the selectivity of the reaction toward cyclic carbonate.

The impact of borane addition was then studied. Immediate polymerisation of the epoxide was evidenced when we introduced the strong Lewis acid BCF, but the weaker Lewis acid BPh<sub>3</sub> led to partial polymerisation. The combination of MgO and BPh<sub>3</sub> led to a reduction of the catalytic activity of the oxide nanoparticles at 150 °C, but to an initiation of the cycloaddition reaction at a lower temperature than with MgO alone. We concluded that the borane played three roles: preactivation of the epoxide, polymerisation of the epoxide, and poisoning of the MgO surface.

Other catalysts were tested both with and without BPh<sub>3</sub>: commercial MgO, CaO, Mg(OH)<sub>2</sub> and Ca(OH)<sub>2</sub>. We observed behaviours expected from the bibliography: commercial MgO was less active than MgO synthesized by precipitation-calcination and calcined at 500 °C, CaO was less active than MgO. However, we also observed unreported catalytic activity of Mg(OH)<sub>2</sub> nanoparticles, as well as the catalytic of Ca(OH)<sub>2</sub>+BPh<sub>3</sub> whereas Ca(OH)<sub>2</sub> alone was not active.

The phosphine PCy<sub>3</sub> was also tested in the reaction and appeared to be an unreported catalyst for the cycloaddition of CO<sub>2</sub> on epoxide despite having a low carbonate selectivity. The par MgO+PCy<sub>3</sub> did not behave very differently from PCy<sub>3</sub> alone. We abandoned the study with phosphines for the following of the project, but an extensive study of the activity of different phosphines in the cycloaddition reaction would be interesting for the bibliography.

For the following of the project, we decided to modify our experimental protocol and to start using solvents. As mentioned earlier, we believed that use of solvent could reduce the epoxide polymerisation activated by borane and mitigate the surface poisoning of MgO nanoparticles. In one of their study, Aresta and coworkers<sup>11</sup> investigated the impact of the solvent on the catalytic performances of Nb catalysts. They found that DMF gave the best performances. Hence, we decided to start with this solvent.

## IV. Cycloaddition in DMF

### 1. Reported impact of DMF in the cycloaddition of CO<sub>2</sub> on epoxides

In their study<sup>11</sup>, Aresta and coworkers compared different solvents. They used xylene, diglyme, DMSO and DMF in the 12 hour long cycloaddition of CO<sub>2</sub> on styrene oxide catalysed by their Nb<sub>2</sub>O<sub>5</sub> catalyst at 135 °C under 50 bar of CO<sub>2</sub>. They found that DMF gave the best results (Table 5:) with a 80 % cyclic carbonate yield against 1 % for both xylene and diglyme, and 5 % for DMSO. However, when comparing the reaction blanc without catalyst, we could see that DMF alone was able to catalyse the reaction with a 35 % carbonate yield. DMF was a better catalyst than Nb<sub>2</sub>O<sub>5</sub> in the other solvents and it allowed to drastically increase its activity. It was also interesting to note that in their study, they mentioned neat reactions where the carbonate selectivity was low and the isomerisation of the epoxide to the aldehyde was predominant. This would correspond to the formation of the secondary product **3** in our Figure 6:.

Solvent	Catalyst	Cyclic carbonate yield
Xylene	Nb <sub>2</sub> O <sub>5</sub>	1 %
	None	0 %
Diglyme	Nb <sub>2</sub> O <sub>5</sub>	1 %
	None	0 %
DMSO	Nb <sub>2</sub> O <sub>5</sub>	5 % + side products
	None	1 % + side products
DMF	Nb <sub>2</sub> O <sub>5</sub>	80 %
	None	35 %

Table 5: Influence of the solvent on the activity of Nb<sub>2</sub>O<sub>5</sub> catalyst in the cycloaddition of CO<sub>2</sub> on styrene oxide at 135 °C for 12 hours. Reproduced from Aresta et al.<sup>11</sup>.

The author proposed that DMF (and amides in general) were good promoters of the reaction by increasing the nucleophilicity of oxygen atom in either the epoxide or CO<sub>2</sub> (Figure 20:). However, they needed a DMF/epoxide ratio superior to 10 to see the catalytic effect of DMF alone. In this activation, DMF interacted through its nitrate electron doublet just like a Lewis base. Since Nb<sub>2</sub>O<sub>5</sub> was a material known for its Lewis acid properties<sup>28</sup>, this would mean that the author evidenced a synergy between a Lewis acid nanoparticle and a molecular Lewis base for the catalysis of the reaction. This was encouraging in the perspective of our NanoFLP project. We hoped that same effect could be detectable with our MgO catalyst, or with our MgO+BPh<sub>3</sub> pair. However, we could fear that this phenomenon would also happen if we used Lewis acids such as borane in DMF for the reaction.

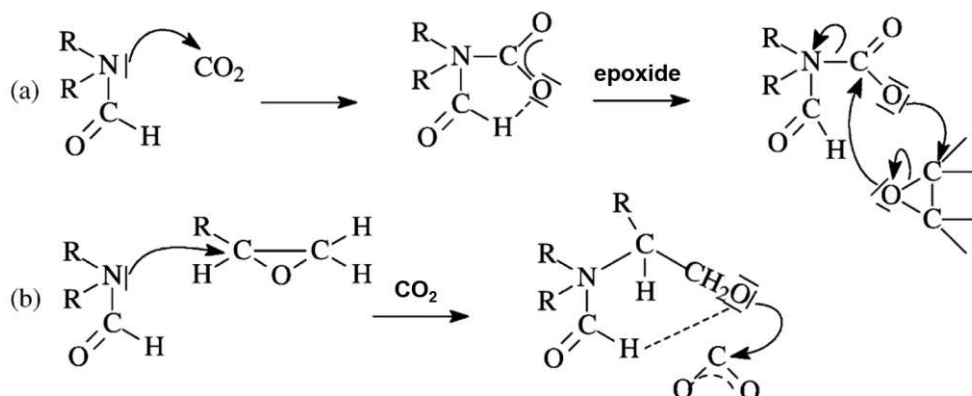
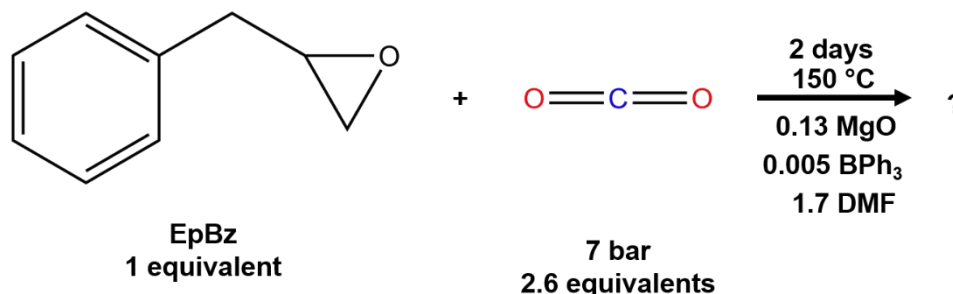


Figure 20: Proposition for the activation of CO<sub>2</sub> (a) and the epoxide (b) by DMF in the cycloaddition reaction. From Aresta et al.<sup>11</sup>.

## 2. Cycloaddition of CO<sub>2</sub> on EpBz in DMF catalysed by MgO+BPh<sub>3</sub>

We decided to conduct an experiment where we added some DMF in the solution but we kept the DMF/epoxide ratio well below 10 to limit catalysis of the reaction by DMF alone, as described by Aresta et al.<sup>11</sup>. We wanted to see if the presence of DMF would increase or decrease the catalytic activity of our MgO catalyst. For comparison, we kept the stoichiometry used in the previous part of the chapter, with the addition of DMF (Scheme 8:).



Scheme 8: Attempt at the cycloaddition of CO<sub>2</sub> on EpBz catalysed by MgO+BPh<sub>3</sub> in DMF.

We made four experiments: one without catalyst and with DMF alone, one with MgO, one with BPh<sub>3</sub> and one with MgO+BPh<sub>3</sub>. Corresponding <sup>1</sup>H and <sup>11</sup>B NMR spectra were shown in Figure 21:. Interestingly, the reaction with DMF alone led to the formation of cyclic carbonate. DMF probably catalysed the reaction on its own. The addition of either MgO or BPh<sub>3</sub> decreased the selectivity toward cyclic carbonate. Calculation of the ratio between the different present species (Table 6:) confirmed this hypothesis.

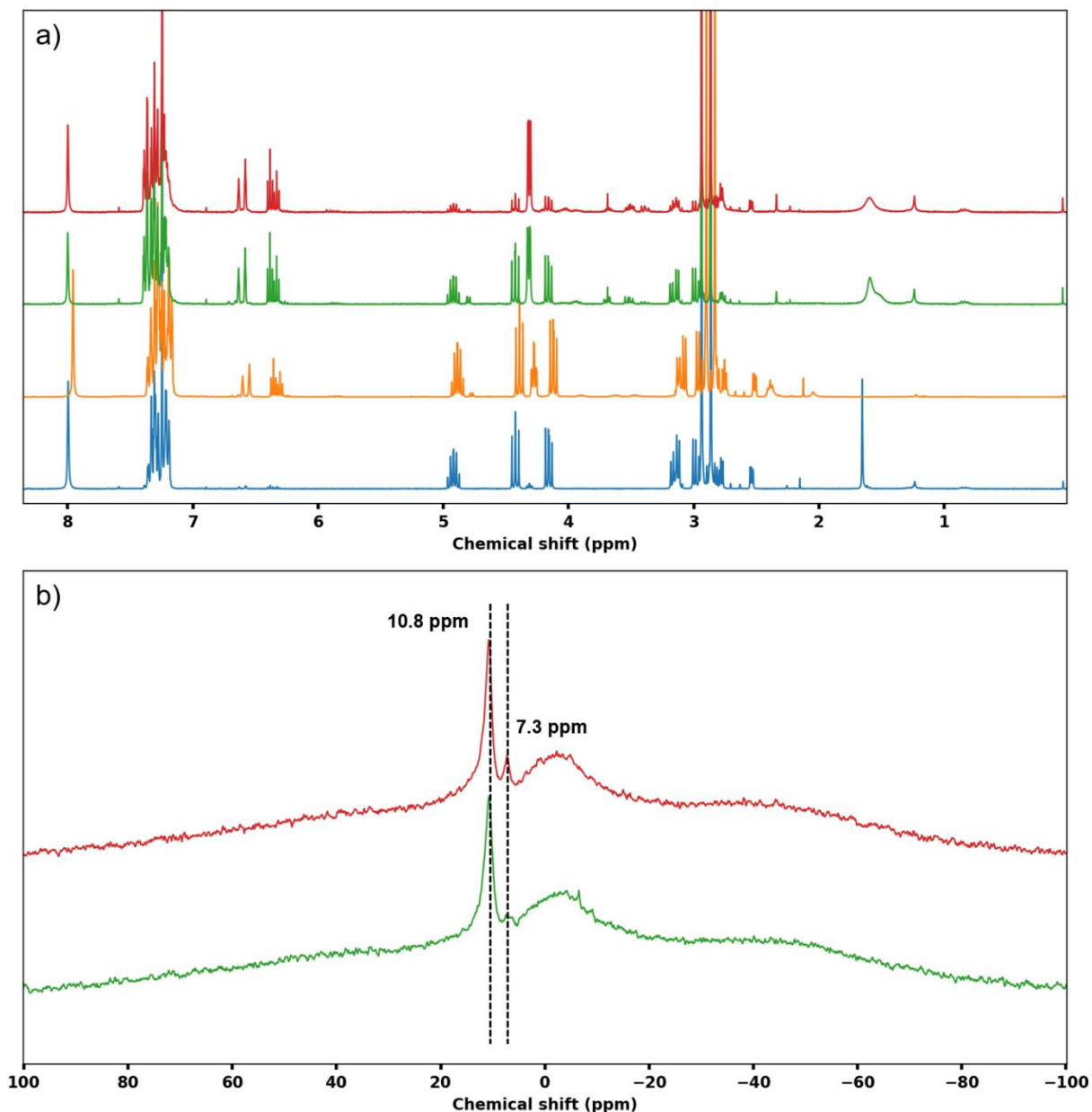


Figure 21: a)  $^1\text{H}$  NMR spectra of the cycloaddition of  $\text{CO}_2$  on EpBz in DMF catalysed by: no catalyst (blue), DMF+MgO (orange), DMF+BPh<sub>3</sub> (green), DMF+MgO+BPh<sub>3</sub> (red). b)  $^{11}\text{B}$  NMR spectra of the cycloaddition of  $\text{CO}_2$  on EpBz in DMF catalysed by: BPh<sub>3</sub> (green), MgO+BPh<sub>3</sub> (red).

The use of DMF alone yielded a 74 % epoxide consumption with an 86 % selectivity toward the cyclic carbonate. There was no polymeric species detected and the two other secondary products were the species **5** (6.5 ppm) and the **1** (triplet at 4.3 ppm) as described in Figure 6:. When adding the MgO, the epoxide consumption increased to 89 % but the carbonate selectivity dropped to 41 %. This was mainly due to an increase of the formation of species **5** (from 0.03 to 0.18 equivalents formed) and **1** (from 0.07 to 0.33 equivalents formed). The addition of BPh<sub>3</sub> increased the epoxide consumption to 100 %, but reduced the carbonate selectivity to 18 %. The secondary product **1** was not detected anymore and we detected instead the secondary product **6**



(doublet at 4.3 ppm). When using MgO+BPh<sub>3</sub>, the consumption decreased to 94 % and the carbonate selectivity to 6 %. The ratio between the different secondary products was roughly the same as for BPh<sub>3</sub>. The <sup>11</sup>B NMR (Figure 21:b) was the same for the experiment with BPh<sub>3</sub> and MgO+BPh<sub>3</sub>: a main peak at 10.8 ppm and a smaller one at 7.3 ppm.

Catalyst	Epoxide	Cyclic carbonate	Sec. Product 3.5ppm	Sec. Product 4.2 ppm	Sec. Product 6.5 ppm
DMF	0.26	0.64	0	0.07	0.03
DMF+MgO	0.11	0.36	0.02	0.33	0.18
DMF+BPh <sub>3</sub>	0	0.18	0.04	0.49	0.28
DMF+MgO+BPh <sub>3</sub>	0.06	0.06	0.08	0.53	0.28

Table 6: Quantities (in equivalent) of the different species at the end of the 48 hours cycloaddition of CO<sub>2</sub> on epoxides in DMF depending on the catalyst.

In contrast to the result obtained by Aresta and co-workers, DMF was able to catalyse the reaction even if the DMF/epoxide ratio was lower than 10. This could be explained by the fact that we used higher temperature than the one used by Aresta (150 °C instead of 135 °C). DMF gave a good selectivity toward the cyclic carbonate with no polymerisation of the epoxide, however secondary products were still visible; this was not mentioned in the reference article. Adding either MgO or BPh<sub>3</sub> increased the consumption of epoxide but drastically reduced the selectivity. For the case DMF+MgO, the epoxide consumption could let us think that DMF and MgO were catalysing the reaction independently (since the consumption with DMF+MgO was approximately equal to the consumption with DMF+consumption with MgO). However, the selectivity decreased, meaning that there was an interaction favouring the formation of secondary products **1** and **5**. In the case of DMF+BPh<sub>3</sub>, we had a complete consumption of the epoxide. BPh<sub>3</sub> was not active on its own, but with help of DMF it catalysed the formation of secondary products **1** and **6**. It was possible that the two peaks appearing in <sup>11</sup>B NMR could be attributed to BPh<sub>3</sub>—DMF adducts. In association with DMF, MgO was less active than MgO+BPh<sub>3</sub> which was less active than BPh<sub>3</sub>. This could be explained by the fact that BPh<sub>3</sub> was a stronger Lewis acid than the MgO Lewis acid sites, and that when mixed with MgO, some of the BPh<sub>3</sub> were coordinated to the surface, hence not interacting with DMF.

#### a. Impact of the reaction temperature

In these 2 days long reactions, we obtained low selectivities (< 50 %) except in the case with DMF alone. As we saw with the study on the activity of phosphines, a low selectivity could be due to some competing reactions between the formation of cyclic carbonate and secondary products.

Thus, we decided to reduce both the time of the experiments and the temperature of the reaction to see if it was possible to obtain better selectivity. Table 7: showed the performances in terms of epoxide consumption and carbonate selectivity for the different experiments. In a 3 hour long reaction, DMF was almost inactive at 150 °C, and no cyclic carbonate was detected at 120 °C. When adding the different catalysts, we could see a trend for the activity and the selectivity both at 120 °C and 150 °C. BPh<sub>3</sub> gave the best results, followed by MgO+BPh<sub>3</sub> and finally MgO. Both the activity and the selectivity of the catalysts were best at 150 °C.

Catalyst	Temperature	Epoxide consumption	Cyclic carbonate selectivity
None	120°C	> 1 %	0 %
MgO		3 %	20 %
BPh <sub>3</sub>		12 %	45 %
MgO+BPh <sub>3</sub>		8 %	39 %
None	150°C	2 %	53 %
MgO		5 %	72 %
BPh <sub>3</sub>		25 %	84 %
MgO+BPh <sub>3</sub>		20 %	76 %

Table 7: 3 hour long cycloaddition of CO<sub>2</sub> on EpBz in DMF catalysed by MgO+BPh<sub>3</sub> at different temperatures.

<sup>11</sup>B NMR analysis of the boron containing experiments (Figure 22:) showed new peaks at -6.7 ppm when only BPh<sub>3</sub> was introduced. This peak was present at both 120 °C and 150 °C, but seemed to be inhibited by the presence of MgO. Interestingly it was not present either in the 2 days long experiment. This could mean that this specie was transient and disappeared after a certain reaction time. In all the experiment we found the peak at 10.8 ppm present in the 2 days long reaction. However, it seemed that in the experiment with MgO+BPh<sub>3</sub> at 150 °C there was a new peak at 0.1 ppm. It was a bit hard to confirm since the peak was broad and was on top of the broad boron signal associated to borosilicate glass. More in depth analysis would be necessary to precisely identify these new boron species.

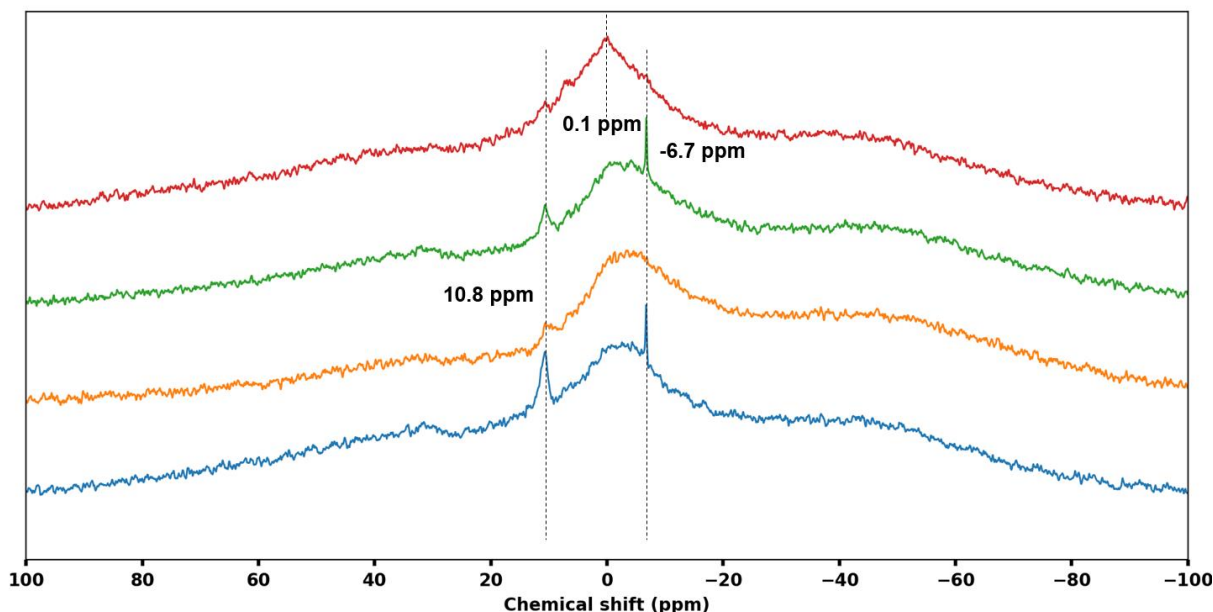


Figure 22: <sup>11</sup>B NMR spectra of the 3 hour cycloaddition reactions in DMF. Blue: BPh<sub>3</sub> 120 °C, orange: MgO+BPh<sub>3</sub> 120 °C, green: BPh<sub>3</sub> 150 °C, red: MgO+BPh<sub>3</sub> 150 °C.

### b. Impact of BPh<sub>3</sub> concentration

We wondered if this boron specie was prevented to form due to its interaction with MgO, so we decided to increase the amount of borane in the reaction to see if we could saturate the MgO sites responsible for the adsorption of this boron specie. We multiplied the amount of BPh<sub>3</sub> by three (7.2 mg, 0.015 equivalents) and kept the other parameters constant. We did the reaction with BPh<sub>3</sub> alone and with MgO+BPh<sub>3</sub>. Figure 23:b showed the boron NMR spectra we obtained at the end of the two experiments.

With BPh<sub>3</sub> we obtained the two peaks at 10.8 ppm and 7.3 ppm present in the 2 days long reaction, the peak at -6.7 ppm present in the 3 hours long reaction, and a new peak at 2.2 ppm. With MgO+BPh<sub>3</sub>, we obtained the same peaks with the notable exception of the peak at -6.7 ppm. In the end, it seemed that increasing the amount of borane did not allow the retention of this peak in presence of MgO, but it allowed the formation of a new specie at 2.2 ppm. This lead us to think that the -6.7 ppm specie reacted with the MgO surface, and was not just adsorbed on it. When we looked at the catalytic performances (Figure 23:a), we saw that increasing the amount of borane did not increase the epoxide consumption by a lot (from 25 % to 29 %), but it decreased the carbonate selectivity (from 84 % to 54 %). However, when MgO was added the catalytic performances remained almost the same. It could be that excess of BPh<sub>3</sub> was not participating in the catalytic reaction, but compensated the borane adsorbed on the MgO surface.

a)	Catalyst	Temperature	Epoxide consumption	Cyclic carbonate selectivity
	$\text{BPh}_3$	150 °C	27 %	54 %
	$\text{MgO}+\text{BPh}_3$	150 °C	29 %	49 %

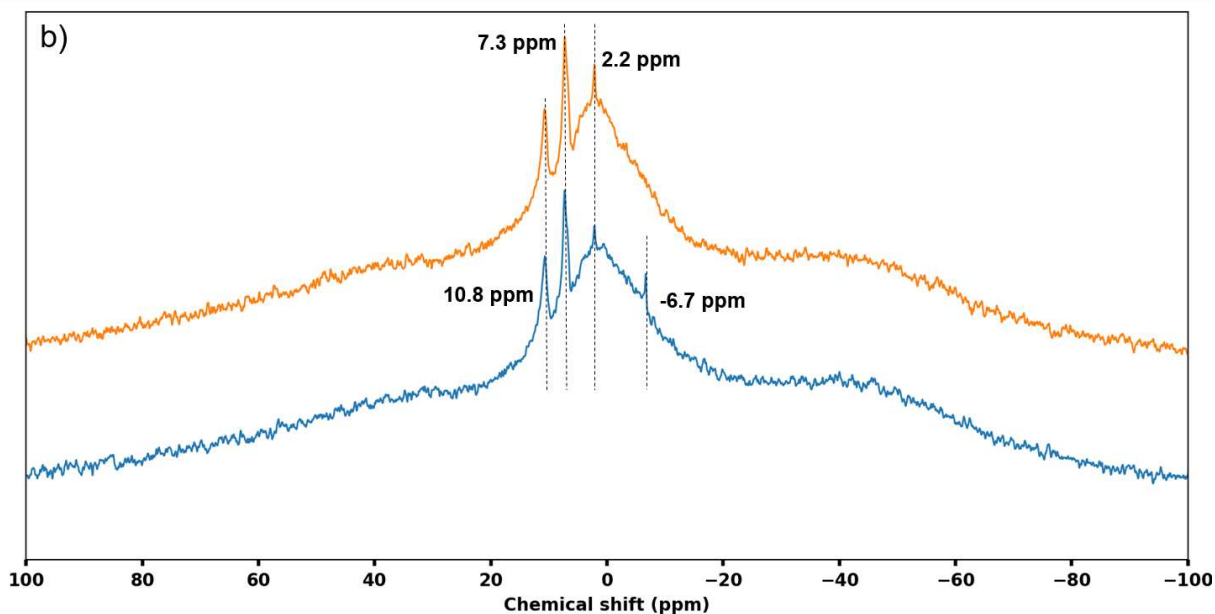


Figure 23: a) Performance of  $\text{BPh}_3$  and  $\text{MgO}+\text{BPh}_3$  (0.015 equivalents of borane instead of 0.005) in the 3 hour cycloaddition of  $\text{CO}_2$  on  $\text{EpBz}$  at 150 °C, b) Corresponding  $^{11}\text{B}$  NMR spectra,  $\text{BPh}_3$  in blue and  $\text{MgO}+\text{BPh}_3$  in orange.

### 3. Conclusion

We saw that DMF was indeed a solvent with unique properties for the cycloaddition of  $\text{CO}_2$  on epoxides. The reason was that DMF activated the reaction if sufficiently in excess. It was able to preactivate the reactants with its amide function, and helped improve the catalytic performances of the Lewis acid catalysts such as  $\text{BPh}_3$ . It also improved the catalytic performances of  $\text{MgO}$ , possibly by making its Lewis acid sites active for catalysis. However, working in DMF also brought some issues, especially in terms of selectivity. The catalyst we had were almost always yielding secondary products in consistent amount, even if it was possible to limit that by playing on the reaction duration. The other problem we faced was the formation of  $\text{BPh}_3$ —DMF adduct. Since DMF was reacting with  $\text{BPh}_3$ , it prevented us from forming the NanoFLP where the borane was activating the  $\text{MgO}$  nanoparticle sites.

Even if the reactivity of  $\text{MgO}$  and/or borane ligands would be lower on their own, it would be more judicious to choose a solvent where the nanoparticles and the borane would interact with each other. However, this interaction should not be too strong for it would poison the active sites of the catalyst. This could be controlled by the strength of the borane we would choose. For example, a solvent where the coordination of the borane on the  $\text{MgO}$  surface would be necessary in order to ensure colloidal stability could be a good idea. Solvent like toluene seemed to be good candidates.

## V. Cycloaddition in toluene

Toluene has been a widely used solvent in organic chemistry and catalysis. It was used for the cycloaddition of CO<sub>2</sub> on epoxides in several studies<sup>1,4,5,11</sup>, but in most of these cases it was not considered as a good solvent. This was probably due to the fact that the low polarity of toluene brought issues with the dispersion of catalysts such as basic oxides. As we saw in Chapter IV, MgO nanoparticles tended to agglomerate in toluene, thus reducing the exposed surface and reducing the catalytic activity of the material. The low solubility of CO<sub>2</sub> in toluene might also be one of the downsides with working in such a solvent.

However, toluene was often used in ring-opening polymerisation and co-polymerisation of epoxides catalysed by boranes<sup>19,20,29,30</sup>. It was not specified why toluene was chosen as the solvent, but we could guess it was for its non-polar character that helped the solubilisation of the different reactants. The high boiling point at 110 °C allowing reflux at this temperature probably was also one of the criteria.

In our case, toluene seemed *a priori* a good solvent to attempt NanoFLP. The low affinity between MgO nanoparticles and toluene would favour the adsorption of borane ligands on its surface. MgO nanoparticles covered with BPh<sub>3</sub> ligands would be dispersible in toluene (Figure 24:a). However, the high solubility of aryl boranes in toluene would reduce the energy needed for the desorption of the borane, thus resulting in a dynamic exchange between ligands adsorbed on the MgO surface and free ligands in the solution (Figure 24:b). EpBz also was soluble on toluene, but the oxygen of the epoxide cycle would be more stable if close to a boron atom or a MgO surface, possibly forming a 3 component adduct MgO-EpBz-BPh<sub>3</sub> (Figure 24:c). These were just qualitative considerations, but it would be interesting somehow to quantify the energy and the exchange constants associated to these equilibria.

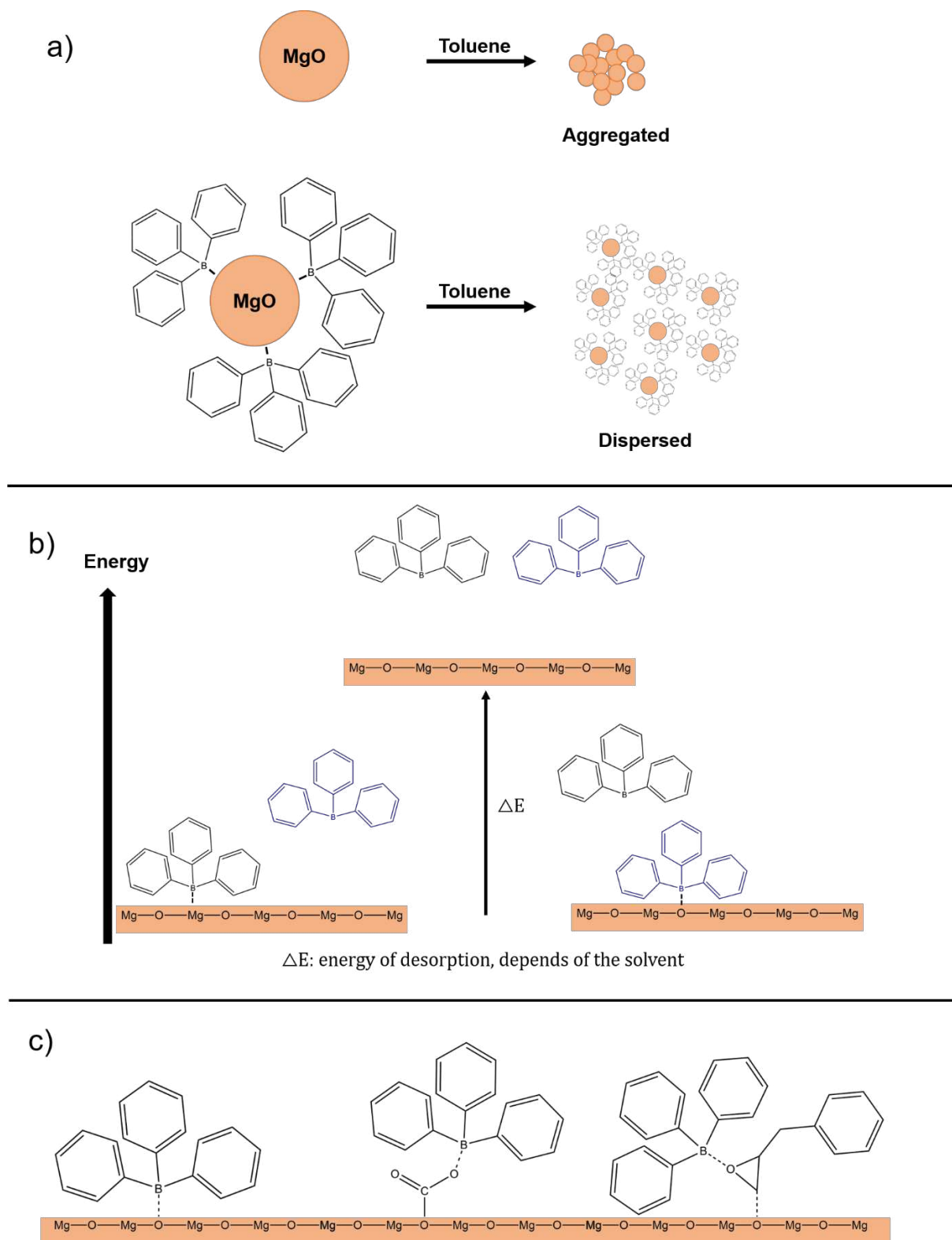
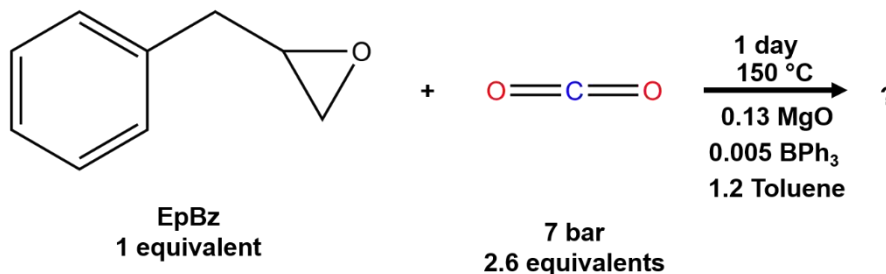


Figure 24: a) Impact of the presence of  $BPh_3$  ligands on the dispersion of MgO nanoparticles in toluene, b) dynamic exchange of  $BPh_3$  ligands in toluene, c) proposition of surface species involving MgO- $BPh_3$  NanoFLP.

## 1. Performance of MgO+BPh<sub>3</sub>

We decided first to keep the volume of solvent we used previously with DMF: 0.5 mL. For toluene, this would correspond to 4.7 mmol, or 1.2 equivalents compared to the epoxide (Scheme 9:). We were still in concentrated conditions, but we wanted to be able to compare the impact of DMF and toluene, and dilute the solution afterward if needed.



*Scheme 9: Attempt at the cycloaddition of CO<sub>2</sub> on EpBz catalysed by MgO+BPh<sub>3</sub> in toluene.*

We did the reaction with and without the presence of BPh<sub>3</sub>; we wanted to study the impact of the solvent on the modification induced by the borane. In neat conditions the borane overall reduced both the activity and the selectivity of the MgO nanoparticles, we hoped that diluting in toluene would change that. Results were presented in Figure 25: . Both of the experiments gave similar results with an epoxide consumption of 6 % and 7 % and a cyclic carbonate selectivity between 60 % and 70 %. The consumption was lower than the one in DMF since toluene was not active in the reaction, and it was lower than the reaction without toluene due to the dilution of the reactants. We realised that even in toluene the selectivity of the reaction was not that good, particularly due to the formation of polymeric products. However, we noted that BPh<sub>3</sub> did not reduce the MgO catalytic activity as it was the case in neat conditions.

As shown in the <sup>1</sup>H NMR spectra (Figure 25:a), the secondary products were mainly the same as in the reaction in neat conditions. We detected traces of DME in the experiment with MgO, probably due to residual traces from a past experiment, we did not consider it to be a product of the reaction. The <sup>11</sup>B NMR spectrum of the reaction with MgO+BPh<sub>3</sub> gave two peaks at 32 ppm and 23 ppm. These were two species that were already detected in the reactions without solvent. 32 ppm peak was associated to BPh(OR)<sub>2</sub>, and 23 ppm peak was associated to B(OR)<sub>3</sub> species. However, we did not detect any other boron species even with three repetitions of the reaction (Annexe 9). This meant that the reaction contained less different boron species, thus potentially simplifying the interpretation.

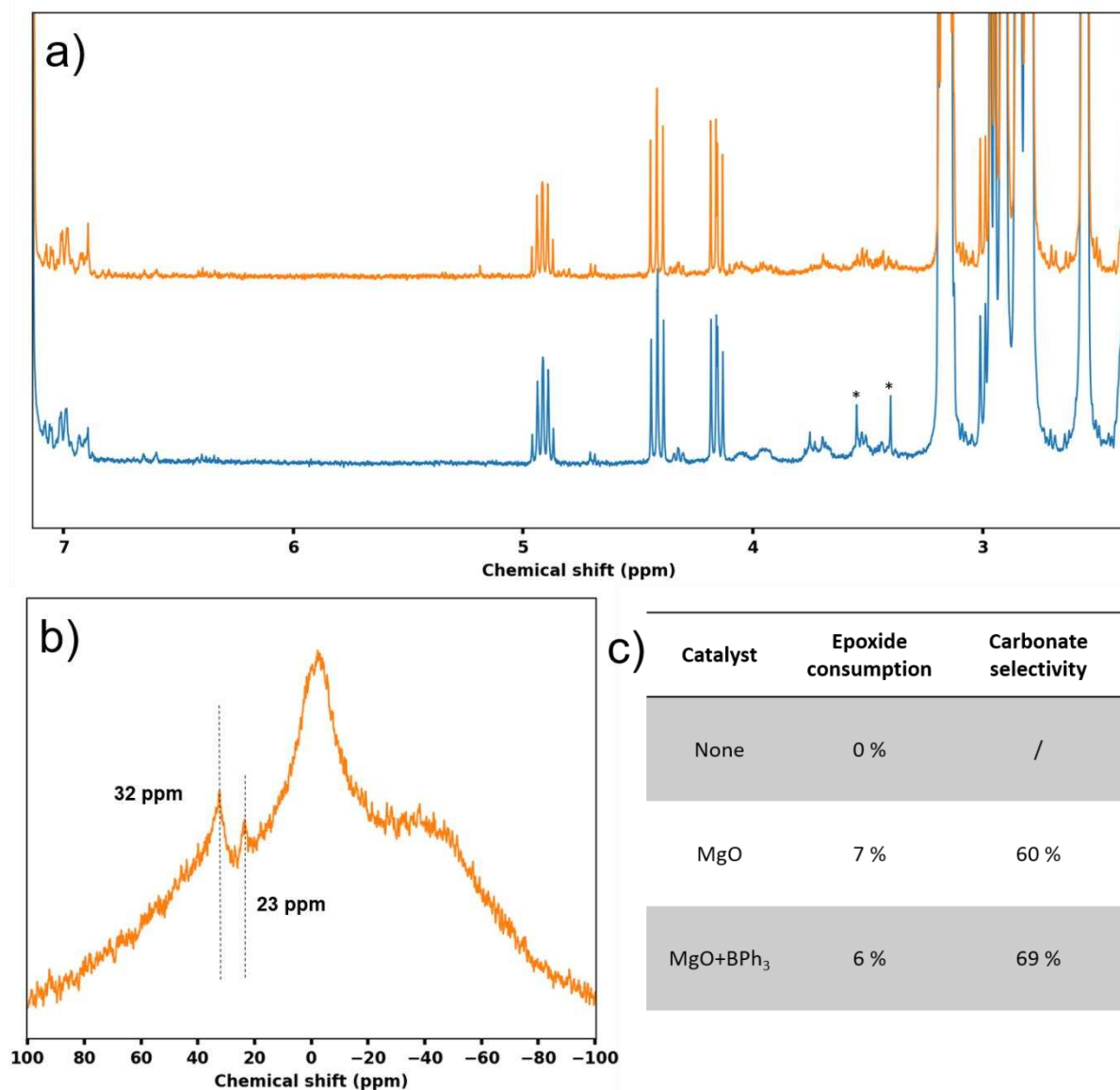
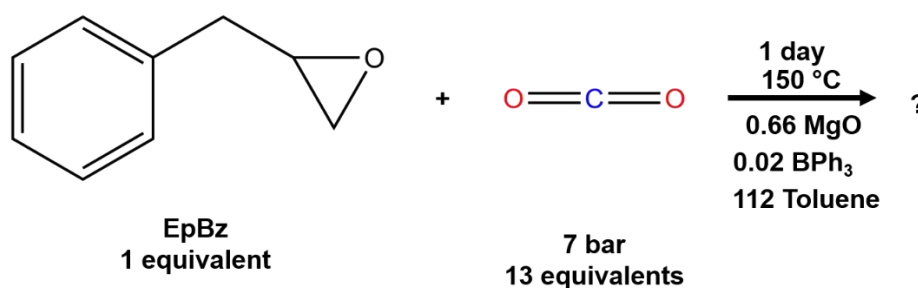


Figure 25: a)  $^1\text{H}$  NMR spectra of the cycloaddition reaction at 150 °C in toluene catalysed by MgO (blue) and MgO+BPh<sub>3</sub> (orange), traces of residual DME from a past experiment was marked with a \* symbol, b)  $^{11}\text{B}$  NMR spectrum of the corresponding experiment with MgO+BPh<sub>3</sub>, c) catalytic performances of the different catalysts.

The dilution with toluene impacted the performance of the MgO+BPh<sub>3</sub> catalyst. Our hypothesis was that toluene allowed a better exchange between the ligands at the surface of MgO nanoparticles. It was possible that in the neat reaction, the MgO surface was blocked by too strongly adsorbed species, thus reducing the catalytic activity of the nanoparticles. The carbonate selectivity was roughly the same than in the neat reaction (between 60 % and 70 %), and the addition of BPh<sub>3</sub> did not drastically modify the selectivity of the MgO catalyst. Since we wanted to increase the selectivity toward the cyclic carbonate, we decided to reduce the overall concentration of the reaction by adding more toluene, and to decrease the amount of epoxide introduced in the reaction. The amount of MgO, BPh<sub>3</sub> and CO<sub>2</sub> were kept constant (Table 8:).



MgO-based catalysts in the cycloaddition of CO<sub>2</sub> on epoxides



Scheme 10: Diluted conditions for the cycloaddition of CO<sub>2</sub> on EpBz catalysed by MgO+BPh<sub>3</sub> in toluene.

Since we decreased the amount of epoxide while keeping the amount of MgO constant, it meant that we increased the relative catalytic loading. We were not surprised to see that the epoxide consumption after one day of reaction was higher in these conditions (Table 8:). We also realised that the carbonate selectivity was slightly higher.

Epoxide	Toluene	Temperature	Duration	Catalyst	Epoxide consumption	Cyclic carbonate selectivity
0.5 mL	0.5 mL	150 °C	1 day	MgO	7 %	60 %
				MgO+BPh <sub>3</sub>	6 %	69 %
0.1 mL	1 mL	150 °C	1 day	MgO	13 %	75 %
				MgO+BPh <sub>3</sub>	13 %	72 %
0.1 mL	1 mL	110 °C	2 days	MgO	7 %	66 %
				MgO+BPh <sub>3</sub>	6 %	66 % (43 %)

Table 8: Performances of MgO and MgO+BPh<sub>3</sub> catalysts in the cycloaddition of CO<sub>2</sub> on EpBz in diluted conditions. Selectivity in parenthesis concerned the selectivity ignoring the dimer formation.

We also did another experiment at 110 °C to see what was the impact of the temperature. We let the reaction run during 2 days to have quantifiable measurements of the consumption and selectivity. To our surprise, the spectrum we obtained was quite different from the one we expected. Just like in one of the experiments conducted in neat conditions (Figure 14:c) we observed the apparition of the same peaks as the cyclic carbonate ones but shifted in terms of chemical displacement (**Erreur ! Source du renvoi introuvable.**). In the previous occurrence, the shift was toward higher chemical displacements, but here it was shifted toward the lower chemical displacements. The chemical displacement shift was not the same between the different peaks, just like it was the case in the reaction in neat conditions. This shift could be due to the dimerization of the cyclic carbonate, as we will discuss it in the next part. In the last line of Table 8:, two numbers were given for the cyclic carbonate selectivity: the first one was the selectivity toward both the cyclic carbonate and the dimer, and the one in parenthesis was the selectivity toward the cyclic carbonate only. When considering both the cyclic carbonate and the dimer, it

seemed that the experiment with MgO and MgO+BPh<sub>3</sub> gave similar results both in terms of epoxide consumption and carbonate selectivity.

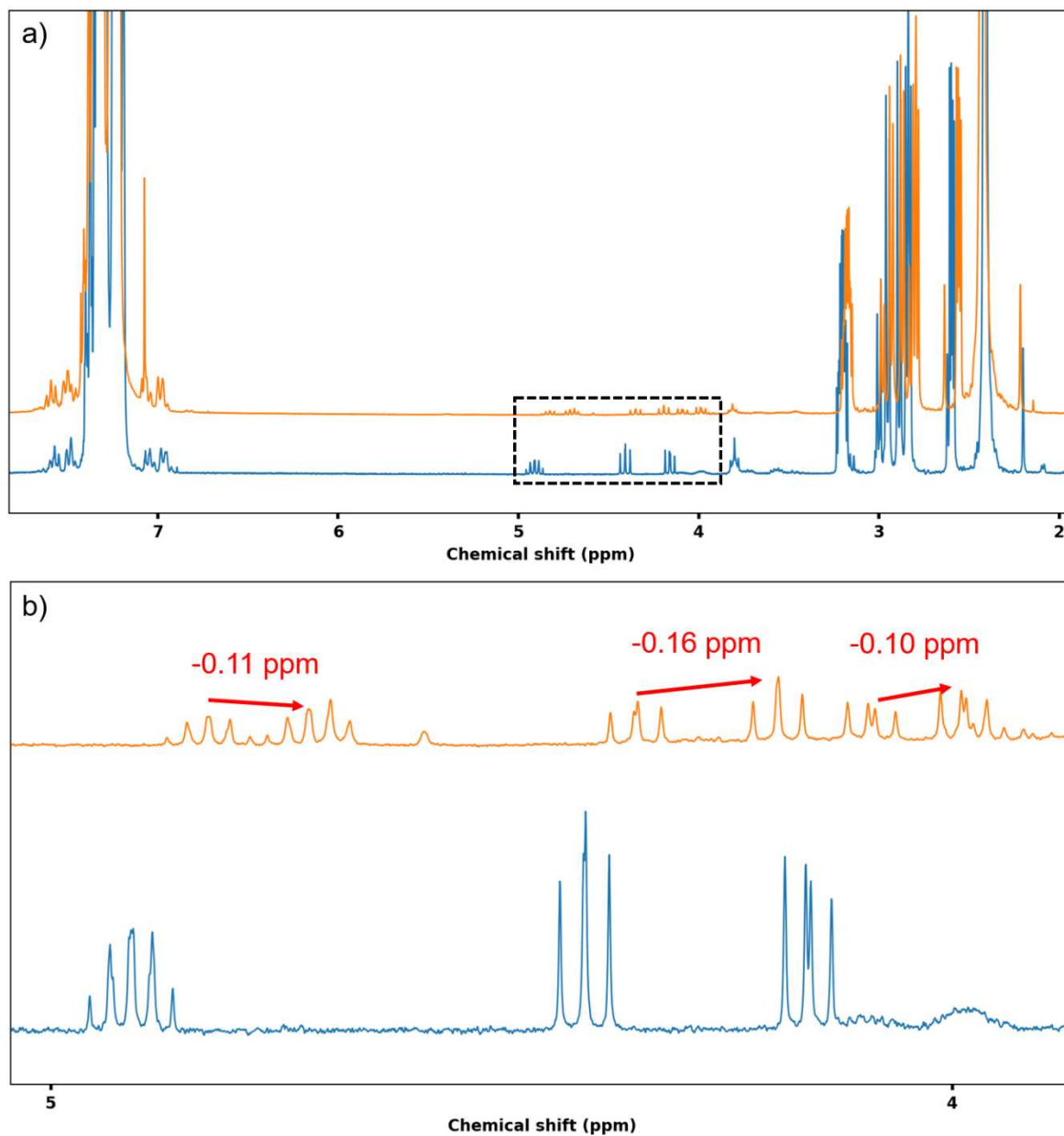


Figure 26: <sup>1</sup>H NMR spectra of the diluted experiments at 150 °C (blue) and at 110 °C (orange). A zoom of the dotted box in a) was given in b) with the chemical shift associated to the cyclic carbonate dimer.

## 2. Dimerization of cyclic carbonate

### a. Identification of the secondary product

When we obtained the shifted cyclic carbonate peaks in our <sup>1</sup>H NMR spectra, we wondered what could be the cause of this shift. The fact that we had a coupling pattern similar to the one of BzD meant that the molecule we obtained had a similar structure in terms of proton, but the shift in chemical displacement indicated that the environment was a little bit different. We had two main hypotheses: the formation of a borane—cyclic carbonate adducts (Figure 27:), or the formation of an oligomer of the cyclic carbonate (Figure 28:).

### Formation of a borane—cyclic carbonate adducts

Since boron—oxygen bonds tended to form easily, we could imagine that BPh<sub>3</sub> interacted with one of the cyclic carbonate oxygen atoms. This would have modified the environment of the protons, thus modifying their chemical displacement. The problem was that we did not see any modification in the <sup>11</sup>B NMR spectra so we could not associate a peak for these species. We could imagine two type of adducts: weak adducts where the B—O bond was not covalent (BzD—BPh<sub>3\_x</sub> with x = 1, 2 or 3), or strong adducts where the B—O bond was covalent (BzD<sup>+</sup>—BPh<sub>2\_x</sub> or BzDH--BPh<sub>2\_x</sub> with x=1, 2 or 3). In the first case, we could imagine that the interaction was not detectable in <sup>11</sup>B NMR due to the weakness of the interaction, and that the only impact was a small shift in the chemical displacement of the protons. In the second case, we could imagine the formation of a covalent B—O bond. However, we knew that no tetravalent boron species were present in the solution, so the boron was necessarily trivalent. We made two hypotheses: one with a charged oxygen atom, and one with a neutral oxygen atom that needed the addition of one proton. This proton could come from residual water present in the solvent. It was difficult to conclude on which of these species could be responsible for the shifted carbonate peaks. The predictions given by ChemDraw were not precise enough to select any of them, and we did not see the peak at 8.0 ppm that should be present in the molecules BzDH—BPh<sub>2\_1</sub> and BzDH--BPh<sub>2\_2</sub>. However, this argument was difficult to clearly consider since this peak could be hidden in the aromatic signal.

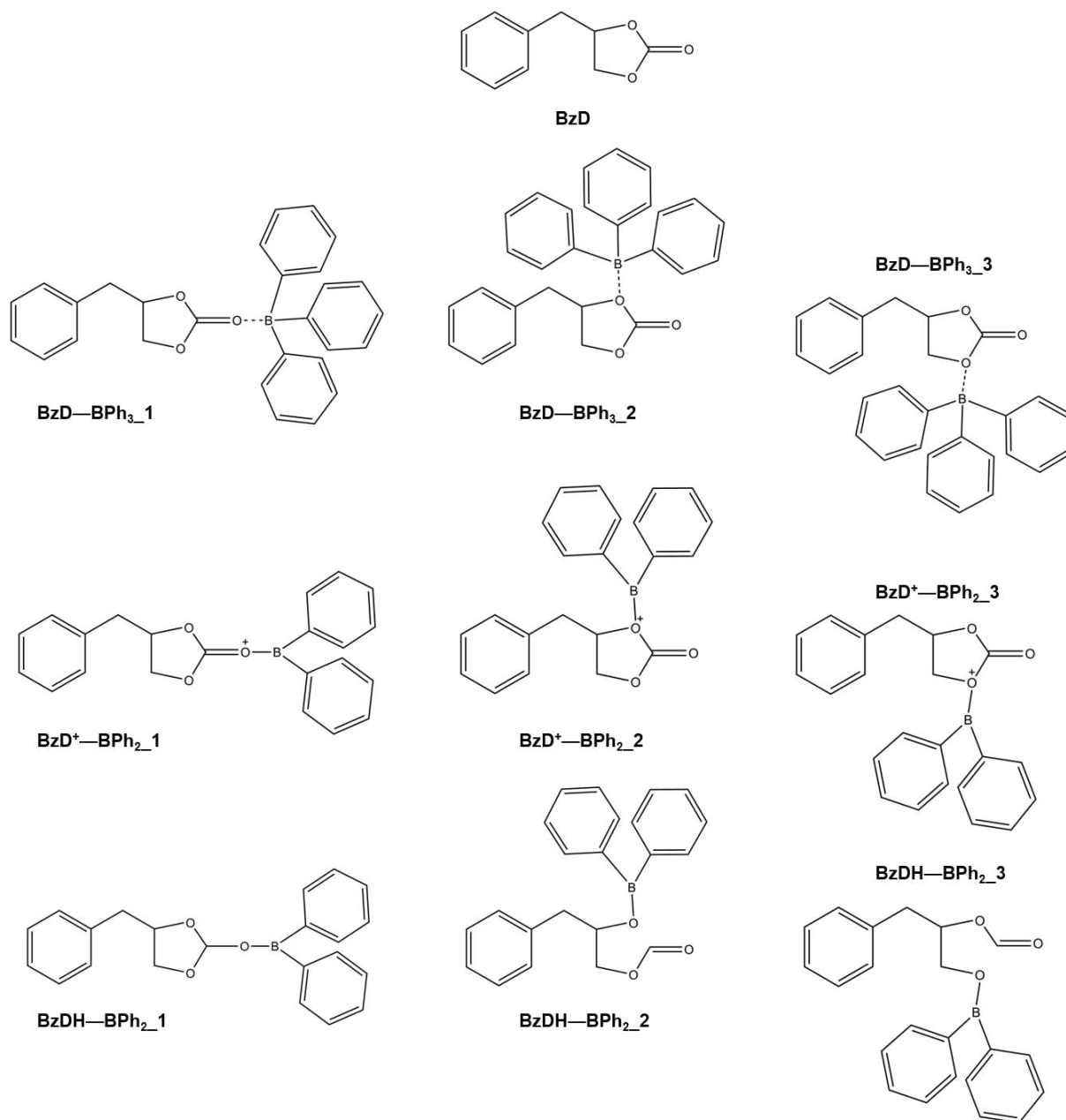


Figure 27: Propositions for cyclic carbonate - borane adducts.

### Formation of cyclic carbonate oligomers

The second hypothesis we had for the origin of the shifted peaks was the formation of a cyclic carbonate oligomer. Indeed, nothing prevented the cycloaddition of CO<sub>2</sub> on two different opened epoxides: the electrophilic carbon of CO<sub>2</sub> could be attacked by the oxygen atom of one epoxide molecule, and the nucleophilic oxygen of CO<sub>2</sub> could attack the carbon of another epoxide molecule. This would lead to the formation of a cyclic dimer of the carbonate (BzD<sub>2</sub>dimer). Actually, it was possible to generalise this idea to as many epoxide molecule as we wanted, leading to the formation of cyclic oligomers. However, this would need a cooperative mechanism that would likely exclude the formation of oligomers with more than 5 carbonates involved. <sup>1</sup>H NMR

spectrum simulation using ChemDraw gave the same estimation for the chemical displacement for the protons on the cycle for the dimer, the trimer, the tetramer, etc. It was not possible to differentiate for example the trimer from the dimer using <sup>1</sup>H NMR, so for simplicity sake we only considered the dimer in the following.

The chemical displacements of the protons on the cycle were a bit higher in the dimer than in the monomer, meaning that it could explain the presence of the chemical shift observed in the previous experiments.

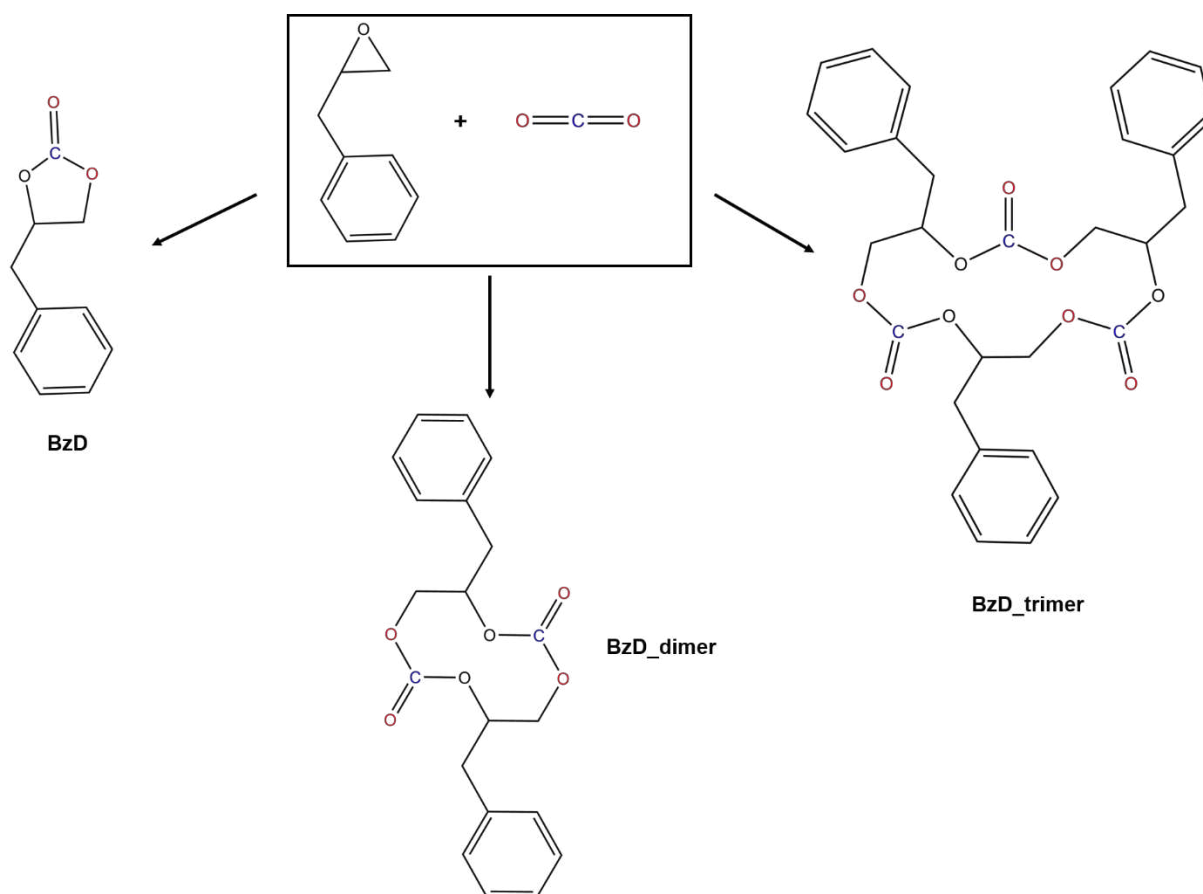


Figure 28: Formation of cyclic monomer, dimer and trimer carbonates from EpBz and CO<sub>2</sub>.

The hypothesis of the formation of cyclic carbonate dimer seemed more realistic than the formation of the borane—cyclic carbonate adducts, especially since we did not detect any modification of the <sup>11</sup>B NMR spectra.

To better understand what was the cause of the apparition of these peaks, we decided to modify several parameters to see how it would impact the shifted peaks. We wondered for example if it was possible to vary the value of the shift, since it seemed not to be the same in the experiment in neat conditions and in the experiment in toluene. We also wondered if it was possible to modify the ratio BzD/BzD\_dimer, by playing on the amount of borane in the reaction for example.

### b. Impact of the borane concentration

We conducted the experiment with the same parameters as previously but we varied the amount of  $BPh_3$  introduced in the reaction from 2.4 mg to 12 mg. Results were shown in Figure 29:a. In these conditions we had an epoxide consumption of 12 % and a selectivity of 70 % toward the cyclic carbonate and 18 % toward the dimer, giving an 88 % selectivity if we summed the two. This was significantly different from the previous experiment where we obtained 6 % consumption, 43 % selectivity toward cyclic carbonate and 22 % selectivity toward the dimer. This could be due to the fact that we used a different batch of  $MgO$  catalyst in this reaction. Hence, we focused on the trend observed when varying the amount of  $BPh_3$  in the solution.

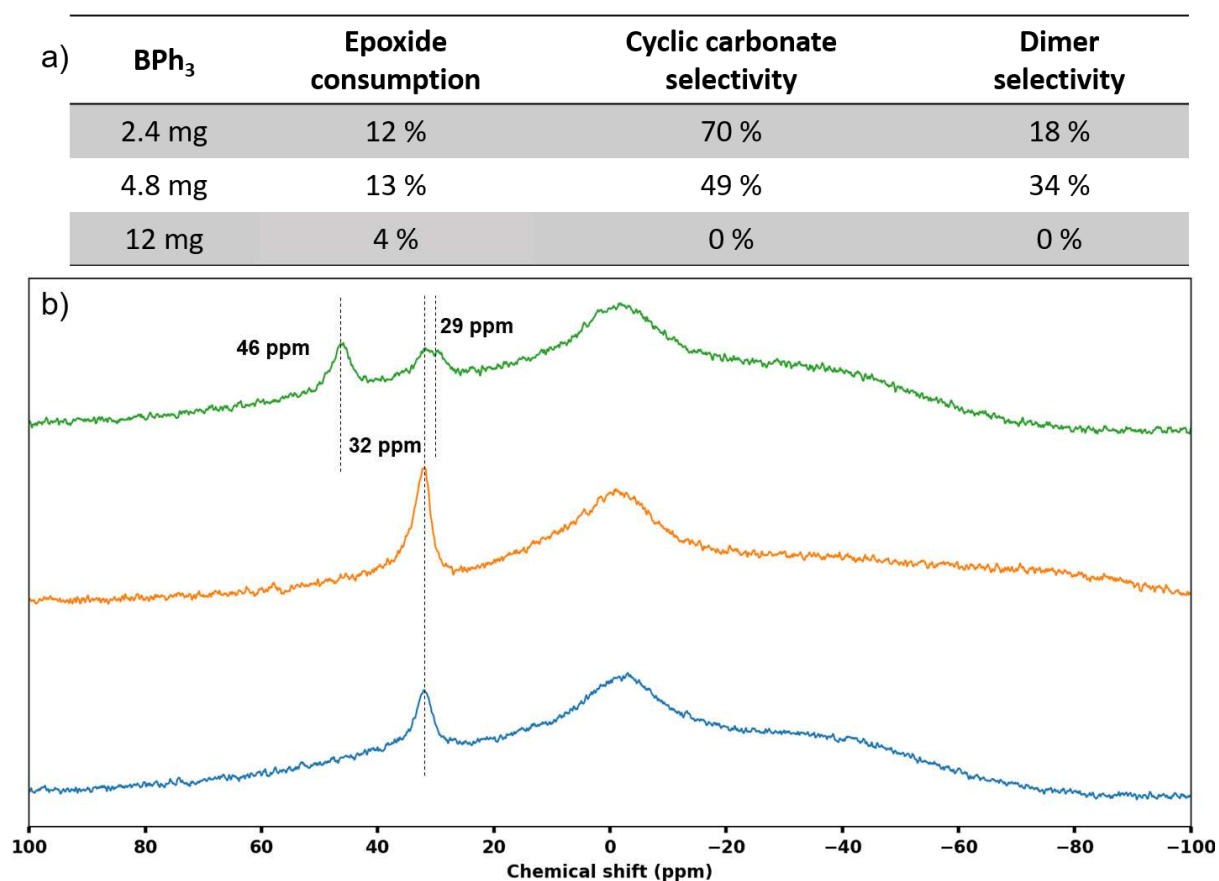


Figure 29: Cycloaddition of  $CO_2$  on  $EpBz$  in toluene catalysed by  $MgO+BPh_3$  with variable amount of borane. a) catalytic performances. b)  $^{11}B$  NMR spectra, blue: 2.4 mg  $BPh_3$ , orange: 4.8 mg  $BPh_3$ , green: 12 mg  $BPh_3$ .

When we increased the amount of borane to 4.8 mg, we could see that the epoxide consumption did not vary significantly, but the selectivity toward the cyclic carbonate dropped to 49 % while the selectivity toward the dimer increased to 34 %. This gave an 83 % selectivity if

summed up, which was not significantly different from the experiment with 2.4 mg borane. When we increased the amount of borane to 12 mg, we could not detect any formation of cyclic carbonate nor dimer. Furthermore, the <sup>11</sup>B NMR spectra (Figure 29:b) showed that the two first experiments only gave the peak at 32 ppm, but the last experiment gave 3 peaks at 46 ppm (attributed to BPh<sub>2</sub>(OH)), one at 32 ppm and one at 29 ppm (attributed to BPh(OH)<sub>2</sub>). Just like in the experiments in neat condition, a high concentration of borane totally prevented the cycloaddition reaction to happen.

We could take two information from these experiments. First, increasing the amount of borane up to a certain point increased the selectivity toward the dimer while keeping the overall selectivity (cyclic carbonate + dimer) and the epoxide consumption unchanged. It could be that the dimerization and the cycloaddition were two different processes happening one after the other: once two cyclic carbonate molecules were formed they combined to form a dimer. Increasing the amount of borane in the reaction would not impact the first reaction but would accelerate the second. Second thing we could see was the fact that an excess of borane seemed to totally kill the reactivity of MgO nanoparticles, thus preventing the formation of cyclic carbonate. We could see that in the last experiment, a part of the borane did not transform into the BPh(OR)<sub>2</sub> specie associated to the 32 ppm peak. Maybe some borane strongly coordinated the MgO surface and prevented the cycloaddition from happening.

### **c. Impact of the NMR tube concentration on chemical displacements**

We were intrigued by the value of the chemical shift between the cyclic carbonate peaks and the dimer ones. As a simple experiment, we decided to vary the reaction crude/CDCl<sub>3</sub> in the NMR tube to see if it would have an impact. Figure 30: showed the different tests we made by controlling the exact amount of reaction crude we introduced in the NMR tube. The experiment was conducted with 0.1 mL of EpBz and 1 mL of toluene at 110 °C for 2 days. We could see that when we measured the NMR spectra of the crude reaction with only 10 μL, the signal was very weak and the peaks of the dimer were not detectable. When we increased the amount of crude in the NMR tube, we could see the peaks of the dimer with a chemical displacement lower than the peaks of the cyclic carbonate (between -0.05 and -0.08 ppm depending on the peak). However, the more we increased the concentration of the tube, the more the shift increased (up to +0.15 ppm). The dimer peaks had a lower chemical displacement than the cyclic carbonate peaks at low concentration, but had a higher chemical displacement than the cyclic carbonate peaks at higher concentration. We could understand why we detected a positive shift in the reaction conducted in neat conditions: the crude was more concentrated since no toluene was present.

a)	CDCl <sub>3</sub> (mL)	Reaction crude (μL)	Shift compared to the 4.9 ppm peak (ppm)	Shift compared to the 4.4 ppm peak (ppm)	Shift compared to the 4.2 ppm peak (ppm)
	0.5 mL	10 μL	/	/	/
	0.5 mL	20 μL	-0.08	-0.05	-0.07
	0.5 mL	50 μL	-0.04	0.0	-0.03
	0.5 mL	100 μL	0.0	0.06	0.02
	0.5 mL	150 μL	0.06	0.10	0.06
	0.5 mL	200 μL	0.10	0.15	0.09

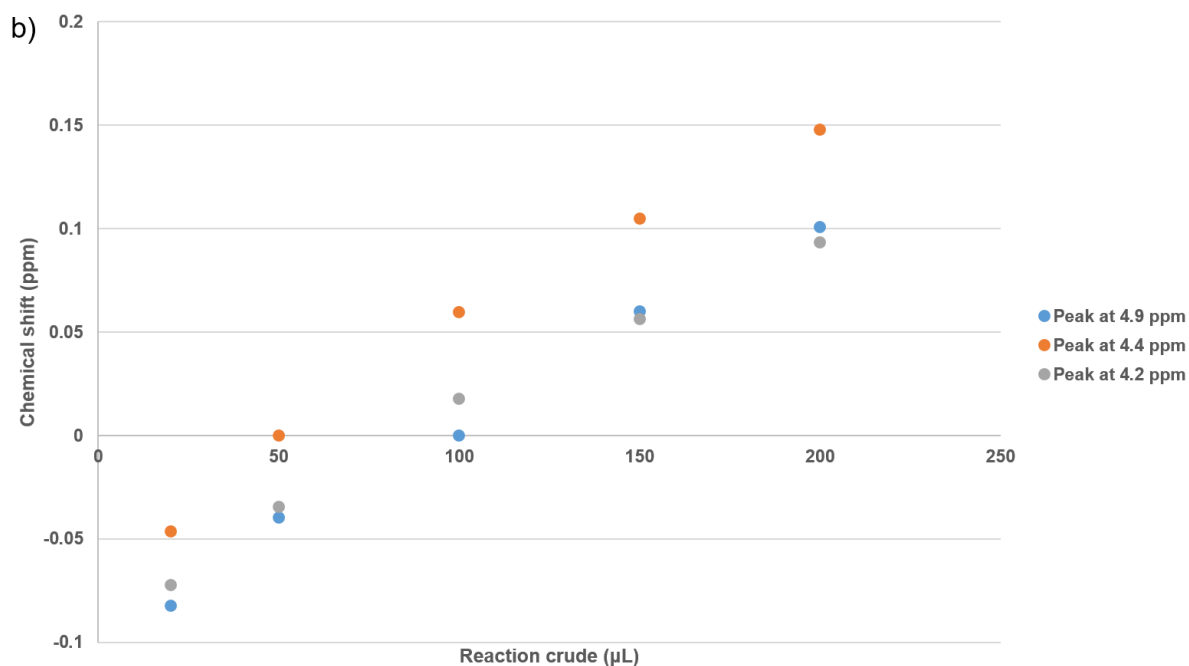


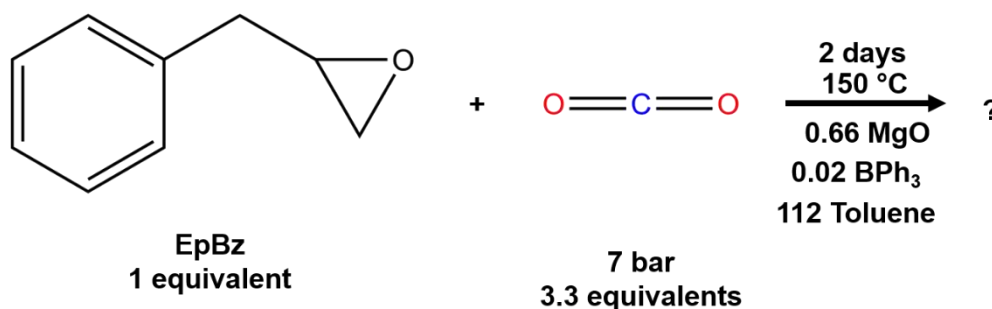
Figure 30: Variation of the chemical shift of the dimer signal compared to the cyclic carbonate signal as a function of NMR tube concentration. a) Numeric values, b) graphic representation.

#### d. Impact of the temperature

As a last experiment, we compared the activity of the MgO+BPh<sub>3</sub> catalyst at 110 °C and 150 °C. We wanted to see if there was a difference in the dimer formation due to temperature. We also decided to increase the concentration of the quantities of the reaction (with the exception of CO<sub>2</sub> since we kept the same pressure as before). The new parameters are the one described in the experimental section (Scheme 11:). Since the solubility of CO<sub>2</sub> in toluene was low, we thought that the concentration of CO<sub>2</sub> in solution would not really be impacted.



MgO-based catalysts in the cycloaddition of CO<sub>2</sub> on epoxides



Scheme 11: Cycloaddition of CO<sub>2</sub> on EpBz in toluene in diluted conditions.

The results of the four experiments (with and without BPh<sub>3</sub>, at 110 °C or 150 °C) were shown in Table 9. We could see that the reaction catalysed by MgO at 150 °C gave a higher epoxide consumption rate than the one at 110 °C (from 3 % to 8 %), but the selectivity toward cyclic carbonate was pretty much similar. When we used MgO+BPh<sub>3</sub>, we did not see the selectivity vary significantly. However, the selectivity toward cyclic carbonate decreased at the advantage of the dimer selectivity. Interestingly enough, the formation of the dimer was more pronounced at 110 °C than at 150 °C. Either the reaction responsible of the formation of the dimer was sensible to temperature, and less dimer was produced at 150 °C, or the reaction was not sensible to temperature and the reduction of the selectivity toward the dimer at 150 °C was only due to the fact that all the other reactions were more efficient at high temperature. At 110 °C, 0.01 equivalent of dimer was produced, which was the same amount as in the reaction at 150 °C. This emphasized the second option.

Temperature	BPh <sub>3</sub>	Epoxide consumption	Cyclic carbonate selectivity	Dimer selectivity
110 °C	0.0 mg	3 %	77 %	0 %
110 °C	9.6 mg	4 %	27 %	36 %
150 °C	0.0 mg	8 %	81 %	0 %
150 °C	9.6 mg	9 %	65 %	15 %

Table 9: Performances of MgO and MgO+BPh<sub>3</sub> catalysts in the cycloaddition of CO<sub>2</sub> on EpBz in diluted conditions in toluene.

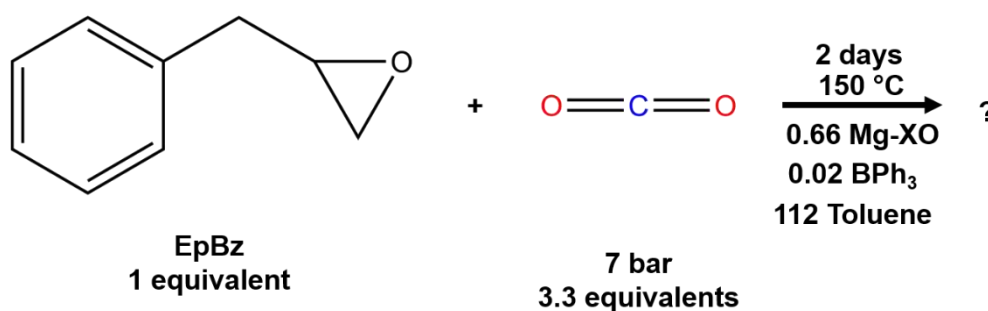
### e. Conclusion

We observed the apparition of an unknown secondary product during the cycloaddition of CO<sub>2</sub> on EpBz catalysed by the pair MgO+BPh<sub>3</sub>. We made several hypotheses on the identification of this secondary product, but in the end we attributed it to the dimerization of cyclic carbonate. Such reaction never was reported in the literature to our knowledge. The BPh<sub>3</sub> reduced the activity of MgO catalysts in term of cyclic carbonate yield, but the overall yield of carbonate+dimer

stayed constant. It was not clear if the reaction was sequential (formation of two carbonates, then formation of the dimer) or simultaneous (formation of the dimer from two molecules of epoxide and two molecules of CO<sub>2</sub>). Reaching 100 % epoxide consumption in a reaction catalysed by MgO nanoparticles, then adding the borane, could bring some answers.

### 3. Performances of modified MgO nanoparticles

Now that we put in evidence a unique phenomenon associated to the interaction between MgO nanoparticles and BPh<sub>3</sub> in the cycloaddition of CO<sub>2</sub> on EpBz, we wanted to try to modify either the MgO nanoparticles or the borane. In a first time, we decided to use the modified MgO catalysts that we synthesized in Chapter III: MgO-CaO nanoparticles and MgO-X (with X = Co, Ni) nanoparticles. We decided to keep the experimental parameters described in the experimental section (Scheme 12:).



Scheme 12: Cycloaddition of CO<sub>2</sub> on EpBz in toluene catalysed by mixed oxides.

#### a. Calcium containing MgO nanoparticles

We had at disposition nanoparticles synthesized by co-precipitation method with a variable amount of calcium. For the sake of simplicity, we called the sample by referring to the introduced ratio Mg/Ca in the synthesis even if we saw that the final nanoparticles did not have the same effective ratio. So the Mg<sub>0.9</sub>O-Ca<sub>0.1</sub>O sample would correspond to the synthesis where 0.9 equivalents of Mg(NO<sub>3</sub>)<sub>2</sub> and 0.1 equivalents of Ca(NO<sub>3</sub>)<sub>2</sub> were introduced initially. Having that in mind, we could compare the catalytic performances of nanoparticles with different calcium content and see how these nanoparticles behaved in presence of a borane ligand. For the catalyst nanoparticles, we pondered the molar mass according to the introduced ratio, giving the formula:

$$\text{Molar\_mass}(\text{Mg}_x\text{O-Ca}_{1-x}\text{O}) = 0.9 \cdot \text{Molar\_mass}(\text{MgO}) + 0.1 \cdot \text{Molar\_mass}(\text{CaO})$$

The results of the catalytic experiment were given in Figure 31: We could see a trend in the efficiency of the mixed oxide catalyst as a function of the calcium loading. If we consider the epoxide consumption (blue circles), we could see that the performance of Mg<sub>x</sub>-Ca<sub>1-x</sub>O first increased to reach its maximum (17 %) at 5 % calcium loading, and decreased to reach 0 % for pure CaO nanoparticles. When we added BPh<sub>3</sub> (orange circles), the tendency was the same, but

the consumption was a bit lower (between 1 and 2 % lower). This trend was found the same for cyclic carbonate yield (blue and orange squares), and cyclic carbonate+dimer yield (orange triangles). The addition of calcium in the MgO nanoparticles up to 5 % loading increased their catalytic activity, while maintaining their selectivity.

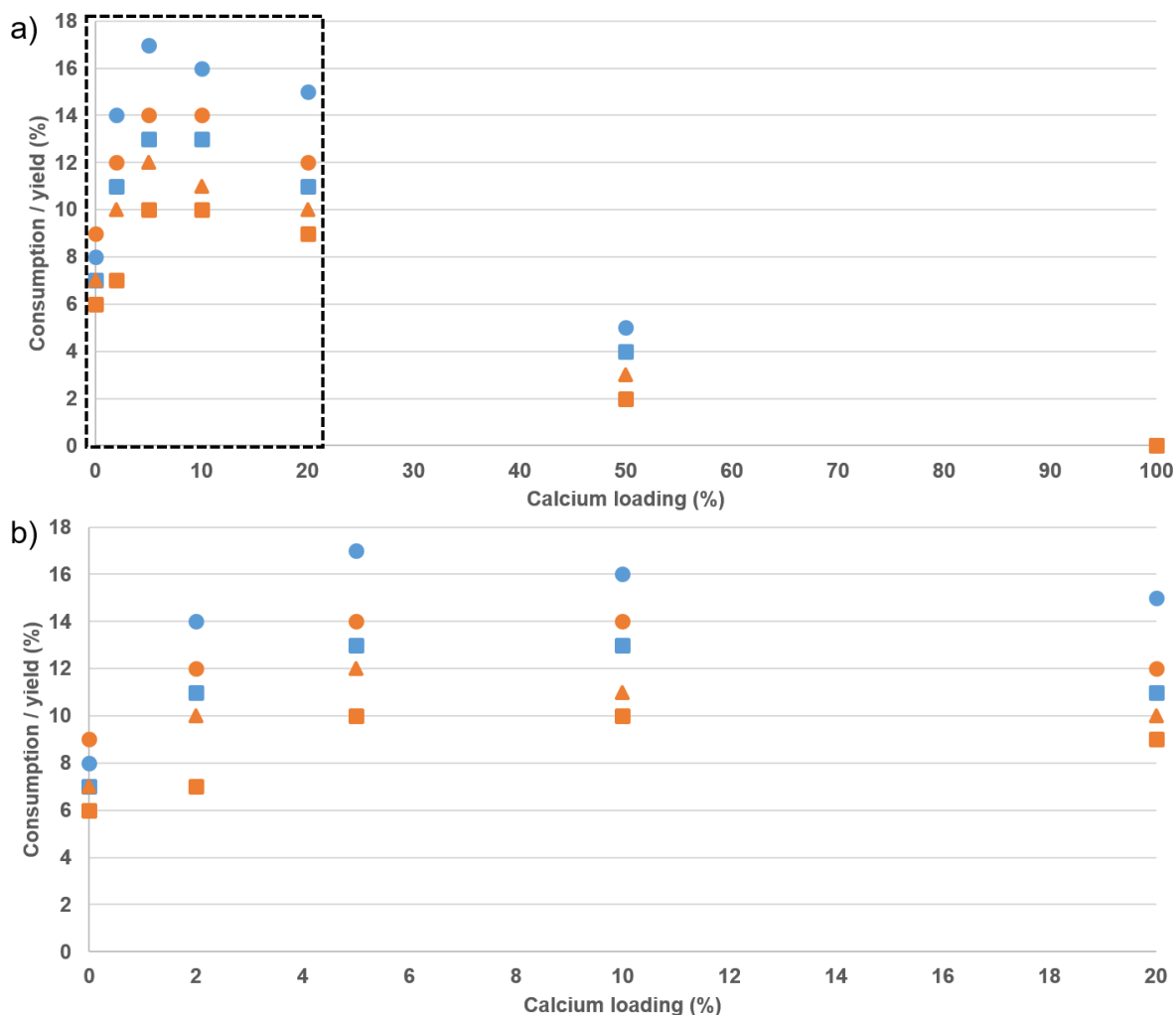


Figure 31: Performances of the Mg<sub>x</sub>-Ca<sub>1-x</sub>O (blue) and Mg<sub>x</sub>-Ca<sub>1-x</sub>O+BPh<sub>3</sub> catalysts in the cycloaddition of CO<sub>2</sub> on epoxide as a function of the calcium loading (circles: epoxide consumption, squares: BzD yield, triangles: BzD+dimer yield).

As explained in Chapter II, incorporation of calcium created more active basic sites, thus enhancing the catalytic activity. However, when the amount of calcium was too high, domains of pure calcium oxide started to grow, and we knew for a fact that pure CaO catalyst was almost inactive in the cycloaddition reaction. This threshold between 5 % and 10 % calcium loading actually corresponded to the increase of the intensity of the CaCO<sub>3</sub> signal in XRD observed in Chapter III. CaCO<sub>3</sub> was not tested in catalysis, but no report mentioned its activity in the cycloaddition of CO<sub>2</sub> on epoxides. The increase of CaCO<sub>3</sub> in the sample was made at the extent of MgO, meaning that the more we added calcium in the sample, the less MgO we had and the activity decreased.

More quantitative considerations on the impact of Ca incorporation in MgO nanoparticles on the catalytic activity would need precise measurements of the true calcium loading in all the samples.

### b. Transition metal containing MgO nanoparticles

We also tested the activity of some of the other bimetallic nanoparticles:  $\text{Mg}_{0.95}\text{O-Ni}_{0.05}$ , and  $\text{Mg}_{0.95}\text{O-Co}_{0.05}$ . We calculated the amount of catalyst needed in the reaction just like we did with the  $\text{Mg}_x\text{O-Ca}_{1-x}\text{O}$  catalysts, by pondering the molar mass by the introduced metal stoichiometry in the synthesis. Figure 32: showed the catalytic performances of these metal containing mixed oxides with and without  $\text{BPh}_3$ . What we could immediately see was that both  $\text{Mg}_{0.95}\text{O-Ni}_{0.05}$  and  $\text{Mg}_{0.95}\text{O-Co}_{0.05}$  were more active than MgO nanoparticles: the epoxide consumption went from 8 % for MgO to 17 % and 22 % for respectively nickel and cobalt containing nanoparticles. However, we could see that the selectivity of the catalysts was lower than for MgO: the carbonate yield went from 7 % for MgO to 9 % and 12 % for Ni and Co containing nanoparticles. When we added  $\text{BPh}_3$  to the catalyst, we could see the formation of the dimer with  $\text{Mg}_{0.95}\text{O-Ni}_{0.05}$  catalyst, but not with  $\text{Mg}_{0.95}\text{O-Co}_{0.05}$  catalyst. With the later, it seemed that only the formation of secondary product increased when adding  $\text{BPh}_3$ , without impacting the formation of BzD or the dimer.

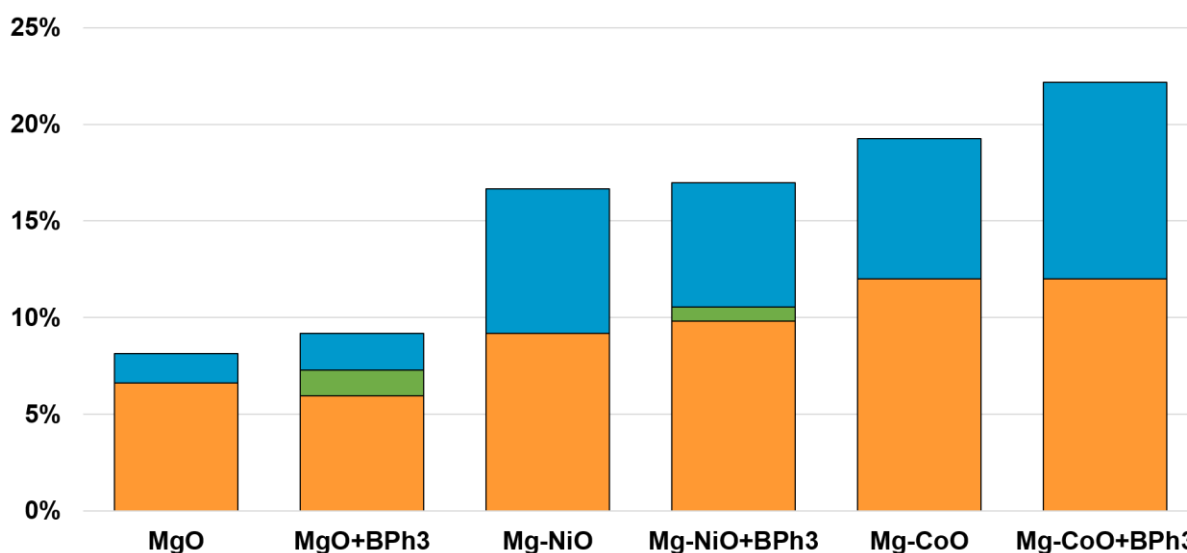


Figure 32: Performances of Mg-XO catalysts with and without  $\text{BPh}_3$  in terms of epoxide consumption (orange+green+blue), cyclic carbonate yield (orange), and dimer yield (green).

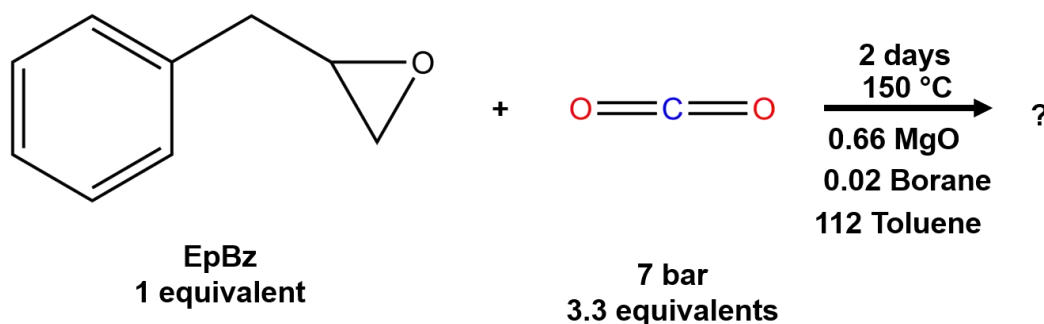
The incorporation of transition metal atoms in the material increased its overall activity. However, if the increase of carbonate yield was measurable, it was smaller than the increase of secondary product formation. The increase of activity happened along a reduction of carbonate selectivity. This could be explained if nickel and cobalt incorporation created stronger acidic sites on the MgO catalyst. This would increase the activity of the catalyst in the cycloaddition reaction, but also in the parasite polymerisation reaction known to be catalysed by Lewis acid sites. When adding  $\text{BPh}_3$  to the reaction, we could see the formation of dimer in small proportion for the nickel containing catalyst (the dimer/carbonate ratio was 23 % for  $\text{MgO+BPh}_3$  and 8 % for

Mg<sub>0.95</sub>-Ni<sub>0.05</sub>O+BPh<sub>3</sub>), but not for the cobalt containing catalyst. This could be due to the fact that the formation of dimer was so low that it was not detectable, or that the cobalt prevented it. Annexe 10 showed the <sup>11</sup>B NMR spectra of the MgO-O+BPh<sub>3</sub> reaction crudes, we only detected the 32 ppm peak.

It could be interesting to see how the atomic ratio X/Mg played a role in the modification of the activity and selectivity of the catalyst, just like we did for the MgO-CaO catalysts. It would be likely that the trend would be the same: at low X loading, the metal atoms would be well dispersed on the MgO catalysts, creating stronger acidic sites and increasing the epoxide consumption. At a certain X/Mg ratio, the metal would start to form pure oxide domains during the precipitation-calcination reaction, and since neither nickel oxides nor cobalt oxides were known for catalysing the cycloaddition reaction, the epoxide consumption would decrease due to a diminution of MgO catalytic sites in the catalyst. It could also be interesting to see how these metal-containing catalysts would behave if we used Lewis base ligands instead of Lewis acids. We saw that the use of phosphines for the catalysis of the reaction was problematic since they catalysed the reaction on their own, but maybe in these diluted conditions and with stronger acid sites on the catalysts we could observe a synergetic effect between metal containing MgO and phosphines.

#### 4. Borane screening

After modifying the nanoparticle of our Lewis acid-base pair, we decided to try other acidic ligands in the cycloaddition reaction along with MgO. We wanted to see if different classes of boron based molecules would give the same dimerization reaction we observed with BPh<sub>3</sub>. Any synergetic change in MgO activity and/or selectivity would be interesting to analyse. For this experiment, we chose different boron based molecules: alkylboranes (BEt<sub>3</sub> and BBu<sub>3</sub>) and chloroboranes (BCl<sub>2</sub>Ph and BCl<sub>3</sub>) for their high Lewis acidity, an arylborane (BMes<sub>3</sub>) for its intermediate Lewis acidity, a borate (B(CH<sub>3</sub>)<sub>2</sub>OCH<sub>3</sub>) for its low Lewis acidity, and a boronic acid (BPh(OH)<sub>2</sub>) for its Brønsted acidity. We kept the stoichiometry of the previous reactions (Scheme 13:).



Scheme 13: Cycloaddition of CO<sub>2</sub> on EpBz in toluene catalysed by MgO and various boranes.

Results of the catalytic tests were given in Figure 33: We could see directly that in term of epoxide consumption, the use of MgO+BCl<sub>2</sub>Ph as catalyst outperformed all the other MgO-borane pairs with a 96 % consumption of the epoxide (against 14 % for the second most performant pair).

The epoxide yield also was the highest compared to the others with a 15 % yield. However, the selectivity toward the cyclic carbonate was quite low: 15 % against 81 % with MgO alone. The pair MgO+BCl<sub>2</sub>Ph managed the activation of the epoxide, but a secondary reaction competed with the cycloaddition, resulting in a low cyclic carbonate selectivity.

For the other borane we used, we could see in some cases the formation of the dimer: with BEt<sub>3</sub>, BBU<sub>3</sub>, B(CH<sub>3</sub>)<sub>2</sub>OCH<sub>3</sub> and B(OH)<sub>2</sub>Ph. We observed either small increases or decreases of the cyclic carbonate+dimer yield for BBU<sub>3</sub>, B(CH<sub>3</sub>)<sub>2</sub>OCH<sub>3</sub> and BCl<sub>3</sub>, B(OH)<sub>2</sub>Ph respectively. The presence of BCl<sub>3</sub> totally blocked the reactivity of MgO, no cyclic carbonate nor dimer were detected. There was overall an increase in the formation of secondary products, with the notable exception of BBU<sub>3</sub> that gave both an increase in cyclic carbonate+dimer yield and selectivity.

We saw in <sup>11</sup>B NMR (Annexe 11) that most of the time, the boron ligand was modified during the reaction, just like we observed with BPh<sub>3</sub>. Strangely enough, we were not able to detect any boron species in the reaction with BMe<sub>3</sub>, and only a weak signal in the reaction with BCl<sub>3</sub>, meaning that the boron atoms might be trapped in a state where they were not detectable (like in a polymer species, or the molecules were not soluble).

### MgO-based catalysts in the cycloaddition of CO<sub>2</sub> on epoxides

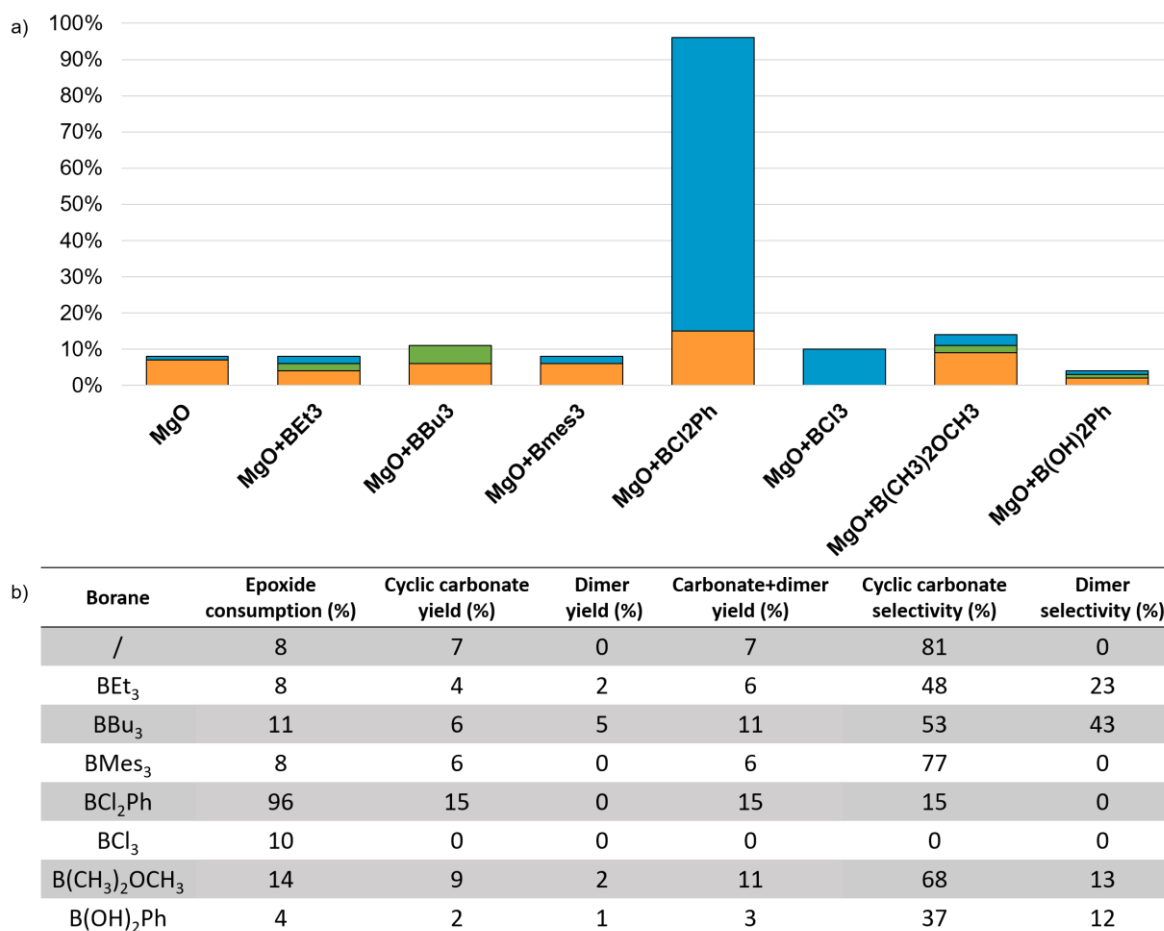


Figure 33: Performances of the different borane ligands in the cycloaddition of CO<sub>2</sub> on EpBz catalysed by MgO. a) Graphic representation of the cyclic carbonate yielded (orange), the dimer yield (green) and the secondary products yield (blue). b) Numerical values of the yields and selectivities of the reactions.

Even if all these trends would have been interesting to dig in, we decided to focus our efforts on the MgO+BCl<sub>2</sub>Ph pair since it gave such drastically different results, with an almost total consumption of the epoxide.

## VI. Understanding the interaction between MgO and BCl<sub>2</sub>Ph

We saw in Chapter IV that BCl<sub>2</sub>Ph had a special interaction with MgO nanoparticles. The colour change we obtained with the formation of NaCl lead us to the conclusion that one of the B—Cl bond was cleaved to form a B—O bond with the MgO surface (Figure 34:).

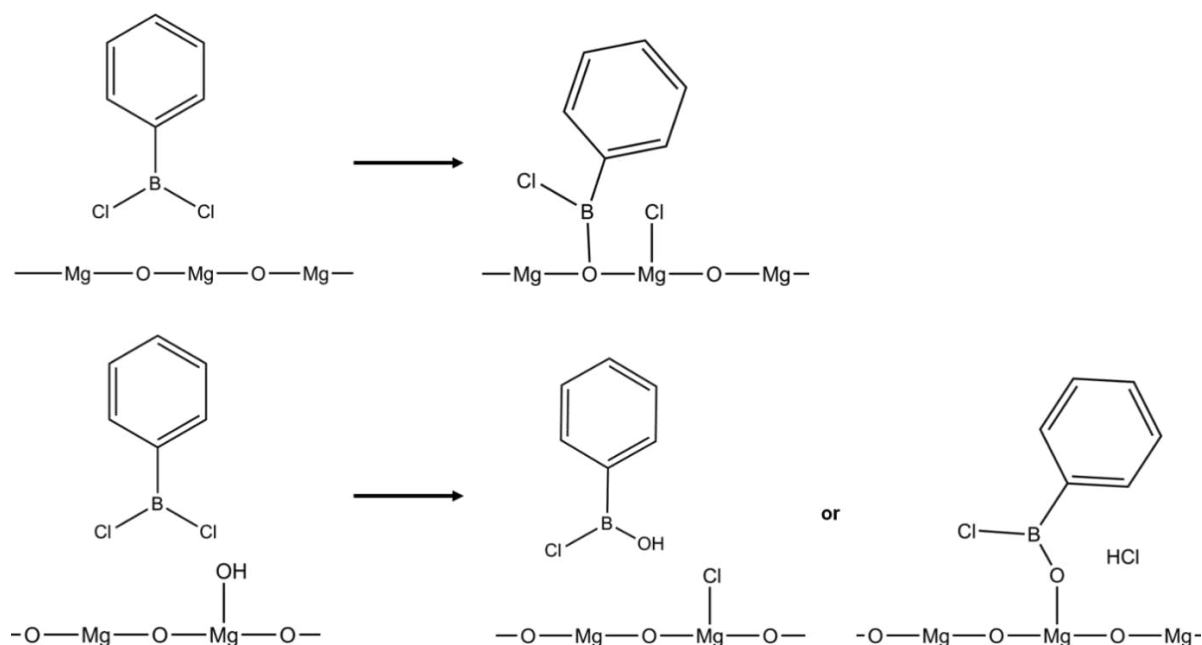


Figure 34: Proposition for BCl<sub>2</sub>Ph adsorption at the surface of MgO nanoparticles.

BCl<sub>2</sub>Ph was a chloroborane not often used in the literature. Chloroboranes in general were used for the synthesis of boron based ligands on transition metal complexes<sup>31</sup>, formation of B—N bonds<sup>32</sup> or B—O bonds<sup>33</sup>. We also found studies showing the potential of chloroboranes for the opening of acetal rings<sup>34</sup>, a result that might be transferred to epoxide or carbonate cycles in some extent. Finally, more recent studies discussed the potential of BCl<sub>2</sub>Ph for surface functionalisation due to the ability of chloroboranes to substitute one of their B—Cl bond to a B—surface bond<sup>35</sup> (Figure 35:).

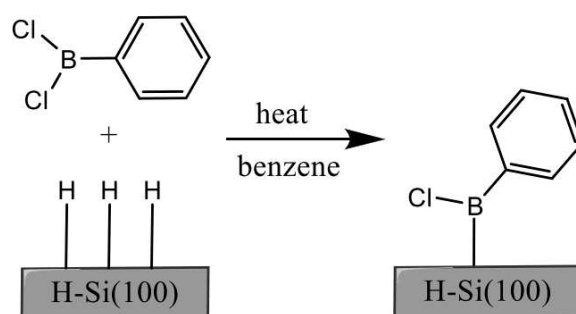


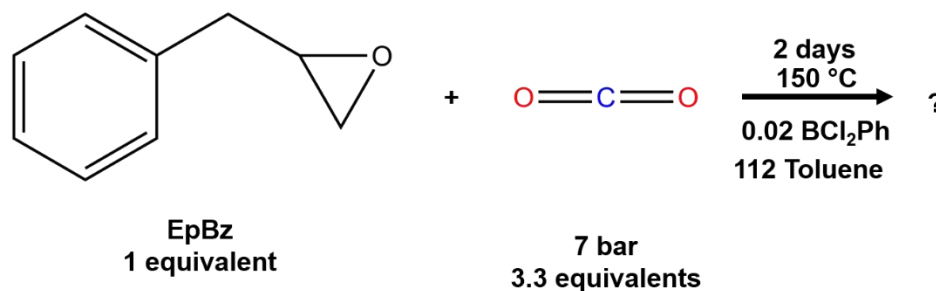
Figure 35: Schematic of the reaction of dichlorophenylborane with H-Si(100), from Frederick et al.<sup>35</sup>.



## 1. Parameter variation

### a. Blanc reaction

The first thing we wanted to verify was if BCl<sub>2</sub>Ph alone was able to catalyse the cycloaddition reaction (or the secondary reactions). We used the same stoichiometry as previously but without the MgO nanoparticles (Scheme 14:).



Scheme 14: Blanc cycloaddition of CO<sub>2</sub> on EpBz in toluene with BCl<sub>2</sub>Ph.

The results of test were given in Figure 36: We could see no formation of cyclic carbonate in <sup>1</sup>H NMR and the epoxide was not totally consumed. However, we could see the appearance of a broad signal corresponding to the formation of polymeric species. This was not a surprise since we knew BCl<sub>2</sub>Ph was a strong Lewis acid<sup>36</sup>. We estimated the epoxide consumption to be around 10 %, but it was difficult to evaluate since the polymer signal was very broad. The <sup>11</sup>B NMR (Figure 36:b) showed two peaks at 29 ppm and 18 ppm, whereas with MgO+BCl<sub>2</sub>Ph as catalyst we could see three peaks at 32 ppm, 29 ppm and a small one at 18 ppm. As mentioned before, these ranges of chemical displacement indicated the formation of B(OR)<sub>2</sub>Ph species (for the 32 and 29 ppm peaks), and of B(OR)<sub>3</sub> species (for the 18 ppm peak). We could not have more precise identification just by <sup>11</sup>B NMR, but we guessed that the epoxide reacted with BCl<sub>2</sub>Ph in a same way as it did with BPh<sub>3</sub> to form borate species (Figure 11:).

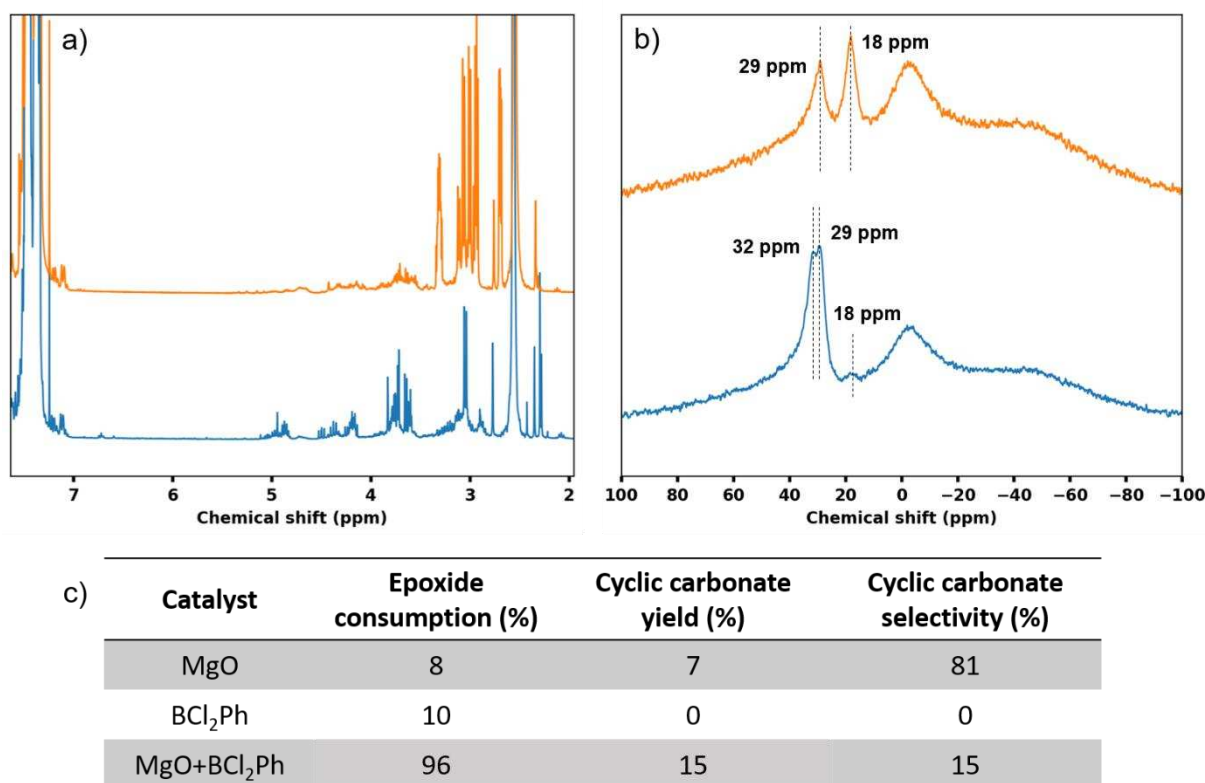


Figure 36: Cycloaddition of  $\text{CO}_2$  on  $\text{EpBz}$  blanc with  $\text{BCl}_2\text{Ph}$ . a)  $^1\text{H}$  NMR spectra of the crude reaction catalysed by  $\text{MgO}+\text{BCl}_2\text{Ph}$  (blue) and  $\text{BCl}_2\text{Ph}$  alone (orange), b)  $^{11}\text{B}$  NMR spectra of the crude reaction catalysed by  $\text{MgO}+\text{BCl}_2\text{Ph}$  (blue) and  $\text{BCl}_2\text{Ph}$  alone (orange), c) numerical values of the performance of the catalyst.

We knew that the reactivity of the  $\text{MgO}+\text{BCl}_2\text{Ph}$  pair was not due to the borane only, the  $\text{MgO}$  nanoparticles were necessary for the reaction to take place.

## b. Kinetic study

Next, we wanted to see if it was possible to improve the selectivity toward the cyclic carbonate. To better understand the reactions responsible to the consumption of the epoxide, we decided to do a kinetic experiment where we varied the duration of the reaction with the  $\text{MgO}+\text{BCl}_2\text{Ph}$  catalyst. We hoped that the secondary reactions occurred after the cycloaddition reaction and that it would be possible to control the selectivity by reducing the reaction duration.

Results were given in Figure 37: The first thing we could see was that the catalytic result of the 48 hours experiment was quite different from the one presented above: the epoxide consumption was 84 % here against 96 % previously, and the carbonate yield was 31 % here against 15 % previously. We will find out later that this could be explained by a variation of the borane loading in the reaction. Since the previous reaction was the first using such low volume of liquid, it was probable that the uncertainty was high on this experiment. If we only compared the result of the kinetic study, we observed the formation of the dimer at 14 hours of reaction. Both

the epoxide consumption and the carbonate yield increased with the reaction duration, but the carbonate selectivity did not vary significantly. This meant that the cycloaddition and the secondary reactions occurred at the same time, and that playing with the reaction duration could not help to increase the carbonate selectivity. The <sup>11</sup>B NMR spectra (Annexe 12) showed the presence of two peaks at 32 ppm and 29 ppm. The intensity ratio between those two peaks stayed constant in the first experiments but changed in the last one.

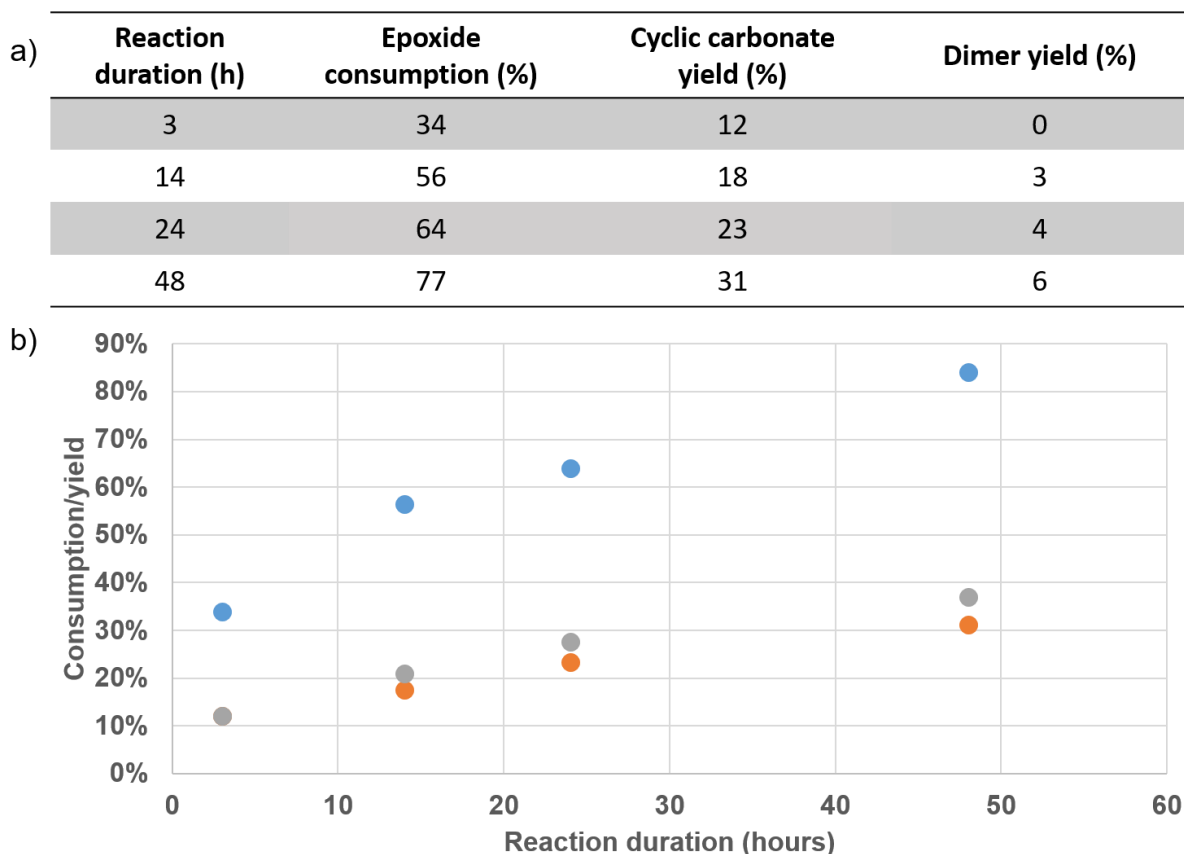


Figure 37: Impact of the reaction duration on the catalytic performance of MgO+BCl<sub>2</sub>Ph in the cycloaddition of CO<sub>2</sub> on epoxide. a) Numerical values, b) graphic representation (blue: epoxide consumption, orange: cyclic carbonate yield, grey: cyclic carbonate+dimer yield).

### c. Impact of the borane loading

The fact that we obtained different results when repeating the 48 hours experiment made us wonder what could have caused this change. We came to the conclusion that it was the precision on the borane loading. We decided to investigate on the impact of the borane loading on the catalytic performances of MgO+BCl<sub>2</sub>Ph, since it seemed to strongly impact the selectivity.

We varied the borane loading from 0.005 equivalents to 0.04 equivalents (Figure 38:). We decided to do the reaction for only 16 hours since we did not want the epoxide to be entirely consumed to compare the variation of consumption induced by the borane loading. We could see that epoxide consumption increased with borane loading, going from 21 % for 0.005 eq. of BCl<sub>2</sub>Ph to 60 % for 0.04 eq. The cyclic carbonate yield also increased, but in a smaller proportion: from

11 % to 16 %. The dimer production seemed not to vary for the three first experiments (2 or 3 %), but dropped to 0 % in the last experiment. It has to be noted that in that last experiment, a broad background was present, probably due to the partial polymerisation of the epoxide, that might have prevented us from detecting the dimer signal. Overall, neither the cyclic carbonate formation nor the dimer formation were strongly impacted by the increase of  $\text{BCl}_2\text{Ph}$  loading, however, the secondary reactions strongly were: the selectivity toward carbonate+dimer went from 60 % to 25 %. The ratio between  $\text{MgO}$  and  $\text{BCl}_2\text{Ph}$  was crucial to control the selectivity of the reaction.

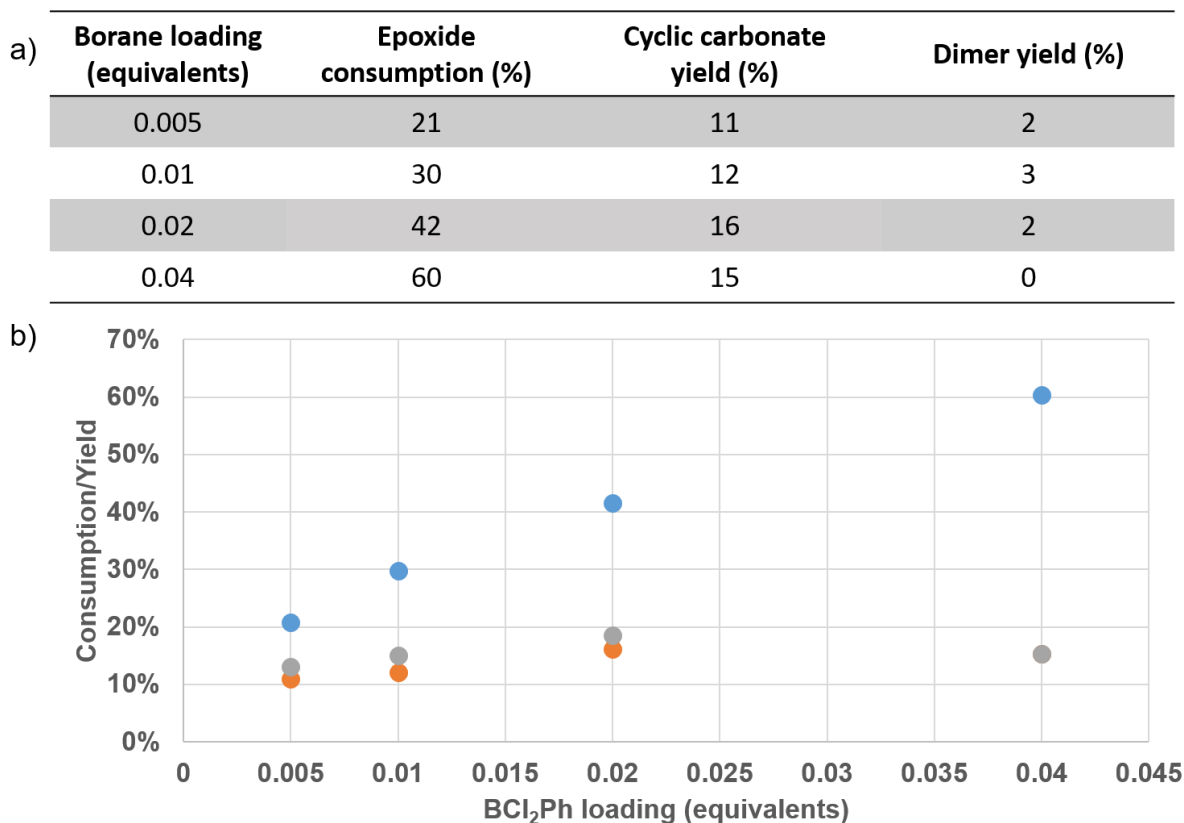


Figure 38: Impact of the borane loading on the catalytic performance of  $\text{MgO}+\text{BCl}_2\text{Ph}$  in the cycloaddition of  $\text{CO}_2$  on epoxide. a) Numerical values, b) graphic representation (blue: epoxide consumption, orange: cyclic carbonate yield, grey: cyclic carbonate+dimer yield).

The  $^{11}\text{B}$  NMR spectra (Figure 39:) showed the presence of the two 32 ppm and 29 ppm in each experiment. However, we could clearly see that the ratio between those two peaks varied. The lower the borane loading was (and the higher the carbonate selectivity was), the higher the 32 ppm/29 ppm ratio was. And the higher the borane loading was, the lower the 32 ppm/29 ppm ratio was. A first interpretation would be that the added borane transformed in the species associated to the 29 ppm peak and that it was responsible for the formation of secondary products.

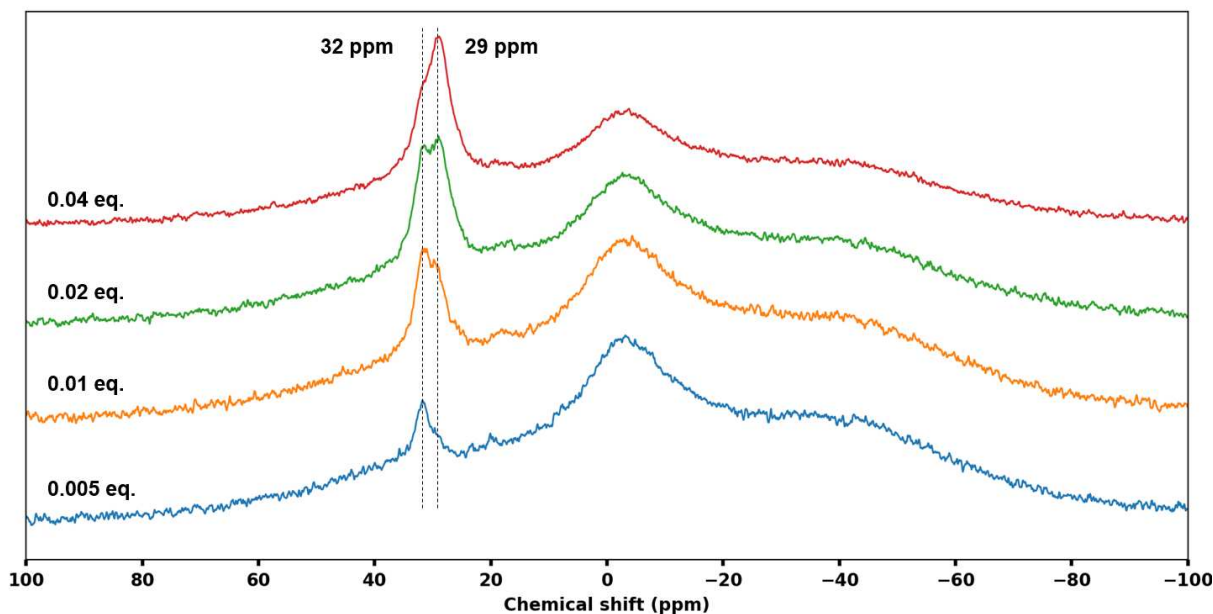


Figure 39: <sup>11</sup>B NMR spectra of the reaction crudes in the study of the impact of BCl<sub>2</sub>Ph (blue: 0.005 borane eq., orange: 0.01 borane eq., green 0.02 borane eq., red: 0.04 borane eq.).

#### d. Impact of temperature

The last parameter we tested to improve the selectivity of the reaction toward cyclic carbonate was the temperature. We decided to do the 2 days reaction at temperature ranging from room temperature to 150 °C (Figure 40:).

We could see that even at room temperature epoxide reacted to form secondary products with a consumption around 15 %. This epoxide consumption probably came from the interaction with BCl<sub>2</sub>Ph. At 100 °C, we started to observe the formation of both the cyclic carbonate and the dimer. Both the formation of the secondary products and the cycloaddition products (cyclic carbonate and dimer) increased with temperature after 100 °C. The selectivity toward the cyclic carbonate and the dimer did not vary that much: between 26 % and 37 % for the first, and between 5 % and 8 % for the second.

The temperature only impacted the selectivity with a threshold between 80 °C and 100 °C. The temperature was high enough for the MgO catalyst to catalyse both the cycloaddition reaction and the secondary reactions.

The <sup>11</sup>B NMR (Annexe 13) did not give any clear trend in the presence of the 32 ppm or 29 ppm peaks. It seemed however that the 32 ppm peak was not present at room temperature and appeared at 80 °C. It was not clear if the 32 ppm peak increased with the temperature.

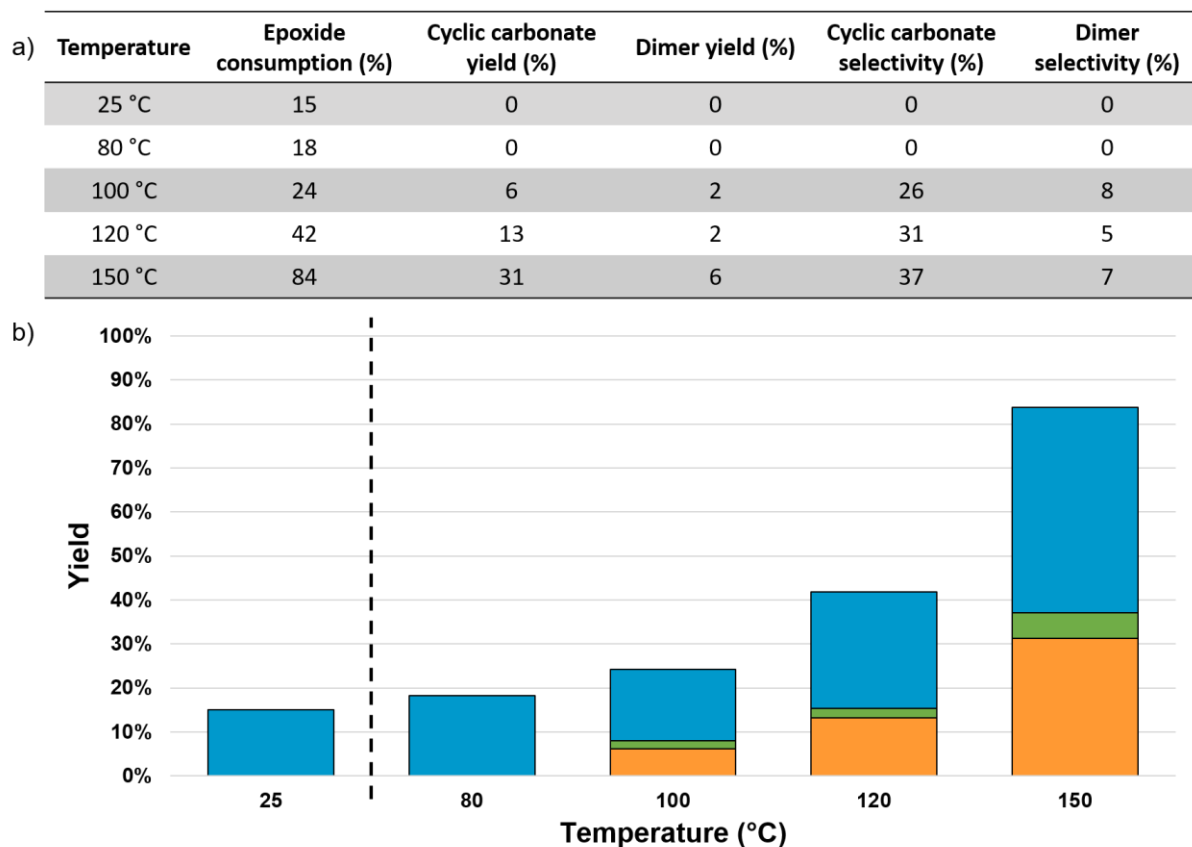
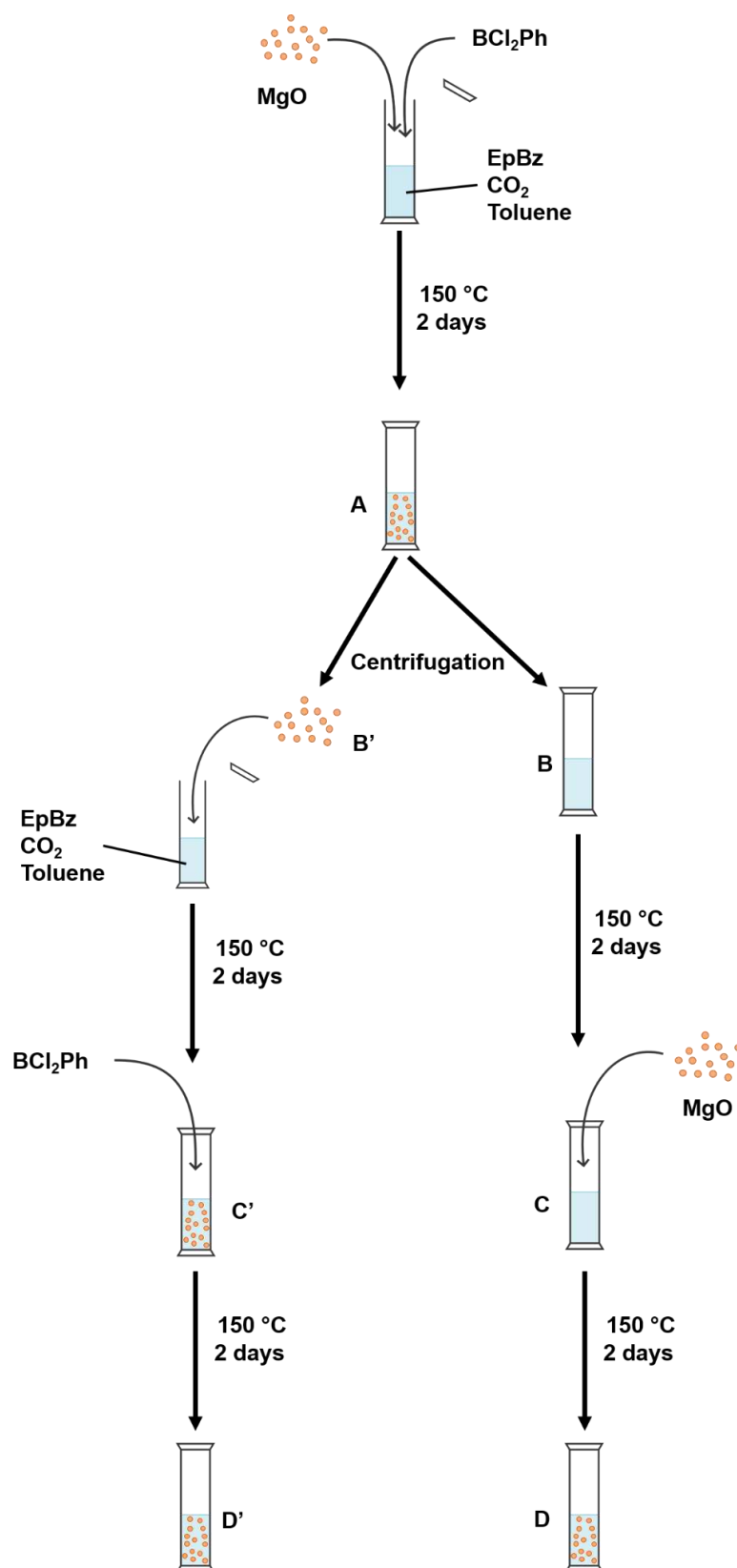


Figure 40: Impact of the temperature on the catalytic performance of  $MgO+BCl_2Ph$  in the cycloaddition of  $CO_2$  on epoxide. a) Numerical values, b) graphic representation (orange: cyclic carbonate yield, green: dimer yield, blue: secondary products yield).

With these tests, we had a first understanding of the elements influencing the synergy between  $MgO$  and  $BCl_2Ph$ . It seemed that the most crucial parameter was the borane loading.

The question now was the following: was the reactivity due to the interaction between  $MgO$  and  $BCl_2Ph$ ? To the borane once it was transformed on the  $MgO$  surface? To the  $MgO$  surface that was modified by the borane? We needed to study the catalyst after the reaction.

## 2. Supernatant activity test



Scheme 15: Supernatant activity test for the cycloaddition of CO<sub>2</sub> on EpBz catalysed by MgO+BCl<sub>2</sub>Ph.

To elucidate the question of who was the real catalyst, we decided to do the reaction in several steps (Scheme 15:). First we did the reaction catalysed by MgO+BCl<sub>2</sub>Ph in conditions where it would not be complete (solution **A**). We chose to work with 0.005 equivalents of BCl<sub>2</sub>Ph for 48 hours at 150 °C. After that we separated the supernatant (**B**) and the nanoparticles (**B'**) by centrifugation. We put the nanoparticles in a fresh catalytic environment without borane and started two reactions: the old medium without the nanoparticles (**C**) and the new medium with the new nanoparticles (**C'**). Then we added fresh MgO nanoparticles and fresh BCl<sub>2</sub>Ph respectively to the first and the second solution and started the reaction again (**D** and **D'**). These different steps would inform us on what part of the system was really responsible of the catalytic activity enhancement of the MgO nanoparticles.

When analysing the results of the catalytic reactions (Figure 41:), we saw that the initial epoxide consumption was 21 % with a 13 % cyclic carbonate yield (**A**). This was coherent with the results obtained in Figure 38:, emphasizing the repeatability of the reaction.

After isolating the nanoparticles, the supernatant was heated at 150 °C for 2 days, and we saw that the composition of the reaction medium did not change (**C**). Neither the cyclic carbonate nor the secondary products evolved. When we added fresh MgO nanoparticles afterward and heated at 150 °C for another 2 days, we saw the consumption of the epoxide (**D**). When subtracting with what was already in the reaction medium, we obtained a 12 % epoxide consumption for a 9 % cyclic carbonate yield. This was comparable with what was expected for fresh MgO nanoparticles (Figure 36:).

On the other hand, we isolated the MgO nanoparticles after the first reaction and put them with fresh reactants but without the borane (**C'**). We could see a 5 % consumption of the epoxide and a 3 % carbonate yield, which was lower than what was expected. When adding fresh BCl<sub>2</sub>Ph in the solution (**D'**), we could observe a 9 % epoxide consumption for a 6 % carbonate yield. The addition of the borane increased the catalytic performances of the old MgO nanoparticles.



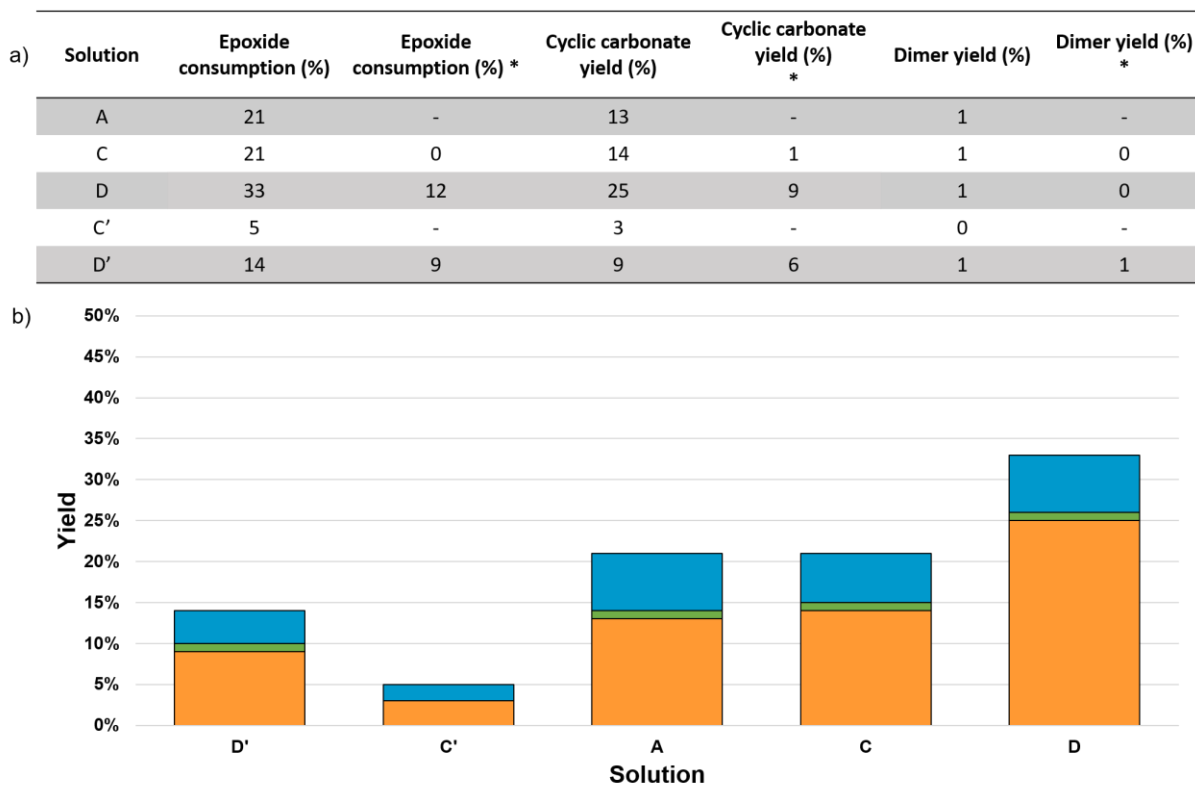


Figure 41: Supernatant activity test for the cycloaddition of CO<sub>2</sub> on EpBz catalysed by MgO+BCl<sub>2</sub>Ph. a) Numerical values (columns with a '\*' are the subtraction with the previous step), b) graphic representation (orange: cyclic carbonate yield, green: dimer yield, blue: secondary products yield)

The <sup>11</sup>B NMR spectra of the different reactions (Annexe 14) only showed the presence of two peaks at 32 ppm and 23 ppm. The 29 ppm peak was not detected. This was coherent with the fact that this peak only appeared when the borane concentration was high.

From this supernatant activity test, we could observe that neither the post catalysis MgO nanoparticles, nor the homogeneous species present in solution were highly active catalyst for the cycloaddition of CO<sub>2</sub> on EpBz. The homogeneous species did not increase the fresh MgO nanoparticles activity when they were added. On the other side, fresh BCl<sub>2</sub>Ph increased the activity of post catalysis MgO nanoparticles. It seemed that the key in the interaction between MgO and BCl<sub>2</sub>Ph was the fact that the chloroborane did not already react with other species in solutions. Fresh BCl<sub>2</sub>Ph was necessary.

### 3. Post mortem analysis

We did the post mortem analysis of the MgO nanoparticles after the catalytic reaction with both XRD and TEM analyses. Results were displayed in Figure 42. When looking at the post mortem diffractogram, we were surprised to observe the presence of a phase that we attributed to NaCl. Upon exposition to air, we also observed that the powder colour changed, going from brown to yellow. This colour change will be discussed later. The TEM micrographs of the post-mortem nanoparticles were similar to those of fresh MgO nanoparticles, it was not possible to tell the difference between the two samples.

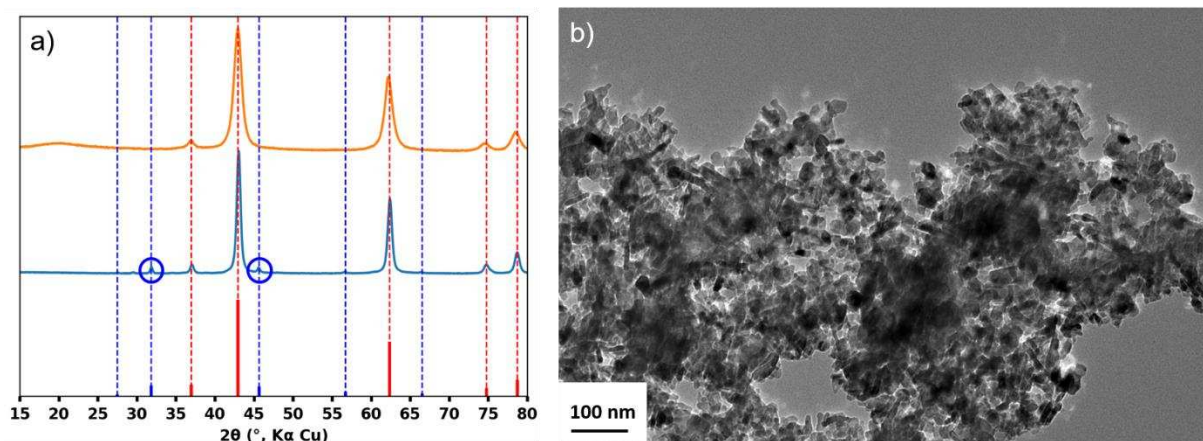


Figure 42: a) XRD pattern of the MgO nanoparticles after the cycloaddition reaction with  $BCl_2Ph$  (blue: MgO, orange:  $MgO_{washed}$ , red bars: MgO reference PDF Card n°00-004-0829, blue bars: NaCl reference PDF Card n°00-005-0628). b) TEM micrograph of the MgO nanoparticles after the cycloaddition reaction.

It was at this moment that we tried to modify the washing step of our nanoparticle synthesis, as presented in Chapter III. When we did the reaction with  $MgO_{washed}$  no trace of NaCl was detected in the post mortem XRD of the nanoparticles. This indicated that the washing steps successfully removed the residual  $Na^+$  cations at the surface of the MgO nanoparticles.

We used  $MgO_{washed}$  nanoparticles in the following part of the project.

#### 4. Mechanism proposition

In order to properly understand the interaction between MgO and BCl<sub>2</sub>Ph during the cycloaddition reaction, we decided to study all the possible interactions one by one. We mixed the different elements (EpBz, CO<sub>2</sub>, MgO<sub>washed</sub>, BCl<sub>2</sub>Ph) in toluene (4 mL) either at room temperature or at 150 °C. The stoichiometry was the same used previously and the duration of each experiment was one day. All the manipulations and washing were made under glovebox. NMR analyses were made in dry toluene-d<sub>8</sub> to reduce the water content, and the XRD were made under inert atmosphere. We defined a nomenclature for the experiment names with the first letter of the present components and the temperature. For example, ECB\_150 corresponded to the experiment with EpBz, CO<sub>2</sub> and BCl<sub>2</sub>Ph at 150 °C. Table 10: gave the name of the experiments for reference.

Name	EpBz	CO <sub>2</sub>	MgO	BCl <sub>2</sub> Ph	Temperature	Name	EpBz	CO <sub>2</sub>	MgO	BCl <sub>2</sub> Ph	Temperature
E_RT	X				25 °C	E_150	X				150 °C
C_RT		X			25 °C	C_150		X			150 °C
M_RT			X		25 °C	M_150			X		150 °C
B_RT				X	25 °C	B_150				X	150 °C
EC_RT	X	X			25 °C	EC_150	X	X			150 °C
EM_RT	X		X		25 °C	EM_150	X		X		150 °C
EB_RT	X			X	25 °C	EB_150	X			X	150 °C
CM_RT		X	X		25 °C	CM_150		X	X		150 °C
CB_RT		X		X	25 °C	CB_150		X		X	150 °C
MB_RT			X	X	25 °C	MB_150			X	X	150 °C
ECM_RT	X	X	X		25 °C	ECM_150	X	X	X		150 °C
ECB_RT	X	X		X	25 °C	ECB_150	X	X		X	150 °C
CMB_RT		X	X	X	25 °C	CMB_150		X	X	X	150 °C
ECMB_RT	X	X	X	X	25 °C	ECMB_150	X	X	X	X	150 °C

Table 10: Name of the different experiments to study the interaction in the cycloaddition of CO<sub>2</sub> on EpBz catalysed by MgO+BCl<sub>2</sub>Ph in toluene at 150 °C for 1 day.

Only the most pertinent results will be detailed below. The other experiments will be described in 0.

### a. One component experiments

Even if we did not expect anything uncommon to happen in the experiments with only one component, we wanted to be sure. Basically, we just put either EpBz, CO<sub>2</sub>, MgO<sub>washed</sub> or BCl<sub>2</sub>Ph in toluene for 1 day either at room temperature or at 150 °C.

#### B\_RT

We observed a modification of the <sup>11</sup>B NMR signal of (Figure 43:). We saw the apparition of a peak at 39 ppm. One possible attribution could be BCl(OR)Ph since we know that the substitution of Cl<sup>-</sup> by OH<sup>-</sup> was possible. The borane could have reacted with residual traces of oxygen containing species (like water) in the solvent.

#### B\_150

Just like at room temperature, we detected a modification of the <sup>11</sup>B NMR signal of BCl<sub>2</sub>Ph (Figure 43:). We could see the apparition of two peaks: one at 37 ppm and one at 29 ppm. A possible attribution would be that the 37 ppm specie corresponded to the 39 ppm specie obtained at room temperature (BCl(OR)Ph), and that the 29 ppm specie corresponded to a B(OR)<sub>2</sub>Ph specie.

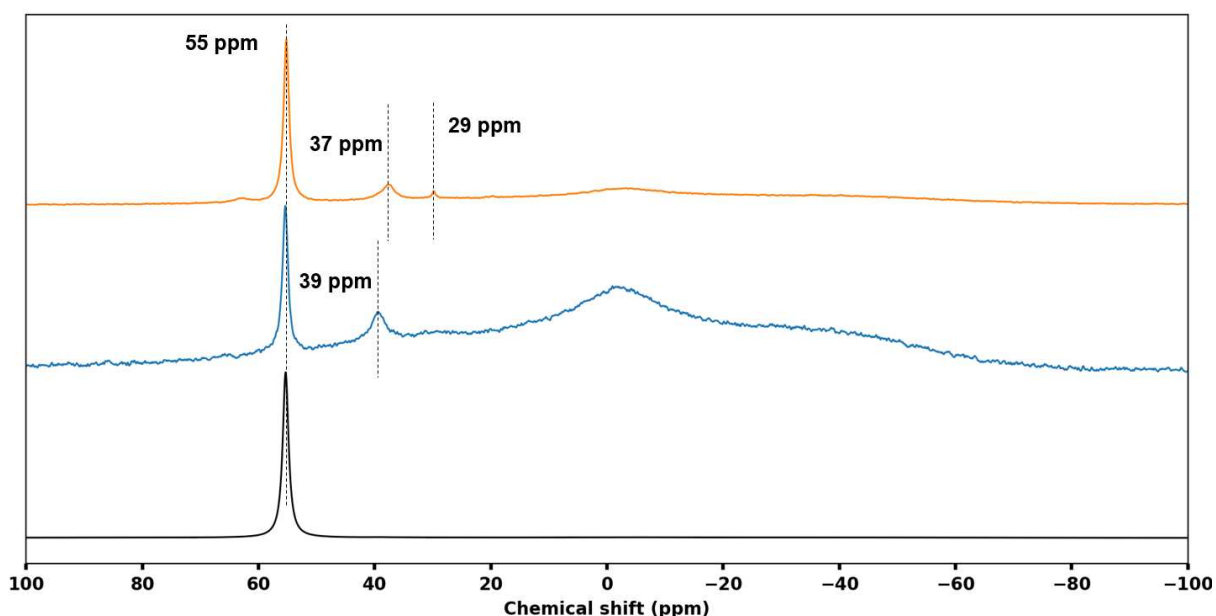


Figure 43: <sup>11</sup>B NMR spectra of BCl<sub>2</sub>Ph reference (back), B\_RT (blue) and B\_150 (orange) in toluene-d<sub>8</sub>.

The experiments with one component did not show any reaction for the epoxide, CO<sub>2</sub> and MgO. However, we saw that some of the borane was consumed to form BCl(OR)Ph and B(OR)<sub>2</sub>Ph (only at 150 °C) species. One explanation could be the reaction between BCl<sub>2</sub>Ph and residual oxygen containing species in the solvent.

**b. Two components experiments**

We expected the reactions with two components to be more informative than the previous ones. We already saw in Chapter IV that MgO nanoparticles reacted with BCl<sub>2</sub>Ph, and we also saw that the chloroborane reacted with the epoxide at room temperature (Figure 40:). These experiments would also inform on the surface state of MgO by IR spectroscopy after the reactions.

**EM\_RT**

Nothing happened in <sup>1</sup>H NMR when exposing the epoxide to MgO<sub>washed</sub> at room temperature for 1 day. However, when doing the post mortem IR spectroscopy of the nanoparticles we could see the apparition of characteristic bands of C—C phenyl vibration around 1500 cm<sup>-1</sup> (Figure 44:b). This indicated that the epoxide was adsorbed on the nanoparticles surfaces. Bulk Mg—O vibration was located at 700 cm<sup>-1</sup>, we did not manage to determine if one of the peaks in this region could correspond to a Mg—O(epoxide) vibration.

**EM\_150**

When we exposed epoxide to MgO<sub>washed</sub> at 150 °C for 1 day, we observed in <sup>1</sup>H NMR the apparition new peaks (Figure 44:a). We identified these products to be isomers of the epoxide: secondary products **3**, **4** and **5** as described in Figure 6:. We estimated the epoxide consumption to be 8 %. The IR spectroscopy also showed the presence of characteristic C—C phenyl bands. MgO<sub>washed</sub> catalysed the isomerisation of EpBz and the latter adsorbed on the nanoparticle surface. It could be interesting to see at what temperature the isomerisation starts, to see if it would be the same temperature for the cycloaddition reaction.

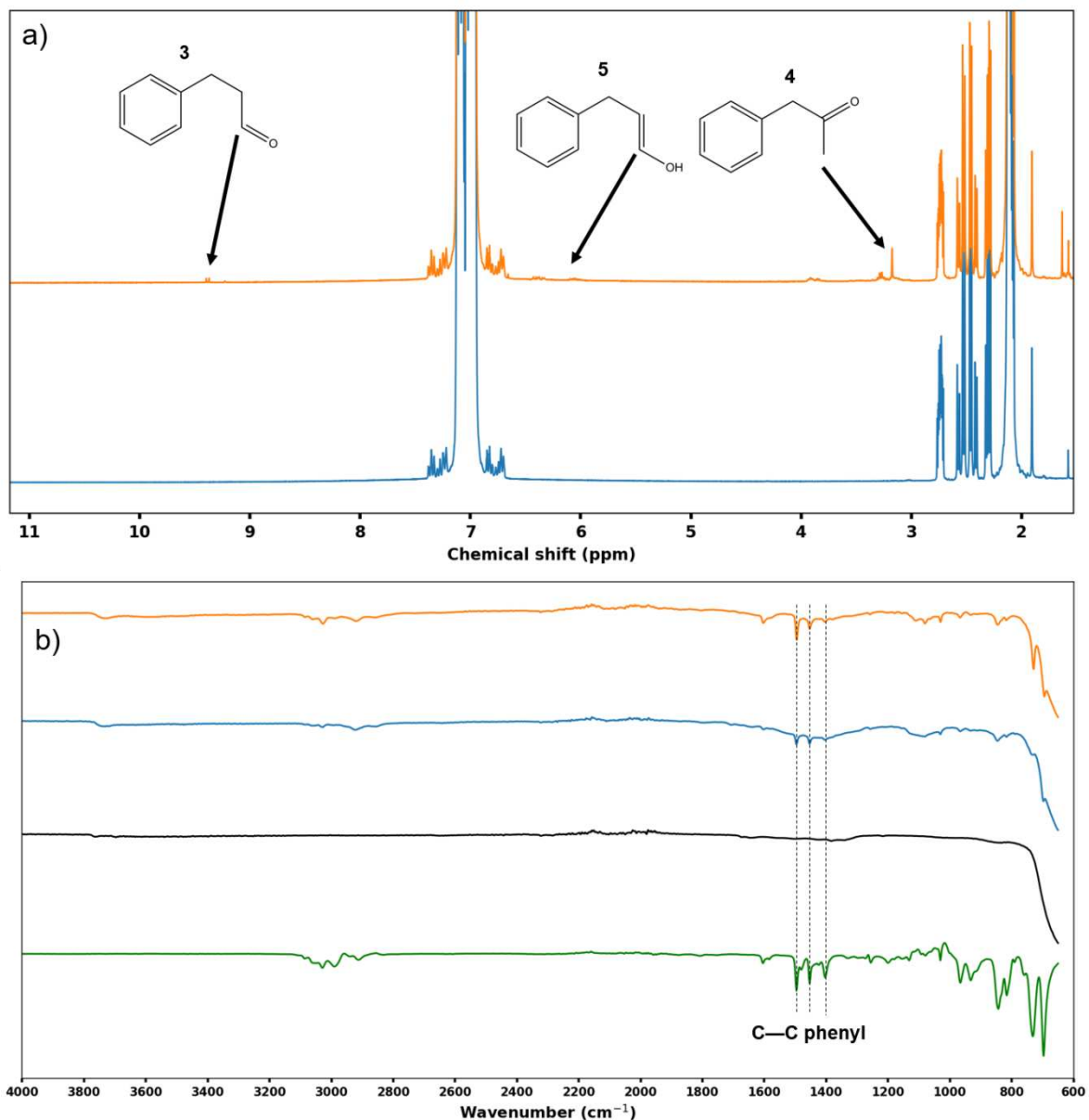


Figure 44: a)  $^1\text{H}$  NMR spectra of EM\_RT (blue) and EM\_150 (orange) in toluene- $d_8$ . Proposition of attribution for secondary products were made based on the molecules presented in Figure 6. b) IR spectra of reference EpBz (green), reference  $\text{MgO}_{\text{washed}}$  (black), EM\_RT (blue) and EM\_150 (orange).

## EB\_RT

When we exposed the epoxide to  $\text{BCl}_2\text{Ph}$  at room temperature for 1 day, we observed in  $^1\text{H}$  NMR the apparition of secondary products (Figure 45:a). We did not manage to identify precisely the different secondary products, but 2D NMR (COSY) allowed to determine that they were two of them (Annexe 15). We used well defined doublets at 3.9 ppm and 3.1 ppm to calculate the NMR epoxide consumption. We estimated the epoxide consumption to be 17 %. The  $^{11}\text{B}$  NMR showed the consumption of  $\text{BCl}_2\text{Ph}$  to form a specie at 29 ppm, corresponding to a  $\text{B}(\text{OR})_2\text{Ph}$  specie.

**EB\_150**

The reaction with the epoxide and the borane at 150 °C for 1 day was similar to the one at room temperature. The secondary products were the same but the epoxide consumption was estimated to 12 %. High temperature possibly reduced the efficiency of the borane induced catalytic reaction, but the effect was small and could be not significant. Repetitions would be necessary to confirm this hypothesis.

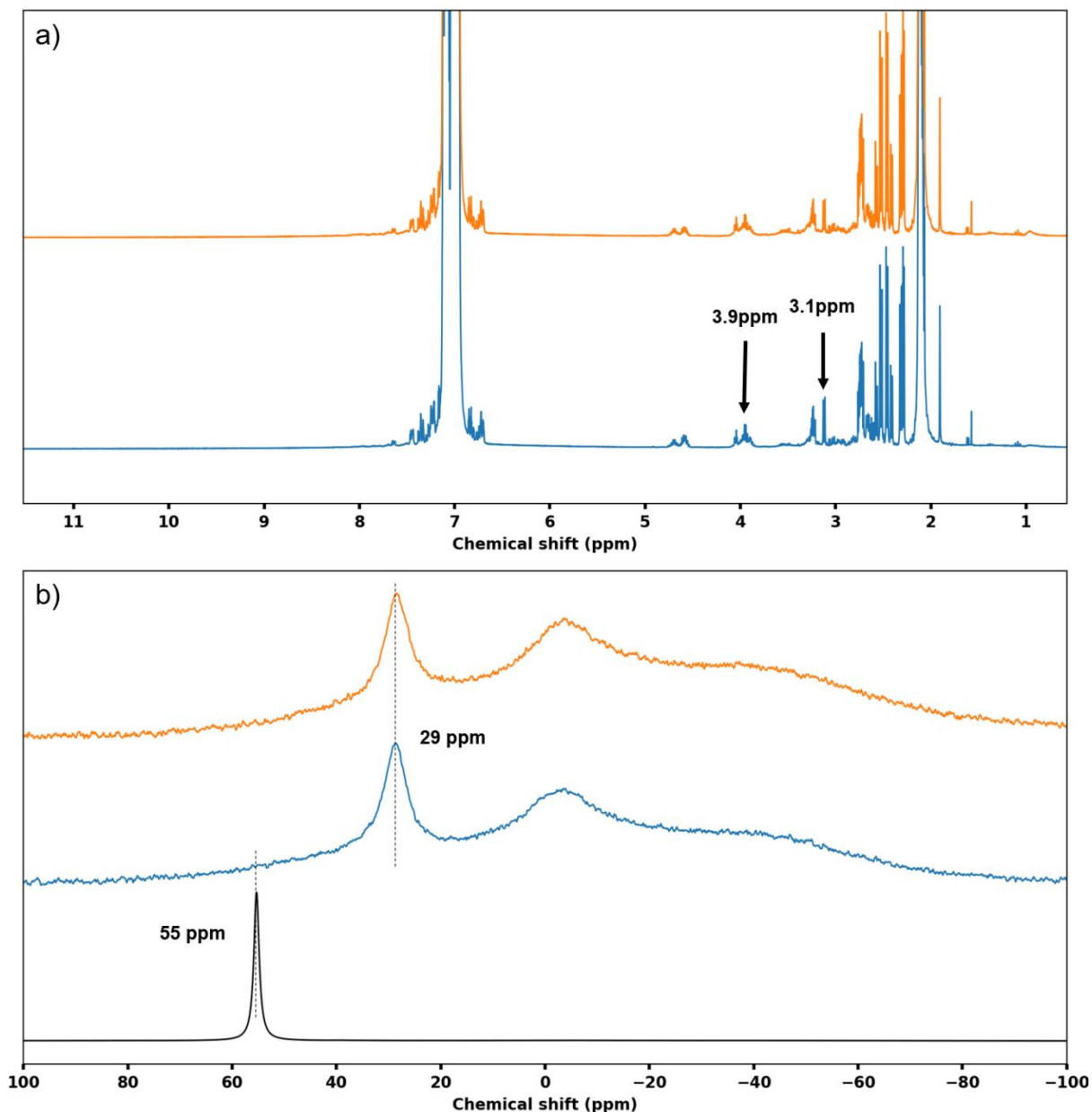


Figure 45: a) <sup>1</sup>H NMR spectra of EB\_RT (blue) and EB\_150 (orange) in toluene-d<sub>8</sub>. b) <sup>11</sup>B NMR spectra of EB\_RT (blue) and EB\_150 (orange) in toluene-d<sub>8</sub>.

**CM\_RT**

When we exposed  $\text{MgO}_{\text{washed}}$  nanoparticles to  $\text{CO}_2$  at room temperature for 1 day, we saw the apparition of new bands in IR spectroscopy (Figure 46:). The bands at 1719, 1525, 1409 and 861  $\text{cm}^{-1}$  corresponded to surface carbonates, and the peaks at 2923  $\text{cm}^{-1}$  corresponded to adsorbed toluene.

**CM\_150**

The same thing happened when we exposed  $\text{MgO}_{\text{washed}}$  to  $\text{CO}_2$  at 150 °C for 1 day. The carbonate band at 1719  $\text{cm}^{-1}$  was not detected, but the other carbonate bands were more intense. Carbonate formation was stronger at 150 °C, which was expected from the results obtained in Chapter IV.

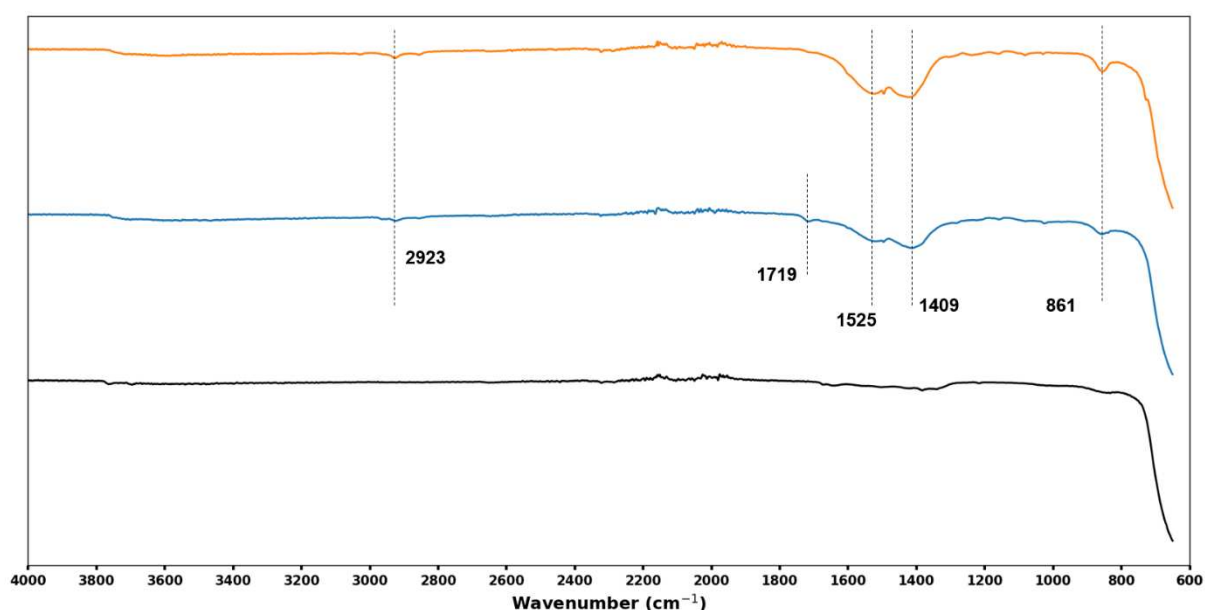


Figure 46: IR spectra of reference  $\text{MgO}_{\text{washed}}$  (black), CM\_RT (blue) and CM\_150 (orange) after drying under inert atmosphere.

**MB\_RT**

When we exposed  $\text{MgO}_{\text{washed}}$  nanoparticles to  $\text{BCl}_2\text{Ph}$  at room temperature for 1 day, we could see that the nanoparticles changed colour and became yellow (Figure 47:a). After centrifugation, the supernatant was transparent and only the sedimented nanoparticles were colored. The colour was due to the nanoparticles and not to homogeneous species in the medium. After exposition to air, the nanoparticles became white. The  $^{11}\text{B}$  NMR spectra showed a partial consumption of the borane to form species at 38 ppm, 30 ppm and 27 ppm (Figure 47:b). They could correspond to  $\text{BCl}(\text{OR})\text{Ph}$  and  $\text{B}(\text{OR})_2\text{Ph}$  species. The IR spectra of the nanoparticles showed the apparition of bands characteristic to phenyl groups around 1500  $\text{cm}^{-1}$ , and a large band at 1300-1400  $\text{cm}^{-1}$  that could correspond to a B—O elongation vibration (Figure 47:c). Contrary with



the adsorption of EpBz on the MgO<sub>washed</sub> surface, the C—C phenyl bands were shifted toward higher wave number.

### MB\_150

The results at 150 °C were similar to the one at room temperature. The colour changes were the same. However, we saw in <sup>11</sup>B NMR spectroscopy that BCl<sub>2</sub>Ph was totally consumed to form a specie at 30 ppm (B(OR)<sub>2</sub>Ph like specie). This was surprising since there was no molecular source of oxygen in the medium. The IR spectroscopy also showed the presence of shifted C—C phenyl bands and a large signal between 1300 and 1400 cm<sup>-1</sup>.

The two components experiments brought interesting information:

- EpBz, CO<sub>2</sub> and MgO adsorbed at the surface of MgO nanoparticles
- MgO catalysed the isomerisation of EpBz at 150 °C
- BCl<sub>2</sub>Ph reacted with the epoxide to form two unknown secondary products
- BCl<sub>2</sub>Ph was consumed when reacting with MgO at 150 °C to form B(OR)<sub>2</sub>Ph species despite the fact that no molecular source of oxygen was present. MgO possibly leached

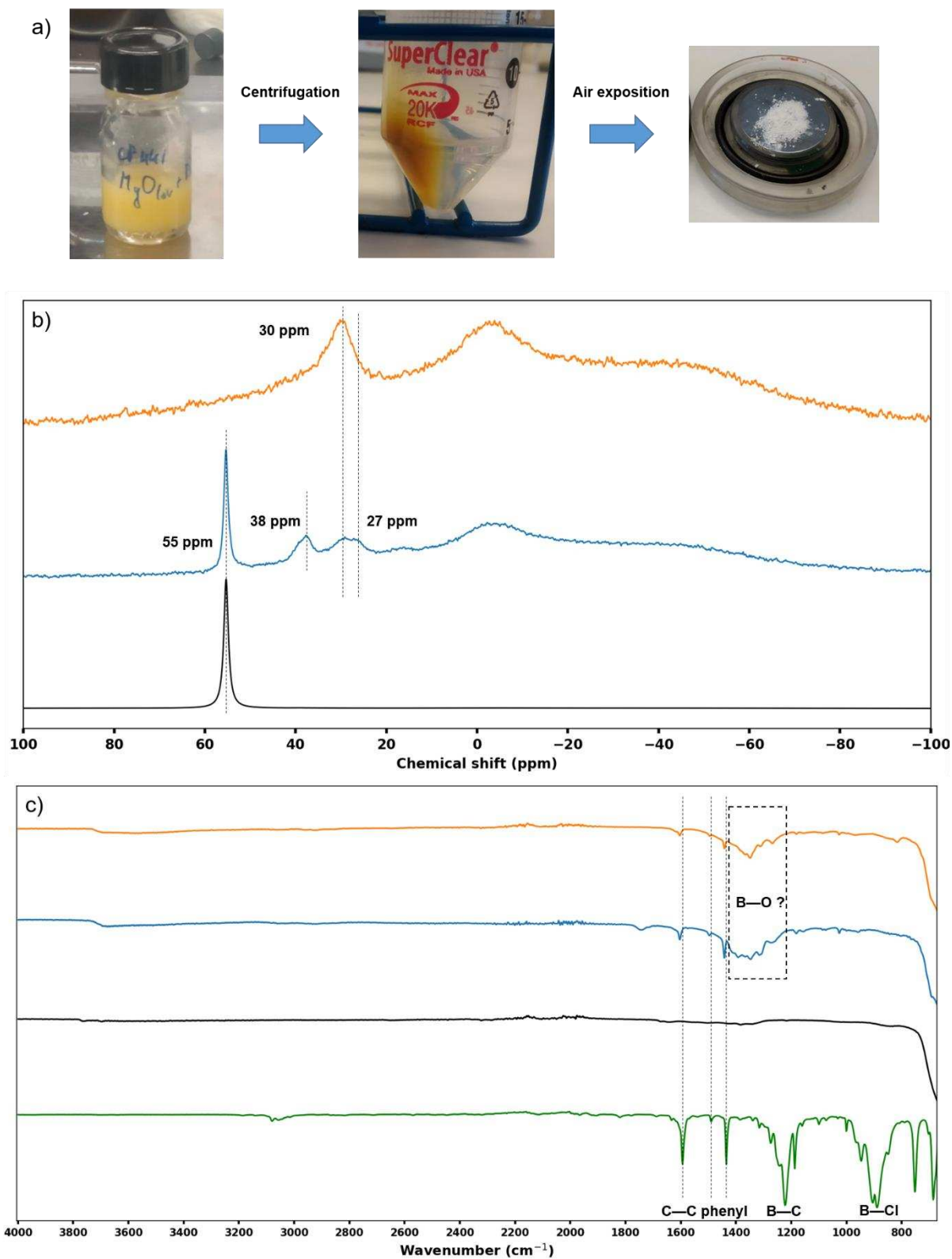


Figure 47: a) Colour change of the  $MgO_{washed}$  nanoparticles after MB\_RT. b)  $^{11}B$  NMR spectra of reference  $BCl_2Ph$  (black), MB\_RT (blue) and MB\_150 (orange) in toluene- $d_8$ . c) IR spectra of reference  $BCl_2Ph$  (green), reference  $MgO_{washed}$  (black), MB\_RT (blue) and MB\_150 (orange).

### c. Three components experiments

The previous experiments showed the interactions between the different components. The question was the following: was the interaction of A+B+C equal to the interaction of (A+B) plus (A+C) plus (B+C), or was there some three component interaction? We already knew that ECM\_150 reaction should result in the formation of the cyclic carbonate, but we wanted to see how MgO+BCl<sub>2</sub>Ph would behave in presence of either EpBz or CO<sub>2</sub>.

#### ECM\_RT

The interaction between the epoxide, CO<sub>2</sub> and MgO<sub>washed</sub> was the same as the interactions with two elements. No epoxide consumption was detected by <sup>1</sup>H NMR (Figure 48:a). We detected the adsorption of EpBz on MgO<sub>washed</sub> nanoparticles thanks to the phenyl vibrations, and we also detected large carbonate bands due to the interaction with CO<sub>2</sub> (Figure 48:b).

#### ECM\_150

At 150 °C, we detected the formation of the cyclic carbonate (Figure 48:a). The epoxide consumption was estimated to 13 % and the carbonate selectivity was 81 %. This was more than what we obtained with classical MgO nanoparticles (7 % epoxide consumption and 60 % carbonate selectivity in Figure 25:c). MgO<sub>washed</sub> nanoparticles were more active and more selective than classical MgO nanoparticles. The IR spectroscopy also showed the adsorption of EpBz and the formation of surface carbonates on the surface of MgO<sub>washed</sub> nanoparticles. We also detected the presence of a band at 1805 cm<sup>-1</sup> that corresponded to C=O elongation vibration. This indicated that some of the formed cyclic carbonate was adsorbed at the surface of the catalyst.

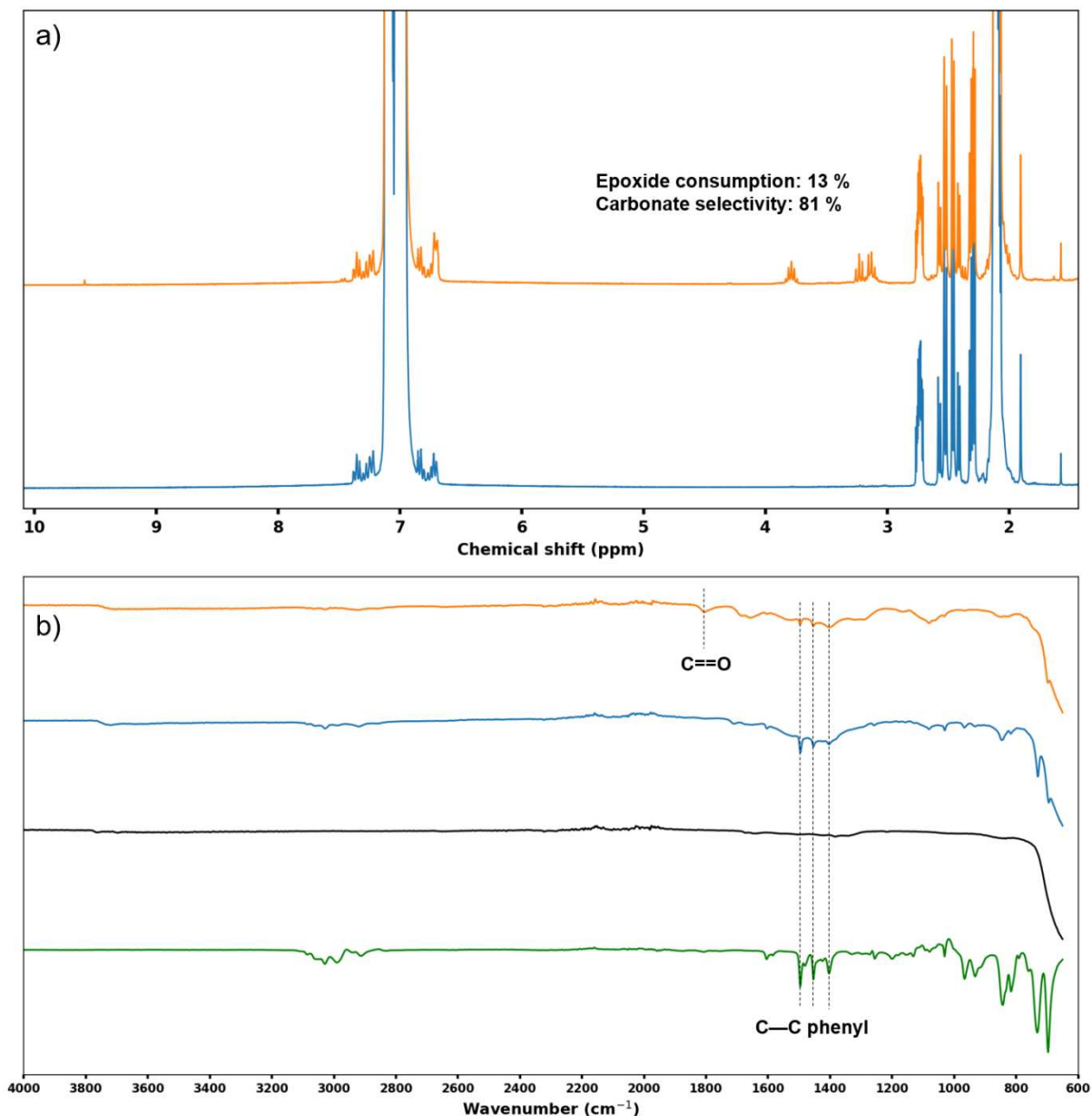


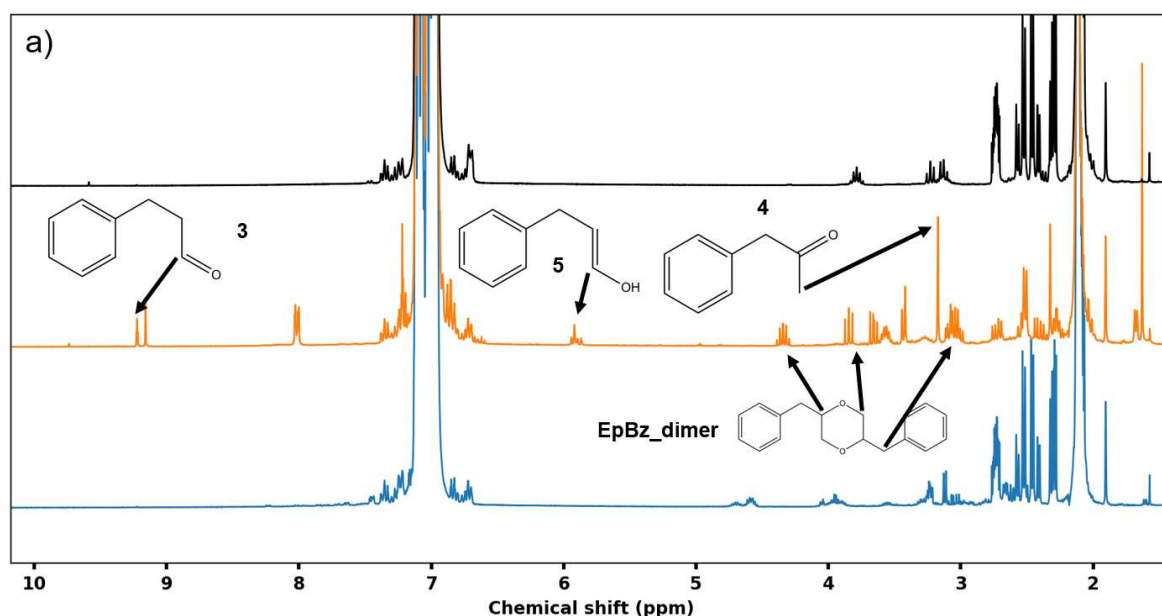
Figure 48: a)  $^1\text{H}$  NMR spectra of ECM\_RT (blue) and ECM\_150 (orange) in toluene- $d_8$ . b) IR spectra of reference  $\text{BCl}_2\text{Ph}$  (green), reference  $\text{MgO}_{\text{washed}}$  (black), ECM\_RT (blue) and ECM\_150 (orange).

## EMB\_RT

When we mixed EpBz,  $\text{MgO}_{\text{washed}}$  and  $\text{BCl}_2\text{Ph}$  at room temperature for 1 day, we observed the same reaction as with EB\_RT (Figure 49:a,b). We observed in  $^1\text{H}$  NMR the formation of two secondary products and estimated the epoxide consumption to be 15 % (it was 17 % in EB\_RT). The  $^{11}\text{B}$  NMR showed the consumption of  $\text{BCl}_2\text{Ph}$  to form a species signing with a peak at 29 ppm. The IR spectra showed the adsorption of both the epoxide and the borane at the surface of the  $\text{MgO}_{\text{washed}}$  nanoparticles through C—C phenyl vibrations, and the presence of a broad signal between 1300 and 1400  $\text{cm}^{-1}$  potentially coming from B—O vibration.

**EMB\_150**

When we mixed EpBz, MgO<sub>washed</sub> and BCl<sub>2</sub>Ph at 150 °C for 1 day, we could not detect the epoxide by <sup>1</sup>H NMR (Figure 49:a). It was consumed and we detected several secondary products. We managed to identify four different products: three of them were already formed in the reaction EM\_150 (secondary products **3**, **4** and **5** as referred Figure 6:), and another specie with a proton signal structure really close to the one of the cyclic carbonate. One proposition we could make was the formation of a dimer of the epoxide, it would have a similar proton structure and chemical displacement as the cyclic carbonate. This was an unreported reactivity between EpBz, MgO and BCl<sub>2</sub>Ph. The <sup>11</sup>B NMR showed the total consumption of BCl<sub>2</sub>Ph to form a specie with a signal at 32 ppm. The IR spectra showed the adsorption of both the epoxide and the borane at the surface of the MgO<sub>washed</sub> nanoparticles through C—C phenyl vibrations, and the presence of a broad signal between 1300 and 1400 cm<sup>-1</sup> potentially coming from B—O vibration. The C—C phenyl signature of the epoxide dimer was probably really close to the one of the epoxide, explaining why we detected the bands even if all the epoxide was consumed.



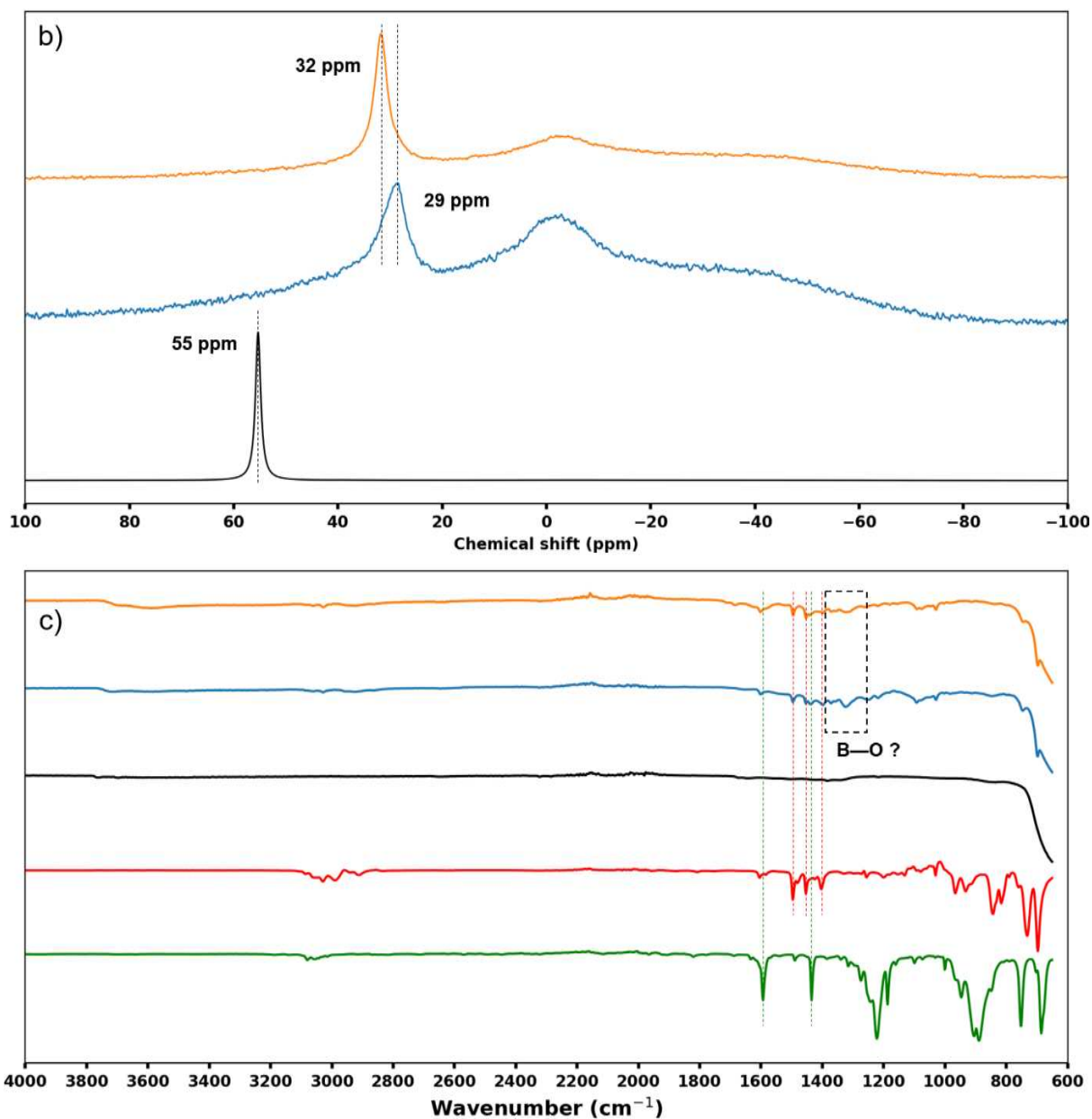


Figure 49: a)  $^1\text{H}$  NMR spectra of reference EMB\_RT (blue), EMB\_150 (orange) and ECB for reference (black) in toluene- $d_8$ . b)  $^{11}\text{B}$  NMR spectra of reference reference  $\text{BCl}_2\text{Ph}$  (black) EMB\_RT (blue) and EMB\_150 (orange) in toluene- $d_8$ . c) IR spectra of reference  $\text{BCl}_2\text{Ph}$  (green), reference  $\text{EpBz}$  (red) reference  $\text{MgO}_{\text{washed}}$  (black), EMB\_RT (blue) and EMB\_150 (orange).

## CMB\_RT

When we mixed  $\text{CO}_2$ ,  $\text{MgO}_{\text{washed}}$  and  $\text{BCl}_2\text{Ph}$  at room temperature for 1 day, we obtained results similar to MB\_RT. We could see in  $^{11}\text{B}$  NMR that  $\text{BCl}_2\text{Ph}$  started to react to form two other species at 39 ppm and 29 ppm. The IR spectrum showed the adsorption of the borane on the  $\text{MgO}_{\text{washed}}$  surface and the formation of carbonates.

**CMB\_150**

When we did the reaction at 150 °C for 1 day, we saw that the borane was entirely consumed to form a specie at 29 ppm. The IR spectrum showed the adsorption of the borane and the formation of carbonates at the surface of MgO<sub>washed</sub>.

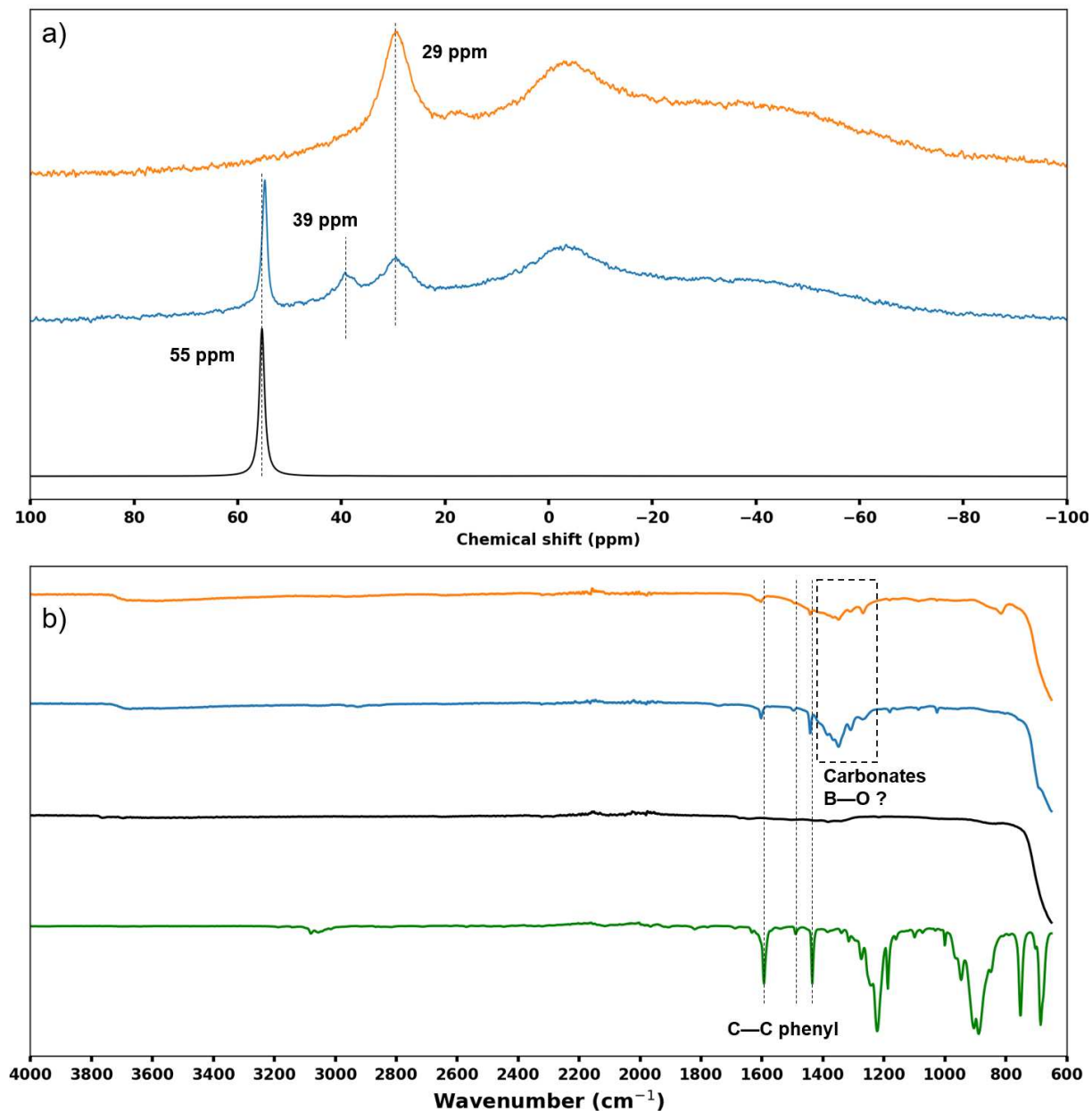


Figure 50: a) <sup>11</sup>B NMR spectra of reference BCl<sub>2</sub>Ph (black) CMB\_RT (blue) and CMB\_150 (orange) in toluene-d<sub>8</sub>. c) IR spectra of reference BCl<sub>2</sub>Ph (green), reference MgO<sub>washed</sub> (black), CMB\_RT (blue) and CMB\_150 (orange).

The three components experiments brought interesting information:

- $\text{MgO}_{\text{washed}}$  nanoparticles were more active than the classical ones
- At room temperature, we did not see any synergy effects
- At 150 °C, the pair  $\text{MgO}_{\text{washed}}+\text{BCl}_2\text{Ph}$  was active in catalysis and consumed all the epoxide. The reaction yielded different secondary products as isomerisation products, dimer of the epoxide, and the secondary products obtained in EB\_RT reaction. The activity of  $\text{MgO}_{\text{washed}}$  in the isomerisation of the epoxide was increased by the presence of  $\text{BCl}_2\text{Ph}$ .
- Considering  $^{11}\text{B}$  NMR,  $\text{BCl}_2\text{Ph}$  transformed either in a 32 ppm specie when interacting with  $\text{MgO}_{\text{washed}}$ , or in a 29 ppm specie when interacting with the epoxide
- $\text{CO}_2$  only interacted in the reaction when  $\text{MgO}_{\text{washed}}$  was present



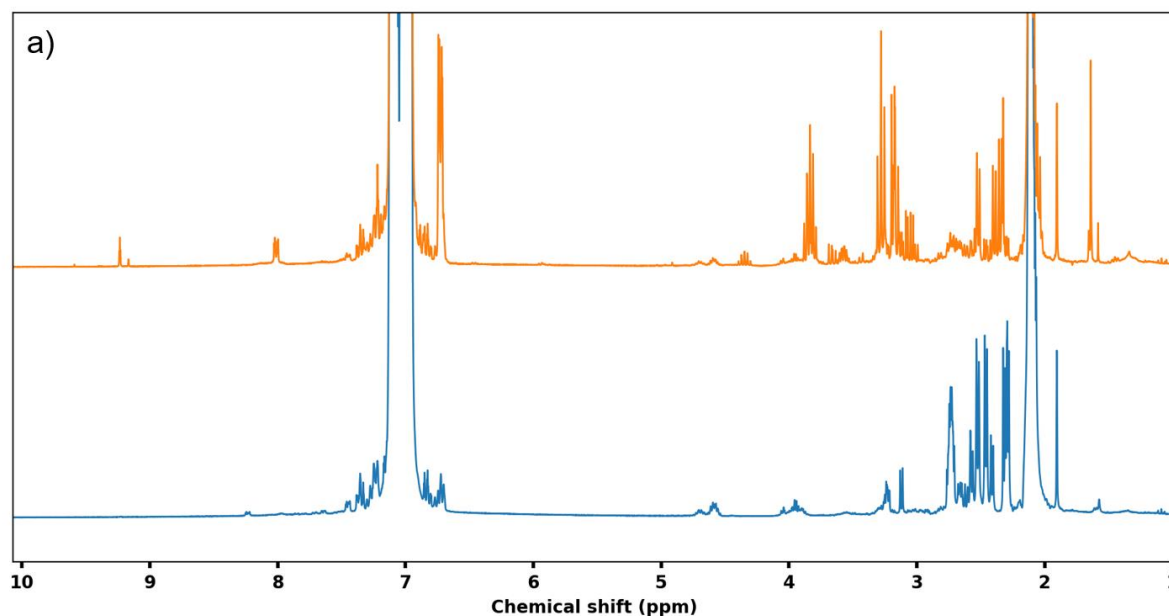
#### d. Four components experiment

##### ECMB\_RT

When mixing the four components EpBz, CO<sub>2</sub>, MgO and BCl<sub>2</sub>Ph at room temperature for 1 day, we could not observe the cycloaddition reaction (Figure 51:). The <sup>1</sup>H NMR showed the formation of the secondary products associated to EB\_RT. The <sup>11</sup>B NMR showed the consumption of the borane into a specie with a peak at 29 ppm just like in EB\_RT. And the IR spectroscopy showed the adsorption of both the epoxide and the at the surface of MgO<sub>washed</sub> nanoparticles. This reaction was the sum of previous reactions EB\_RT, EM\_RT, CM\_RT and MB\_RT.

##### ECMB\_150

When doing the reaction at 150 °C, we observed the total consumption of the epoxide in <sup>1</sup>H NMR, alongside the formation of the cyclic carbonate (Figure 51:a). We estimated the carbonate selectivity to be 66 %, which was higher than what we obtained with classical MgO nanoparticles (it was around 20 % in similar conditions). It confirmed the fact that MgO<sub>washed</sub> nanoparticles were more active and more selective toward cyclic carbonate than the classical ones. We could recognise the different secondary products: the products from the EB\_RT, the isomerisation products from EM\_150, and the epoxide dimer from EMB\_150. The <sup>11</sup>B NMR showed the absence of the BCl<sub>2</sub>Ph peak and the formation of two peaks at 32 and 29 ppm. The IR spectrum showed the adsorption of the borane, the epoxide and the cyclic carbonates. Just like with the EMB\_150 reaction, it was probable that the phenyl signature of the epoxide and the cyclic carbonate were very close. The C—C phenyl vibrations associated to the epoxide were probably those of the cyclic carbonate.



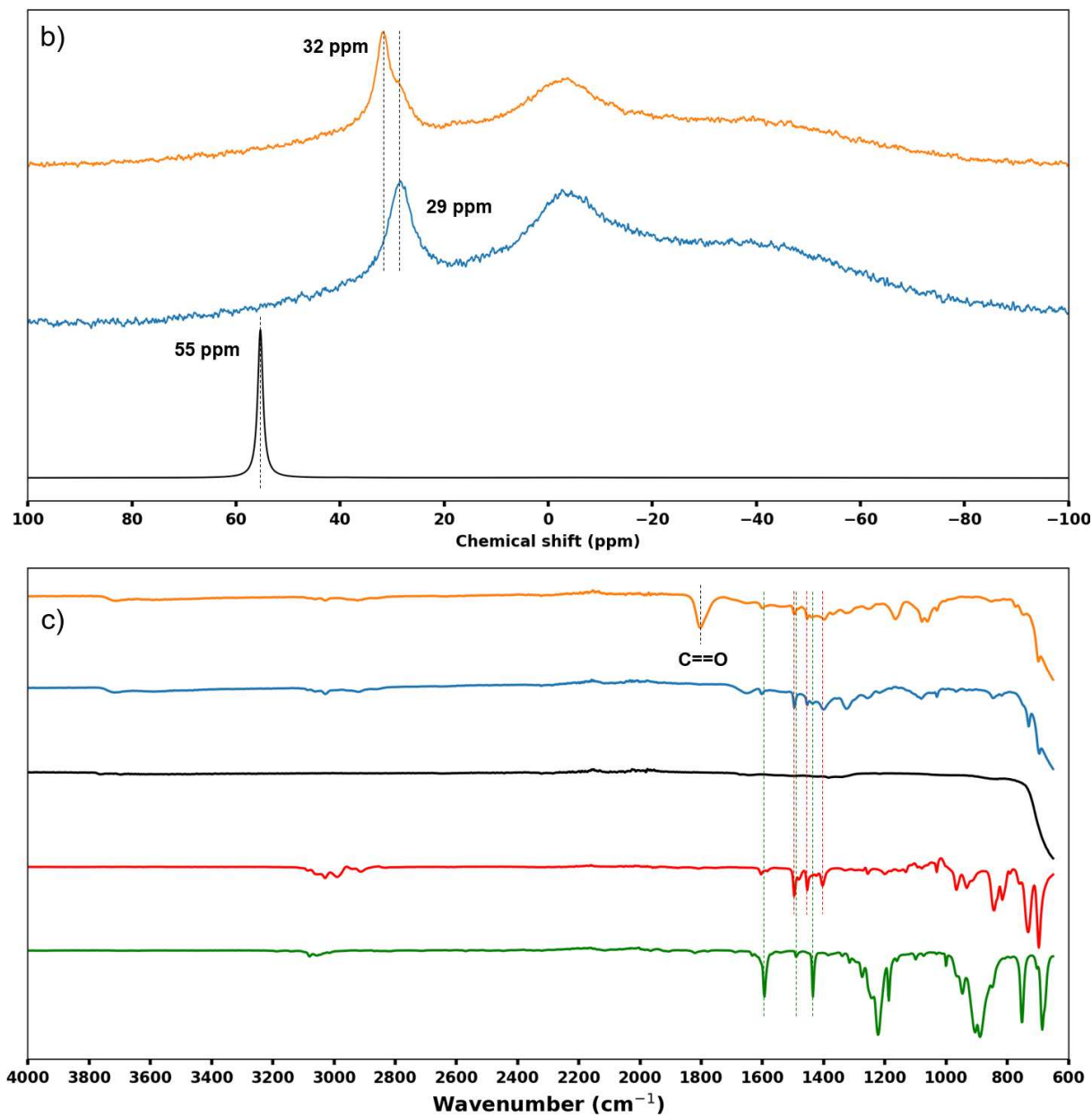


Figure 51: a)  $^1\text{H}$  NMR spectra of reference ECMB\_RT (blue), ECMB\_150 (orange) in toluene- $d_8$ . b)  $^{11}\text{B}$  NMR spectra of reference reference  $\text{BCl}_2\text{Ph}$  (black) ECMB\_RT (blue) and ECMB\_150 (orange) in toluene- $d_8$ . c) IR spectra of reference  $\text{BCl}_2\text{Ph}$  (green), referecne EpBz (red) reference  $\text{MgO}_{\text{washed}}$  (black), ECMB\_RT (blue) and ECMB\_150 (orange).

### e. Mechanism proposition

From the previous experiments, we could try to give an idea of what was happening in the four components reaction.

#### Propositions:

- When we mixed MgO and BCl<sub>2</sub>Ph, the borane chemisorbed on the nanoparticles with a cleavage of the B—Cl bond. In presence of a surface hydroxide, the adsorption could lead to either the formation of HCl or BCl(OH)Ph (Figure 52:). The reaction could occur two times to produce B(OH)<sub>2</sub>Ph, thus explaining the presence of the peaks at 38 and 30 ppm in <sup>11</sup>B NMR.

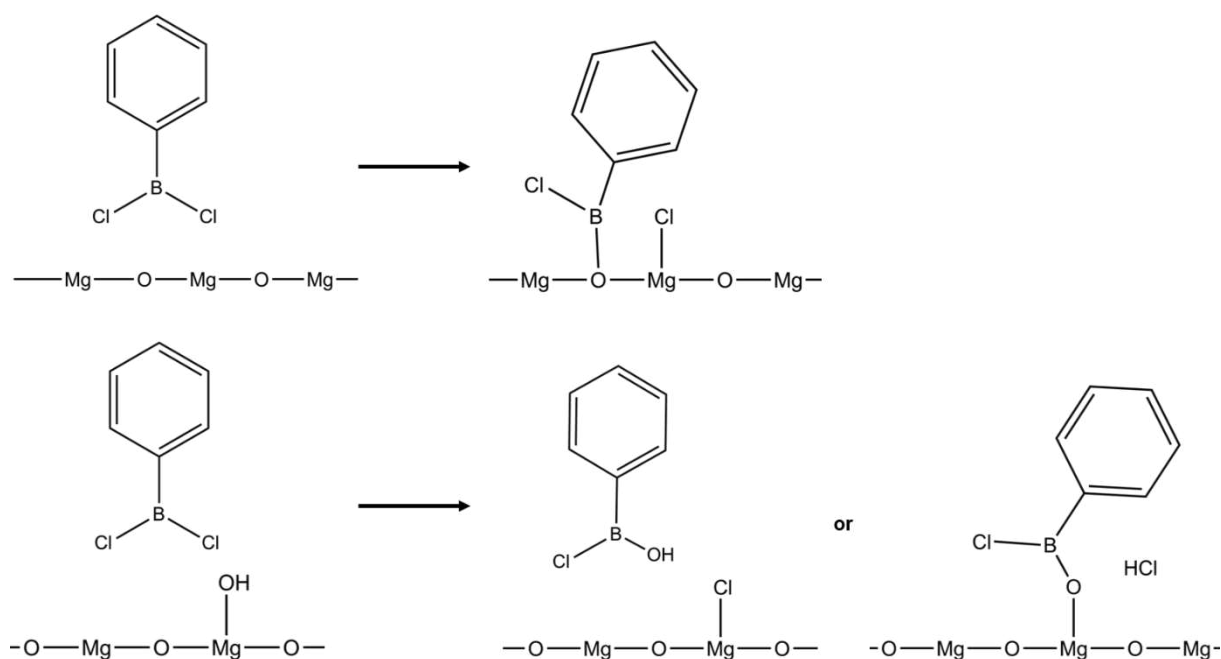


Figure 52: Proposition for the adsorption of BCl<sub>2</sub>Ph on MgO surface.

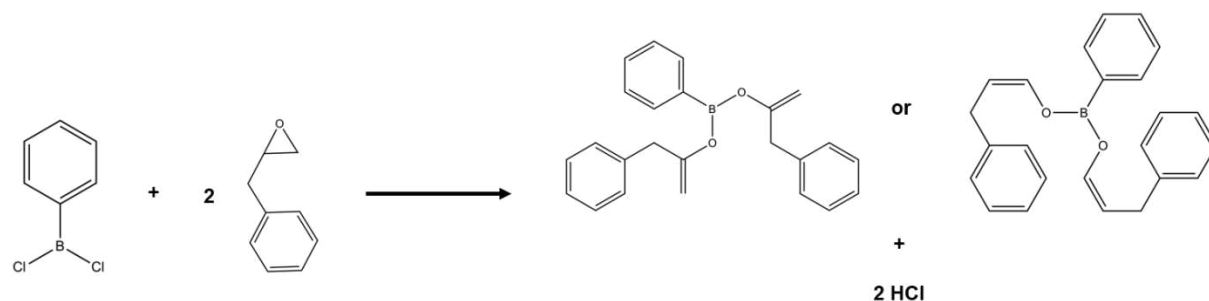


Figure 53: Proposition of the reaction between BCl<sub>2</sub>Ph and EpBz.

## Chapter V

- When we mixed EpBz and BCl<sub>2</sub>Ph, the borane was totally consumed to form a 32 ppm specie, potentially attributed to B(OR)<sub>2</sub>Ph species (Figure 53:). The reaction also produced secondary products that we could not identify precisely.
- When we mixed EpBz and MgO, the epoxide adsorbed at the surface and the acidobasic properties of the surface managed to catalyse the isomerisation (Figure 54:a)
- CO<sub>2</sub> was not reacting with EpBz nor BCl<sub>2</sub>Ph when MgO was not present.
- When we mixed EpBz, MgO and BCl<sub>2</sub>Ph, the adsorbed borane helped to open the epoxide cycle, thus facilitating the isomerisation reactions (Figure 54:b). The dimerisation of the epoxide would follow the same first steps, but the opened epoxide cycle would react with another epoxide molecule to form the dimer (Figure 55:).
- When CO<sub>2</sub> was present in the reaction medium, carbonates formed on the surface of MgO nanoparticles. These carbonates reacted with the opened epoxide molecule, whether they were stabilised by the borane or not (Figure 56:).

MgO-based catalysts in the cycloaddition of CO<sub>2</sub> on epoxides

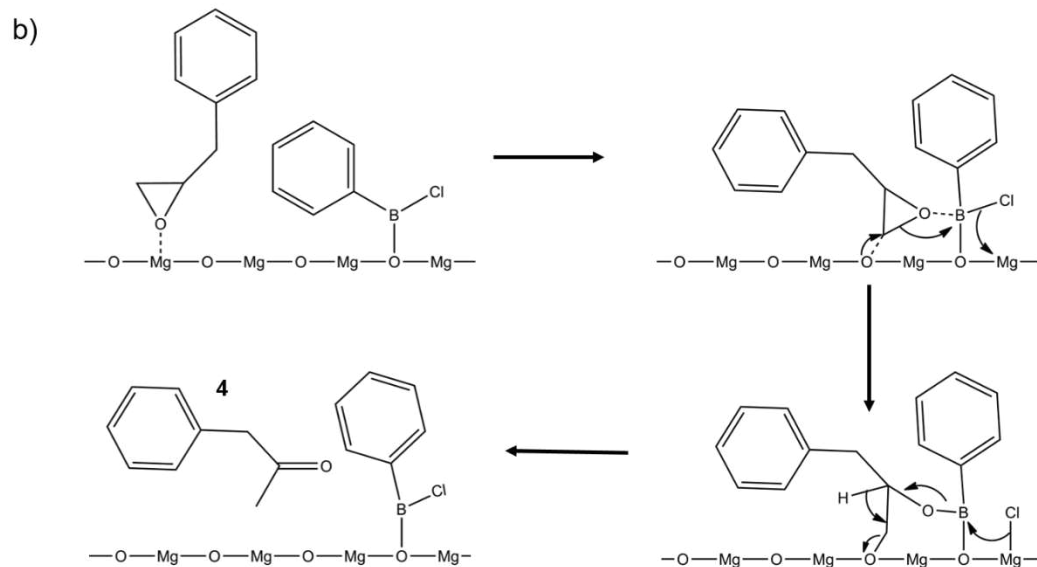
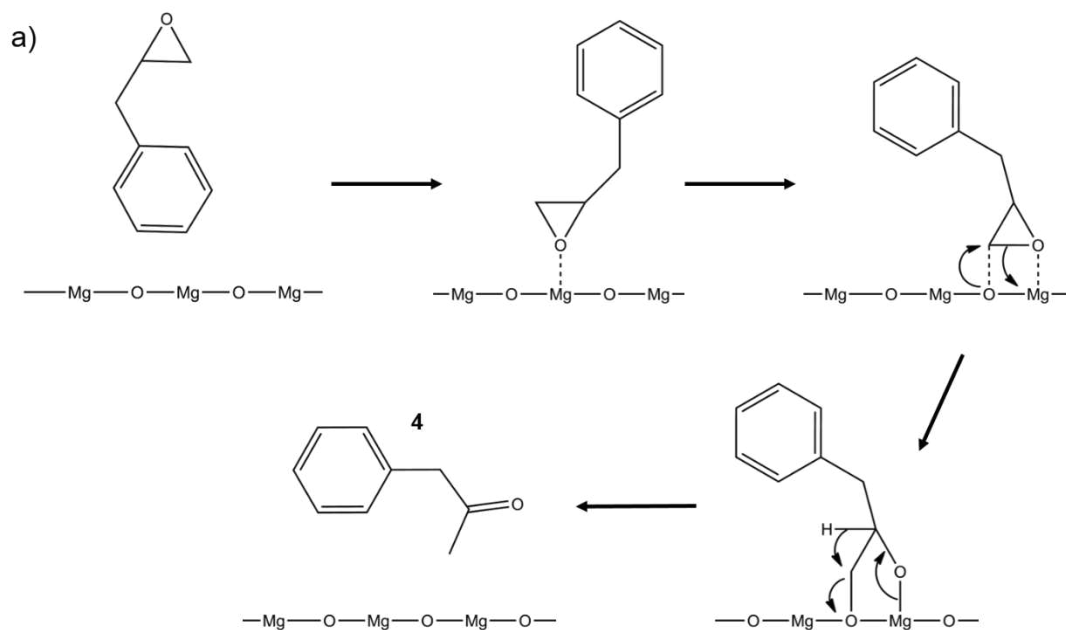


Figure 54: a) Proposition for the isomerisation of EpBz on MgO surface, b) Proposition for the isomerisation of EpBz on MgO surface in presence of BCl<sub>2</sub>Ph.

## Chapter V

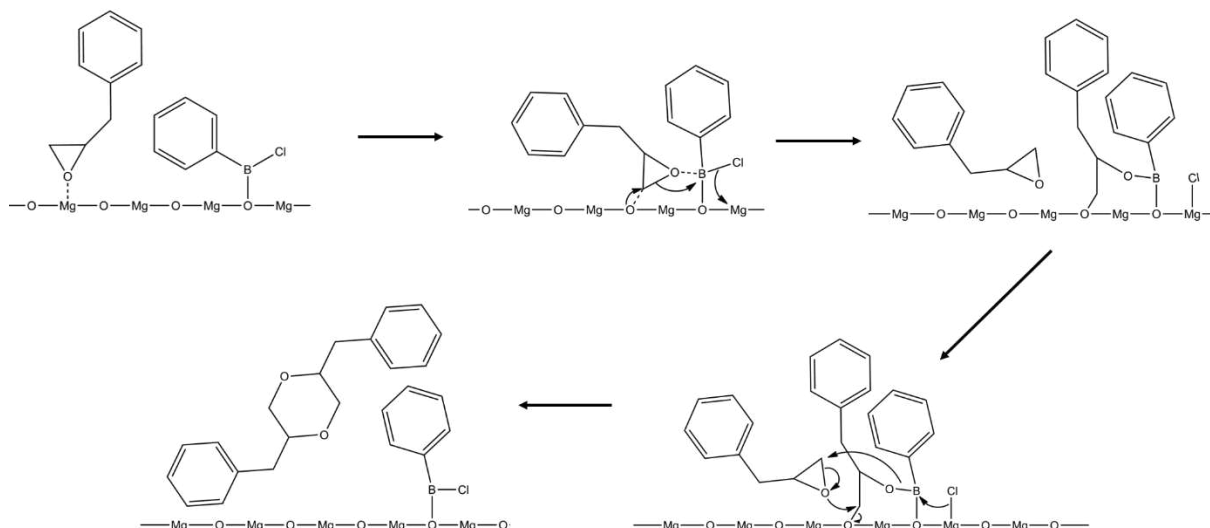


Figure 55: Proposition for the dimerisation of EpBz on MgO surface in presence of  $\text{BCl}_2\text{Ph}$ .

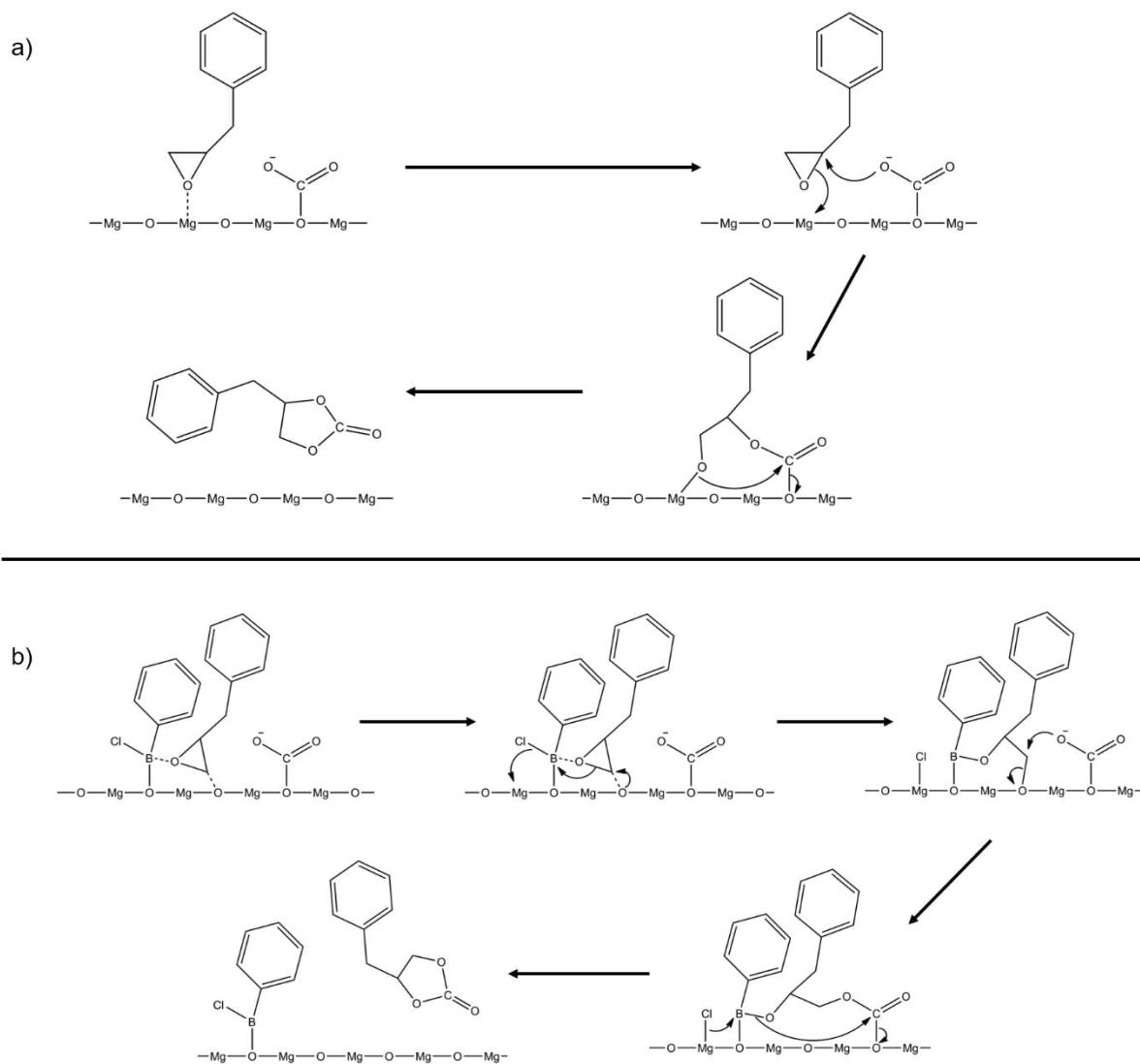


Figure 56: a) Proposition for the cycloaddition of  $\text{CO}_2$  to EpBz on MgO surface, b) Proposition for the cycloaddition of  $\text{CO}_2$  to EpBz on MgO surface in presence of  $\text{BCl}_2\text{Ph}$ .

### Interrogations:

- It was not clear what were the boron species signing at 32 and 29 ppm at the end of the cycloaddition reaction in presence of BCl<sub>2</sub>Ph. These species were not active in catalysis but seemed linked to the selectivity of the reaction toward cyclic carbonate (the higher the selectivity, the higher the 32/29 peak ratio).
- We did not detect the 18 ppm peak in <sup>11</sup>B NMR in all these experiments, whereas we detected it in previous reactions when mixing EpBz and BCl<sub>2</sub>Ph (Figure 36:). This might be due to the experiment duration that was not the same.
- We did not know what was the nature of the interaction between boranes adsorbed on the MgO nanoparticles and boranes dissolved in the solution. The supernatant experiment indicated that neither MgO with adsorbed BCl<sub>2</sub>Ph alone nor dissolved boranes without MgO nanoparticles were active. Dynamic exchanges between adsorbed and dissolved borane species might exist.
- The impact of the solvent was not studied here, but it would give interesting information. For example, the mechanism we proposed involved the adsorption of Cl<sup>-</sup> ions at the surface of the MgO nanoparticles; a more polar solvent would allow the solvation of the ions, thus modifying the catalytic activity.
- We saw in the borane screening (Figure 33:) that MgO+BCl<sub>3</sub> was not active at all in catalysis, but we had no idea why. Maybe the borane was too strongly adsorbed on the MgO surface and maybe the presence of the phenyl group in BCl<sub>2</sub>Ph brought some steric hindrance. It would be hard to tell without making a comparative study of the reactivity of BCl<sub>3</sub>, BCl<sub>2</sub>Ph, BClPh<sub>2</sub> and BPh<sub>3</sub> used with MgO nanoparticles.

## VII. Conclusion

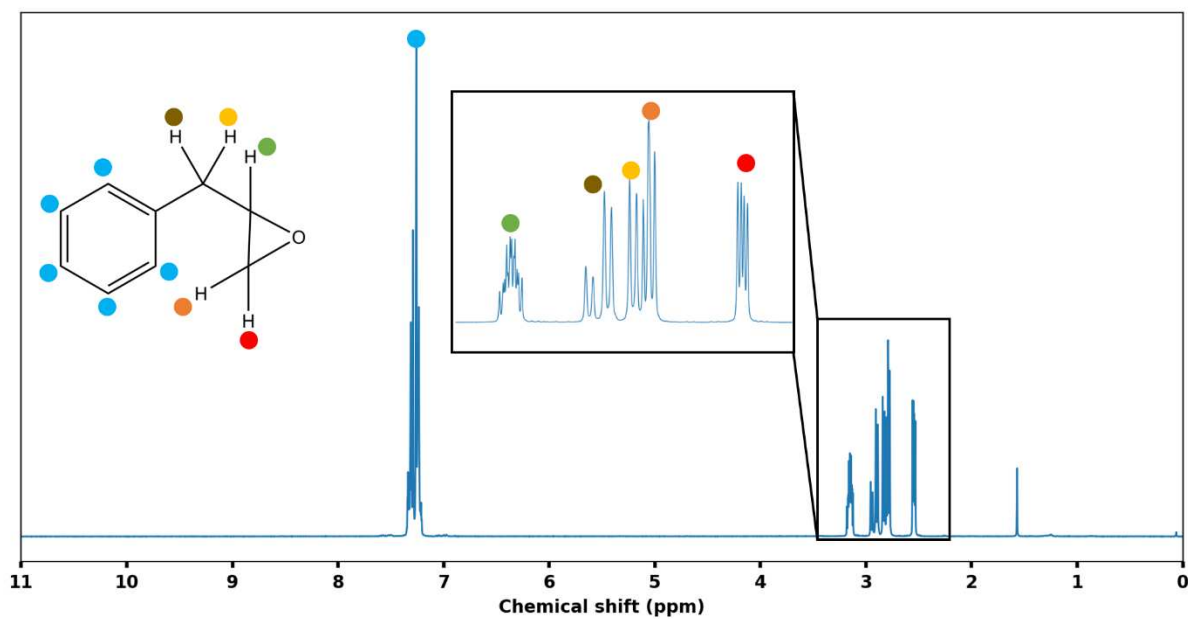
In this chapter, we studied extensively the cycloaddition of CO<sub>2</sub> on (2,3-epoxypropyl)benzene catalysed by MgO nanoparticles. A first short bibliographic review presented the reaction, its mechanism and the main reported homogeneous and heterogeneous catalysts. Using the study of Tu et al.<sup>21</sup> as a starting point, we studied the activity of the MgO nanoparticles synthesized by precipitation-calcination in Chapter III in the catalytic reaction. We evidenced the formation of secondary products not mentioned in the reference paper and proposed an identification. Influence of several parameters such as temperature and reaction duration on the selectivity of the catalyst were studied. We observed the unreported catalytic activity of Mg(OH)<sub>2</sub> nanoparticles and PCy<sub>3</sub> in the cycloaddition reaction.

Addition of triphenylborane in the reaction was performed. We observed a diminution of the catalytic activity of MgO nanoparticles when working in neat conditions. In toluene however, we observed the unreported formation of cyclic carbonate dimer. Impact of temperature, reaction duration and borane concentration on the formation of this new product was studied.

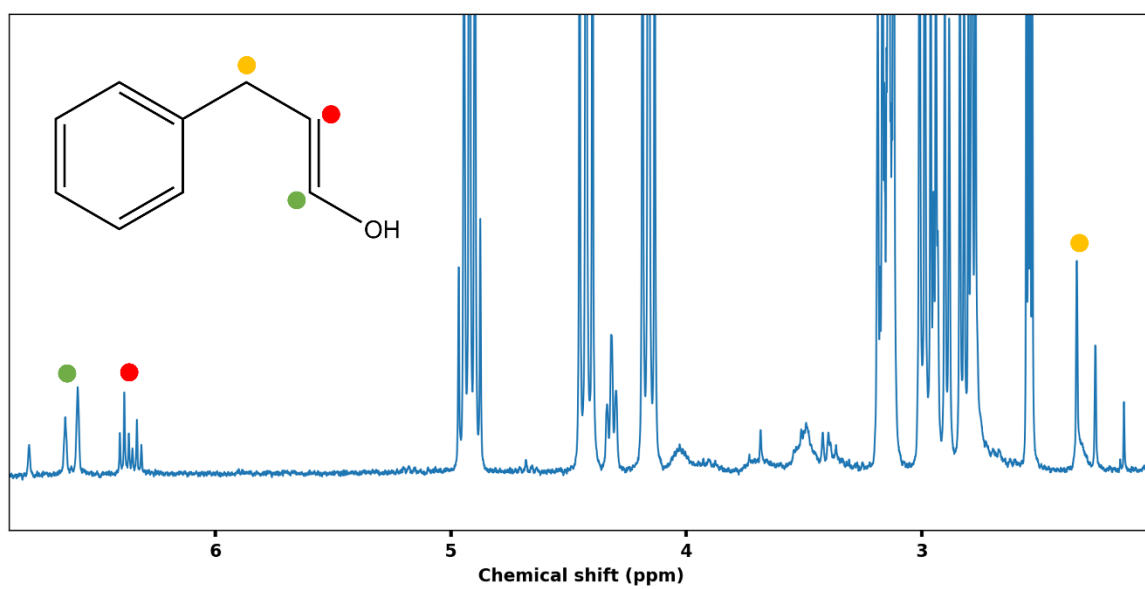
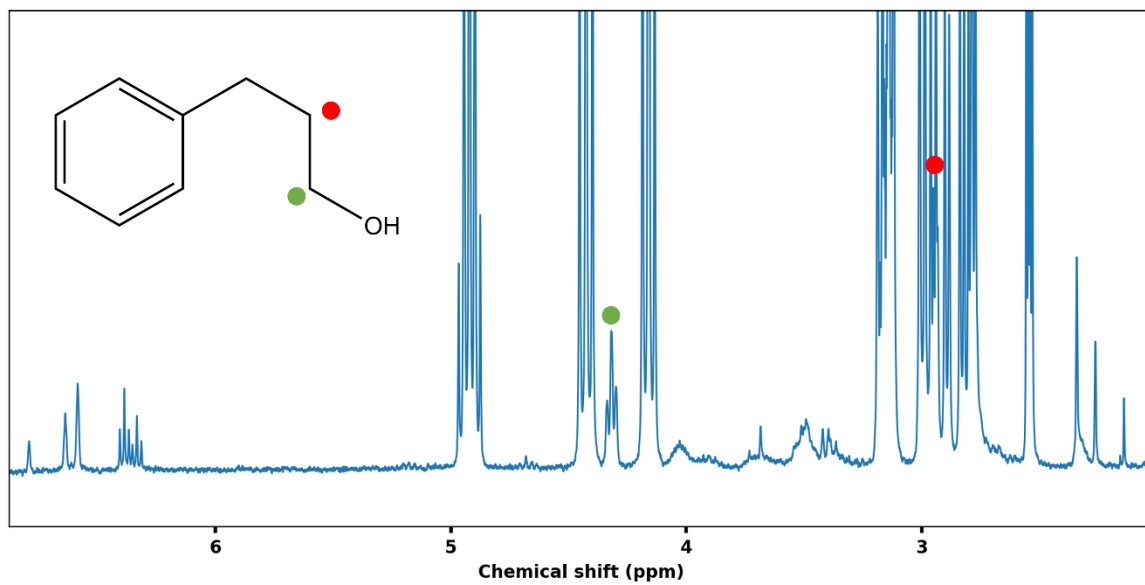
Finally, we reported an unprecedented synergetic effect of MgO nanoparticles and the chloroborane BCl<sub>2</sub>Ph. The epoxide consumption increased drastically but the selectivity decreased. Optimisation of reaction parameters allowed to improve the cyclic carbonate selectivity. A detailed study of the catalytic reaction with MgO+BCl<sub>2</sub>Ph was performed to unveil the origin of this synergy and reaction mechanisms were proposed for the formation of the different products.



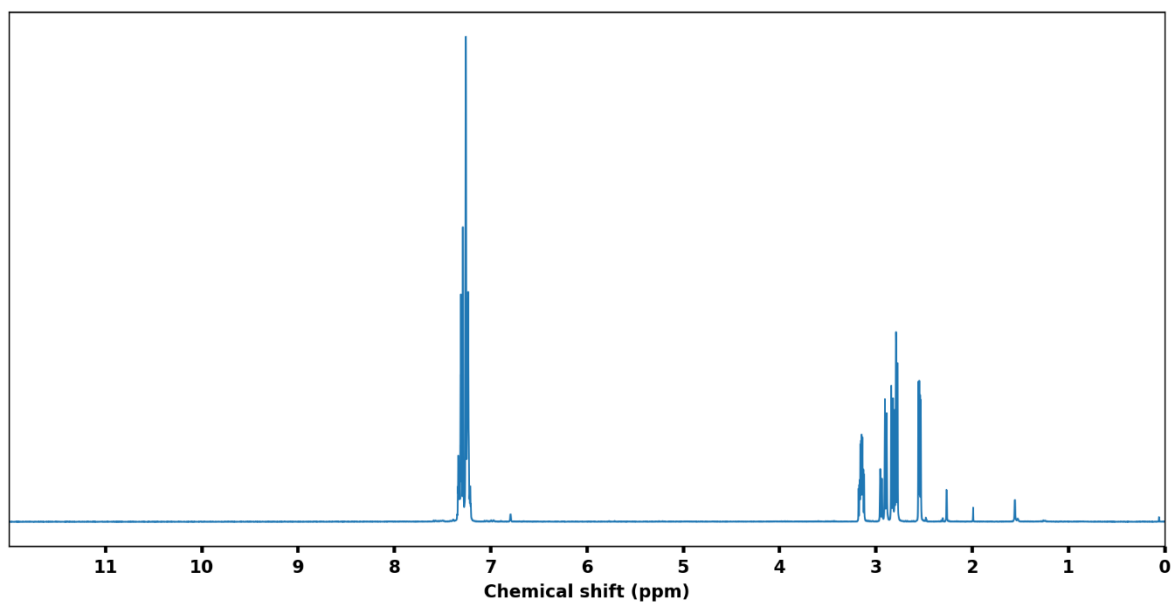
## VIII. Annexes



Annexe 1. <sup>1</sup>H NMR reference of (2,3-epoxypropyl)benzene in CDCl<sub>3</sub>.



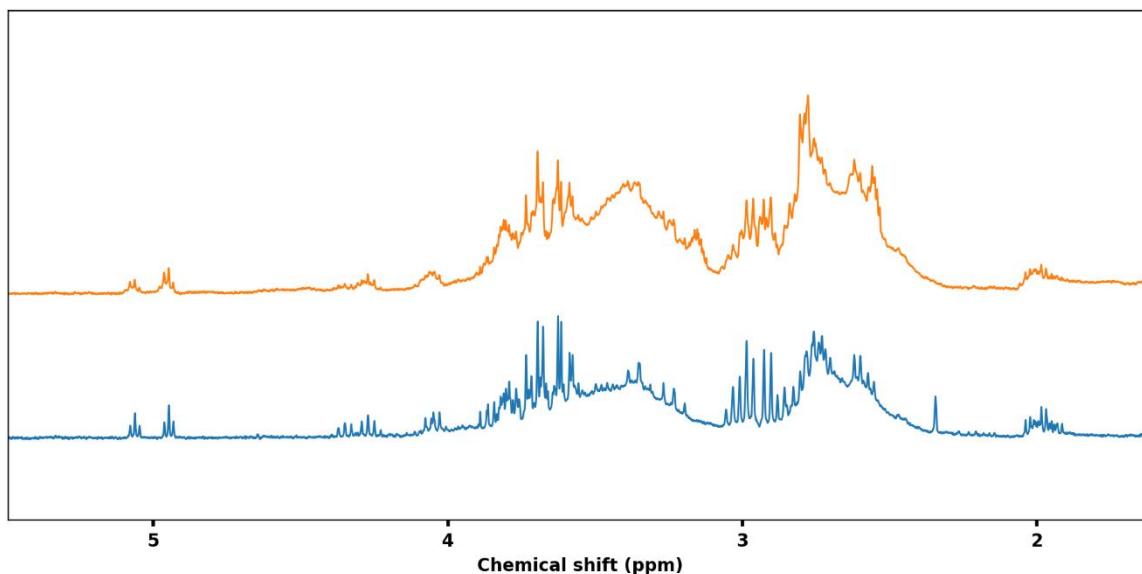
*Annexe 2. Proposition of the attribution of the unidentified  $^1\text{H}$  NMR peaks to the secondary products **1** (top spectrum) and **5** (bottom spectrum).*



Annexe 3. <sup>1</sup>H NMR spectrum of the blanc of reaction in neat conditions.

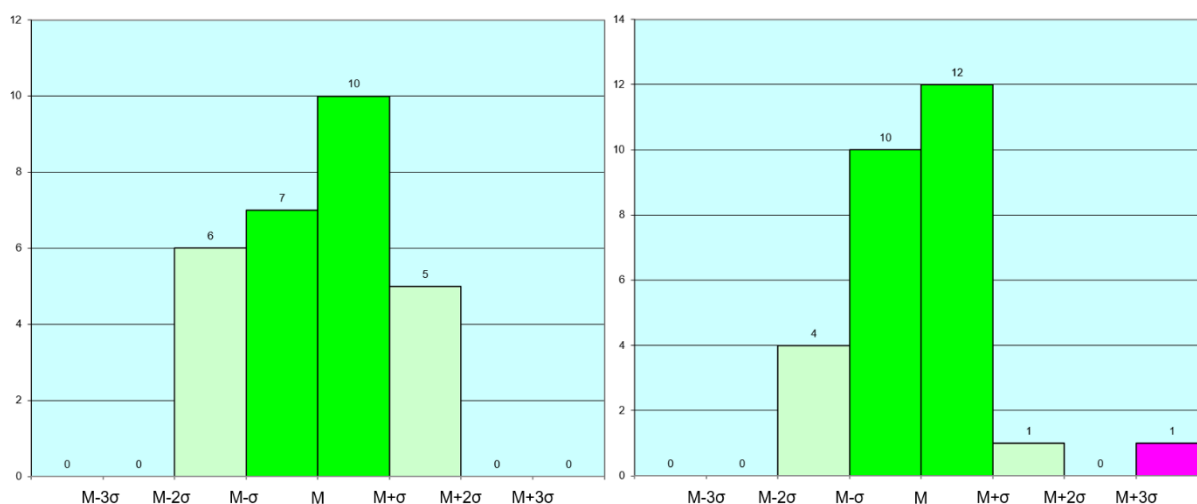
Species	3 h	12 h	48 h	72 h	120 h
Epoxide	0.95	0.92	0.85	0.67	0.25
Cyclic carbonate	0.02	0.06	0.09	0.21	0.56
Sec. Product 3.5ppm	0.02	0.02	0.05	0.12	0.09
Sec. Product 4.2 ppm	0	0	0	0.01	0.07
Sec. Product 6.5 ppm	0	0	0	0	0.03

Annexe 4. Evolution of the quantities (in equivalent) of the different species in the cycloaddition of CO<sub>2</sub> on epoxides in neat conditions depending of the duration of reaction.

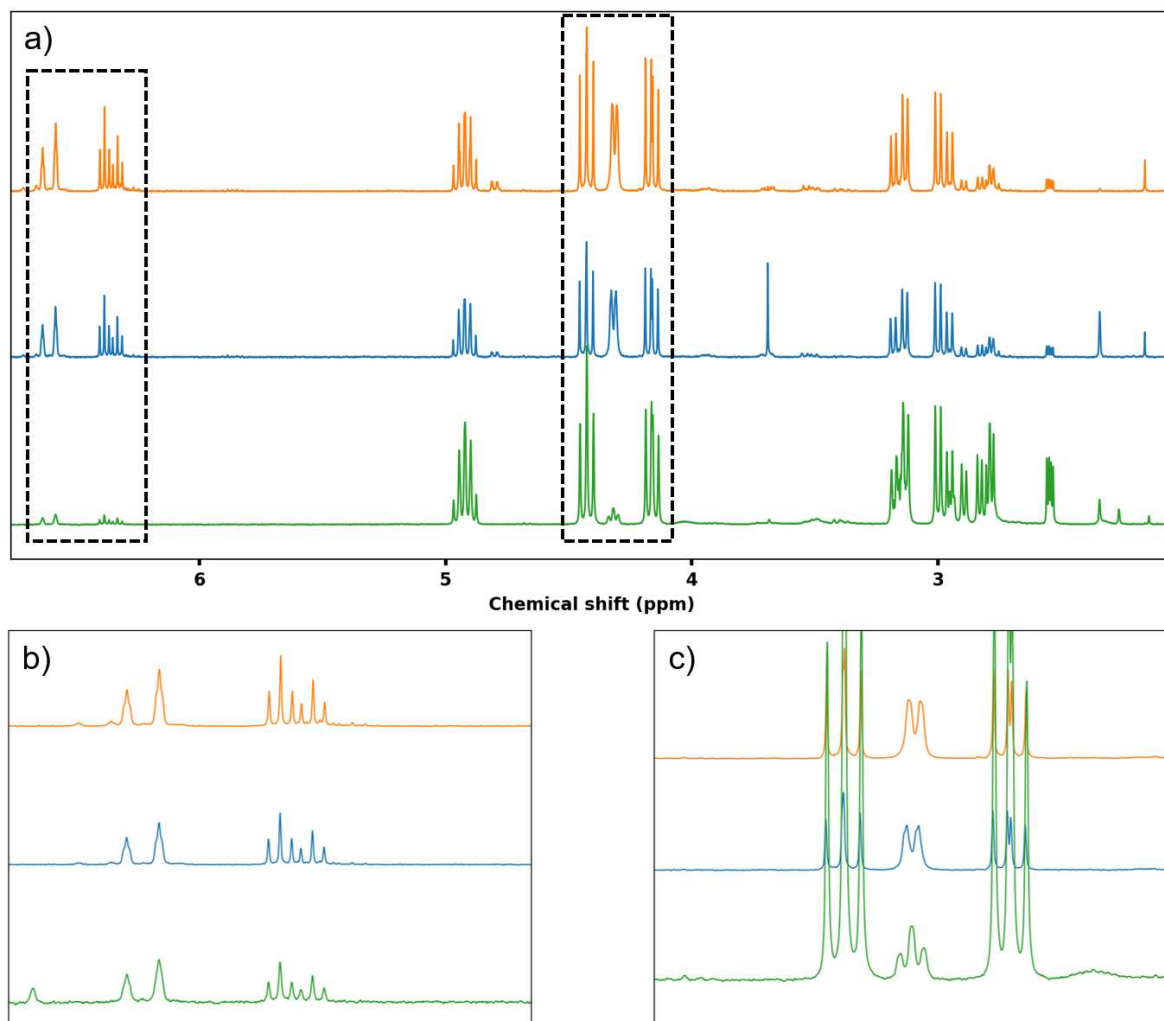


Annexe 5.  $^1\text{H}$  NMR spectrum of two repetitions of the same polymreisation reaction between EpBz and BCF.

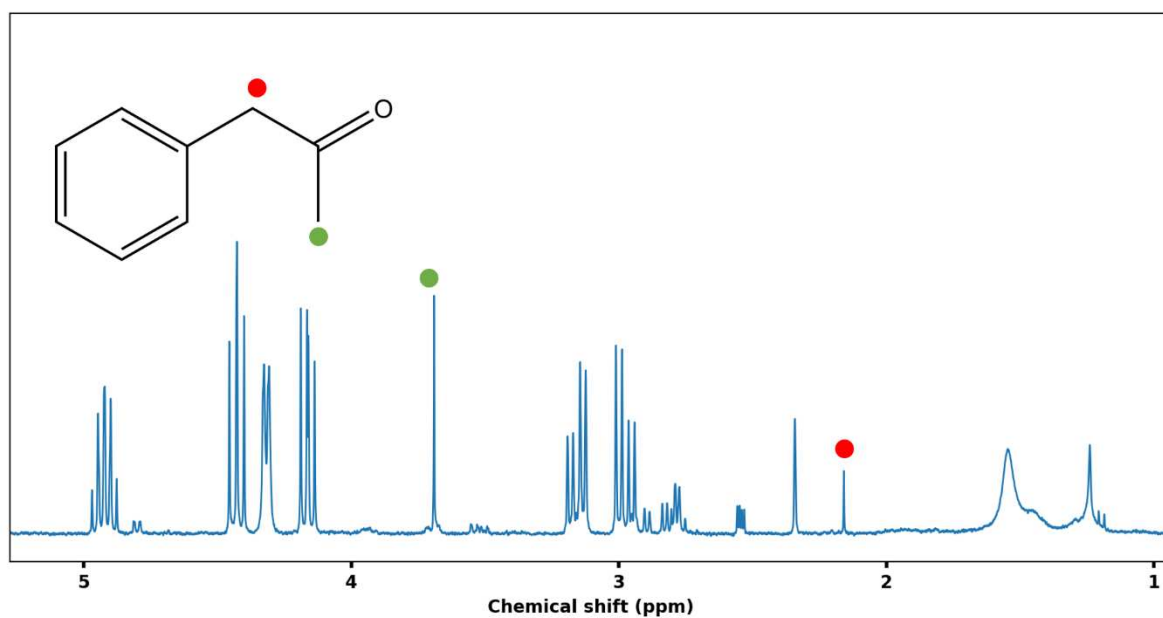
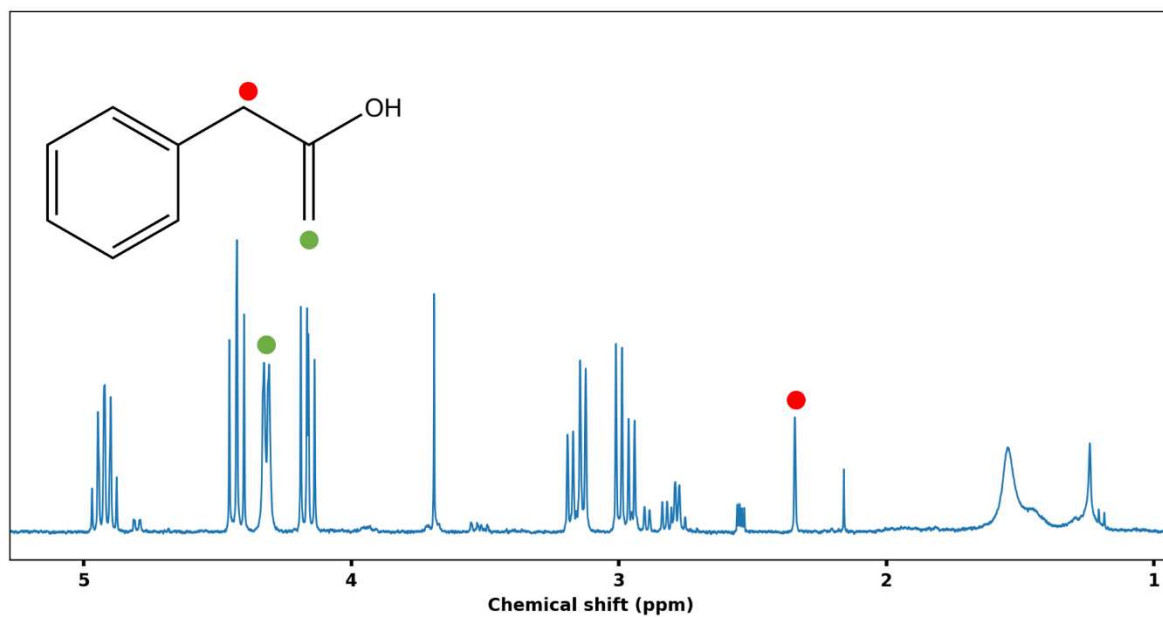
The Grubb's test is a statistical tool used to detect outlier point in a dataset supposed to follow a normal distribution. The idea is to consider the data as random points extracted from a Gaussian distribution with the mean ( $M$ ) and the standard deviation ( $\sigma$ ) of the dataset. We evaluate the likeliness of the lower and higher value points in terms of probability (the size of the dataset is taken into account). A point is considered suspicious if the probability of obtaining this value is lower than 5 %. A point is considered if the probability of obtaining this value is lower than 1 %.



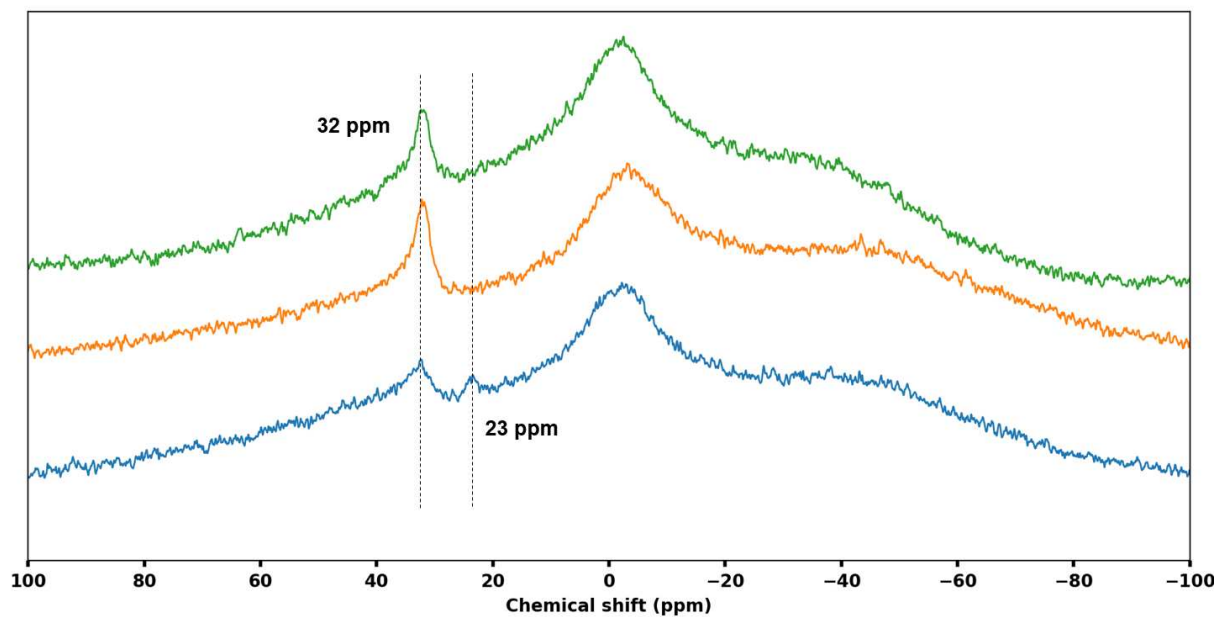
Annexe 6. Grubb's test for a dataset following a normal distribution (left) and for the same data set where an aberant point was added (right).



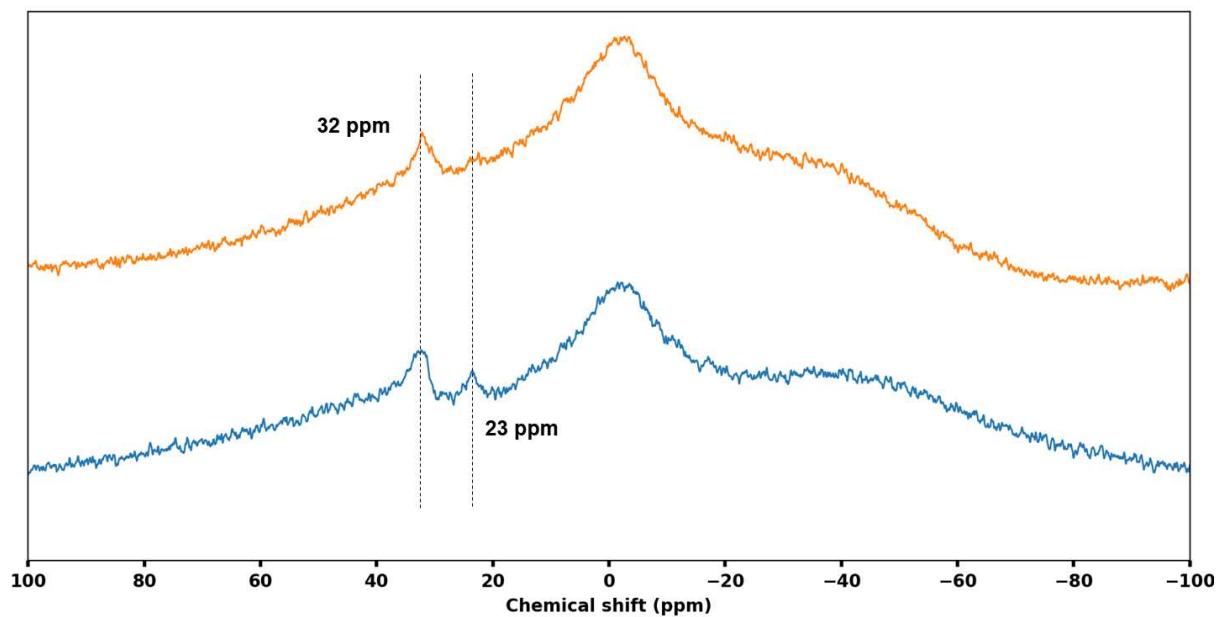
Annexe 7. Close look comparison of the <sup>1</sup>H NMR spectra of MgO (green, 5 days reaction), PCy<sub>3</sub> (blue, 2 days reaction) and MgO+PCy<sub>3</sub> (orange, 2 days reaction). a) full spectrum, b) zoom on the 6.5 ppm signal (green spectrum was amplified for better comparison), c) zoom on the 4.3 ppm signal (green spectrum was amplified for better comparison).



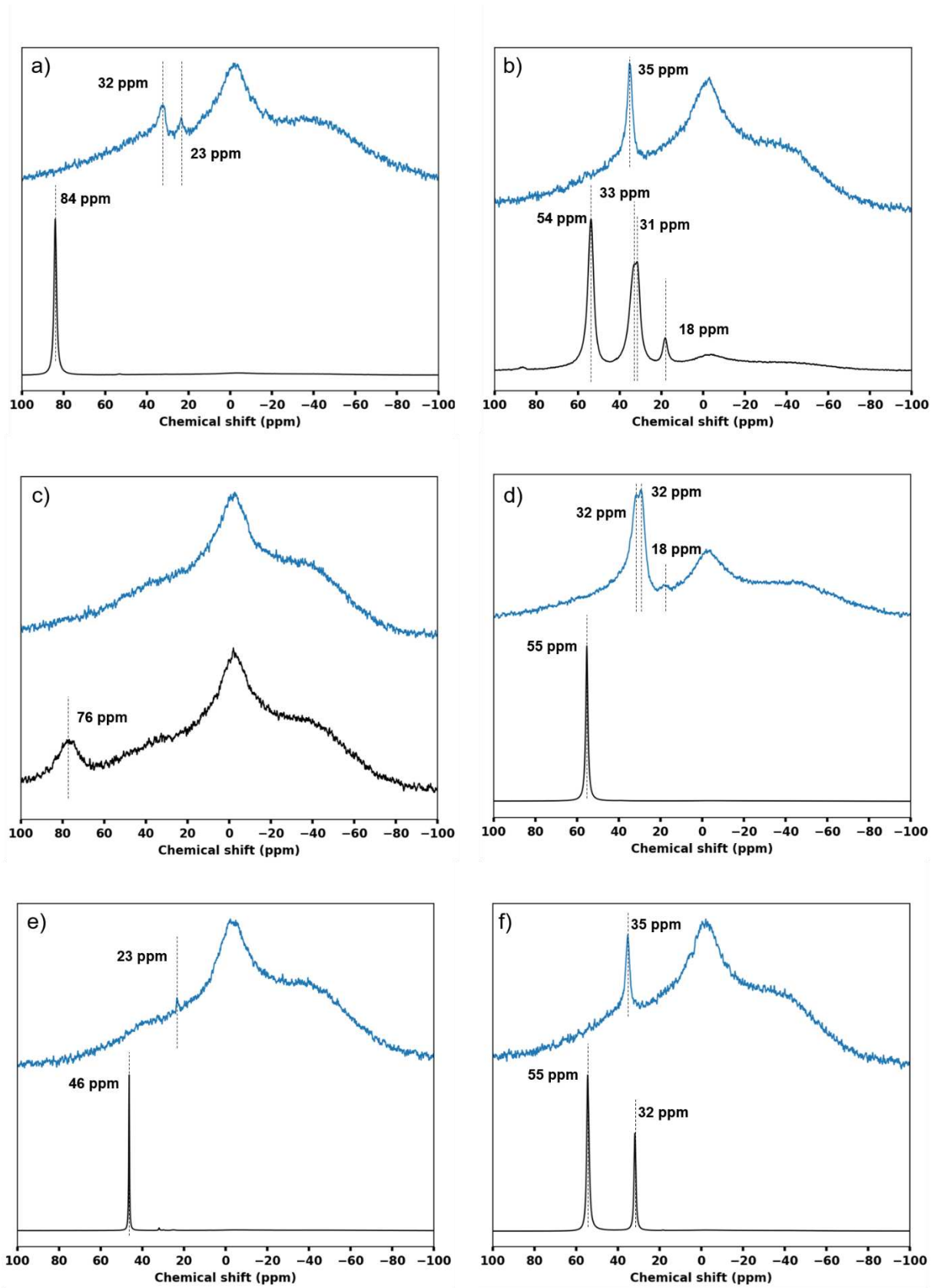
Annexe 8. Proposition of the attribution of the unidentified  $^1\text{H}$  NMR peaks to the secondary products **6** (top spectrum) and **4** (bottom spectrum).



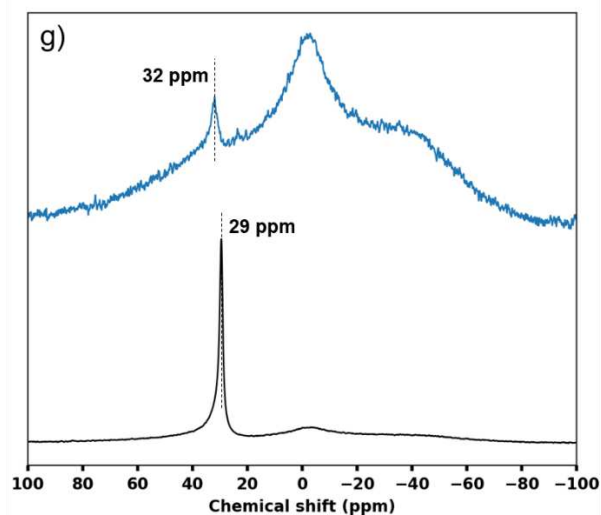
Annexe 9. <sup>11</sup>B NMR spectra of the cycloaddition reaction in toluene. Blue: 0.5 mL EpBz, 0.5 mL toluene, 150 °C, 1 day. Orange: 0.1 mL EpBz, 1 mL toluene, 150 °C, 1 day. Green: 0.1 mL EpBz, 1 mL toluene, 110 °C, 3 days.



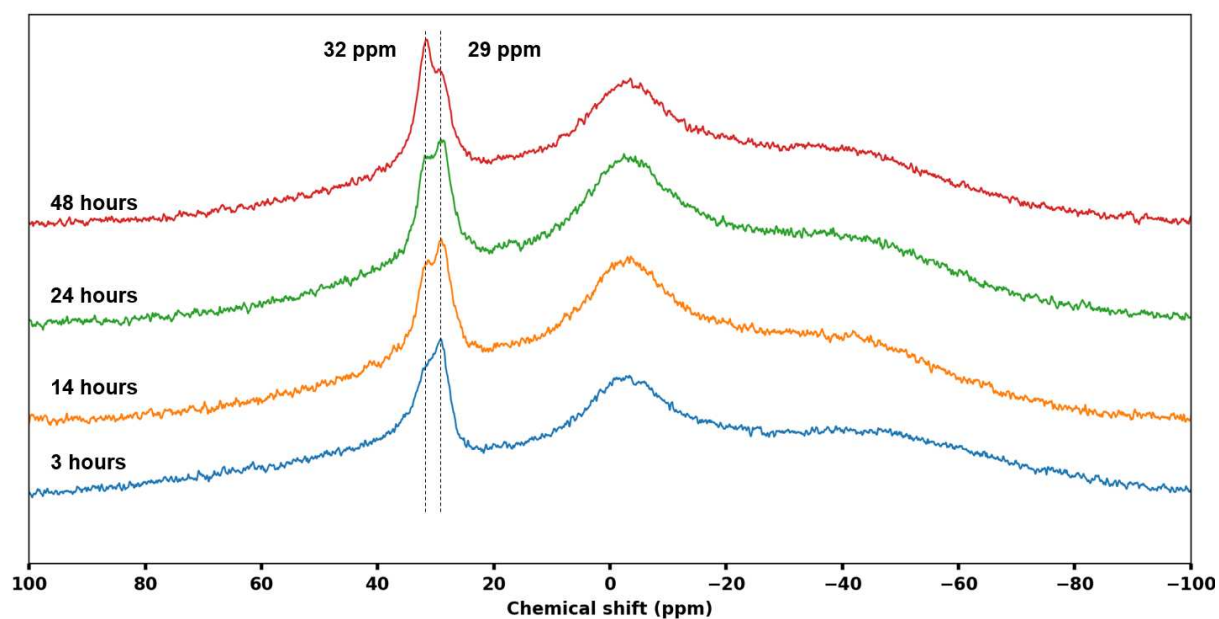
Annexe 10. <sup>11</sup>B NMR spectra of the cycloaddition reaction in toluene. Blue: Mg<sub>0.95</sub>-Ni<sub>0.05</sub>O+BPh<sub>3</sub>, Orange: Mg<sub>0.95</sub>-Co<sub>0.05</sub>O+BPh<sub>3</sub>.



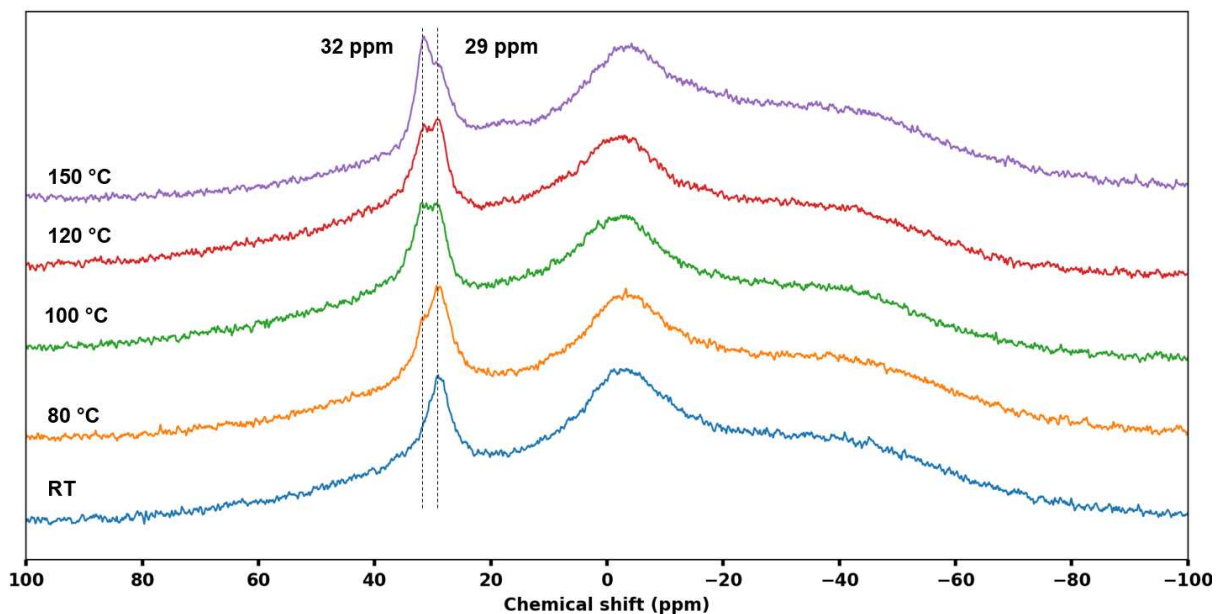




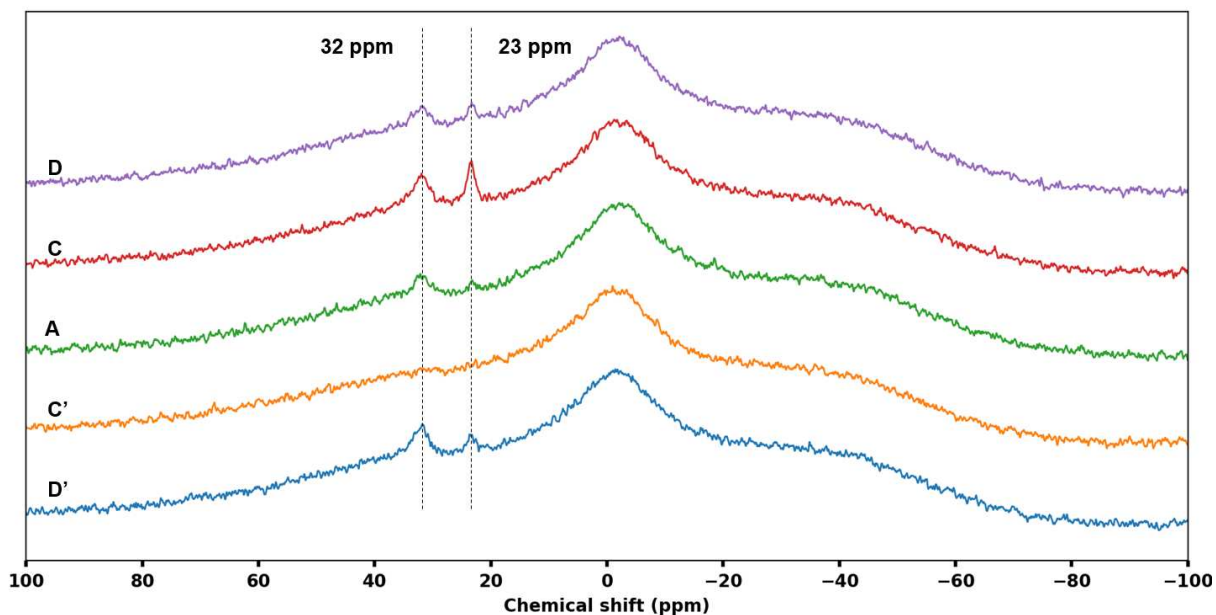
Annexe 11. <sup>11</sup>B NMR spectra of the reaction crudes of the borane screening (blue: reaction crude, black: reference). a) BEt<sub>3</sub>, b) BBu<sub>3</sub>, c) BMes<sub>3</sub>, d) BCl<sub>2</sub>Ph, e) BCl<sub>3</sub>, f) B(CH<sub>3</sub>)<sub>2</sub>OCH<sub>3</sub>, g) B(OH)<sub>2</sub>Ph.



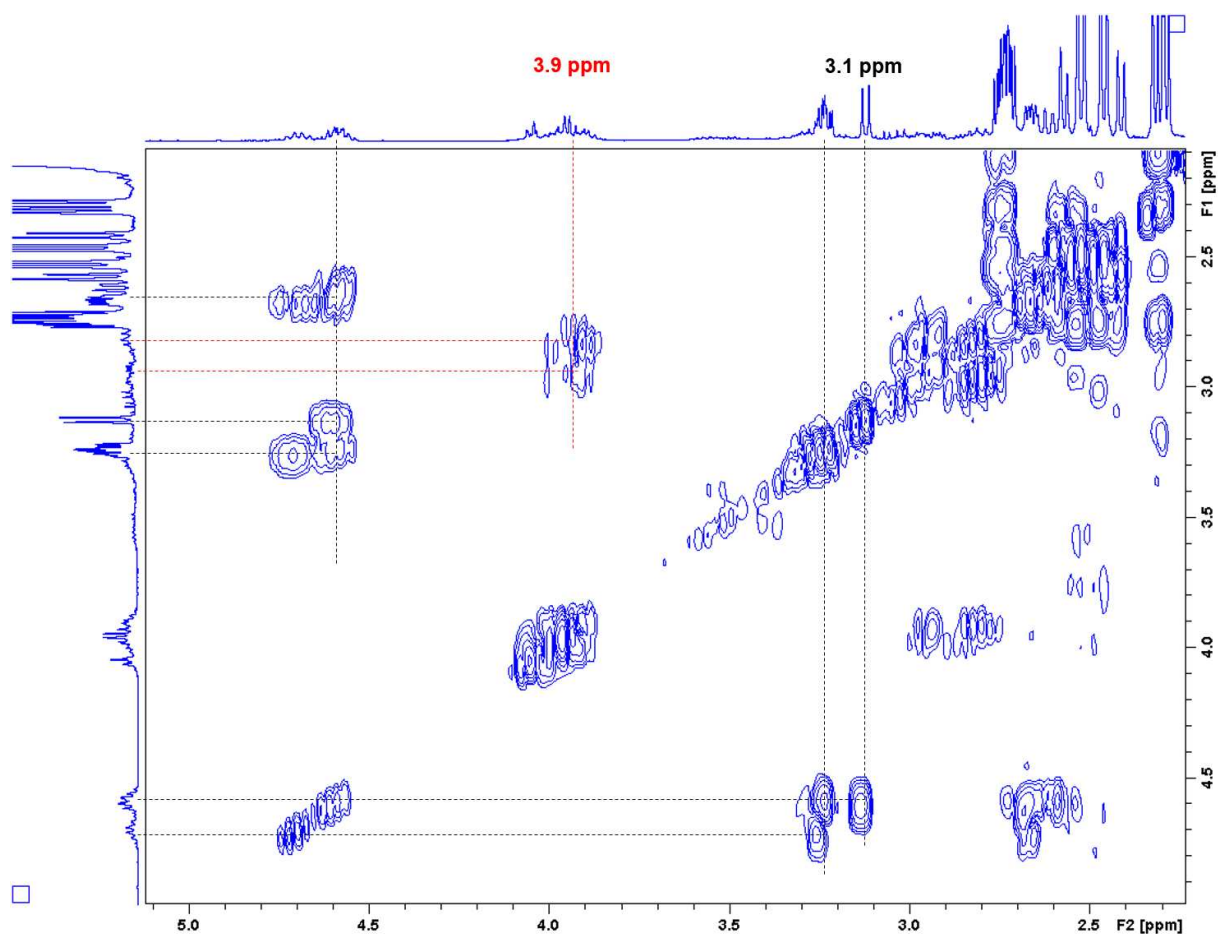
Annexe 12. <sup>11</sup>B NMR spectra of the reaction crudes of the kinetic study of the cycloaddition reaction catalysed by CO<sub>2</sub>+BCl<sub>2</sub>Ph (blue: 3 hours, orange: 14 hours, green: 24 hours, red: 48 hours).



Annexe 13.  $^{11}\text{B}$  NMR spectra of the reaction crudes of the temperature study of the cycloaddition reaction catalysed by  $\text{CO}_2 + \text{BCl}_2\text{Ph}$  (blue: room temperature, orange: 80 °C, green: 100 °C, red: 120 °C, purple: 150 °C).



Annexe 14.  $^{11}\text{B}$  NMR spectra of the reaction crudes of the supernatant test of the cycloaddition reaction catalysed by  $\text{CO}_2 + \text{BCl}_2\text{Ph}$  (blue: solution D', orange: solution C', green: solution A, red: solution C, purple: solution D).



Annexe 15. 2D COSY analysis for the identification of the secondary products in the EB\_RT experiment.

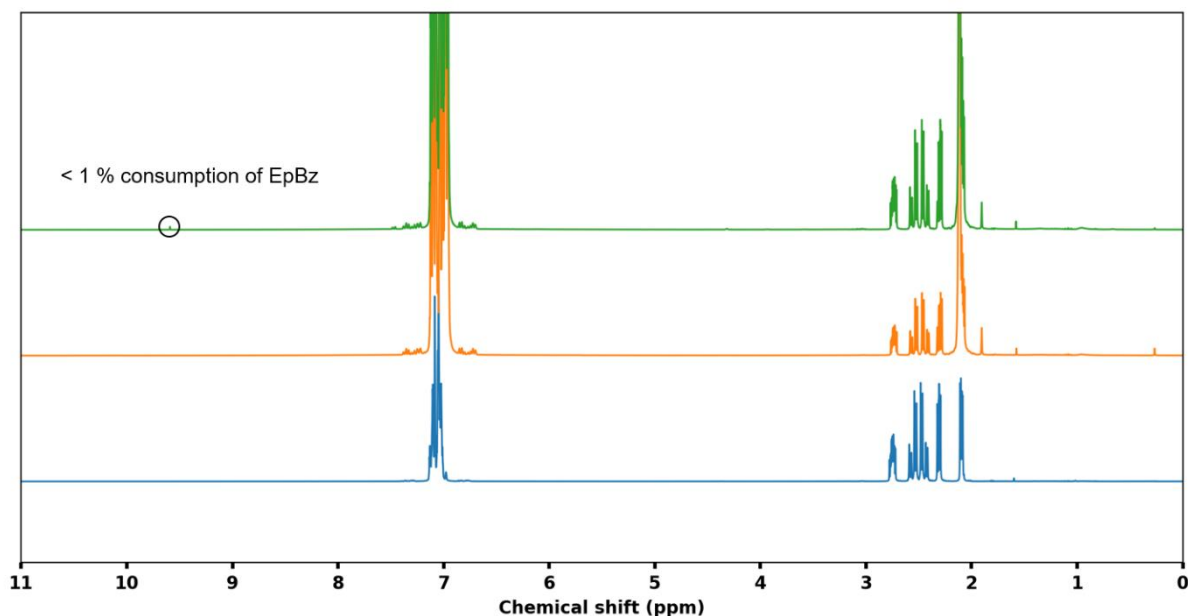
## Annexe 16. Mechanism proposition for the activity of $\text{MgO}+\text{BCl}_2\text{Ph}$ in the cycloaddition of $\text{CO}_2$ on EpBz: minor results

### E\_RT

As expected, nothing happened when diluting the epoxide EpBz in toluene for one day at room temperature (Annexe 17).

### E\_150

After one day at 150 °C, we detected a small peak at 9.6 ppm (Annexe 17). It could correspond to an aldehyde signal. However, the integration was really small (less than 1 % of the epoxide) so it was possibly an impurity.



Annexe 17.  $^1\text{H}$  NMR spectra of EpBz reference (blue), E\_RT (orange) and E\_150 (green) in toluene- $d_8$ .

### C\_RT

Nothing was detected in the experiment, even in  $^{13}\text{C}$  NMR spectroscopy. We saw a bubbling when releasing the pressure of the autoclave; dissolved  $\text{CO}_2$  probably left the solution when preparing the NMR tube.

### C\_150

Results at 150 °C were the same as at room temperature.

**M\_RT**

Nothing was detected in the experiment.

**M\_150**

Nothing was detected in the experiment.

**EC\_RT**

Nothing happened when exposing the epoxide to CO<sub>2</sub> at room temperature for 1 day.

**EC\_150**

Nothing happened when exposing the epoxide to CO<sub>2</sub> at 150 °C for 1 day.

**CB\_RT**

Nothing happened when we exposed BCl<sub>2</sub>Ph to CO<sub>2</sub> at room temperature for 1 day.

**CB\_150**

Nothing happened when we exposed BCl<sub>2</sub>Ph to CO<sub>2</sub> at 150 °C for 1 day.

**ECB\_RT**

The results of the interaction between EpBz, CO<sub>2</sub> and BCl<sub>2</sub>Ph at room temperature for 1 day was identical to EB\_RT. The CO<sub>2</sub> was spectator.

**ECB\_150**

The results of the interaction between EpBz, CO<sub>2</sub> and BCl<sub>2</sub>Ph at 150 °C for 1 day was identical to EB\_150. The CO<sub>2</sub> was spectator.

## Bibliography

- (1) Dai, W.-L.; Luo, S.-L.; Yin, S.-F.; Au, C.-T. The Direct Transformation of Carbon Dioxide to Organic Carbonates over Heterogeneous Catalysts. *Appl. Catal. A Gen.* **2009**, *366* (1), 2–12. <https://doi.org/10.1016/j.apcata.2009.06.045>.
- (2) Dai, W.-L.; Yin, S.-F.; Guo, R.; Luo, S.-L.; Du, X.; Au, C.-T. Synthesis of Propylene Carbonate from Carbon Dioxide and Propylene Oxide Using Zn-Mg-Al Composite Oxide as High-Efficiency Catalyst. *Catal. Letters* **2010**, *136* (1–2), 35–44. <https://doi.org/10.1007/s10562-009-0198-2>.
- (3) Kiatkittipong, K.; Mohamad Shukri, M. A. A.; Kiatkittipong, W.; Lim, J. W.; Show, P. L.; Lam, M. K.; Assabumrungrat, S. Green Pathway in Utilizing CO<sub>2</sub> via Cycloaddition Reaction with Epoxide—A Mini Review. *Processes* **2020**, *8* (5), 548. <https://doi.org/10.3390/pr8050548>.
- (4) North, M.; Pasquale, R.; Young, C. Synthesis of Cyclic Carbonates from Epoxides and CO<sub>2</sub>. *Green Chem.* **2010**, *12* (9), 1514. <https://doi.org/10.1039/c0gc00065e>.
- (5) Bobadilla, L. F.; Lima, S.; Urakawa, A. Cycloaddition of CO<sub>2</sub> and Epoxides over Reusable Solid Catalysts. In *Advanced Catalytic Materials*; John Wiley & Sons, Inc.: Hoboken, NJ, USA, 2015; pp 271–312. <https://doi.org/10.1002/9781118998939.ch8>.
- (6) Nikhil, M.; Eswara, P. Carbonate Market Statistics, Trends | Industry Analysis 2030 <https://www.alliedmarketresearch.com/carbonates-market> (accessed Aug 19, 2022).
- (7) AHER, R. D. Patent-One Step Preparation of Cyclic Carbonates, 2013.
- (8) Schubert. Production of Cyclic Carbonate. 5,153,333, 1992.
- (9) Wang, L.; Zhang, G.; Kodama, K.; Hirose, T. An Efficient Metal- and Solvent-Free Organocatalytic System for Chemical Fixation of CO<sub>2</sub> into Cyclic Carbonates under Mild Conditions. *Green Chem.* **2016**, *18* (5), 1229–1233. <https://doi.org/10.1039/C5GC02697K>.
- (10) Castro-Osma, J. A.; Alonso-Moreno, C.; Lara-Sánchez, A.; Martínez, J.; North, M.; Otero, A. Synthesis of Cyclic Carbonates Catalysed by Aluminium Heteroscorpionate Complexes. *Catal. Sci. Technol.* **2014**, *4* (6), 1674–1684. <https://doi.org/10.1039/C3CY00810J>.
- (11) Aresta, M. Nb(V) Compounds as Epoxides Carboxylation Catalysts: The Role of the Solvent. *J. Mol. Catal. A Chem.* **2003**, *204–205*, 245–252. [https://doi.org/10.1016/S1381-1169\(03\)00305-4](https://doi.org/10.1016/S1381-1169(03)00305-4).
- (12) Yamaguchi, K.; Ebitani, K.; Yoshida, T.; Yoshida, H.; Kaneda, K. Mg–Al Mixed Oxides as Highly Active Acid–Base Catalysts for Cycloaddition of Carbon Dioxide to Epoxides. *J. Am. Chem. Soc.* **1999**, *121* (18), 4526–4527. <https://doi.org/10.1021/ja9902165>.
- (13) Dorskocil, E. J.; Bordawekar, S. V.; Kaye, B. G.; Davis, R. J. UV–Vis Spectroscopy of Iodine Adsorbed on Alkali-Metal-Modified Zeolite Catalysts for Addition of Carbon Dioxide to Ethylene Oxide. *J. Phys. Chem. B* **1999**, *103* (30), 6277–6282. <https://doi.org/10.1021/jp991091t>.
- (14) Chen, X.; Sun, J.; Wang, J.; Cheng, W. Polystyrene-Bound Diethanolamine Based Ionic Liquids for Chemical Fixation of CO<sub>2</sub>. *Tetrahedron Lett.* **2012**, *53* (22), 2684–2688.

<https://doi.org/10.1016/j.tetlet.2012.03.058>.

- (15) Zhao, Y.; Tian, J.-S.; Qi, X.-H.; Han, Z.-N.; Zhuang, Y.-Y.; He, L.-N. Quaternary Ammonium Salt-Functionalized Chitosan: An Easily Recyclable Catalyst for Efficient Synthesis of Cyclic Carbonates from Epoxides and Carbon Dioxide. *J. Mol. Catal. A Chem.* **2007**, *271* (1–2), 284–289. <https://doi.org/10.1016/j.molcata.2007.03.047>.
- (16) Xiao, L.-F.; Li, F.-W.; Xia, C.-G. An Easily Recoverable and Efficient Natural Biopolymer-Supported Zinc Chloride Catalyst System for the Chemical Fixation of Carbon Dioxide to Cyclic Carbonate. *Appl. Catal. A Gen.* **2005**, *279* (1–2), 125–129. <https://doi.org/10.1016/j.apcata.2004.10.022>.
- (17) Watile, R. A.; Deshmukh, K. M.; Dhake, K. P.; Bhanage, B. M. Efficient Synthesis of Cyclic Carbonate from Carbon Dioxide Using Polymer Anchored Diol Functionalized Ionic Liquids as a Highly Active Heterogeneous Catalyst. *Catal. Sci. Technol.* **2012**, *2* (5), 1051. <https://doi.org/10.1039/c2cy00458e>.
- (18) Mori, K.; Mitani, Y.; Hara, T.; Mizugaki, T.; Ebitani, K.; Kaneda, K. A Single-Site Hydroxyapatite-Bound Zinc Catalyst for Highly Efficient Chemical Fixation of Carbon Dioxide with Epoxides. *Chem. Commun.* **2005**, No. 26, 3331. <https://doi.org/10.1039/b502636a>.
- (19) Andrea, K. A.; Plommer, H.; Kerton, F. M. Ring-Opening Polymerizations and Copolymerizations of Epoxides Using Aluminum- and Boron-Centered Catalysts. *Eur. Polym. J.* **2019**, *120*, 109202. <https://doi.org/10.1016/j.eurpolymj.2019.08.029>.
- (20) Chakraborty, D.; Rodriguez, A.; Chen, E. Y. X. Catalytic Ring-Opening Polymerization of Propylene Oxide by Organoborane and Aluminum Lewis Acids. *Macromolecules* **2003**, *36* (15), 5470–5481. <https://doi.org/10.1021/ma034050a>.
- (21) Tu, M.; Davis, R. J. Cycloaddition of CO<sub>2</sub> to Epoxides over Solid Base Catalysts. *J. Catal.* **2001**, *199* (1), 85–91. <https://doi.org/10.1006/jcat.2000.3145>.
- (22) Gawande, M. B.; Bonifácio, V. D. B.; Luque, R.; Branco, P. S.; Varma, R. S. Solvent-Free and Catalysts-Free Chemistry: A Benign Pathway to Sustainability. *ChemSusChem* **2014**, *7* (1), 24–44. <https://doi.org/10.1002/cssc.201300485>.
- (23) Palazzolo, A.; Carenco, S. Phosphines Modulating the Catalytic Silane Activation on Nickel-Cobalt Nanoparticles, Tentatively Attributed to Frustrated Lewis Pairs in a Colloidal Solution. *Chem. Mater.* **2021**, *33* (19), 7914–7922. [https://doi.org/10.1021/ACS.CHEMMATER.1C03105/ASSET/IMAGES/LARGE/CM1C03105\\_0005.JPEG](https://doi.org/10.1021/ACS.CHEMMATER.1C03105/ASSET/IMAGES/LARGE/CM1C03105_0005.JPEG).
- (24) Henderson, W. A.; Streuli, C. A. The Basicity of Phosphines. *J. Am. Chem. Soc.* **1960**, *82* (22), 5791–5794. <https://doi.org/10.1021/ja01507a008>.
- (25) Huang, J.-W.; Shi, M. Chemical Fixation of Carbon Dioxide by NaI/PPh<sub>3</sub>/PhOH. *J. Org. Chem.* **2003**, *68* (17), 6705–6709. <https://doi.org/10.1021/jo0348221>.
- (26) Sun, J.; Wang, L.; Zhang, S.; Li, Z.; Zhang, X.; Dai, W.; Mori, R. ZnCl<sub>2</sub>/Phosphonium Halide: An Efficient Lewis Acid/Base Catalyst for the Synthesis of Cyclic Carbonate. *J. Mol. Catal. A Chem.* **2006**, *256* (1–2), 295–300. <https://doi.org/10.1016/j.molcata.2006.05.004>.
- (27) KIM, H.; BAE, J.; LEE, J.; KWON, O.; JELLIARKO, P.; LEE, S.; LEE, S. Phosphine-Bound Zinc Halide Complexes for the Coupling Reaction of Ethylene Oxide and Carbon Dioxide. *J.*

- Catal.* **2005**, 232 (1), 80–84. <https://doi.org/10.1016/j.jcat.2005.01.033>.
- (28) Nakajima, K.; Baba, Y.; Noma, R.; Kitano, M.; N. Kondo, J.; Hayashi, S.; Hara, M. Nb 2 O 5 ·nH 2 O as a Heterogeneous Catalyst with Water-Tolerant Lewis Acid Sites. *J. Am. Chem. Soc.* **2011**, 133 (12), 4224–4227. <https://doi.org/10.1021/ja110482r>.
- (29) Andrea, K. A.; Kerton, F. M. Triarylborane-Catalyzed Formation of Cyclic Organic Carbonates and Polycarbonates. *ACS Catal.* **2019**, 9 (3), 1799–1809. <https://doi.org/10.1021/acscatal.8b04282>.
- (30) Zhang, C.-J.; Wu, S.-Q.; Boopathi, S.; Zhang, X.-H.; Hong, X.; Gnanou, Y.; Feng, X.-S. Versatility of Boron-Mediated Coupling Reaction of Oxetanes and Epoxides with CO 2 : Selective Synthesis of Cyclic Carbonates or Linear Polycarbonates. *ACS Sustain. Chem. Eng.* **2020**, 8 (34), 13056–13063. <https://doi.org/10.1021/acssuschemeng.0c04768>.
- (31) Dunne, J. F.; Su, J.; Ellern, A.; Sadow, A. D. A New Scorpionate Ligand: Tris(4,4-Dimethyl-2-Oxazolinyl)Borate and Its Zirconium(IV) Complexes. *Organometallics* **2008**, 27 (11), 2399–2401. <https://doi.org/10.1021/om800252p>.
- (32) Niedenzu, K.; Beyer, H.; Dawson, J. W. Boron-Nitrogen Compounds. VI. Amino-Phenylboranes. *Inorg. Chem.* **1962**, 1 (4), 738–742. <https://doi.org/10.1021/ic50004a004>.
- (33) Kun Lau, C.; Mintz, M.; Bernstein, M. A.; Dufresne, C. Dichlorophenylborane a New Reagent for the Preparation of 2-Phenyl-4H-1,3,2-Benzodioxaborins. *Tetrahedron Lett.* **1993**, 34 (35), 5527–5530. [https://doi.org/10.1016/S0040-4039\(00\)73872-X](https://doi.org/10.1016/S0040-4039(00)73872-X).
- (34) Bonner, T. G.; Lewis, D.; Rutter, K. Opening of Cyclic Acetals by Trichloro-, Dichloro-, and Tribromo-Borane. *J. Chem. Soc. Perkin Trans. 1* **1981**, 0 (0), 1807. <https://doi.org/10.1039/p19810001807>.
- (35) Frederick, E.; Campbell, Q.; Benavidez, A.; Wheeler, D. R.; Misra, S. Reaction of Dichlorophenylborane with H-Si(100). *ACS Omega* **2021**, 6 (49), 33645–33651. <https://doi.org/10.1021/acsomega.1c04619>.
- (36) Sivaev, I. B.; Bregadze, V. I. Lewis Acidity of Boron Compounds. *Coord. Chem. Rev.* **2014**, 270–271 (1), 75–88. <https://doi.org/10.1016/j.ccr.2013.10.017>.





# **Chapter VI**

## **Conclusion and perspectives**



We now arrived at the end of this PhD project. In this last chapter, we wanted to sum up the main results of our work and give some perspectives on our contribution in the NanoFLP project.

### **Contextualisation**

The first chapter of our study was dedicated to a brief reminder of the physic principles behind greenhouse effect and global warming. These problematics have been strong drivers for scientific research. We believed that the scientific community should have a common basic knowledge of these problematic so that each discipline could contribute to the development of solutions. We showed that even if CO<sub>2</sub> capture and valorisation would not solve the climate issue on its own, it had a role to play in the future to quickly reduce emissions linked to fossil fuel consumption and compensating for unavoidable CO<sub>2</sub> emissions in other area.

### **Defining the philosophy of our work**

The second chapter of our study was dedicated to the CO<sub>2</sub> valorisation through catalysis. We explored the different direct application of CO<sub>2</sub> and the industrial processes valorising CO<sub>2</sub> such as urea production. We showed that these processes often required high temperature and pressure as well as expensive catalysts. We detailed emerging promising valorisation pathways such as electroreduction of CO<sub>2</sub> and Frustrated Lewis Pair catalysis.

Emerging from these fields of research, we presented the concept of NanoFLP, where frustrated Lewis pairs would form at the interface between the surface of a nanoparticle and adsorbed ligands. We investigated on the best candidates to form such NanoFLP and ended up with a proposition. Alkaline-earth oxides, known for their Lewis base surface properties, would be the nanoparticles. Boranes, often use in molecular FLP chemistry, would be the ligands.

We ended up with a plan of action for the future of the project:

- Study the synthesis of alkaline-earth oxides
- Study the adsorption of borane on alkaline-earth oxides
- Study the catalytic properties of the nanoparticle—ligand pair in catalysis of the cycloaddition of CO<sub>2</sub> on epoxides

### **Alkaline-earth oxide synthesis**

In the third chapter, we synthesized MgO nanoparticles using the precipitation-calcination pathway and showed the importance of calcination temperature on the nanoparticles morphology. We were surprised to observe a drastic impact of the washing steps of the Mg(OH)<sub>2</sub> intermediate on the final properties of the MgO nanoparticles both in terms of morphology and crystallite sizes. We also synthesized CaO nanoparticles using the same pathway.

We synthesized mixed oxide nanoparticles using the same precipitation-calcination pathway. We studied the influence of the initial Mg/Ca ratio in MgO-CaO mixed oxides and showed the existence of thresholds where certain phases appeared in XRD. We synthesized MgO-XO

nanoparticles with X = Co, Ni and Cu with a fixed ratio Mg/X = 95/5. We showed that transition metals were not homogeneously dispersed on MgO with our method using STEM-EDX. However, we did not detect phase segregation in XRD.

We did a first test of the MgO nanoparticles in the Claisen-Schmidt condensation of benzaldehyde on acetophenone to form chalcone. The catalyst we synthesized was active in the reaction with a similar result to what was obtained in the literature. We even tried a first attempt at NanoFLP catalysis by adding borane in the solution, but we obtained a decrease of the catalytic activity. We concluded that we needed a better understanding of the MgO-borane interaction before our catalytic studies.

## **Borane adsorption at the surface of MgO nanoparticles**

The fourth chapter focused on the adsorption of CO<sub>2</sub> and boranes at the surface of MgO nanoparticles. We first used deconvolution to have a better understanding on carbonate formation at the surface of MgO, showing preferential adsorption modes. We studied how these carbonates would evolve when the nanoparticles were exposed to pure CO<sub>2</sub> and showed that it modified the adsorption mode. We also looked at MgO synthesized in different conditions and showed that both the calcination temperature and the washing steps impacted the final surface carbonates.

We studied the adsorption of boranes on the surface of MgO and showed that in presence of CO<sub>2</sub>, MgO nanoparticles with triphenylborane ligands reacted. We observed the formation of new peaks in IR, potential B—O or B—C bonds, as well as the disappearance of the B—C band of molecular BPh<sub>3</sub>. We observed a similar phenomenon with B(OH)<sub>2</sub>Ph.

Finally, we observed an unprecedented reaction between MgO and the chloroborane BCl<sub>2</sub>Ph. We postulated an adsorption mechanism as well as the degradation of the MgO-BCl<sub>2</sub>Ph in presence of water allowing to explain the different observations.

## **Cycloaddition of CO<sub>2</sub> on epoxides catalysed by borane functionalised MgO**

The fifth chapter of our study was dedicated to the study of the cycloaddition reaction involving CO<sub>2</sub> and EpBz to form the corresponding cyclic carbonate. We studied the reaction extensively and several points stood out concerning the efficiency of MgO-borane catalysts:

- In neat conditions, BPh<sub>3</sub> adsorption reduced the activity of the MgO catalyst
- In toluene, BPh<sub>3</sub> modified the selectivity without modifying the activity of the MgO catalyst, allowing the formation of the dimer of the cyclic carbonate
- In toluene, BCl<sub>2</sub>Ph drastically increased the activity of the MgO catalyst but reduced its selectivity. We varied the parameters to find conditions limiting the selectivity loss and proposed a mechanism behind the reactivity enhancement.

Other minor results were found, such as the activity of phosphines or DMF as catalyst.

## Final thoughts and perspectives

In the end, we believe the major result of this PhD project is the discovering of the interaction between MgO and BCl<sub>2</sub>Ph. We did not find any reference of such a phenomenon in the literature. We made propositions to explain the adsorption of BCl<sub>2</sub>Ph at the surface of MgO nanoparticles and the catalytic activity of MgO+BCl<sub>2</sub>Ph in the cycloaddition of CO<sub>2</sub> on epoxide. However, lots of variables could still be explored:

- Interaction between MgO and other chloroboranes such as BCl<sub>3</sub> and BClPh<sub>2</sub>. We already showed that MgO+BCl<sub>3</sub> was not active in catalysis despite the observed colour modification of the nanoparticles. A detailed study would bring information on the role of phenyl versus chloride in BCl<sub>2</sub>Ph.
- Interaction between MgO and halogenoboranes in general such as BX<sub>3</sub>, BX<sub>2</sub>Ph, and BXPh<sub>2</sub> with X = F, Br and I. It would inform on the role of chloride in the interaction.
- Interaction between BCl<sub>2</sub>Ph and other types of MgO. It could inform if a specific crystallographic facet interacts with the chloroborane. Taking some time to synthesize MgO particles with a fine control of the exposed crystallographic facets could be valuable. High Resolution Transmission Electron microscopy (HRTEM) can allow the identification of the exposed crystallographic facets.
- Interaction between BCl<sub>2</sub>Ph and other oxides such as CaO, SrO, CeO<sub>2</sub>, Al<sub>2</sub>O<sub>3</sub>, etc. It would inform if the interaction is specific to MgO or if it is extendable to other basic and non-basic oxides.
- Cycloaddition with other epoxides. We only worked with (2,3epoxypropyl)benzene, it would be interesting to see if smaller epoxides would behave differently, or if the bulkiness of EpBz played a role in the interaction.
- Cycloaddition reactions with higher pressure of CO<sub>2</sub>. As mentioned in Chapter V, we believe that the CO<sub>2</sub> concentration in solution can influence the selectivity of the reaction toward the production cyclic carbonate. It would be interesting to confirm this hypothesis.

In regard to the NanoFLP project, we managed to find a system where nanoparticles with Lewis base surface properties and molecular Lewis acids had a synergetic impact on the catalytic activity in the cycloaddition of CO<sub>2</sub> on epoxides. In this regard, it was a success. Still, could this interaction be attributed to NanoFLP? We believe that our current comprehension of the system could not allow us to answer to the question. A detailed study of the impact of the bulkiness and the acidity of the chloroborane could unveil some trends allowing to confirm or infirm a NanoFP mechanism. DFT calculations could also provide interesting information on the nature of the MgO-BCl<sub>2</sub>Ph interaction like the geometrical configuration of the adsorbed borane and its interaction with CO<sub>2</sub> and with the epoxide.



# Appendix





## I. List of reactants

*Note: If not precised, the chemicals were used as received without purification.*

### Solvents

Toluene (99.8 %), DMF (99.8 %) were purchased from Sigma-Aldrich. Ethanol (96 %) was purchased from VWR.

### Nanoparticle synthesis

NaOH (98 %),  $\text{Mg}(\text{NO}_3)_2 \cdot \text{H}_2\text{O}$  (99.999 %),  $\text{Ca}(\text{NO}_3)_2 \cdot 4\text{H}_2\text{O}$  (99 %) and  $\text{Cu}(\text{NO}_3)_2 \cdot 3\text{H}_2\text{O}$  (99 %) were purchased from Sigma-Aldrich,  $\text{Ni}(\text{NO}_3)_2 \cdot 6\text{H}_2\text{O}$  (98 %) and  $\text{Co}(\text{NO}_3)_2 \cdot 6\text{H}_2\text{O}$  (98 %) were purchased from Alpha Aesar.

### Boranes

Tris(pentafluorophenyl)borane (97 %), triphenylborane (95 %) and phenylboronic acid (97 %) were purchased from STREM Chemicals. Dichlorophenylborane (97 %), triethylborane (solution 1M in THF), tributylborane (solution 1M in THF) and diethylmethoxyborane (solution 4M in THF) were purchased from Acros Organics, trimesitylborane (97 %) and boron trichloride (solution 1M in toluene) were purchased from Sigma-Aldrich.

### Catalysis

Benzaldehyde (99.5 %), acetophenone (99 %), chalcone (98 %), (2,3-Epoxypropyl)benzene (98 %) were purchased from Sigma-Aldrich.  $\text{CO}_2$  (99.9 %) was purchased from Air Liquide.

Air-sensitive chemicals were kept inside an argon glovebox from MBraun.



Figure 1: Glovebox under argon atmosphere.

## II. Experimental setups

### Nanoparticle synthesis

The syntheses presented in Chapter III were performed in borosilicate glassware purchased from VWR. Magnetic stirring was provided by an IKA RCT Basic heating plate. Drying and calcination were made in a Nabtherm LT1300 muffle furnace.

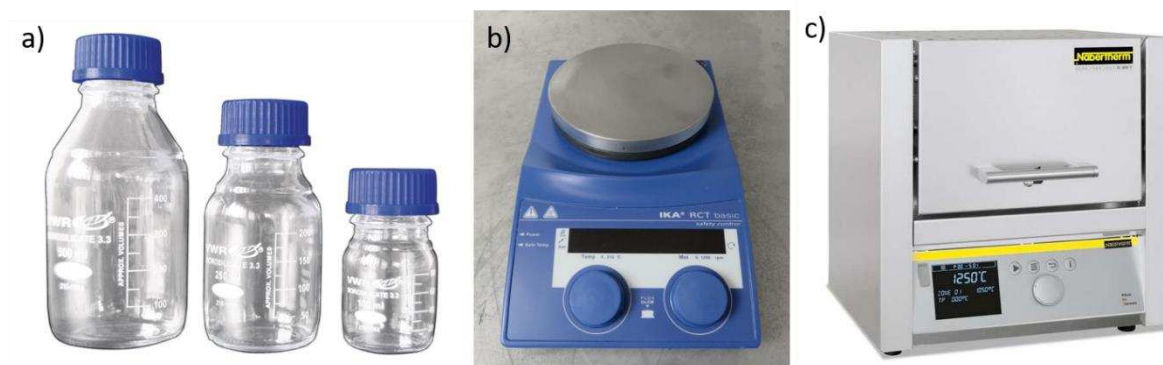


Figure 2: Typical equipment used for nanoparticle synthesis. a) Borosilicate vessels, b) heating plate, c) muffle furnace.

### CO<sub>2</sub> and borane adsorption experiments

CO<sub>2</sub> and borane adsorption experiments presented in Chapter IV were performed either in glass autoclaves from Buchi when CO<sub>2</sub> was involved, or in 5 mL vials from VWR when it was not the case. A custom gas system was used to fill the autoclave with CO<sub>2</sub>, N<sub>2</sub> or to connect the autoclave to a vacuum pump. The vial/autoclave was placed in an oil bath when heating was required.



Figure 3: Typical equipment used for adsorption reactions. a) Vials, b) autoclaves, c) gas system.

## Catalysis experiments

Claisen-Schmidt condensation reactions presented in Chapter III were performed in regular glassware under  $N_2$  with the use of a Schlenk ramp. The round-bottom flask was heated with a heating mantle; the temperature was controlled using a thermocouple inserted in a glass finger in contact with the solution.

Cycloaddition reactions presented in Chapter V were performed in the same autoclaves as the adsorption experiments. Oil bath was used to control the temperature of the reaction.

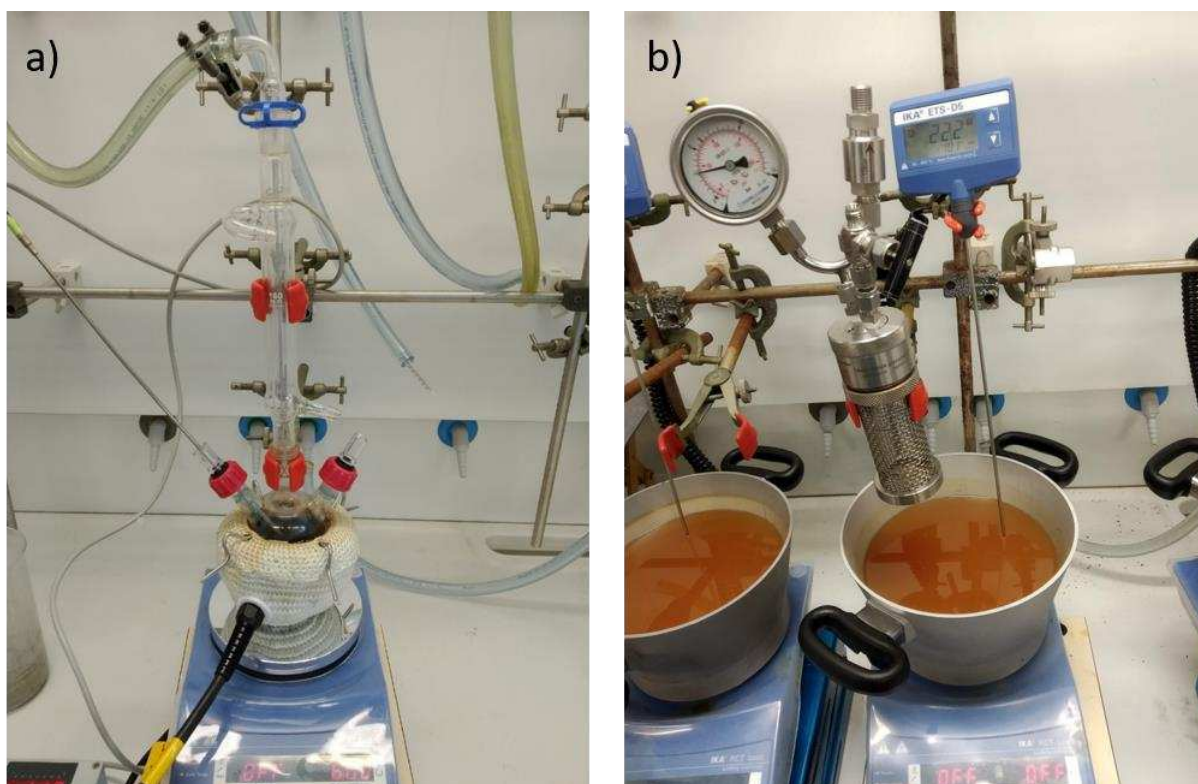


Figure 4: Typical experimental setup for: a) Claisen-Schmidt condensations, b) cycloaddition reactions.

### III. Characterisation techniques

#### Powder X-Ray Diffraction (XRD)

X-Ray diffraction patterns of dry powders were measured on a Bruker D8 diffractometer using Cu K $\alpha$  radiation at 1.5406 Å. Typical diffractograms were collected with steps of 0.05 ° and a scanning speed of 1 s/point. Debye-Scherrer analyses were conducted using the DiffracEva software. Used PDF cards reference were given in Table 1:

Phase	Mineral	PDF Card number
Mg(OH) <sub>2</sub>	Brucite	01-071-5972
MgCO <sub>3</sub>	Magnesite	01-071-1534
MgO	Periclase	00-004-0829
Ca(OH) <sub>2</sub>	Portlandite	00-044-1481
CaCO <sub>3</sub>	Calcite	00-005-0586
CaCO <sub>3</sub>	Vaterite	00-041-1475
CaO	Lime	00-037-1497
NaNO <sub>3</sub>	Nitratine	00-036-1474
NaCl	Halite	00-005-0628

Table 1: XRD references and PDF card numbers.

#### Transition Electron Microscopy (TEM)

For TEM analysis, a drop of diluted solution of nanoparticles dispersed in ethanol or toluene was allowed to dry on an amorphous carbon coated copper grid. TEM micrographs were collected with a TWIN 120 (TECNAI SPIRIT) operating at 120 kV.

#### Fourier Transform Infrared Spectroscopy (FTIR)

Infrared spectra were measured with a Spectrum 400 PerkinElmer spectrometer. The solids were pressed on the crystal in Attenuated Total Reflectance (ATR) mode and the transmittance was recorded on the 4000-600 cm<sup>-1</sup> range with steps of 0.5 cm<sup>-1</sup>. Deconvolution of the bands was performed using a modified version of the WinPlotr software from the FullProf suite. This software was initially designed to deconvolute XRD diffractograms, we wrote a Python script to adapt it for deconvolution of IR spectra.

#### Nuclear Magnetic resonance (NMR)

NMR experiments were performed on a Bruker AVIII 300 MHz. For catalysis, an aliquot of the solution was collected and directly mixed in 0.5 mL of CDCl<sub>3</sub> or toluene-d<sub>8</sub>. Spectra were

acquired after locking to the deuterated solvent signal and shimming. Typical  $^1\text{H}$  NMR spectra were acquired in 3 minutes and treated with TopSpin software. Typical  $^{11}\text{B}$  NMR spectra were acquired in 10 minutes and treated with TopSpin software. An echo was used to eliminate the boron component coming from the borosilicate glass of the NMR tube.

### **Scanning Transmission Electron Microscopy with energy Dispersive X-Ray (STEM-EDX)**

For STEM-EDX analysis, a drop of diluted solution of nanoparticles dispersed in ethanol or toluene was allowed to dry on an amorphous carbon coated copper grid. STEM-EDX micrographs and elemental analyses were collected with a JEM-2100 plus (JEOL) operating at 200 kV.

## IV. Contribution to published articles

During this PhD, I was involved in different side studies all part of the NanoFLP project that led to the publication of articles.

### Work on molybdenum containing nanoparticles XANES spectroscopy

In this work, we studied the X-ray Absorption Near Edge Structure (XANES) spectra of Mo containing materials. More precisely, we proposed a method to interpret the Mo  $L_{2,3}$  edges to determine the oxidation state and the geometrical environment of molybdenum in the analysed samples. We did these analyses at synchrotron SOLEIL on the LUCIA beamline. My specific contribution in this study was the preparation and the measurements of the referenced samples, as well as a critical review of the draft article.

Freitas, A. P.; André, R. F.; Poucin, C.; Le, T. K.-C.; Imbao, J.; Lassalle-Kaiser, B.; Carencó, S. Guidelines for the Molybdenum Oxidation State and Geometry from X-Ray Absorption Spectroscopy at the Mo  $L_{2,3}$  -Edges. *J. Phys. Chem. C* **2021**, *125* (32), 17761–17773. <https://doi.org/10.1021/acs.jpcc.1c01875>.

### Work on nickel@cobalt core-shell nanoparticles synthesis

In this work, we studied the synthesis of nickel@cobalt core-shell nanoparticles synthesis. We used a colloidal synthesis using  $Ni(acac)_2$  and  $Co_2(CO)_8$  as metal precursors, oleylamine as the solvent and trioctylphosphine (TOP) as a controlling agent. Impact of the TOP concentration and temperature ramps on the morphology of the nanoparticles were studied. The nanoparticles were studied using X-Ray diffraction (XRD), transmission electron microscopy (TEM), X-ray Absorption near Edge Structure spectroscopy (XANES), Extended X-ray absorption fine structure (EXAFS) and X-Ray photoelectron spectroscopy (XPS). My specific contribution in this work was the synthesis of the nanoparticles, the analysis of the XRD data and the writing of a part of the corresponding part of the article.

Palazzolo, A.; Poucin, C.; Freitas, A. P.; Ropp, A.; Bouillet, C.; Ersen, O.; Carencó, S. The Delicate Balance of Phase Speciation in Bimetallic Nickel Cobalt Nanoparticles. *Nanoscale* **2022**, *14* (20), 7547–7560. <https://doi.org/10.1039/D2NR00917J>.